

# Ultrafast Dynamics in Light-Harvesting Molecules with Optical and X-ray Spectroscopies

Hamburg, July 2021

*Tae Kyu Choi*

*FXE, European XFEL*

European X-Ray Free-Electron Laser Facility GmbH

Holzknoppel 4

22869 Schenefeld

Germany



# Ultrafast Dynamics in Light-Harvesting Molecules with Optical and X-ray Spectroscopies

**DISSERTATION**

zur Erlangung des Doktorgrades  
an der Fakultät für Mathematik, Informatik und  
Naturwissenschaften  
Fachbereich Chemie der Universität Hamburg

vorgelegt von

**Tae Kyu Choi**

aus Chuncheon, Südkorea

Hamburg

2021

Gutachter der Dissertation: Prof. Dr. Wojciech Gawelda  
Prof. Dr. Gabriel Bester

Gutachter der Disputation: Prof. Dr. Wojciech Gawelda  
Prof. Dr. Gabriel Bester  
Prof. Dr. Nils Huse  
Prof. Dr. Simone Mascotto  
Prof. Dr. Robin Santra

Datum der Disputation: 24.09.2021

Vorsitzender des Prüfungsausschusses: Prof. Dr. Gabriel Bester

---

# Contents

<b>List of publications</b> .....	<b>7</b>
<b>Zusammenfassung</b> .....	<b>8</b>
<b>Abstract</b> .....	<b>9</b>
<b>Acknowledgements</b> .....	<b>10</b>
<b>1 Introduction</b> .....	<b>12</b>
<b>2 Theoretical background</b> .....	<b>15</b>
2.1 Coordination chemistry .....	15
2.1.1 Cyclometalation and carbene coordination .....	18
2.1.2 Solvation and magnetism .....	19
2.2 Optical light-matter interaction.....	19
2.2.1 Absorption bands .....	20
2.2.2 Relaxation dynamics .....	23
2.2.3 Remark: Dark chemistry.....	27
2.3 X-ray light-matter interaction .....	27
2.3.1 X-ray absorption.....	28
2.3.2 X-ray fluorescence .....	36
2.3.3 Remark: Resonant inelastic X-ray scattering .....	42
<b>3 Experimental methodology</b> .....	<b>45</b>
3.1 Time-resolved experiments.....	45
3.2 Femtosecond optical laser system .....	48
3.2.1 Experimental setup at University of Bern .....	51
3.3 Synchrotron light source.....	54
3.3.1 11-ID-D Endstation at APS .....	58
3.4 X-ray free-electron laser (XFEL) .....	61
3.4.1 BL3EH2 Endstation at SACLA .....	63
3.4.2 FXE Endstation at European XFEL .....	66
<b>4 5d<sup>6</sup> Ir(III)-Co(III) photocatalyst</b> .....	<b>69</b>
4.1 Introduction.....	70
4.2 Experimental details .....	74
4.3 TOAS on Ir(III) photosensitizers .....	75

4.4	TOAS on Ir(III)-Co(III) triads .....	77
4.5	Conclusion and outlook.....	79
<b>5</b>	<b>4d<sup>6</sup> Ru(II)-Mo(VI) photocatalyst .....</b>	<b>81</b>
5.1	Introduction.....	82
5.2	Experimental details .....	84
5.3	TOAS on Ru(II) photosensitizers.....	85
5.4	TOAS on Ru(II)-Mo(VI) dyad .....	87
5.5	Conclusion and outlook.....	89
<b>6</b>	<b>4d<sup>6</sup> Ru(II) photosensitizer .....</b>	<b>92</b>
6.1	Introduction.....	93
6.2	Experimental details .....	96
6.3	Time-resolved EXAFS on Ru(II) photosensitizers .....	97
6.4	Lifetime studies in acetonitrile and water .....	101
6.5	Conclusion and outlook.....	102
<b>7</b>	<b>3d<sup>10</sup> Cu(I) photosensitizer .....</b>	<b>104</b>
7.1	Introduction.....	105
7.2	Experimental details .....	108
7.3	Femtosecond-resolved K $\alpha$ and K $\beta_{1,3}$ XES.....	109
7.4	Femtosecond-resolved K $\beta_{2,5}$ XES and XSS.....	114
7.5	Conclusion and outlook.....	116
<b>8</b>	<b>3d<sup>6</sup> Fe(II)-Co(III) photocatalyst .....</b>	<b>118</b>
8.1	Introduction.....	119
8.2	Experimental details .....	122
8.3	Femtosecond-resolved XES on Fe(II)-Co(III) dyad .....	123
8.4	Femtosecond-resolved XES on Fe(II) photosensitizer .....	128
8.5	Conclusion and outlook.....	131
<b>9</b>	<b>Outlook and perspective .....</b>	<b>133</b>
<b>A</b>	<b>PETRA III P01 data reduction .....</b>	<b>135</b>
<b>B</b>	<b>SACLA XES data reduction .....</b>	<b>138</b>
<b>C</b>	<b>Python data analysis codes.....</b>	<b>140</b>

<b>D</b>	<b>Supplementary information</b> .....	<b>141</b>
D.1	Chapter 4.....	141
D.2	Chapter 5.....	146
D.3	Chapter 6.....	147
D.4	Chapter 7.....	149
D.5	Chapter 8.....	151
<b>E</b>	<b>List of hazardous substances</b> .....	<b>154</b>
<b>F</b>	<b>Bibliography</b> .....	<b>155</b>
	<b>Eidesstattliche Versicherung</b> .....	<b>171</b>

---

# List of publications

- 1 Galler, A., Gawelda, W., Biednov, M., Bömer, C., Britz, A., Brockhauser, S., **Choi, T.-K.** *et al.* Scientific instrument Femtosecond X-ray Experiments (FXE): instrumentation and baseline experimental capabilities. *J. Synchrotron Rad.* **26**, 1432-1447 (2019).
- 2 Khakhulin, D., Otte, F., Biednov, M., Bömer, C., **Choi, T.-K.** *et al.* Ultrafast X-ray Photochemistry at European XFEL: Capabilities of the Femtosecond X-ray Experiments (FXE) Instrument. *Appl. Sci.* **10**, 995 (2020).
- 3 **Choi, T.-K.** *et al.* Femtosecond Molecular Flattening in  $[\text{Cu}(\text{dmp})_2]^+$  Probed by X-ray Emission Spectroscopy and Solution Scattering. *International Conference on Ultrafast Phenomena 2020*, 10.1364/UP.2020.Th1A.5 (2020).
- 4 Nazari Haghighi Pashaki, M., **Choi, T.-K.** *et al.* Unveiling the origin of photo-induced enhancement of oxidation catalysis at Mo(VI) centres of Ru(II)-Mo(VI) dyads. *Chem. Commun.* **57**, 4142-4145 (2021).
- 5 Huber-Gedert, M., Nowakowski, M., Kertmen, A., Burkhardt, L., Lindner, N., Schoch, R., Herbst-Irmer, R., Neuba, A., Schmitz, L., **Choi, T.-K.** *et al.* Fundamental Characterization, Photophysics and Photocatalysis of a Base Metal Iron(II)-Cobalt(III) Dyad. *Chem. Eur. J.* **27**, 9905-9918 (2021).

---

# Zusammenfassung

Lichtsammelnde Materialien, wie der Farbstoff N719, wurden als eine der Energiequellen der nächsten Generation eingeführt. Photophysikalische und elektrochemische Studien an solchen Systemen wurden durchgeführt, um die Lichtsammelphänomene zu verstehen, wobei ein besonderes Interesse an edelmetallfreien Photosensibilisatoren und Photokatalysatoren besteht. Die Realisierung von ultrakurzen optischen und Röntgenpulsen, zusammen mit ihren spektroskopischen Anwendungen, ermöglichte es, die entsprechenden ultraschnellen Veränderungen in den Photosensibilisatoren und Photokatalysatoren fein zu verfolgen, sowohl global als auch lokal.

Diese Studie untersucht die ultraschnelle Dynamik der Energieumwandlung in Modellkomplexen mittels ultraschneller optischer und röntgentechnischer Methoden, um weitere Einblicke in deren stationäre Leistungen zu erhalten. Unterschiede im optischen Absorptionsspektrum in Bezug auf die Ankunftszeitänderungen zwischen zwei Pulsen zeigten eine globale Wechselwirkung in einem bimetallic Photokatalysator wie Ir(III)-Co(III)-Triaden, Ru(II)-Mo(VI)-Dyaden und Fe(II)-Co(III)-Dyaden. Komplementäre, zeitaufgelöste Röntgenabsorptions- und -emissionsspektroskopie visualisierte die elektronischen und geometrischen Strukturänderungen des Elements, die inhärent die relevanten chemischen Ereignisse in photoaktiven Molekülen wie Ru(II), Cu(I) und Fe(II)-Photosensibilisatoren auslösen. Diese Studie zeigt, dass die 3d-Chelate nach der Ladungstrennung einen Femtosekunden schnellen Symmetriebruch durchlaufen, der oft nicht-strahlend rekombiniert, während die 4d- und 5d-Chelate mit ihrem chemischen Potential im Zustand der Ladungstrennung die nahegelegenen Elektronendichten so stören können, dass entweder eine chemische Energie oder ein Elektron auf der Pikosekunden-Zeitskala übertragen wird.

---

# Abstract

Light-harvesting materials, such as the N719 dye, have been introduced as one of the next-generation energy sources. Photophysical and electrochemical studies on such systems have been carried out to understand the light-harvesting phenomena with a particular interest in noble-metal free photosensitizers and photocatalysts. The realization of ultrashort optical and X-ray pulses together with their spectroscopic applications enabled to finely trace the corresponding ultrafast changes in the photosensitizers and photocatalysts, both globally and locally.

This study investigates the ultrafast dynamics of energy conversion in model complexes by means of ultrafast optical and X-ray methods to obtain more insights into their steady state performances. Differences in the optical absorption spectrum with respect to the arrival time changes between two pulses revealed a global interaction in a bimetallic photocatalyst such as Ir(III)-Co(III) triads, Ru(II)-Mo(VI) dyads, and Fe(II)-Co(III) dyads. Complementary to this, time-resolved X-ray absorption and emission spectroscopy visualized the electronic and geometric structure changes of the target element that inherently trigger the relevant chemical events in photoactive molecules like Ru(II), Cu(I), and Fe(II) photosensitizers. This study finds that the 3d-chelates undergo a femtosecond symmetry breaking after the charge separation that often recombines non-radiatively, whereas the 4d- and 5d-chelates with their chemical potential in the charge separation state can perturb the nearby electron densities such that either a chemical energy or an electron gets transferred on the picosecond timescale.

---

# Acknowledgements

This was quite an amount of knowledge and experience for such a novice like me within ~4 years of the Ph.D. course, and it was only possible with uncountable helps from my lovely people in all around the world.

First of all, I would love to thank both Prof. Dr. Christian Bressler and Prof. Dr. Wojciech Gawelda who offered me a Ph.D. position in FXE group at European XFEL, and taught me a lot of great lessons for the last four years. All the chances of networking, experiments, conferences, and publications were only possible with their helps. Particularly, I will never forget our funny memories at the XAFS 2018 conference in Kraków. :)

I would also like to thank other FXE (ex-)members who helped and encouraged me a lot during my stay at FXE, Dr. Chris Milne, Dr. Andreas Galler, Dr. Dmitry Khakhulin, Dr. Peter Zalden, Dr. Frederico Alves Lima, Dr. Katharina Kubicek, Dr. Angel Rodriguez-Fernandez, Dr. Sophie Canton, Dr. Alexander Britz, Dr. Mykola Biednov, Dr. Yifeng Jiang, Dr. Vandana Tiwari, Dr. Fernando Ardana-Lamas, Dr. Christina Bömer, Michael Diez, Florian Otte, Martin Knoll, Paul Frankenberger, and Timo Korsch. In addition, I appreciate all the helps from the European XFEL staff members and Ph.D. students in many different occasions, special thanks to Dr. Vasilii Bazhenov, Prof. Dr. Adrian Mancuso, Halimah Shie, Julia Galler, Dr. Chan Kim, Dr. Yoonhee Kim, Dr. Huijong Han, Dr. Tokushi Sato, Benoit Rio, René Wagner, Dr. Jia Liu, Marieke Sander, Dr. Frank Poppe, Karina Kazarian, Torsten Lange, Gabriella Mulá-Mathews, and Maik Neumann.

The whole Ph.D. course was under the IMPRS-UFAST graduate school at DESY, and there I would love to thank Dr. Julia Quante, Dr. Neda Lotfiomran, Dr. Sang-Kil Son, Prof. Dr. Nils Huse, Dr. Aleksandr Kalinko, Dr. Chiwon Lee, Hyein Hwang, Kyung-Min Lee, Jihyun Jeong, Dr. Young Yong Kim, Dr. Sihyun Sung, Manuel Harder, Daniel Haynes, and Ivette Bermúdez Macias for their numerous supports (special thanks to Prof. Dr. Gabriel Bester for his second supervision!). Also, from the University of Hamburg many people helped me, and I would like to thank Dr. Young-Joo Lee for her valuable advices.

After all, I learned significant amount of my current knowledge and hands-on experiences at SACLA during my internship stay for about two years, and I sincerely thank Dr. Makina Yabashi, Dr. Tetsuo Katayama, and Yasuko Matsumoto for their invaluable supports. In line with this, I would also like to thank all our collaborators

in various research projects so far, Prof. Dr. Andrea Cannizzo, Dr. Maryam Nazari Haghghi Pashaki, Prof. Dr. Anne-Kathrin Duhme-Klair, Dr. Xiaoyi Zhang, Dr. Kristoffer Haldrup, Dr. György Vankó, Dr. Jakub Szlachetko, Dr. Tom Penfold, Prof. Dr. Matthias Bauer, Dr. Michał Nowakowski, and Marina Huber-Gedert for their time to discuss with me.

Apart from the scientific activities, many precious memories with colleagues and friends helped me a lot to ease the arrival and settlement in Hamburg. A big hand goes to the FXE geeks, especially Dr. Christina Bömer, Michael Diez, and Florian Otte at the same office, always sharing lots of humors and laughs, hanging out together to the cool places and bars in Hamburg, such an everyday chit-chat really relaxed my Ph.D. studies. At the same time, I would love to thank Dr. Katharina Kubicek and René Wagner for sharing their time with me while I was writing the thesis, our regular dinner was one of my most important escape at that time. Countless barbecues, parties, picnics, Kohltours, Feierabendbierchen also with the korean society in Hamburg should be equally recognized, I am literally so much grateful for everything that I could receive during my Ph.D. course. One thing I must mention is the business trips that I made to the various occasions, I thank for all the supports on that way and really enjoyed the travels.

Last but not least, I would like to thank all my old friends and my beloved family, relatives who still cheer me up from Korea, and a special thanks goes to the family Heinrich and my love Vanessa Heinrich, who support me a lot in every single sense.

Finally, I would like to thank you for visiting and taking your time to read my thesis.

# 1 Introduction

Microscopic to macroscopic world, and vice versa.

The motivation to study physical chemistry became clearer during my doctoral course. That is, what has been described in modern physics with computational methods for microscopic world can be effectively correlated to macroscopic world *via* physical chemistry, such that one can "see" and understand the system from both points of view. In this regard the thesis will try to visualize both microscopic and macroscopic perspectives on light-harvesting materials, primarily consisting of inorganic chelates in solution phase. That means, the inorganic chelates in solution phase for light-harvesting applications will be investigated not only by applying quantized pictures to the system but also by translating them into chemistry terms of thermodynamics and kinetics. Furthermore, this thesis will also try to resolve the phenomena in time especially when it comes to the very first step of light-harvesting, unveiling the so-called ultrafast dynamics on picosecond or femtosecond timescale that determines how the intermediate and steady states of the system can be accomplished to chemically react further.

Inorganic chelates in solution (condensed) phase for light-harvesting applications have recently attracted a number of physicists, chemists, and other scientists all over the world not only because they in fact appear often in nature but also because their photophysical and electrochemical properties can be easily tuned compared to the organic counterparts, due predominantly to their rather simpler symmetry and thus clearer valence orbital energetics. In addition, the inorganic chelates are more robust with higher quantum yields of photoabsorption and luminescence owing to the strong ligand field in their ligand coordination. Hence, these inorganic chelates are frequently applicable to converting the solar energy to a transient molecular dipole, i.e. a transient electric potential ( $<1 \mu\text{s}$ ) inside the system, that can trigger consequent chemical reactions like photosynthesis. Although many of them have been quite thoroughly characterized in their ground and excited states, the underlying ultrafast electron and energy transfer processes in higher time resolution are still yet to be fully explored, in particular when the molecular orbitals, spin states, and vibrations in the excited state are strongly coupled to each other.

This thesis will therefore exploit the time-resolved experimental methodologies with ultrashort optical and X-ray pulses, to elucidate the ultrafast dynamics in some of the representative 5d-, 4d-, and 3d-chelates. Global interactions in a supramolecular photocatalyst for example can be observed with the optical probe window, whereas a local electronic or geometric structure change requires rather the X-ray probe window. The ultrafast phenomena interpreted with quantized energy and momentum diagrams will be then correlated to the infinite timescale properties, namely the steady state characteristics, further gaining insights into the corresponding light-harvesting reactions. At the end of the thesis we will realize how unique the light-harvesting processes are in terms of energy transformation, since the photon energy absorption at selective wavelengths by the inorganic chelates can lead to different reaction or relaxation pathways accordingly, which is not common in electrochemical and thermodynamical methods.

Chapter 2 starts with reviewing how the inorganic chelates in solution phase are understood in coordination chemistry. The ligand coordination to metal ion hybrid orbitals and the following  $\pi$ -donation backbonds configure a certain molecular symmetry and valence orbital energetics by the ligand field. This accompanies some characteristic optical absorption bands, at which the photoexcitation results in the localization of the excited electron either on the ligand or in the metal ion, eventually decaying back to the ground state radiatively or non-radiatively. The X-ray photoabsorption in contrast leads to a core-hole intermediate state that will be instantaneously refilled by an outer-shell electron, emitting the respective X-ray fluorescence. The photoelectron interacting with the coordination shell structure, and the final state of the X-ray fluorescence interacting with the spin density in the system, reveal the local electronic and geometric structures.

In Chapter 3, the time-resolved experiments with ultrashort optical and X-ray pulses will be reviewed. A brief history of the femtosecond optical laser system is followed by an actual setup at University of Bern that was employed for the transient optical absorption spectroscopy experiments in Chapter 4 and 5. Another brief history of the synchrotron light source will explain how the extremely bright and collimated X-ray pulses are generated that can be used for the optical pump X-ray probe absorption experiments (Chapter 6). Moreover, the recent realization of the X-ray free-electron lasers further enables to simultaneously monitor the femtosecond electronic and nuclear dynamics in a photosensitizer or photocatalyst, disentangling its strongly coupled degrees of freedom (Chapter 7 and 8). The relevant experimental setups in 11-ID-D endstation at Advanced Photon Source and in BL3EH2 endstation at SPring-8 Angstrom Compact free-electron LAser will be described.

In Chapter 4, the Ir(III)-Co(III) bimetallic photocatalysts with a newly synthesized

bridging ligand were subjected to the transient optical absorption spectroscopy, to visualize the ultrafast intramolecular electron transfer from the Ir(III) to Co(III) moiety that facilitates the photocatalytic proton reduction. An effective quenching of the excited electron density with a  $\sim 100$  ps time constant was observed, although its arrival in the Co(III) moiety was not detected.

In Chapter 5, a biomimetic Mo(VI) catalyst covalently linked to a Ru(II) photosensitizer was studied with the transient optical absorption spectroscopy method to elucidate the light-induced activation mechanism in the bimetallic photocatalyst. By comparing with the spectroelectrochemical oxidation spectrum of the catalytic Mo(VI) complex, a photo-induced intramolecular electron transfer from the vicinity of the Mo(VI) moiety towards the Ru(II) moiety was unveiled to occur on the picosecond timescale.

In Chapter 6, the geometric structures of the light-switching and photo-oxidizing Ru(II) photosensitizers in their excited states were obtained by exploiting the time-resolved X-ray absorption spectroscopy. The homo- and heteroleptic Ru(II) complexes with the localized excited electron on different ligands hardly showed any difference, even though the solvent molecule coordination effect and the thermal population of the metal-centered excited state were consistently observed.

In Chapter 7, the femtosecond-resolved X-ray emission spectroscopy and solution scattering experiments were simultaneously conducted on a model Cu(I) photosensitizer, to unravel its strongly coupled electronic and nuclear dynamics for the first picosecond after the optical photoabsorption. A molecular symmetry breaking with a 400-700 fs time constant was clearly identified together with the coherent vibrational wavepacket, but the spin-flip of the excited electron was not able to be distinguished within the probe time window.

In Chapter 8, a novel Fe(II)-Co(III) photocatalyst was subjected to the femtosecond-resolved X-ray emission spectroscopy experiments, because the intramolecular excited electron transfer from the Fe(II) to Co(III) moiety had not been detected by the transient optical absorption spectroscopy. A chemical energy transfer instead of the electron transfer was proven to occur on the femtosecond timescale, inducing the second excited electron in the Co(III) moiety.

---

## 2 Theoretical background

Science without numbers and equations is just a novel.

2.1	Coordination chemistry	15
2.1.1	Cyclometalation and carbene coordination	18
2.1.2	Solvation and magnetism	19
2.2	Optical light-matter interaction	19
2.2.1	Absorption bands	20
2.2.2	Relaxation dynamics	23
2.2.3	Remark: Dark chemistry	27
2.3	X-ray light-matter interaction	27
2.3.1	X-ray absorption	28
2.3.2	X-ray fluorescence	36
2.3.3	Remark: Resonant inelastic X-ray scattering	42

Before we start our journey to the time-resolved spectroscopy science, we will review some theoretical backgrounds for the inorganic chelates in solution phase as well as the optical and X-ray light-matter interaction. This thesis does not include all details behind the theories presented because either these are presumed to be known or these are beyond the scope of this thesis and can be found elsewhere. An additional purpose of this chapter is to make sure that we are sharing the same background knowledge and terminologies for later discussions. This chapter therefore consists of an overview on coordination chemistry, optical light-matter interactions for ultrafast optical photon energy transformation, and X-ray light-matter interactions for mapping the electronic and geometric structure of the inorganic chelates in solution phase.

---

### 2.1 Coordination chemistry

Coordination chemistry is one of the most important chemistry branches covering the science of transition metal complexes, which involves numerous applications in real world. The formation of transition metal complexes, namely one metal ion and more than one ligand molecule binding to each other as the simplest example, is thermodynamically favourable and can be also described as Lewis-acid and Lewis-base reaction. That means, two nonbonding electrons from the ligand molecule



**Figure 2.1:** A number of cobalt chelates in solution phase with different colors, i.e. different valence electronic structures absorbing selective wavelengths of incident visible light.

are donated to a vacant  $sp^n d^m$ -hybrid orbital from the metal ion, forming a covalent bond. The covalency of the bonds between the metal ion and the ligands depends on the effective partial charge of the ligands, and this affects the orbital energetics at the valence-level as well as the core-level of the metal ion [118; 42; 98].

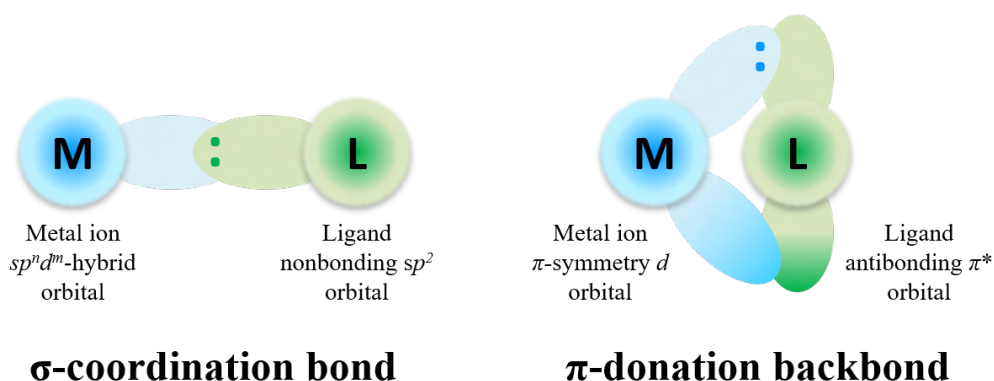


**Figure 2.2:** Schematic illustration of  $\sigma$ -coordination bond and  $\pi$ -donation backbond in transition metal complexes. The  $\pi$ -donation backbond follows the  $\sigma$ -coordination bond to balance the excessive electron density on the metal ion [98].

During the formation of a  $\sigma$ -coordination bond, a  $\pi$ -donation backbond follows with an overlap between an occupied  $\pi$ -symmetry  $d$ -orbital of the metal ion and an antibonding  $\pi^*$  orbital of the ligand, to balance the excessive electron density on the metal ion [98]. These valence orbital overlaps, i.e. bindings between the metal ion and the ligands, therefore configure a certain molecular symmetry to achieve the lowest potential energy of the system, exhibiting its structured energetics in optical absorption range (Fig. 2.1). In other words, the so-called ligand field ( $\Delta$ ) *via*  $\sigma$ - and  $\pi$ -character overlaps splits the valence molecular orbitals into a few energy levels

according to the symmetry, making the photoabsorption at certain wavelengths be more probable (Fig. 2.3).

The  $\pi$ -donation backbonds, which connect the valence occupied d-orbitals of the metal ion to the lowest unoccupied ligand  $\pi^*$  orbitals, play a very important role in so-called Metal-to-Ligand Charge Transfer (MLCT) transitions, leading to the transient molecular dipole which can trigger further chemical reactions for the light-harvesting. These MLCT transitions as well as core-to-valence and valence-to-core transitions, whose probabilities are highly dependent on the valence orbital overlaps between the metal ion and the ligands, will be discussed in later sections.

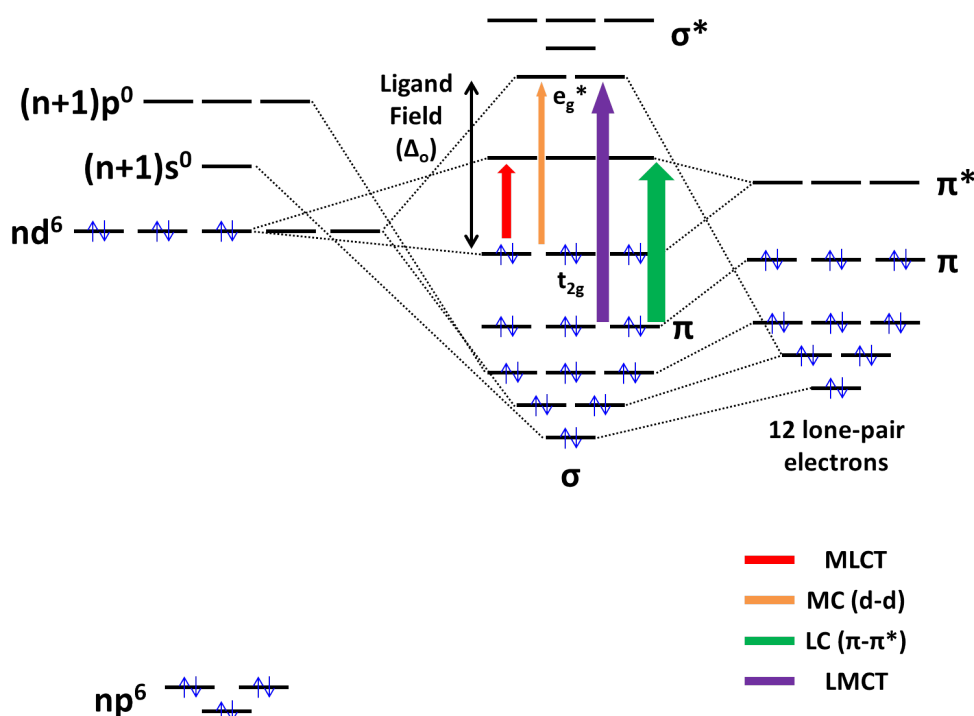


**Figure 2.3:** A simplified molecular orbital diagram of the  $nd^6$  transition metal complexes in octahedral symmetry (6 coordinations) represented with four probable photoexcitation pathways (MC = Metal-Centered, LC = Ligand-Centered, LMCT = Ligand-to-Metal Charge Transfer). Left-hand side represents the atomic orbitals of the metal ion, and right-hand side represents the molecular orbitals of the ligands. The color and thickness of each arrow indicate the relative photon energy needed for the corresponding dipole transition and its relative probability respectively. Here we assume that the ligands contain  $\pi$ -conjugation, which is in fact the primary case in this thesis. The ligand field splitting in  $nd$ -orbitals by  $\Delta_0$  stems from the  $\sigma$ - ( $d_{x^2-y^2}, d_{z^2}$ ) and  $\pi$ -symmetry ( $d_{xy}, d_{xz}, d_{yz}$ ) overlaps with the ligand valence orbitals.

## 2.1.1 Cyclometalation and carbene coordination

The ligand field, which determines the valence orbital energetics and thus the excited electron dynamics, varies on how the coordination bonds are formed. An electron lone-pair from nitrogen  $2sp^2$ -orbital is the most frequent source of the coordination bond, but that from carbon  $2sp^2$ -orbital is also commonly considered if necessary.

Two types of the carbon coordination will be introduced and discussed in this thesis; a cyclometalation reaction and a persistent carbene coordination. The cyclometalation mostly occurs on pyrolysis of the reaction mixture consisting of metal salt (M-X) and ligand molecule with good leaving group (H-C-...-N; [20]). According to the charge balance in this reaction (Fig. 2.4), the carbon atom after the reaction possesses one excessive electron in its nonbonding  $2sp^2$ -hybrid orbital which is coordinated to the metal ion [132; 48]. That means a negative formal charge on the carbon atom is exposed to the metal ion, influencing the valence electronic structure of the chelate *via* its ligand field [60]. In result the MLCT excited state on this cyclometalated ligand ( $\pi^*$  orbital) becomes energetically higher, letting the metal-to-ligand charge transfer be more directional to other ligands [15].

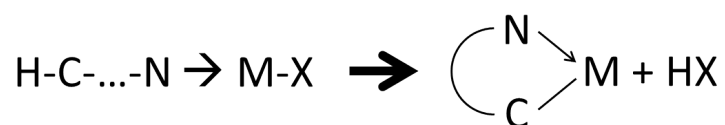


**Figure 2.4:** Cyclometalation. N = donor nitrogen, M = metal ion, H = leaving group (Figure from [20]).

On the other hand, a persistent carbene molecule such as N-heterocyclic carbene (NHC) contains a neutral carbon atom with two unshared valence electrons that is ready to coordinate. The stabilized carbon atom *via* the  $\sigma$ -coordination bond therefore does not have any  $\pi$ -character bond, i.e. any  $\pi$ -donation backbond with the metal ion. The NHC ligand is thus also called as a  $\pi$ -deficient ligand, and cannot balance the excessive electron density on the metal ion properly. Hence the MC excited state of the chelates with the NHC ligand, where an excited electron occupies one of  $e_g^*$  orbitals (Fig. 2.3), becomes energetically higher and less probable to be populated, whereas the MLCT excited state on the NHC ligand ( $\pi^*$  orbital) becomes relatively lower and more probable to be populated.

## 2.1.2 Solvation and magnetism

Once the orbital energetics in the inorganic chelates are settled by effective nuclear charges, valence hybridized orbitals of the metal ion coordinated with  $\sigma$ -donations from the ligand molecules, and accompanying  $\pi$ -back donations from the metal ion highest occupied molecular orbitals (HOMOs) to the ligand lowest unoccupied molecular orbitals (LUMOs), which collectively cause a certain symmetry in the molecular structure and thus the "ligand field", now the inorganic chelates are ready to be dissolved in solvent. Contrary to gas phase or lattice structure, in solution phase which is still a condensed phase, the inorganic chelates are so-called solvated by the surrounding solvent molecules. The solvation process in general equilibrates the system by forming its own "field" as well, in accordance with the local effective dipole moments of the solute and solvent molecules [153; 157]. The solvation shells, i.e. the solvent cages, consequently affect the valence orbital energetics of the solute.

Besides, when the ligand field becomes weaker by certain external stimuli such as temperature, pressure, or photoexcitation, some inorganic chelates especially from period 4 rearrange its electronic structure to reach the new lowest potential energy of the system [59]. This often returns unpaired parallel valence electrons resulting from coulomb interaction terms and spin-orbit coupling, forming a magnetic field in the system. This magnetic field from higher multiplicity in the inorganic chelates in turn affects the electric dipole transition processes like photon energy absorption and emission. Detailed discussion on the solvation effect as well as the magnetism will be however directly referred to at each relevant case in following sections and chapters.

---

## 2.2 Optical light-matter interaction

Since there is a sun, the optical light-matter interaction is always, everywhere on Earth. One should therefore notice that this means not only optical scattering but also optical photoabsorption and consequent photoemission or photodegradation may happen anytime if available.

The optical light-matter interaction, predominantly between visible light and valence electrons, covers from classical Fresnel equation to modern nonlinear optics. Optical photon energy ranges from  $\sim 1.5$  eV to  $\sim 3.5$  eV, and is in the low-energy limit of Compton scattering ( $\nu \ll \frac{m_e c^2}{h}$ ), thus when the optical photon interacts with the valence electrons Rayleigh scattering primarily happens rather than inelastic scattering, although Raman scattering can also happen. That means, the bound electrons in the valence orbitals with their oscillation frequency comparable to that of incident light accelerate by the electric field and resonate in phase with its polarization,

emitting the same photon energy in the same polarization (dipole radiation).

The refractive index  $n(\lambda)$  of the medium, namely the phase velocity  $\frac{c}{n(\lambda)}$  of electromagnetic wave in the medium, and the symmetry inside the medium are also very important in optical light-matter interaction especially when it comes to the optical laser, where the fluence of light can become so high that nonlinear effects occur. In this thesis however we will mostly consider particle-like properties of visible light, i.e. Einstein coefficients, and accompanying energy transformation between the optical photon and the bound valence electron. Here we assume that only one electron interacts with one photon at a time.

## 2.2.1 Absorption bands

Optical photoabsorption such as MLCT or LC transition (Fig. 2.3) is a dipole transition of a valence electron from an energetically lower state to a higher state or even continuum upon visible light absorption, or an imaginary part of the refractive index  $n(\lambda)$  of the medium. A well-known diagram and equation for the optical photoabsorption, i.e. optical attenuation, is the Beer-Lambert Law;

$$I(\lambda) = I_0(\lambda) * e^{-\epsilon(\lambda)cl} \quad (2.1)$$

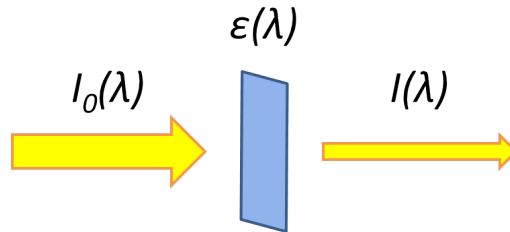


**Figure 2.5:** A representative illustration of Beer-Lambert law. Apart from scatterings and nonlinear effects, photoabsorption has the largest cross section particularly at low photon energy.

where  $I_0(\lambda)$  is the incident photon flux and  $I(\lambda)$  is the transmitted photon flux,  $\epsilon(\lambda)$  is the molar attenuation coefficient of the absorbent in case of solution phase,  $c[M]$  is the molar concentration of the absorbent and  $l[cm]$  is the optical path length. The molar attenuation coefficient  $\epsilon(\lambda)$  is directly related to the attenuation cross section  $\sigma(\lambda)$  of the absorbent like,

$$\sigma(\lambda)[cm^2] \sim 3.82353216 * 10^{-21} * \epsilon(\lambda) \quad (2.2)$$

Therefore by measuring  $-\ln \frac{I(\lambda)}{I_0(\lambda)}$  at certain absorbent concentration and optical path

length, we obtain  $\epsilon(\lambda)$  and  $\sigma(\lambda)$ . This wavelength-dependent attenuation coefficient or cross section indicates how probable the dipole transition upon corresponding photon energy absorption in the target system is, i.e. Einstein  $B_{12}$  coefficient.

The dipole transition from the ground state (GS) to the excited state (ES) and vice versa is instantaneous that all relevant coordinates or degrees of freedom in the inorganic chelates can be assumed to be stationary during the transition process (Franck-Condon principle). Thus, the vibrational overlap as well as the electronic space and spin overlap between the GS and the ES are maximized at higher vibrational level of the ES than that of the GS, resulting in so-called vibrationally "hot" excited state [186]. This region in a potential energy surface (PES) diagram with relevant coordinates to the inorganic chelates, where the dipole transition proceeds under the Franck-Condon principle, is therefore called as Franck-Condon region. This principle is one of the most important rules in spectroscopy and quantum chemistry, because the excessive vibrational energy not only triggers coherent nuclear motions at certain frequencies but also allows an additional access to other excited states while it dissipates into different nuclear and electronic degrees of freedom in the relaxation process.

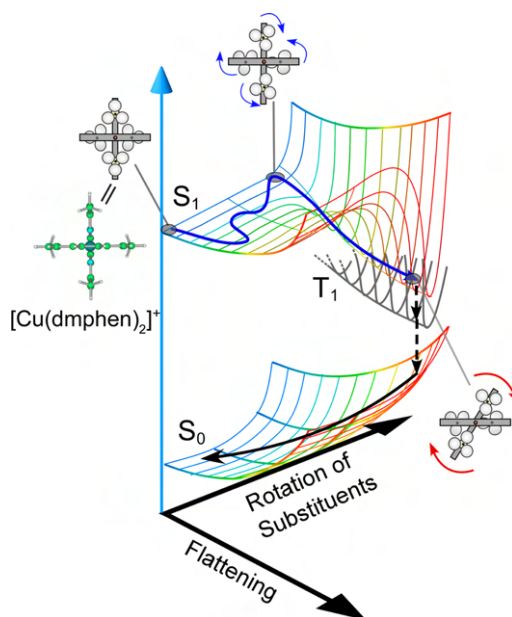


**Figure 2.6:** One example of the Franck-Condon principle represented in the PES diagram of a Cu(I) model complex (Figure from [94]). The sky blue arrow and the dashed arrow indicate two Franck-Condon regions where the relevant dipole transition occurs to a higher vibrational level of the final state.

Figure 2.7 shows optical photoabsorption spectra of several Fe(II) chelates with (pseudo-)octahedral symmetry in different solvents as an example [112]. Let's

first have a look on  $[\text{Fe}(\text{bpy})_3]^{2+}$  ( $\text{bpy} = 2,2'$ -bipyridine) in water. If we imagine a very similar molecular orbital diagram for this chelate with the one in Fig. 2.3, we recognize that the dipole transitions between 300 nm and 700 nm are not delta functions, i.e. not occurring in a very narrow photon energy range precisely from A state to B state, but rather broadened and overlapped with each other. This reflects not only the complexity of the valence orbital energetics in the inorganic chelates, but also the fundamental limit of probing the exact electronic structure inside the material. That is, the valence molecular orbitals consist of coupled electron clouds that are vulnerable to thermodynamic parameters like temperature or pressure, as well as nearby circumstances such as solvent molecules or dissolved oxygen surrounding the inorganic chelates, rearranging its electronic structure accordingly into a new equilibrated state and consequently allowing some additional dipole or even quadrupole transitions. Room temperature, namely  $\sim 25$  meV, for example may perturb the dipole transitions between different vibrational levels, and different solvent environments may vary the dipole transitions significantly. The fundamental limit in optical spectroscopy predominantly originates from instrumentation, in other words the incident electromagnetic wave is not ideally monochromatic, leading to the broadened dipole transitions in Gaussian profile. All these factors collectively result in the so-called absorption "bands".

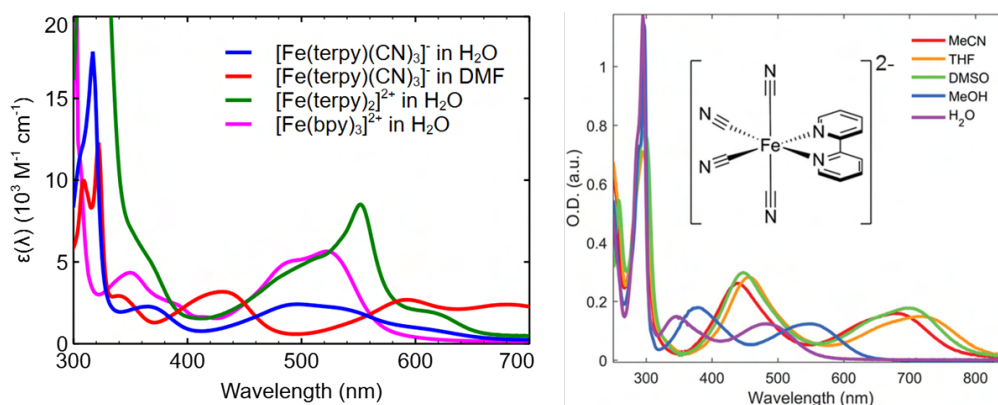


**Figure 2.7:** Optical photoabsorption spectra of several Fe(II) chelates with (pseudo-)octahedral symmetry in different solvents (terpy = 2,2';6',2"-terpyridine; Figure from [112]).

In case of  $[\text{Fe}(\text{bpy})_3]^{2+}$  in water, the absorption bands below  $\sim 320$  nm correspond to LC transitions (from ligand  $\pi$  to ligand  $\pi^*$ ), meaning that these absorption bands are characteristics of bpy-ligand. At least two absorption bands lie between  $\sim 320$  nm and  $\sim 400$  nm with the tails from the LC absorption bands overlapped, which correspond to MLCT transitions (from metal ion  $t_{2g}$  to ligand  $\pi^*$ ). Additional two absorption bands between  $\sim 460$  nm and  $\sim 560$  nm also correspond to MLCT transitions, but from the GS to the lowest singlet MLCT excited state (molecular spin multiplicity = 1), i.e. the lowest Franck-Condon state.

The analogous interpretation of the absorption bands can be applied to other Fe(II) chelates.  $[\text{Fe}(\text{terpy})_2]^{2+}$  in water however shows an additional MLCT absorption band above  $\sim 600$  nm, which corresponds to the spin-forbidden dipole transition from the singlet GS directly to the triplet MLCT excited state (molecular spin multiplicity = 3). Such a transition is formally forbidden by selection rule, but can be partially allowed especially when the molecular symmetry is not perfect and the nuclear vibrations of the chelates are coupled to its valence molecular orbitals, so that the spin-forbidden dipole transition gains some probability *via* overlapped spin-allowed transitions. Same applies to  $[\text{Fe}(\text{terpy})(\text{CN})_3]^-$  in water where one terpy-ligand is replaced by three cyanides, thus the molecular symmetry is even further broken. The absorption bands of  $[\text{Fe}(\text{terpy})(\text{CN})_3]^-$  change significantly however in DMF, demanding an additional perspective for its interpretation (solvatochromic effect).

In comparison with another similar case [112], where two bpy-ligands of  $[\text{Fe}(\text{bpy})_3]^{2+}$  are replaced by four cyanides, the same solvatochromic effect is observed particularly in the solvents with -OH hydroxyl group. The effect has been ascribed to the interaction of strong Lewis acidity solvents such as water or MeOH with the nitrogen lone-pair of the cyanide ligand, destabilizing the LUMOs on bpy-ligand. Hence the lowest MLCT absorption band corresponds to the lowest singlet MLCT excited state on the bpy- or terpy-ligand, and the second lowest MLCT absorption band corresponds to energetically higher MLCT excited state on the bpy- or terpy-ligand. Back to the  $[\text{Fe}(\text{terpy})(\text{CN})_3]^-$  in DMF, an absorption band above  $\sim 640$  nm is then attributed to the triplet MLCT excited state, and another between  $\sim 330$  nm and  $\sim 360$  nm is attributed to energetically much higher MLCT excited state on the bpy- or terpy-ligand.

Optical photoabsorption is a unique way of energy transformation in which the incident photon energy is harvested into the potential energy of the absorbent. Unlike electrochemical or thermal excitation, with the photon energy one can selectively approach to a specific excited state, being able to tune the behaviour of an excited electron, i.e. a quasi-particle, in a desired way.

## 2.2.2 Relaxation dynamics

Once a valence electron is promoted to the excited state manifold with an excessive vibrational energy, this intermediate state relaxes non-adiabatically within so-called ultrafast timescale, generally shorter than a  $\mu\text{s}$ , releasing its potential energy into different nuclear and electronic degrees of freedom and eventually getting back to the lowest equilibrium state, i.e. the GS. The intermediate state here is defined as an excited state where a vacancy in the HOMO orbital appears and in turn an

excited electron is present in one of the LUMO orbitals, thus forming a transient dipole moment inside the chelate under adjusted effective nuclear charges and shielding effects. In this state the ligand field predominantly becomes weaker due to a newly occupied antibonding molecular orbital and affects the electronic structure accordingly, which often stabilizes itself with higher multiplicity particularly in Fe(II) or Co(III)  $3d^6$  chelates.

Throughout the thesis we will primarily deal with the MLCT excited state, because in general compared to other excited states one can utilize the incident photon energy most efficiently [141]. According to the selection rule, the singlet MLCT state ( $^1\text{MLCT}$  state) is the most probable intermediate state right after the optical photoabsorption in the inorganic chelates. In this  $^1\text{MLCT}$  state, where the chelate still retains its symmetry, i.e. the Franck-Condon state, the chelate can fluoresce the same photon energy as the incidence by directly relaxing back to the GS [25; 69; 24; 94], or another competing relaxation pathway is a so-called intersystem crossing (ISC), flipping the spin state of an excited electron in  $^1\text{MLCT}$  manifold to the triplet ( $^3\text{MLCT}$  state; molecular spin multiplicity = 3). This spin-flip is very favourable since the  $^1\text{MLCT}$  and  $^3\text{MLCT}$  states are energetically and spatially so close to each other, proceeding typically within 100 fs which is way faster than the fluorescence ( $\sim 10$  ns), dominating the first relaxation pathway.

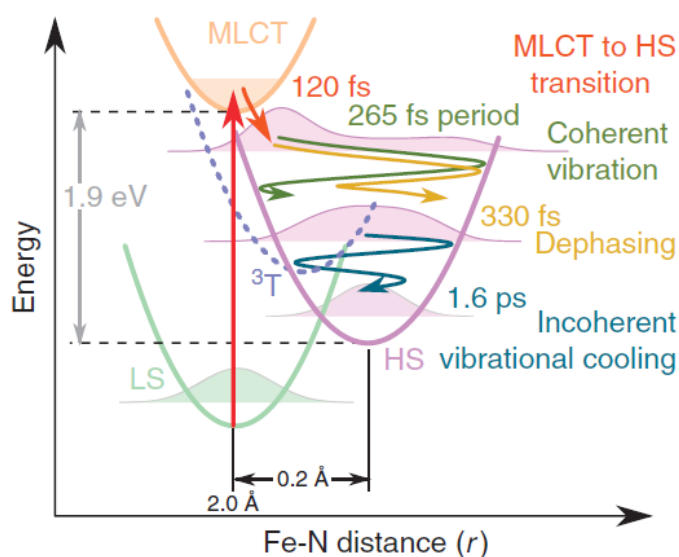


**Figure 2.8:** Schematic illustration of the relaxation dynamics in  $[\text{Fe}(\text{bpy})_3]^{2+}$  upon 530 nm photoexcitation, represented in Fe-N distance coordinate (LS = Low-Spin, HS = High-Spin; Figure from [123]).

At the same time the excessive vibrational energy in the  $^1,^3\text{MLCT}$  manifold starts dissipating into a few nuclear coherent motions at certain matching frequencies (Fig. 2.8). While following relevant relaxation dynamics proceed, the nuclear wavepacket

dephases and broadens non-adiabatically with its damping time constant of a few hundred of femtosecond [123].

The weakened ligand field also plays a very important role in the beginning of the relaxation as we shortly discussed, not only by rearranging the electronic structure but also by distorting the molecular symmetry accordingly to lower the overall energy of the chelate (Jahn-Teller effect). The Jahn-Teller effect as well as the coherent nuclear vibration is usually stronger where the electron density associated with the coordination bonds is more concentrated, i.e. in 3d-chelates than in 4d- or 5d-chelates. Hence the 3d-chelates, for example  $[\text{Fe}(\text{bpy})_3]^{2+}$  (Fig. 2.8), tend to undergo the spin-allowed transition named as spin crossover (SCO) from the  $^3\text{MLCT}$  state to a so-called HS state (molecular spin multiplicity  $> 3$ ) *via* the  $^3\text{MC}$  state (each of two parallel unpaired electrons in  $e_g^*$  and  $t_{2g}$  orbital respectively), and the distortion of its geometric structure from the Franck-Condon state to further minimize the overall energy of the intermediate state. Such a non-radiative decay from the MLCT state to the MC state also competes with another spin-forbidden radiative decay getting back to the GS, which thus phosphoresces a lower photon energy than the incidence [152]. The chelates with relatively weak ligand field (small  $\Delta$ ) therefore exhibit the high spin multiplicity as well as the distorted molecular structure without any phosphorescence upon photoexcitation, whereas the chelates with strong ligand field (large  $\Delta$ ) show the phosphorescence for a comparatively long lifetime, i.e.  $> 1$  ns, and keep its molecular symmetry [59].

The transient dipole moment in the  $^3\text{MLCT}$  state is not only the driving force to trigger the sequential reactions *via* energy transfer, but also the vulnerable instant where an electron acceptor can formally oxidize the chelate [141]. Thus residing in the  $^3\text{MLCT}$  state long enough for the following reactions to take place is the key of designing the light-harvesting inorganic chelates. In case of the 4d- and 5d-chelates, the ligand field is strong enough to have the  $^3\text{MLCT}$  state as the lowest excited state with a bit of exceptions in Ru(II)  $4d^6$  chelates [60]. In the 3d-chelates however, especially the Fe(II) or Co(III)  $3d^6$  chelates, the ligand field is often so weak that the LS to HS transition (SCO) dominates the second relaxation pathway, typically within 1 ps.

In this regard one way of tuning the ligand field in  $3d^6$  chelates is the NHC ligand coordination, replacing the nitrogen coordinations with the carbon ones. As we briefly reviewed in Section 2.1.1, the unbalanced electron density on the metal ion from the NHC ligand coordination consequently makes the MC excited states be energetically higher (Fig. 2.9), such that either the  $^3\text{MLCT}$  state or the  $^3\text{MC}$  state becomes the lowest excited state of the  $3d^6$  chelate, eventually extending the lifetime of the transient dipole moment in the  $^3\text{MLCT}$  state.

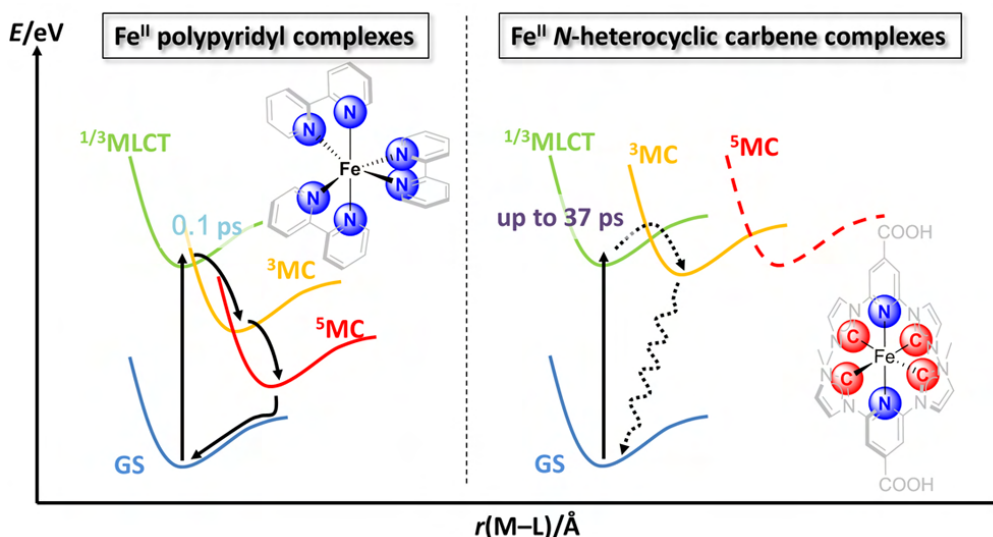


**Figure 2.9:** Comparison of the relaxation dynamics in  $[\text{Fe}(\text{bpy})_3]^{2+}$  (left) and one of the Fe(II) NHC chelates (right), where 4 nitrogen coordinations are replaced with carbon ones, represented in a simplified PES diagram of each system (Figure from [130]).

The third relaxation pathway from the MC excited states back to the GS is formally spin- and symmetry-forbidden and non-radiative, thus taking usually longer than  $\sim 100$  ps [24]. This relaxation is however still favourable because in the MC states the molecular symmetry is broken by the weakened ligand field, namely an occupied  $\sigma^*(e_g^*)$  molecular orbital, making the actual transitions be coupled with other dipole-allowed relaxation processes.

From the flashback to Fig. 2.3, we recognize that the excited electron, i.e. the quasi-particle, can be present in either a  $\pi^*$  molecular orbital or a  $\sigma^*$  molecular orbital, each of which corresponds to the MLCT state or the MC state respectively. Hence there are not many different options for the relaxation pathways in the inorganic chelates, but the complexity of it in fact comes from numerous couplings between vibrations, spin states, and orbitals at the valence-level. After each dipole transition between two quantum states, the vibrational level in the final state is higher than that in the initial state (Franck-Condon principle), and a so-called vibrational cooling to the lowest vibrational level in the final state takes usually a few to tens of picoseconds [34; 175]. The solvent cages also respond to the relaxation dynamics in the inorganic chelates upon photoexcitation, and the consequent rearrangement of the solvation shells proceeds on different timescales depending on the solvent viscosity and the number of nuclei involved, ranging from few tens of femtoseconds to hundreds of picoseconds [126; 180; 26].

### 2.2.3 Remark: Dark chemistry

What causes a chemical reaction? A spontaneous chemical reaction in a closed system occurs in the direction of lowering its free energy, i.e. the new equilibrium. A collision between reactants is a prerequisite for the spontaneous chemical reaction in a mobile phase, with exceptions of self-decomposition or isomerization. Rate-determining steps in the reaction could be therefore the collision of the reactants in a proper orientation, or the activation energy of the reaction to be overcome (Maxwell-Boltzmann distribution). Hence the chemical reaction is often limited by general diffusion processes, but still proceeds as long as the free energy of the system can be lowered.

As we briefly remarked before, the optical photoabsorption is a unique way of energy transformation since the resulting excited state, in other words the activated complex, can possess an enough potential energy to overcome the reaction barrier and thus open up the following reactions which are otherwise not at all spontaneous. At the same time however, many important chemical reactions in nature such as catalysis do not require visible light (dark chemistry). Thus what we have discussed in this section is not much relevant to the dark chemistry, but is yet essential for the light-driven chemistry like photosynthesis.

---

## 2.3 X-ray light-matter interaction

Unlike visible light, X-ray is neither always nor everywhere on Earth, but it is nevertheless familiar to us thanks to its useful applications in practice. X-ray, in German word Röntgenstrahlung, is defined as photon whose energy is between  $\sim 0.1$  keV and  $\sim 100$  keV, or electromagnetic wave whose wavelength is between  $\sim 12.4$  nm and  $\sim 0.124$  Å, although both soft X-ray region up to  $\sim 1$  keV and hard X-ray region above  $\sim 10$  keV can be also classified as extreme ultra-violet (EUV or XUV) and Gamma-ray respectively. Since such a broad range of photon energy can be identified as X-ray but the light-matter interaction quite differs depending on the photon energy, commonly the X-ray science differentiates it into the soft X-ray (up to  $\sim 3$  keV) and the hard X-ray (above  $\sim 5$  keV). The photon energy between  $\sim 3$  keV and  $\sim 5$  keV is often named as tender X-ray, but this photon energy is less accessible either due to the limited number of available photon sources or interesting scientific cases. This thesis will predominantly handle the hard X-ray and its interaction with the core-level electrons in the metal ion, because these are highly relevant to mapping the electronic and geometric structure of the inorganic chelates rather than other X-ray regime.

The hard X-ray photon energy covers from K-shell absorption edge of Titanium to that

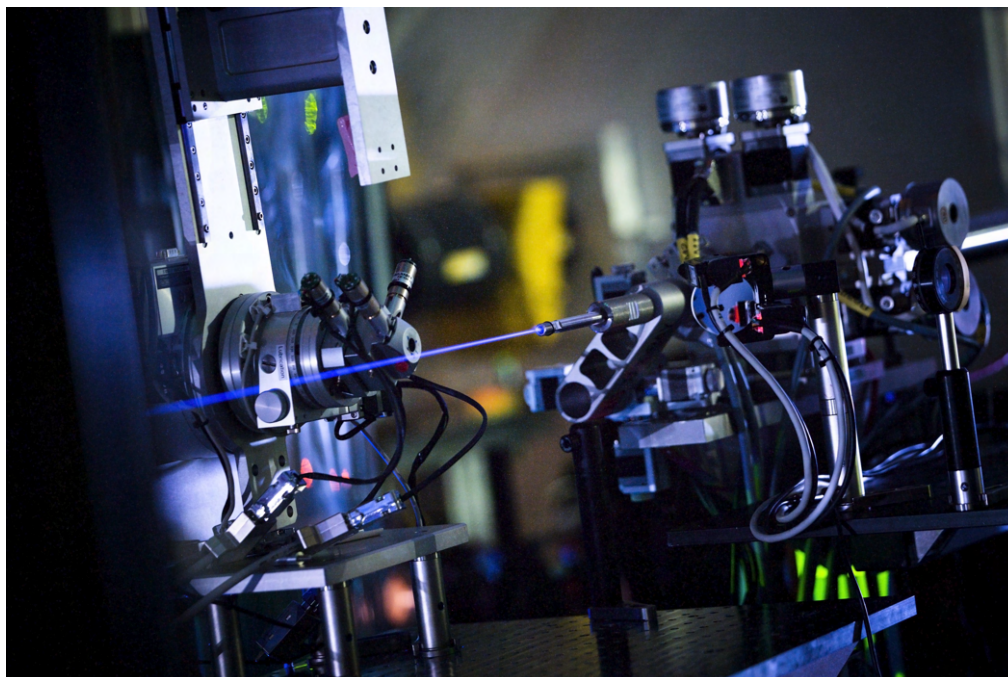


**Figure 2.10:** The femtosecond, coherent hard X-ray beam from the SASE1 undulator at European XFEL. The fluorescence emitted by irradiated nitrogen molecules in air was recorded (Figure from European XFEL).

of all base and noble metals, and the hard X-ray wavelength ranges from  $\sim 2.48 \text{ \AA}$  to  $\sim 0.124 \text{ \AA}$  which is on the scale of all kinds of chemical bond lengths or even shorter. Hence the hard X-ray is the best probe for the inorganic chelates in solution phase not only to element-specifically investigate its electronic structure by K-shell core-hole spectroscopy, but also to directly observe the distribution of chemical bond lengths inside by X-ray solution scattering. In the end, strongly coupled ultrafast dynamics in the inorganic chelates upon optical photoexcitation can be disentangled with these simultaneous and complementary hard X-ray techniques.

### 2.3.1 X-ray absorption

The hard X-ray light-matter interaction is by itself an established research field concerning the refractive index  $n(\lambda)$  smaller than 1 in any material (thus the phase velocity  $\frac{c}{n(\lambda)}$  of the X-ray in any material "exceeds" the speed of light in vacuum) and the Bragg's law (reflection geometry; the Laue equations in transmission geometry won't be discussed in this thesis). Moreover when it comes to the X-ray optics, one should take account of both the real and imaginary part of the refractive index at certain incident photon energy in certain material, since the X-ray photoabsorption and accompanying thermal deformation (heat load) of the material can affect its

refractive index accordingly. This is also important in terms of the loss of X-ray photon flux, and in case of Bragg diffraction resulting changes in the lattice constant of the crystal can broaden the diffracted beam in energy.

In this thesis the incident photon energy between  $\sim 7$  keV and  $\sim 22$  keV will be primarily discussed, and as shown in Fig. 2.11, within this range the X-ray photoabsorption dominates the light-matter interaction unless the incident angle is close to the critical angle of the surface material or satisfies the Bragg's condition, although for light elements such as carbon or nitrogen the incoherent (e.g. Compton) scattering processes start dominating above  $\sim 20$  keV. Therefore, in the following sections and chapters the K-shell core-hole spectroscopy upon X-ray photoabsorption will be the central topic.

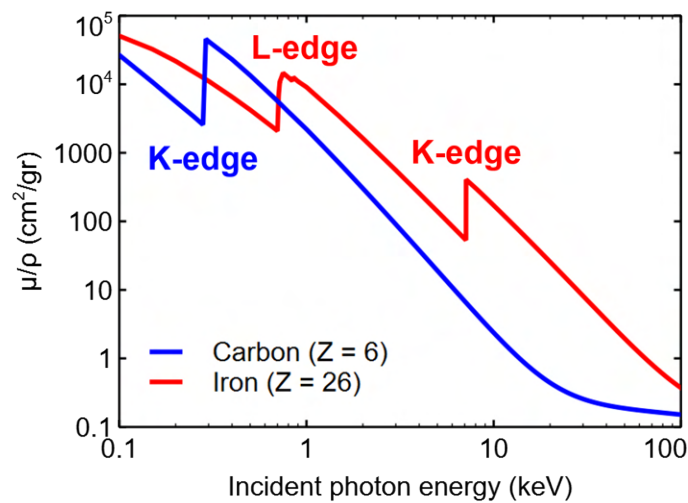


**Figure 2.11:** X-ray mass attenuation coefficients for all the cross sections in carbon and iron. The X-ray photoabsorption is the main process that causes X-ray attenuation in carbon and iron up to  $\sim 20$  keV (Figure from <https://xraypy.github.io/XrayDB/>).

The K-shell core-hole spectroscopy in general consists of X-ray absorption spectroscopy (XAS) and X-ray emission spectroscopy (XES). Briefly speaking, the incident hard X-ray photon ejects one of the K-shell electrons in the metal ion, i.e. one of the  $1s^2$  electrons by photoelectric effect, either completely (photoelectron) or into one of the unoccupied (and also the unpaired) valence orbitals depending on the photon energy (see also the Fermi's golden rule from time-dependent perturbation theory). In other words, as the incident photon energy gets higher across the so-called K-edge (K-shell absorption edge) of the metal ion, the  $1s$  electron undergoes a dipole transition first to the unoccupied or unpaired valence orbital (pre-edge absorption), and afterwards to the continuum (post-edge absorption), becoming a photoelectron whose energy is approximately the difference between the incident photon energy and the binding energy of itself.

Right after this dipole transition, one core-hole in the K-shell thus appears which will be immediately refilled by one of the outer electrons in the metal ion, releasing the corresponding potential energy difference in hard X-ray fluorescence. Such a dipole-allowed transition therefore only involves 2p- and 3p-orbitals in case of the 3d-chelates, and the X-ray fluorescence from each orbital is called as  $K\alpha$  and  $K\beta_{1,3}$  emission lines respectively. Another very small cross section still exists at higher fluorescence energy than the  $K\beta_{1,3}$  emission lines, namely the  $K\beta_{2,5}$  emission lines, which involve not only the quadrupole transitions from 3d-orbitals but also the so-called cross-over transitions from ligand  $2sp^2$ - and  $\pi$ -orbitals. The cross-over transitions are possible thanks to the valence orbital overlaps between the metal ion and the ligands, and will be discussed in the following section. The consequent hole state in the outer shell after the hard X-ray fluorescence will be then refilled by either an electron from the valence orbitals or the photoelectron from the X-ray photoabsorption (the Auger effect will be also discussed in the following section).

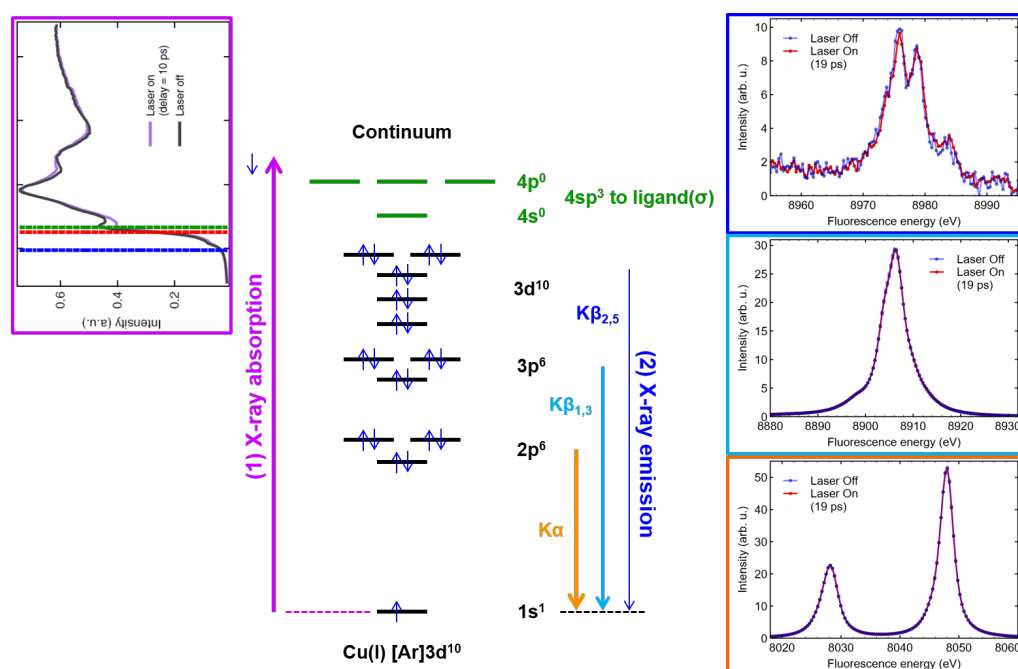


**Figure 2.12:** K-shell core-hole spectroscopy on a Cu(I) model complex in solution phase. The simplified atomic orbital diagram represents the core-hole intermediate state right after the X-ray absorption and before the X-ray emission. The corresponding XAS spectrum (Figure from [102]) and XES spectra are also shown.

Hence, the XAS is optimal to investigate the unoccupied valence electronic structure as well as the first and second coordination shell structure, whereas the XES is unique for studying the occupied core- and valence-level electronic structure, both in an element-specific manner. Figure 2.12 shows an example of the K-shell core-hole spectroscopy.

X-ray absorption fine structure (XAFS) refers to the complex absorption feature in the vicinity of the K-edge of target element, including the pre-edge structure and the so-called white line (intense absorption peaks near the K-edge). The region is also named as X-ray absorption near edge structure (XANES; Fig. 2.13), and its complexity originates not only from the coupled valence molecular orbitals but also from the core-hole intermediate state. That means, in case of single atom XANES in gas phase such as noble gases its spectrum is relatively featureless, and when it comes to the specific chemical environment surrounding the target element its spectrum shows quite consistent XAFS features (Fig. 2.15). It is trivial that the core-hole intermediate state (Fig. 2.12) is extremely unstable, and thus perturbs the effective nuclear charge as well as the overall electron clouds accordingly. In terms of the Fermi's golden rule this state is the final state of a dipole transition upon the X-ray absorption, and the probability of this transition, i.e. the photoabsorption cross section, therefore reflects the strength of the coupling between the initial state (GS) and the final perturbed state. In other words, the XANES feature is often difficult to be attributed to one particular transition, but rather to the mixture of many different contributions in the complex system (e.g. the coupled valence molecular orbitals getting further perturbed in the final state).

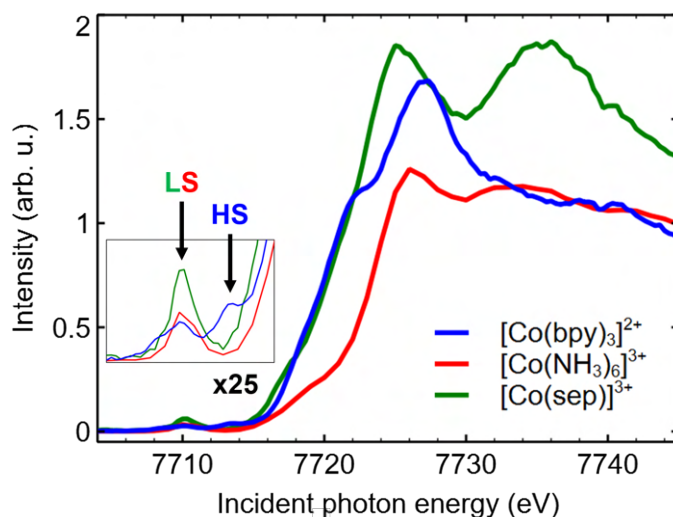


**Figure 2.13:** XANES spectra of three cobalt chelates (sep = sepulchrates) in solution phase measured with  $K\alpha_1$  high-energy-resolution fluorescence detection (HERFD) technique. All three complexes have 6 nitrogen coordinations and (pseudo-)octahedral symmetry. The pre-edge structure clearly identifies the spin density in each system, whereas the post-edge structure does not show any straightforward information.

The pre-edge structure however is sensitive to the molecular symmetry and spin density (Fig. 2.13), mainly because the corresponding dipole transition concerns the core-to-valence transition (1s to 3d for the 3d-chelates) which is formally symmetry-forbidden. This is yet another privilege of the K-shell core-hole

spectroscopy compared to its soft X-ray counterpart ( $L_3$ -shell core-hole spectroscopy), namely the dipole-forbidden core-to-valence and valence-to-core transitions become partially allowed if the molecular symmetry gets distorted or the spin density gets coupled to other degrees of freedom, such that the pre-edge absorption gains high sensitivity to the valence electronic and geometric structure [74].

It is noteworthy that the binding energy of the 1s electron is not necessarily equal to the K-edge energy, since the final state of the K-edge absorption, i.e. the core-hole intermediate state, affects the energy needed for the transition. Once the incident photon energy exceeds the K-edge energy, the 1s electron becomes a photoelectron with the extra kinetic energy being the difference between the incident photon energy ( $E_i$ ) and the K-edge energy ( $E_K$ ), and propagates to the neighboring ligand system as an outgoing quantum wave with its wavenumber  $k$ .

$$k = \frac{2\pi}{\lambda} = \sqrt{\frac{2m_e(E_i - E_K)}{h}} \quad (2.3)$$

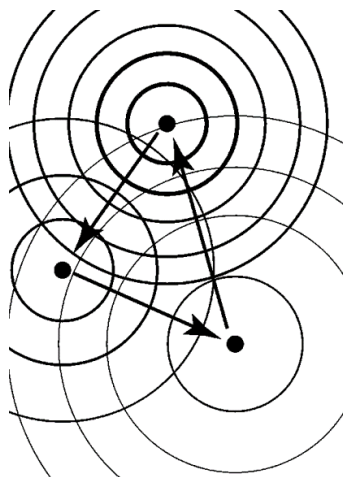


**Figure 2.14:** Pictorial view of the multiple scattering of an outgoing wave off neighboring atoms (Figure from [164]). The topmost atom is the original source of the wave, which diffracts first off the atom at the lower left and finally off the atom at the lower right. Each successive outgoing spherical wave is weaker, which is reflected in the thickness of the spherical wavefronts.

where  $\lambda$  is the de Broglie wavelength of the photoelectron,  $m_e$  is the electron mass, and  $h$  is the reduced Planck constant. The photoelectron wave will then reflect off of the nearest atom once encountered, and in turn reflects another quantum wave back toward the origin, so will other nearby atoms reflect the photoelectron wave back towards the original atom (Fig. 2.14; [164]). The amplitude of all the reflected quantum waves at the X-ray absorbing atom add either constructively or destructively to the outgoing photoelectron wave and hence modulate the transition matrix element in the Fermi's golden rule between the initial state (GS) and the final core-hole state, which controls the strength of the corresponding X-ray photoabsorption. Because this

interference pattern changes with the energy of the photoelectron, i.e. its de Broglie wavelength  $\lambda$ , the matrix element and consequently the X-ray absorption will exhibit similar oscillations (Fig. 2.15). These generally weak oscillatory wiggles beyond about 30 eV above the K-edge are termed EXAFS (extended X-ray absorption fine structure).

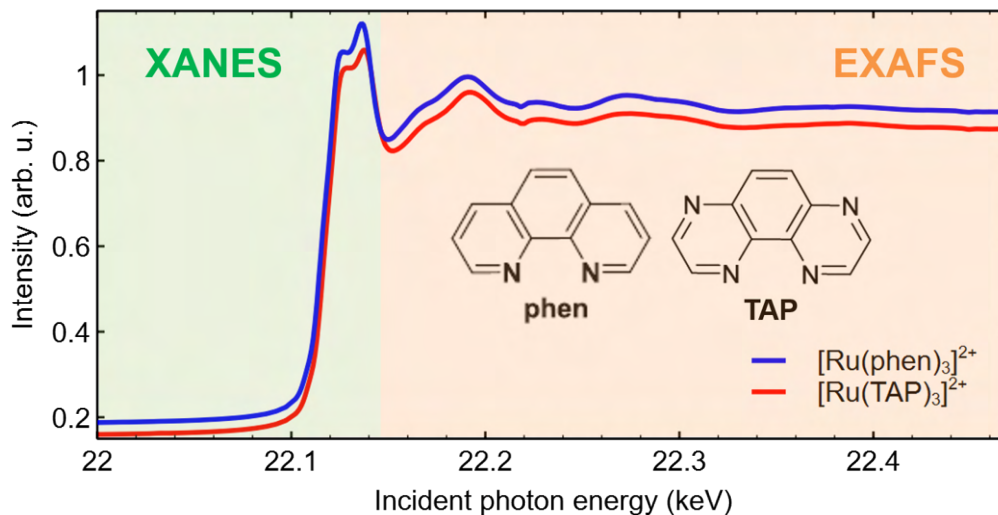


**Figure 2.15:** XANES and EXAFS spectra of two ruthenium chelates in solution phase (phen = 1,10-phenanthroline; TAP = 1,4,5,8-tetraazaphenanthrene) measured in total-fluorescence-yield (TFY) mode. Given the similar chemical environment near the Ru(II) ion, the XANES features as well as the EXAFS features of  $[\text{Ru}(\text{phen})_3]^{2+}$  and  $[\text{Ru}(\text{TAP})_3]^{2+}$  are almost identical.

The EXAFS contains precise information about the local atomic structure around the atom that absorbed the X-ray, namely the first and second coordination shell structure in case of the inorganic chelates. This is because the final core-hole state, i.e. the photoelectron state, and its wavelike nature must interfere with the neighboring atomic structure as noted above. The theory of EXAFS has been therefore quantitatively parameterized like the following equation,

$$\chi(k) = S_0^2 \sum_R N_R \frac{|f_{\text{eff}}(k)|}{kR^2} * \sin(2kR + 2\delta_c + \Phi) e^{-2R/\lambda_k} e^{-2\sigma^2 k^2} \quad (2.4)$$

where the structural parameters are the interatomic distances  $R$ , the coordination number  $N_R$ , and the temperature-dependent root-mean-square (rms) fluctuation in bond length  $\sigma$ , which should also include effects due to structural disorder. In addition,  $|f_{\text{eff}}(k)|$  is the effective backscattering amplitude,  $\delta_c$  is central-atom partial-wave phase shift of the final state [164], and  $\lambda_k$  is the energy-dependent mean-free-path of the photoelectron predominantly limited by inelastic losses as the quantum wave traverses the material. For a wave reflected straight back by a neighboring shell of atoms in distance  $R$ , the phase difference between the outgoing photoelectron wave

and the reflected wave is approximately  $2kR$ . Thus the dependence of the oscillatory structure on interatomic distance and energy is clearly reflected by the  $\sin(2kR)$  term. The decay of the wave due to the mean-free-path or finite lifetime (including core-hole lifetime) of the photoelectron is captured by the exponential term  $e^{-2R/\lambda_k}$ . The phase shifts  $\delta_c$  and  $\Phi$  account for the difference between the measured and geometrical interatomic distances. The Debye-Waller factor, i.e. the vibrational damping,  $e^{-2\sigma^2 k^2}$  is due partly to thermal effects, which cause all of the atoms to jiggle around their equilibrium atomic positions. Finally, the overall amplitude factor  $S_0^2$  is a many-body effect due to the relaxation of the system in response to the creation of the core-hole (the shielding effect becomes weaker and the electrons become more stable). The normalized EXAFS spectrum  $\chi(k)$  is obtained from,

$$\chi(k) = [\mu(k) - \mu_0(k)]/\Delta\mu_0 \quad (2.5)$$

where the X-ray absorption coefficient  $\mu(k)$  without the atomic-like background absorption  $\mu_0(k)$  is normalized by  $\Delta\mu_0$  [164], and conventionally defined with respect to the photoelectron momentum index  $k$  (2.3).

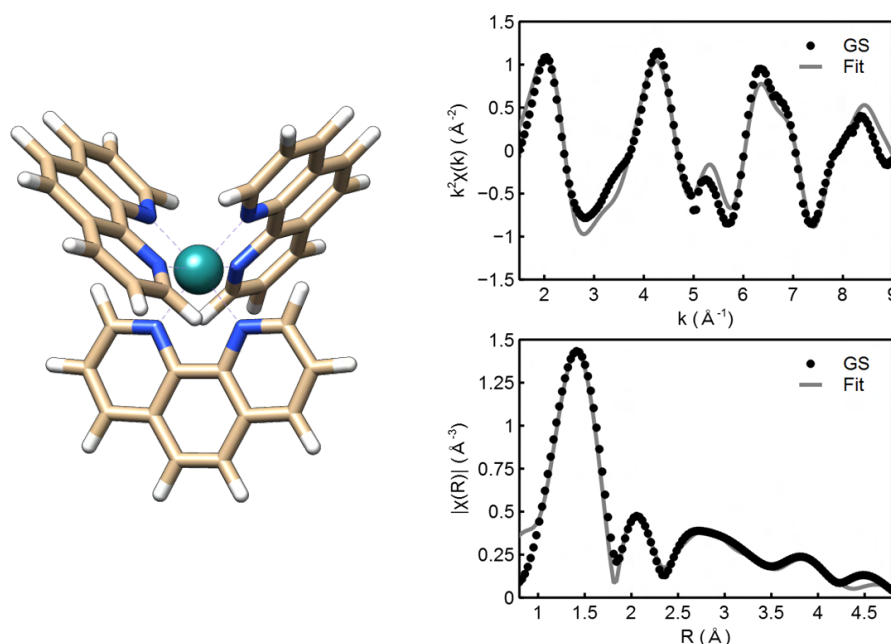


**Figure 2.16:** (left) A geometric structure of  $[\text{Ru}(\text{phen})_3]^{2+}$  illustrated by Chimera (center oceanblue: Ru(II), blue: nitrogen, beige: carbon, white: hydrogen), (right) the normalized EXAFS spectrum of  $[\text{Ru}(\text{phen})_3]^{2+}$  from Fig. 2.15 weighted by  $k^2$  (above) and its Fourier transform  $|\chi(R)|$  (below). The fitting result of the EXAFS equation (2.4) to the experimental data is also shown. The interatomic distance to the first coordination shell is  $\sim 0.5$  Å shorter than the geometrical value ( $R \sim 2.06$  Å), since the standard equation (2.4) does not include the 1s core-hole lifetime-broadening effect especially for the element with  $Z > 40$  [181].

Figure 2.16 shows the  $\chi(k)$  spectrum of  $[\text{Ru}(\text{phen})_3]^{2+}$  weighted by  $k^2$  as an example, along with the fitting result of the EXAFS equation (2.4) to the experimental data ( $S_0^2 \sim 0.91$ ,  $R \sim 2.06 \text{ \AA}$ ,  $N_R = 6$ ,  $\sigma^2 \sim 0.0021$ ; detailed data process and fitting procedure can be found in Chapter 6). The Fourier transform of the  $\chi(k)$  spectrum corresponds to the effective radial distribution function  $|\chi(R)|$ , with peaks near the first few neighboring shell distances [164]. Although the  $|\chi(R)|$  reveals several peaks up to  $\sim 4 \text{ \AA}$  or longer (Fig. 2.16), for the inorganic chelates only the first and second coordination shell structure could be clearly identified owing to the  $e^{-2R/\lambda_k}$  term. That means, the effective mean-free-path of the photoelectron wave is limited by not only the inelastic losses on the way of propagation but also the 1s core-hole lifetime, so that the coordination shells further away cannot significantly interact with the quantum wave [181].

The 1s core-hole lifetime refers to the decay time constant of the 1s core-hole state by the X-ray fluorescence, and this restricts the spatial resolution in the  $|\chi(R)|$  in terms of the limited mean-free-path, which simultaneously indicates that the energy resolution in the  $\chi(k)$  spectrum is also limited. Through the Heisenberg uncertainty principle, any state with a finite lifetime does not have a sharp, delta-function-like energy level, but rather a lifetime-broadened energy level. This gives rise to an energy uncertainty of the level inversely proportional to its lifetime, i.e.  $t \sim h/\Delta E$ .

In case of the optical photoabsorption, the excited state lifetime generally ranges from  $\sim 1 \text{ ps}$  to  $\sim 1 \text{ \mu s}$ , which returns the energy uncertainty of  $\sim 1 \text{ meV}$  or smaller that is negligible compared to the half width at half maximum (HWHM) of a usual femtosecond pulse in energy. On the other hand, the excited state lifetime upon the X-ray photoabsorption, namely the 1s core-hole state lifetime in our case, is  $\sim 1 \text{ fs}$  or even shorter for the transition metal elements and this leads to the energy uncertainty of  $\sim 1 \text{ eV}$  or larger [116]. In other words, the final state of the X-ray absorption is uncertain in energy, making the XAFS (XANES + EXAFS) spectrum be broadened.

As we discussed earlier on the energy-broadening in the optical absorption bands, i.e. the fundamental limit of probing the exact electronic structure inside the material, for K-shell core-hole spectroscopy the fundamental limit usually lies on the 1s core-hole lifetime-broadening, namely the natural level width of the corresponding K-shell, which results in the broadened dipole transitions in Lorentzian profile [181]. The lifetime-broadening effect is frequently found in X-ray spectroscopies, especially if the core-shell is so deep in potential energy that its absorption edge is in the hard X-ray region [116]. Hence this effect will be also one of the central topics in the following sections.

## 2.3.2 X-ray fluorescence

Now we are in the second phase of the X-ray photoelectric effect upon the X-ray absorption (Fig. 2.12). As noted earlier, the 1s core-hole in the intermediate state will be refilled after its lifetime in accordance with the selection and golden rule, i.e. the highest probability lies on the 2p to 1s dipole transition ( $K\alpha$  emission lines) followed by the 3p to 1s dipole transition ( $K\beta_{1,3}$  emission lines). Thus, for the X-ray fluorescence the initial state is the 1s core-hole state and the final state is yet another core- or valence-hole state, not the GS (Fig. 2.17). That means, the X-ray fluorescence rate is now determined by the strength of the coupling between the lifetime-broadened 1s core-hole state and the final lifetime-broadened core- or valence-hole state.

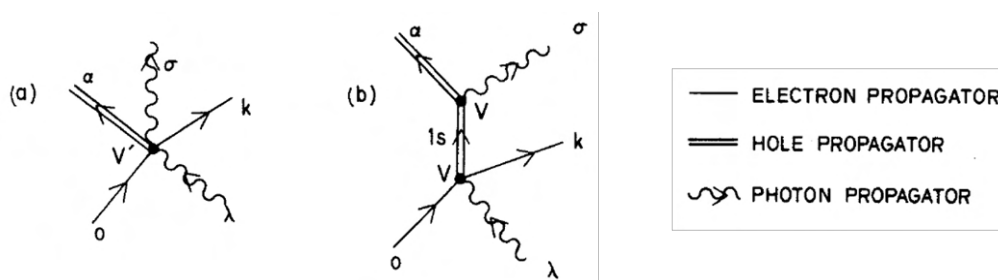


**Figure 2.17:** (a) The first- and (b) second-order processes in the X-ray photoelectric effect (Figure from [181]). In the first-order transition an atom in the GS ( $o$ ) absorbs an X-ray photon in mode  $\lambda$ , and the atom gets excited to a photoelectron state  $k$  with the refilled core-hole by an outer electron from a state  $\alpha$ , which consequently emits the X-ray fluorescence  $\sigma$ . In the second-order diagram, now there is a core-hole lifetime which delays the refilling process.

In the previous section, the critical factors for the XAS on the inorganic chelates were the incident photon energy and the corresponding final state of the X-ray absorption, even though this is quite complicated for the inorganic chelates. The resulting core-hole state has a very short lifetime which leads to the lifetime-broadened X-ray absorption in Lorentzian profile (the K-level width in HWHM,  $\Gamma_K$ ; [116]). The 1s core-hole will be then occupied by the  $2p_{3/2}$  electron in case of the  $K\alpha_1$  emission, and the  $2p_{3/2}$  electron undergoes the  $2p_{3/2}$  core-hole lifetime-broadened transition to the 1s core-hole lifetime-broadened energy level (the  $L_3$ -level width in HWHM,  $\Gamma_{L_3}$ ; [45]).

Therefore, the natural shape of an emission line in the frequency or energy scale is a Lorentzian, according to the both classical and quantum theory [84]. This is observed in practice for a large number of  $K\alpha$  emission lines, and they are highly symmetric and can be represented by a Lorentzian profile. By contrast, it is also well-known that the experimentally observed  $K\alpha$  and  $K\beta_{1,3}$  emission lines of the 3d transition metals are pronouncedly asymmetric. The first appearance of the asymmetric features was clearly found at an incident photon energy coinciding with the threshold for the

creation of a 1s3d two-hole configuration (multi-electron excitation; [84]). In other words, the 3d electron as well as the 1s electron gets photoexcited once the incident photons have sufficient energy, and the presence of a 3d "spectator"-hole during the emission process introduces additional splitting in the initial and final energy levels, consequently increasing the number of distinct transition lines [45].

Accordingly, Hölzer *et al.* were able to show that the line shapes of the Cu  $K\alpha$  and  $K\beta_{1,3}$  emission lines can be fully accounted for by contributions from 3d-spectator transitions only, in addition to the diagram ones (pure one-hole, single-electron transitions; [84]). Nevertheless, to fully interpret the origins of the emission lines we should also consider the ligand field multiplet structure of each emission line, if needed including the molecular orbital theory, and the electron-electron interactions as well as the corresponding spin-orbit coupling [74].

In other words, the emission processes in the 3d transition metals are highly dependent on the spin state of the electron taking part in the transition, namely if the 1s electron is spin up for example (Fig. 2.12), the 2p or 3p electron refilling the 1s core-hole should be spin up as well. Due to the large overlap between the 2p (3p) and the 3d wave functions [74], the exchange interactions between the 2p or 3p core-hole and the 3d electrons are considerable especially if the 3d electrons are unpaired, affecting the  $K\alpha$  and  $K\beta_{1,3}$  emission processes magnetically. That is how the emission lines get sensitive to the spin density in the 3d-chelates, and why the emission lines become pronouncedly asymmetric (for high Z materials, such as rhodium or uranium, where the 3p spin-orbit splitting is large enough, the  $K\beta_1$  and  $K\beta_3$  emission line appear distinct and symmetric; [74]).

In addition to the Lorentzian nature of the line shapes, the Gaussian broadening from the instrumental factors contributes inevitably, and this aspect will be further discussed in Chapter 3 and 7.

With a deeper understanding of the X-ray fluorescence processes, we will now discuss the  $K\alpha$ ,  $K\beta_{1,3}$ , and  $K\beta_{2,5}$  emission lines of the 3d-chelates by taking advantage of the  $[\text{Cu}(\text{dmp})_2]^+$  ( $\text{dmp} = 2,9\text{-dimethyl-1,10-phenanthroline}$ ) photosensitizer data as an example (Fig. 2.12). Even though no single theoretical spectrum will be introduced in this thesis (the theoretical spectra can be found in [74; 45] for instance), we will try to analyse and interpret the emission lines by fitting the Voigt profile  $V(x; \sigma, \gamma)$  (a probability distribution given by a convolution of a Lorentzian distribution  $L(x; \gamma)$  and a Gaussian distribution  $G(x; \sigma)$ ; see below).

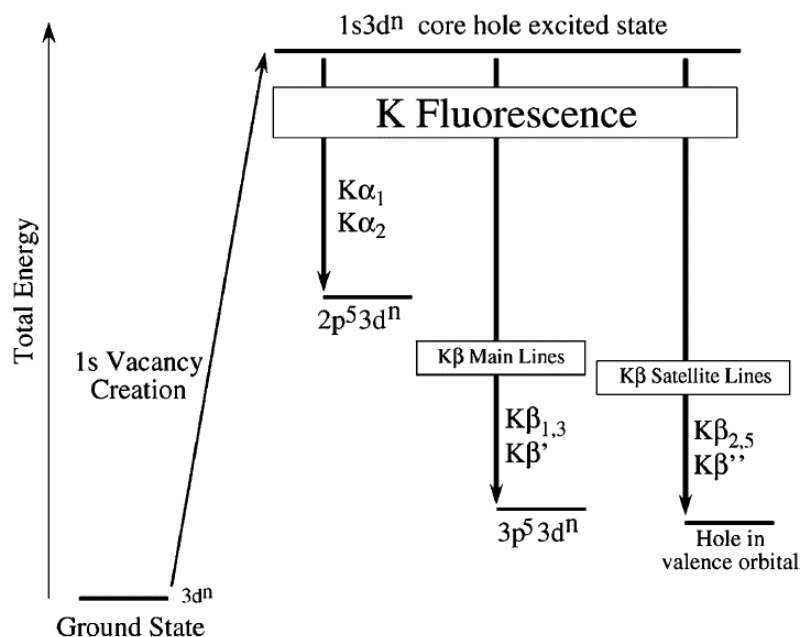


**Figure 2.18:** The simplified energy scheme and nomenclature for the X-ray fluorescence processes in the 3d-chelates upon the K-edge absorption (Figure from [74]). The respective electronic configuration denotes the corresponding hole state. Here, only the diagram transitions are indicated.

$$V(x; \sigma, \gamma) = \int_{-\infty}^{\infty} G(x'; \sigma) L(x - x'; \gamma) dx'$$

$$G(x; \sigma) = \frac{1}{\sigma\sqrt{2\pi}} \exp\left(-\frac{x^2}{2\sigma^2}\right)$$

$$L(x; \gamma) = \frac{\gamma/\pi}{x^2 + \gamma^2}$$

The Voigt profile is chosen to cover both the natural Lorentzian line width and the instrumental Gaussian line width [134; 1; 106]. The data presented in this section were measured with the incident photon energy of  $\sim 10$  keV ( $\sim 1$  keV above the Cu K-edge). Detailed experimental conditions can be found in Chapter 7.

Figure 2.19 shows the  $K\alpha$  emission spectrum of the  $[\text{Cu}(\text{dmp})_2]^+$  photosensitizer. The main two peaks of  $K\alpha_1$  and  $K\alpha_2$  stem from the  $2p_{3/2}$  and  $2p_{1/2}$  to  $1s$  dipole transition respectively. The fluorescence energy splitting between  $K\alpha_1$  and  $K\alpha_2$  ( $\sim 20$  eV) originates from strong spin-orbit interaction of the  $2p$  core-hole in the final state of the  $K\alpha$  fluorescence [45; 74]. The best fitting required two Voigt profile components for the  $K\alpha_1$  but only one component for the  $K\alpha_2$ , mainly due to the very weak intensity of a potential  $K\alpha_{22}$  emission line which was therefore difficult to be fit [45]. As denoted next to the  $K\alpha_1$  emission line, the  $K\alpha_{11}$  fluorescence corresponds to the  $2p_{3/2}$  to  $1s$  diagram transition with only one core-hole involved, whereas the

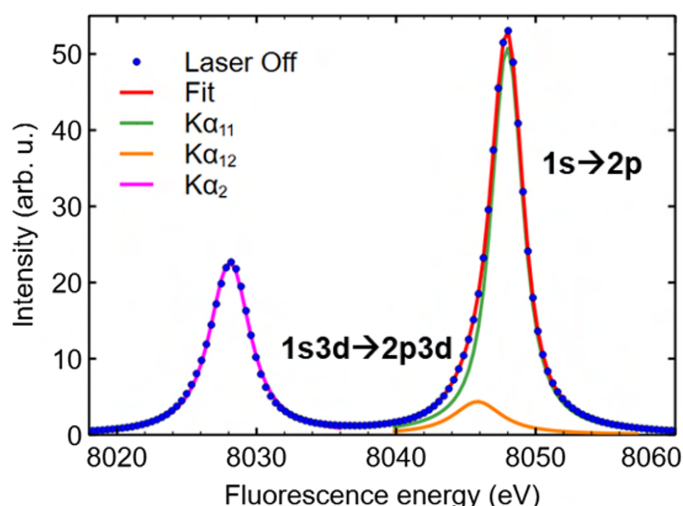


**Figure 2.19:**  $K\alpha$  emission lines from the  $[\text{Cu}(\text{dmp})_2]^+$  photosensitizer analysed by fitting the Voigt profile components [45; 134]. The corresponding initial and final hole states to the emission lines are denoted. Detailed data process and fitting procedure can be found in Appendix B and C.3.

$K\alpha_{12}$  fluorescence represents the  $2p_{3/2}$  to  $1s$  dipole transition in the presence of an additional  $3d$  spectator-hole created by the so-called double-ionization (two-electron excitation; [45]). The additional fluorescence energy splitting between  $K\alpha_{11}$  and  $K\alpha_{12}$  ( $\sim 2$  eV) is hence owing to the exchange interaction between the  $2p$  core-hole and the  $3d$  electrons [74].

Figure 2.20 shows the fitting result of Voigt profile components to the  $K\beta_{1,3}$  emission spectrum of the  $[\text{Cu}(\text{dmp})_2]^+$  photosensitizer. The best fitting required 5 Voigt profile components, each of which is attributed to  $K\beta_1$ ,  $K\beta_3$ ,  $K\beta'_1$ ,  $K\beta'$ , and KMN emission lines [45; 54]. The main two peaks of  $K\beta_1$  and  $K\beta_3$  stem from the  $3p_{3/2}$  and  $3p_{1/2}$  to  $1s$  diagram transition respectively, but this time the fluorescence energy splitting between them is  $\sim 10$  times smaller ( $\sim 2$  eV) than that between the  $K\alpha_1$  and  $K\alpha_2$ , owing to much weaker spin-orbit interaction of the  $3p$  core-hole in the final state of the  $K\beta_{1,3}$  fluorescence [45; 74]. However, in case of the  $K\beta_{1,3}$  fluorescence the electron-electron interactions between the  $3p$  and  $3d$  wave functions are  $\sim 3$  times stronger, which thus result in its distinct and asymmetric spectrum line shape with  $K\beta'_1$  and  $K\beta'$  spectator-hole satellite lines present [74].

The spectator-hole satellite lines correspond to the  $3p_{3/2}$  and  $3p_{1/2}$  to  $1s$  dipole transition under the  $(3p, 3d)$  exchange interaction after the double-ionization [45; 74]. That means, an additional hole to the  $1s$  core-hole appears simultaneously in  $3d$ - (or even in  $3p$ -,  $3s$ -) orbital during the 10 keV photoabsorption, and the following spin density from the unpaired electrons in  $M$ -shell as well as the  $3d$  spectator-hole

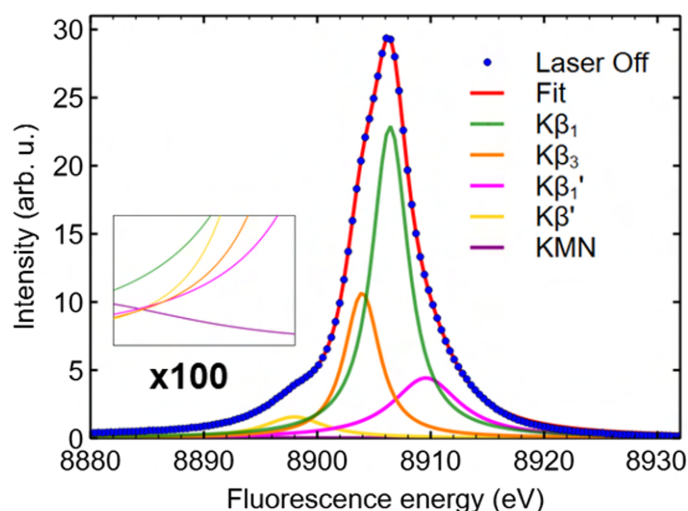


**Figure 2.20:**  $K\beta_{1,3}$  emission lines from the  $[\text{Cu}(\text{dmp})_2]^+$  photosensitizer analysed by fitting the Voigt profile components [45; 134]. Detailed data process and fitting procedure can be found in Appendix B and C.3.

affects the  $K\beta_{1,3}$  fluorescence. Therefore, the  $K\beta'_1$  and  $K\beta'$  spectator-hole satellite lines appear at either lower or higher fluorescence energy than the  $K\beta_1$  and  $K\beta_3$  diagram transitions, and become much broader than the  $K\beta_1$  and  $K\beta_3$  emission lines due primarily to the abovementioned interactions. In addition, a very weak and broad KMN satellite line appears from the radiative Auger decay, i.e. the  $K\beta_{1,3}$  fluorescence loses its partial energy to the M-shell to N-shell excitation (double-ionization during the emission; [54]).

The  $K\beta_{2,5}$  emission spectrum of the  $[\text{Cu}(\text{dmp})_2]^+$  photosensitizer was sharply resolved (Fig. 2.21), although the signal-to-noise ratio (SNR) is much lower than that of the  $K\alpha$  and  $K\beta_{1,3}$  emission spectra. The origins of the  $K\beta_{2,5}$  emission lines are predominantly the cross-over transitions from the ligand  $2sp^2$ - and  $\pi$ -orbitals [74]. The main two peaks right below the pre-edge absorption energy of  $[\text{Cu}(\text{dmp})_2]^+$  (8979.5 eV; [102]), which represents the quadrupole-allowed transitions of the 1s electron to the unoccupied 3d-orbitals, correspond to the dipole-allowed transitions of an electron from the HOMOs to the metal ion 1s core-hole.

In fact, an additional  $K\beta''$  satellite line from the ligand  $2sp^2$ -orbital to the metal ion 1s core-hole (this transition is not dipole-forbidden since the center of symmetry of two orbitals are different; [74]) should appear  $\sim 10$  eV below the main  $K\beta_{2,5}$  fluorescence in case of the nitrogen coordination [138; 134; 159; 43; 196]. However, in our case the  $K\beta''$  satellite line was not clearly observed owing to an overlapping KNN satellite line (radiative Auger decay; the  $K\beta_{2,5}$  fluorescence loses its partial energy to the valence shell to continuum excitation [54]) at the similar fluorescence energy. Instead, other

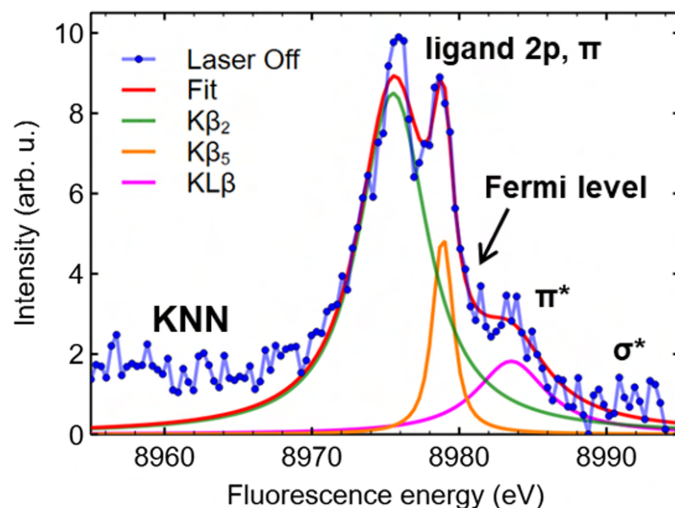


**Figure 2.21:**  $K\beta_{2,5}$  emission lines from the  $[\text{Cu}(\text{dmp})_2]^+$  photosensitizer analysed by fitting the Voigt profile components [54; 134]. The final hole states of the emission lines as well as the KNN satellite line are denoted. Detailed data process and fitting procedure can be found in Appendix B and C.3.

peaks above the Fermi level were clearly observed, and these satellite lines result from the so-called shake (or multiple electronic) transitions due mainly to the 1s core-hole [74]. As we shortly discussed earlier, within the 1s core-hole lifetime the weakened screening effect causes a readjustment of the overall electron clouds to the perturbed potential, letting some LUMOs like ligand  $\pi^*$  or  $\sigma^*$  orbital be temporarily occupied and thus the cross-over transitions from the LUMOs to the metal ion 1s core-hole be possible [74]. Furthermore, an additional spectator-hole from the double-ionization and the following exchange interactions as well as the molecular orbital theory, will further increase the number of factors associated with the  $K\beta_{2,5}$  emission lines. For instance, we expect the  $\text{KL}\beta$  emission line appearing at  $\sim 8990$  eV [73], which corresponds to the  $K\beta_{1,3}$  fluorescence in presence of the 2p core-hole and the 1s core-hole ( $\text{Zn}(\text{Z}+1)$   $L_3$ -edge +  $\text{Cu } K\beta_{1,3}$  -  $\text{Cu } L_3$ -edge  $\sim 8990$  eV), because the 10 keV incoming photon energy was enough to create an additional 2p core-hole to the 1s core-hole ( $\text{Cu } K$ -edge +  $\text{Zn}(\text{Z}+1)$   $L_3$ -edge  $\sim 10$  keV).

Up to now we have discussed how the hard X-ray photons are absorbed and emitted by the inorganic chelates. Indeed, these are not simple in the condensed phase especially with the deep core-hole in presence, and this thesis has only shown a few specific cases with very limited level of the theory, namely the fitting analysis provided is only phenomenological. Nevertheless, we will be able to extract the chemical information of our interest from the X-ray spectroscopic data we measured, in accordance with our understanding from this chapter.

As a remark here, the resulting hole state in the outer shell in response to the reoccupied 1s core-hole in the third phase of the X-ray photoelectric effect upon X-ray absorption, will be refilled by either an electron from the valence orbitals or the photoelectron from the X-ray absorption. The Auger effect is a non-radiative decay in the second phase of the X-ray photoelectric effect, where the dipole transition from the outer shell to the 1s core-hole emits not the photon but the Auger electron, whose kinetic energy becomes then approximately the difference between the  $K\alpha_2$  fluorescence energy and the  $L_3$ -edge energy in case of the  $KL_2L_3$  Auger transition. While the Auger process is the main relaxation process after the soft X-ray absorption, the radiative decay becomes dominant in the hard X-ray regime.

### 2.3.3 Remark: Resonant inelastic X-ray scattering

As pointed out earlier, the first appearance of the asymmetric features in the emission lines was clearly found at an incident photon energy coinciding with the threshold for the creation of a 1s3d two-hole configuration [84]. In other words, the  $2p_{3/2}$  core-hole lifetime-broadened transition to the 1s core-hole lifetime-broadened energy level ( $K\alpha_1$  emission) is dependent on the incident photon energy. In the previous section, we discussed the  $K\alpha$ ,  $K\beta_{1,3}$ , and  $K\beta_{2,5}$  emission lines of the  $[Cu(dmp)_2]^+$  upon 10 keV photoabsorption ( $\sim 1$  keV above the Cu K-edge, where the EXAFS feature is no longer present). What will happen to the emission lines if the incident photon energy gets closer to the Cu K-edge, or even to the pre-edge structure?

The pre-edge absorption (core-to-valence transition; 1s to 3d for the 3d-chelates) is the resonant excitation especially for the  $K\beta_{2,5}$  emission (valence-to-core transition; 3d to 1s for the 3d-chelates although it is only quadrupole-allowed), and in terms of the one photon-in, one photon-out concept (Fig. 2.17), the other emission processes can be treated as inelastic X-ray scattering processes. Hence, the resonant inelastic X-ray scattering (RIXS) spectroscopy is to map the inelastically scattered emission lines while scanning the resonant excitation energies across the pre-edge structure.

In this section, we will again refer to the same energy scheme (Fig. 2.22) as Fig. 2.18, and accordingly indicate the total energy of the intermediate state, where the excited 1s electron is in one of the LUMOs, with the incident photon energy  $\Omega$ , and the total energy of the final state, where the excited 1s electron is still in the same LUMO but one of the 2p or 3p electrons undergoes the dipole transition to the 1s core-hole, with the energy transfer  $\Omega - \omega$  (not with the fluorescence energy  $\omega$ ; [74]). In this way, the RIXS spectra can be viewed as a map of the final states in the vicinity of the intermediate states. That means, through the RIXS plane we are able to monitor both the final states approachable from one specific intermediate state, and the

intermediate states that can proceed to one specific final state. Moreover, one of the main transition channels ( $\omega$ ) between the initial and final states can be chosen to probe the transition rates in the XANES region (Fig. 2.13).

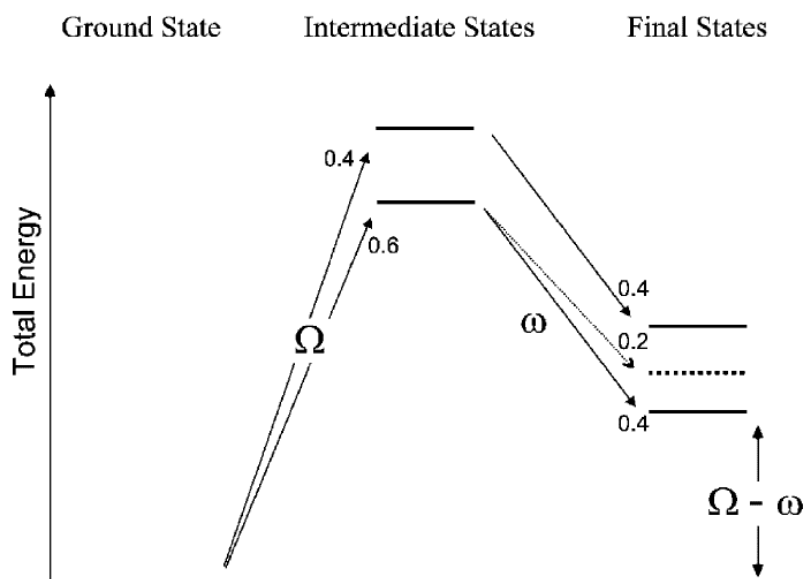


**Figure 2.22:** The simplified energy scheme and nomenclature for the RIXS processes (Figure from [74]). The relative transition intensities are given as an example. Here, only the diagram transitions are indicated.

In the XANES region, particularly below the K-edge, the excited 1s electron is in one of the unoccupied or unpaired valence orbitals, and the X-ray fluorescence processes proceed in the presence of a spectator-"electron" [74]. Therefore, the final states near the pre-edge structure become more characteristic to the electronic structure of the corresponding molecular system. Figure 2.23 shows the 1s2p RIXS plane of the  $[\text{Co}(\text{bpy})_3]^{2+}$  in solution phase as an example (same data with Fig. 2.13; the 1s2p RIXS planes of other cobalt chelates can be found in Appendix A). The final states near the pre-edge structure clearly separate themselves from the strong dipole-allowed K-edge absorption, and exhibit distinct features of the  $[\text{Co}(\text{bpy})_3]^{2+}$ , even though they are very weak owing to the quadrupole transitions.

The two strong transition channels between the initial and final states are the  $K\alpha_1$  and  $K\alpha_2$ , and the XAFS measurement technique along the specific channel is called as HERFD (Fig. 2.13), since one particular final configuration is observing the X-ray absorption rates across the XAFS range, excluding any other line width broadening effects from other final configurations. The XAFS spectrum can be recorded by either measuring the transmitted photon flux or the TFY (Fig. 2.15), but both techniques measure the line width broadening effects from all final electronic configurations. Thus, as long as the instrumental Gaussian line width does not overwhelm the natural

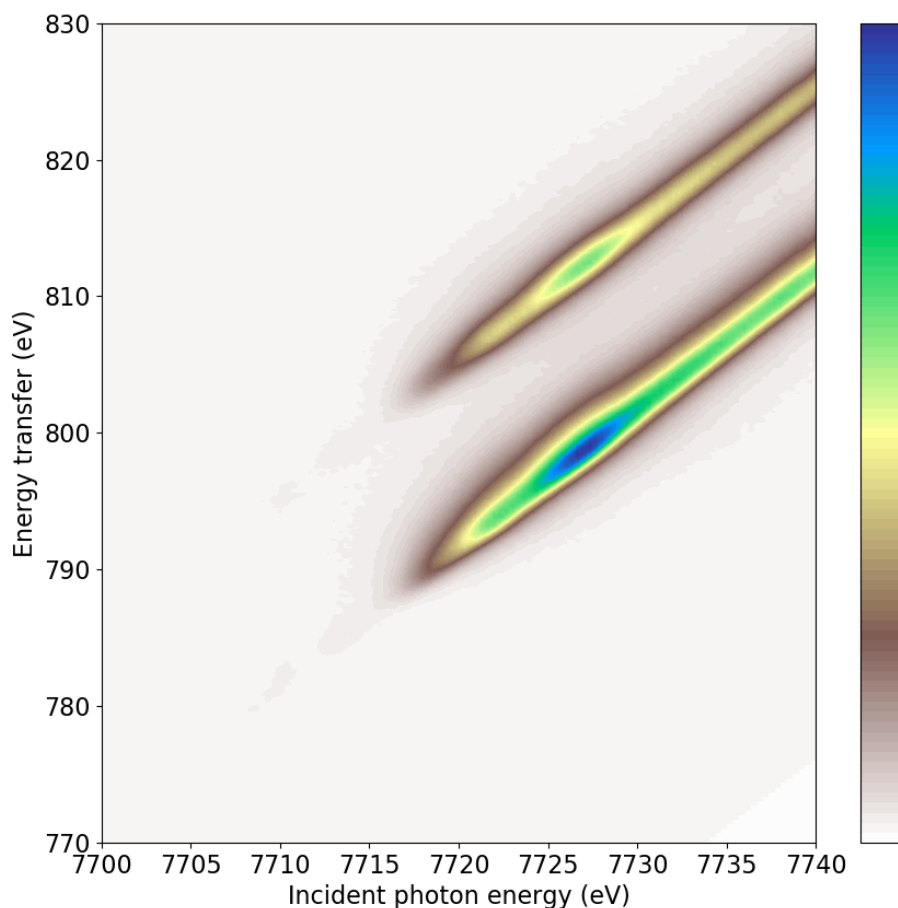


**Figure 2.23:** 1s2p RIXS plane of  $[\text{Co}(\text{bpy})_3]^{2+}$  in solution phase. The instrumental Gaussian line width was  $\sim 1$  eV in full width at half maximum (FWHM). The horizontal axis also corresponds to the total energy of the intermediate state, and the vertical axis to the total energy of the final state. The two strong transition channels represent the  $K\alpha_1$  and  $K\alpha_2$ , which are asymmetric due to the multiplet interaction [74].

Lorentzian line width, the HERFD technique improves the energy resolution of the XAFS spectrum [74].

The  $K\alpha_1$  and  $K\alpha_2$  emission lines along the y-axis at an incident photon energy close to the Co K-edge are still asymmetric, due primarily to the multiplet interaction. The characteristic pre-edge features can be also interpreted by analysing the spectra on the x- and y-axis [74]. Hence, the very advantage of the RIXS spectroscopy is to effectively separate out the lowest unoccupied molecular orbitals localized on the metal ion using the hard X-rays, to investigate the valence electronic structure in a much detailed manner.

---

## 3 Experimental methodology

Seeing is believing, and believing is seeing.

3.1	Time-resolved experiments .....	45
3.2	Femtosecond optical laser system.....	48
3.2.1	Experimental setup at University of Bern.....	51
3.3	Synchrotron light source.....	54
3.3.1	11-ID-D Endstation at APS.....	58
3.4	X-ray free-electron laser (XFEL) .....	61
3.4.1	BL3EH2 Endstation at SACLA.....	63
3.4.2	FXE Endstation at European XFEL.....	66

The inorganic chelates consist of a metal ion with deeply localized core electrons, and the ligands coordinated to the valence hybridized orbitals of the metal ion. Optical and hard X-ray photons interact with the inorganic chelates in many different ways, mostly depending on their photon energy. But when it comes to the photoabsorption, the annihilation of a photon leads to an excited state which will decay through various intermediate states and processes, on the ultrafast timescale ( $<1 \mu\text{s}$ ).

Following the discussions in Chapter 2, this chapter will be dedicated to the instrumentations for the study of ultrafast dynamics upon the optical or X-ray photoabsorption. Firstly, the basic idea of the time-resolved experiments with so-called ultrashort pulses will be discussed, and then the femtosecond optical laser system as well as the endstations at synchrotron light source and X-ray free-electron laser (XFEL) facilities employed for this thesis will be introduced. This thesis however does not cover all the details behind the experimental setups presented, since these are beyond the scope of the thesis and can be found elsewhere.

---

### 3.1 Time-resolved experiments

How do we resolve dynamics in time? We need first of all our "eye" to process the transmitted signal from the dynamics. For instance, we perceive the optical signal from our daily dynamics *via* our eyes, and the timescale of the dynamics typically ranges from a second to an hour. We can further resolve the dynamics into

a much shorter time domain, once the recording frequency of our eye gets higher. Nowadays one can reach the recording frequency of  $\sim 1$  MHz or higher by exploiting an "electronic" eye (detector), thus achieve the time resolution of  $\sim 1$   $\mu$ s or shorter. But what if the dynamics of our interest occur on even shorter timescales than a microsecond, e.g. the very first step of photosynthesis within a picosecond?

For such an ultrafast regime, we can think of employing the ultrashort pulses. That means, two ultrashort pulses with a certain arrival time delay between them interact with the system of our interest. The first pulse (pump pulse) initiates the relevant ultrafast dynamics in the system and the second pulse (probe pulse) then takes a snap shot of the dynamics after the time delay. The snap shot contains the integrated information within the full width at half maximum (FWHM) of the pulse in time domain, which therefore determines the time resolution of the measurement. For example, if the FWHM of the pulse in time is on the order of a few femtoseconds, the dynamics taking place for longer than a picosecond can be resolved by applying the time delay of few tens of femtoseconds between the pump and probe pulses. The probe pulse with the integrated information of the dynamics after the time delay within its FWHM will be then recorded by a detector.

The ultrashort pulses can be in principle anything, e.g. light, electron bunches, pulsed magnetic fields, electrochemical potentials, temperature and pressure. Their Gaussian broadening in time domain generally confines the time resolution of the measurement, although a shorter resolution can be achieved by so-called self-referenced techniques [81; 46]. In this thesis, we will focus on deciphering the ultrafast dynamics in the light-harvesting inorganic chelates, hence the pump pulse will be an optical laser. The relaxation dynamics upon optical photoexcitation will be thus monitored by recording the probe pulse in the order of the varying time delay, i.e. the varying difference in propagated distances between the pump and probe pulses ( $\sim 3$   $\mu$ m corresponds to  $\sim 10$  fs). For the global and localized investigation of the relevant dynamics, in this thesis we will exploit the optical and hard X-ray photons as the probe pulses respectively, and conduct so-called pump-probe experiments.

Figure 3.1 shows an overview of the time-resolved pump-probe experimental methodologies used for this thesis. The core concept here is again the ultrashort pump and probe pulses approaching the sample with a time delay of  $t$  (the generalized parameters for both pulses are summarized). Before the interaction with the sample system, both pump and probe pulses are characterized first ( $I_0$ ). The optical pump pulse promotes the system to the excited state of our interest, and the following optical or hard X-ray probe pulse then once more promotes the excited state system after the time delay of  $t$ , capturing either the global electron density ( $I_1$ ) or the localized electronic structure (XAS, XES; see also the Section 2.3) in the excited

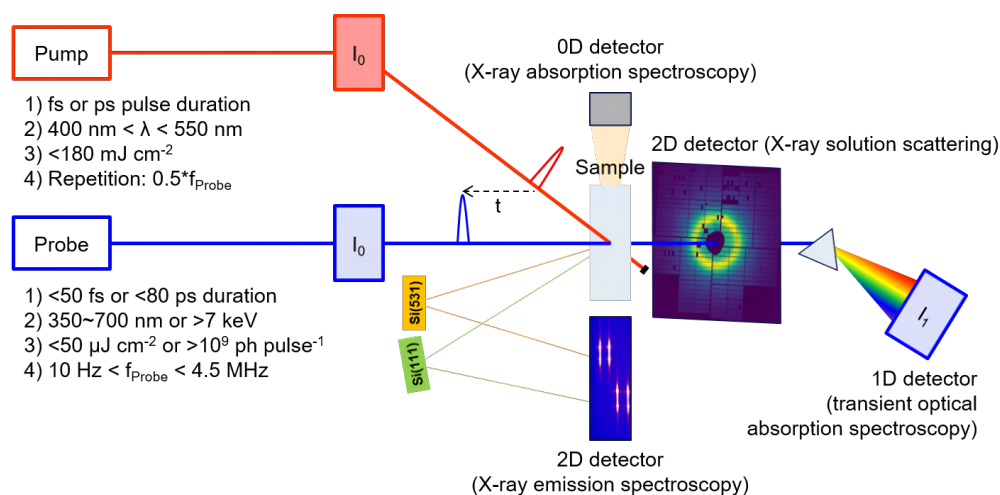


**Figure 3.1:** A simplified scheme of the time-resolved pump-probe experimental methodologies used for this thesis. The generalized parameters for the pump and probe pulses are summarized. The pump and probe pulses are diagnosed prior to the interaction with the sample system. The probed signals with and without the optical excitation can be read out by different detectors in different geometries.

state respectively. In addition, the X-ray solution scattering (XSS) measurement can be conducted simultaneously in optical pump hard X-ray probe experiment [113; 117; 63; 109], to further disentangle the nuclear dynamics from the electronic ones. That means, the probe pulse recording the ultrafast dynamics can deliver different information at the same time, which will be read by either single-shot detectors (1D) or charge-integrating detectors (0D, 2D) in different geometries. The pump pulse only interacts with the sample system at the half repetition rate of the probe pulse, such that the probed signals with and without the optical excitation can be compared (here we assume that either the target system completely recovers back to the GS before the next probe pulse, or the system is being renewed faster than the repetition rate).

In the following sections, details on the light sources for the pump and probe pulses as well as the spectroscopic methods in both optical and hard X-ray regime will be discussed. Depending on the timescale of our interest, the pulse duration (FWHM) of the optical pump can be either shorter than  $\sim 50 \text{ fs}$  or longer than  $1 \text{ ps}$ . The corresponding Fourier-transform-limited spectral bandwidth then restricts the minimum possible FWHM of the pump pulse spectrum (uncertainty principle), which is usually still broader than the lifetime-broadened energy level of the excited state ( $\sim 1 \text{ meV}$  or smaller) as denoted earlier. In other words, there is the fundamental limit of exploiting the ideally monochromatic photon energy for the pump pulse. These are however not that critical to the probe pulse whose spectral bandwidth is much broader or pulse duration is inherently longer than the Fourier-transform-limit. Moreover,

we will briefly cover the two-photon absorption process in which an energetically twice higher resonant state results from the simultaneous absorption of two identical photons, once the pump laser fluence exceeds the linear one-photon absorption regime (this is a nonlinear optical process and different with the double-ionization process discussed in Section 2.3.2).

---

## 3.2 Femtosecond optical laser system

The light-harvesting phenomena to convert photon energy into useful chemical energy start with a separation of charge that creates the chemical potential, i.e. the transient dipole moment, inside the inorganic chelates that is needed to drive further chemical reactions [141]. Although important equilibrium and global events in chemistry occur on much longer timescale, these events are inherently triggered by changes at early times and short distances such as bond vibrations and atomic fluctuations in the picosecond to nanosecond time domain [36]. Accordingly, a complete picture of a relevant chemical event implies following its temporal evolution from the shortest time onward.

Not only because we are interested in the light-harvesting phenomena but also because no electronics can measure the probed signal in the picosecond or shorter time domain, such a time resolution is achieved by exploiting the pump-probe scheme with the ultrashort pulses. These are limiting our stimulus pump pulse only to the optical laser, but in many instances non-light-driven ultrafast dynamics in chemistry can be mimicked by triggering them with the optical photons [36].

Since the first coherent light pulse was constructed in 1960 [133], there have been tremendous improvements on the shortest possible pulse duration, the highest possible laser power, the frequency tunability from the deep UV (DUV) to the mid-IR, and the best SNR within a reasonable data accumulation time [10]. In their early stages, ultrafast studies had to rely on the accidental coincidence of given laser lines (mostly from sub-ps dye lasers) with molecular absorptions, both in the spectrum of the GS and the excited state absorption (ESA) spectrum of the intermediates. In prominent cases, this was already sufficient for a crucial breakthrough in understanding the underlying mechanism [203]. In other cases however, a fair amount of "chemical intuition" had to be added to resolve any ambiguities. Ideally, the photoexcitation should not be chosen by instrumental constraints but in accordance with the ultrafast dynamics of our interest [142].

The 1990s have witnessed a revolution in ultrashort laser technology, thanks to the advent of solid state active materials like Ti:sapphire, and powerful mode-locking

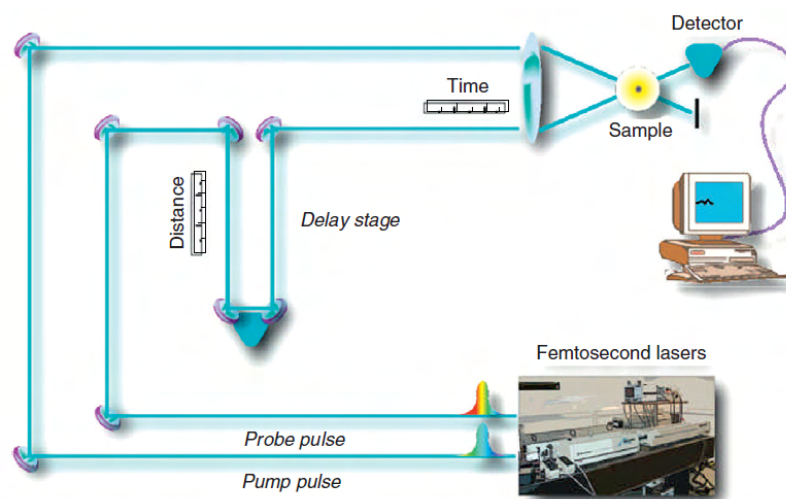


**Figure 3.2:** A representative illustration of the femtosecond-resolved pump-probe experiment (Figure from [36]). The focused pump and probe pulses on the sample position interact with the light-harvesting inorganic chelates, and the detector reads out the resulting probe pulse.

techniques such as Kerr lens mode-locking (KLM; [31]). With these advances, femtosecond optical lasers have gained remarkable reliability and user-friendliness, becoming "turn-key" devices available to a wide community of non-specialists. Another landmark of femtosecond laser technology has been the chirped pulse amplification (CPA) technique [31], which enabled increasing the laser intensity by 2 to 3 orders of magnitude, from the mJ to the multi-J level. Such an increase in peak power makes it possible to access a whole new class of nonlinear optical phenomena, triggering a renaissance in the field of nonlinear optics. Parallel to these developments has been the discovery of novel nonlinear optical crystals, such as  $\beta$ -barium borate (BBO) and lithium triborate (LBO), combining improved optical characteristics (high nonlinear optical coefficients, low group velocity dispersion (GVD), and broad transparency ranges) with high damage thresholds [31].

The tunable frequency of the femtosecond optical laser is obtained by the optical parametric amplification (OPA) of the KLM Ti:sapphire laser amplified by the CPA technique. A collinear OPA together with difference frequency mixing gives access to the spectral range from near-IR to mid-IR, whereas a noncollinear geometry (NOPA) with the help of frequency doubling and sum frequency mixing allows for the shortest pulses from the UV to the near-IR [142]. This development enabled a number of choices for the selective dipole transitions, thereby dramatically enlarging the range of ultrafast dynamics that can be studied with transient optical absorption spectroscopy (TOAS).

The available tunability can be also used to probe the intermediate states from the

selective photoexcitation. However, employing probe pulses that cover an ultrabroad spectral range at once greatly simplifies the experiment. The wider the probe spectrum, the more spectral signatures of the intermediate states involved in the ultrafast dynamics can be monitored simultaneously, which significantly facilitates the assignment of the underlying transient species. Towards this goal, one approach is to exploit the broadband NOPA pulses that have a Fourier-transform-limit of only a few femtoseconds [142]. Combining such a probe pulse with a narrowband NOPA excitation allows us to achieve a time resolution in the sub-100 fs regime, which is tailored to the investigation of the fastest nuclear and electronic dynamics [94; 24].

The alternative approach is to use supercontinua. These are generated by focusing an ultrashort laser pulse under proper conditions into optically nonlinear transparent media like gases, liquids, photonic crystal fibers and solids [142]. The supercontinua from bulk materials have been shown to be a very broad and smooth spectrum, high temporal and spatial coherence and a very high pulse-to-pulse energy stability [142]. Hence in our TOAS experiments for Chapter 4 and 5, we employed the frequency-doubled NOPA pump pulse centered at ~425 nm ( $\Delta\lambda \sim 3$  nm; MLCT transition), and the supercontinuum probe pulse ranging from ~320 nm to ~720 nm generated by focusing a fraction of the Ti:sapphire laser source into a 5-mm-thick  $\text{CaF}_2$  crystal [156].

The idea of the TOAS is rather simple; the excited state system after the interaction with the pump pulse (~425 nm) absorbs the following probe pulse (~320 nm to ~720 nm). In addition to the ESA, which characterizes the corresponding transient species, the stimulated emission (SE; Einstein coefficient  $B_{21}$ ) can also happen. The so-called transient absorption (TA) spectrum is then plotted by subtracting the GS absorption spectrum from the ES one ( $\epsilon_{ES}(\lambda) - \epsilon_{GS}(\lambda) = \Delta\epsilon(\lambda)$ ), and thus shows in general three types of the probed signals (Fig. 3.3; [36]). The ground state bleach (GSB) signal indicates an absorption band in the GS disappearing in the ES, and accordingly a new ESA band arises usually at a lower photon energy (unoccupied valence electronic structure now seen by ES, not GS). The SE signal appears as a negative feature at the lowest photon energy, since the probed signals are recorded by the detector in transmission mode (Fig. 3.1), and the corresponding transition proceeds under the Franck-Condon principle (Fig. 2.6).

The very advantage of the TOAS compared to other transient optical spectroscopic methods is that the recovery of the GS and the relaxation dynamics of the ES can be detected simultaneously. That means the relaxation pathways to the GS can be distinguished from those to other excited state manifold. Detailed data reduction and fitting analysis as well as the experimental setup will be followed in the next section, Chapter 4 and 5.

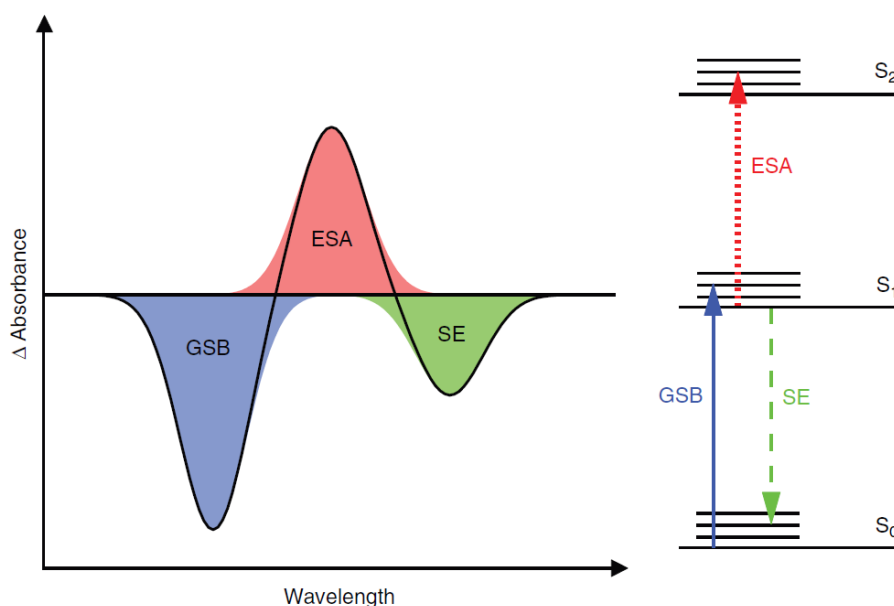


**Figure 3.3:** (left) A simplified scheme of the three representative signals in an optical TA spectrum and (right) the corresponding transitions described in a PES diagram (Figure from [36]). The dipole transitions occur under the Franck-Condon principle.

### 3.2.1 Experimental setup at University of Bern

The TOAS experiments for Chapter 4 and 5 were carried out at University of Bern (Prof. Dr. Andrea Cannizzo, Dr. Maryam Nazari) in May 2018 and December 2017 respectively. Herein the experimental setup (Fig. 3.4) will be briefly introduced focusing primarily on the pump and probe pulse generation processes. Further information on other components and aspects can be found in [156].

The oscillator is a KLM Ti:sapphire designed by Kapteyn-Murnane laboratories, pumped by a continuous wave (CW) 5W pump at 532 nm (Finesse from Laser Quantum). The oscillator output (80 MHz repetition rate, at 795 nm with a bandwidth of 12 nm) is used to seed a Ti:sapphire chirped pulse amplifier (Legend Elite by Coherent), pumped with a DARWIN-527 from Quantronix. The output of the cavity is a 5 kHz laser pulse, horizontally polarized, with max. pulse energy of  $\sim 0.5$  mJ at 800 nm and pulse duration of  $\sim 100$  fs (FWHM). The output of the amplifier is sent to a commercial NOPA, tunable between 500 nm and 750 nm, with a pulse duration of  $\sim 35$  fs and a spectral bandwidth of  $\sim 50$  nm (TOPAS-White by Light conversion). The NOPA is used to generate ultrashort tunable and broadband pulses over the visible range of the spectrum.

Pump beam generation is divided into visible and DUV spectral regions. In order

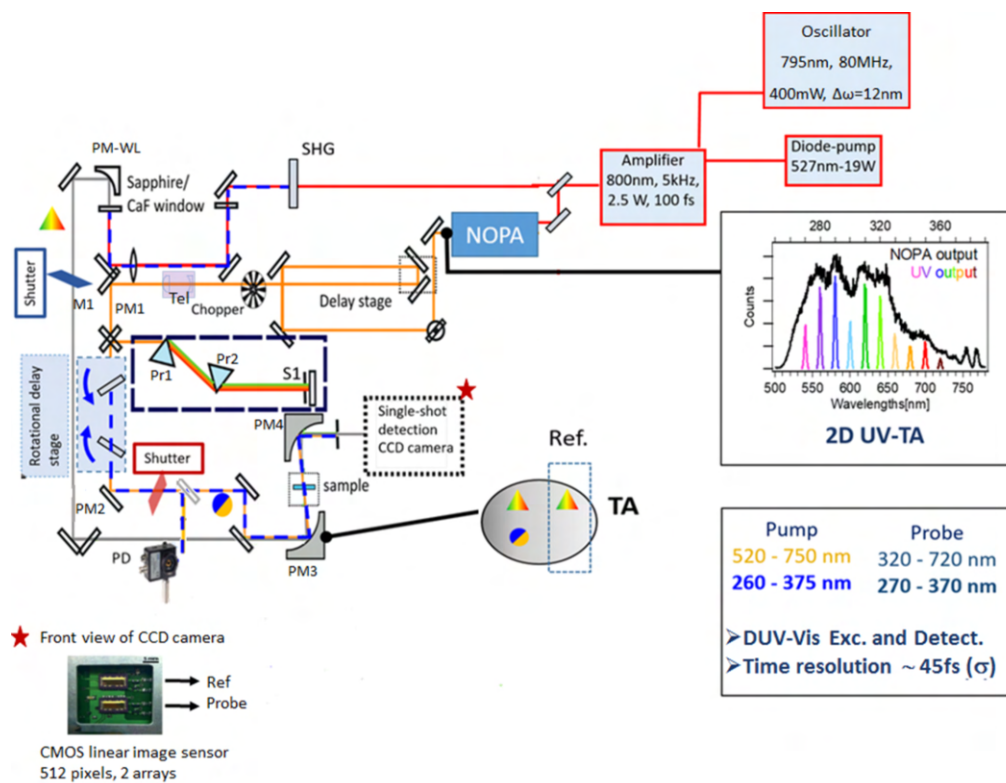


**Figure 3.4:** A layout of the femtosecond-resolved pump-probe experimental setup at University of Bern (Figure from [156]).

to generate visible pump pulses, the NOPA output is tuned to the desired pump wavelength between 500 nm and 750 nm, with typically 30 nm bandwidth (FWHM). Sometimes the pump bandwidth was reduced to have a more selective excitation of electronic transition by inserting a slit in a two prism based compressor on the path, where the pump pulse was dispersed (S1). For sake of completeness, the prism compressor is built with two highly dispersive SF11 prisms (Pr1 and Pr2). For the pump pulses in the DUV region, the visible NOPA output is focused by a parabolic mirror with  $f = 150$  mm (PM1) on a BBO crystal with 250  $\mu\text{m}$  thickness and then frequency doubled by choosing the right phase matching angle [31]. The max. energy per generated pump pulse was  $\sim 1$   $\mu\text{J}$  with a bandwidth of  $\sim 2$  to 3 nm (FWHM). A 250  $\mu\text{m}$  thickness was chosen to have sufficient excitation intensity without an important degradation of the time resolution.

The supercontinuum generation for the broadband femtosecond probe pulse ( $\sim 320$  nm to  $\sim 720$  nm) was achieved by focusing a small fraction of the Ti:sapphire laser source onto a 5-mm-thick  $\text{CaF}_2$ . Several phenomena like self-phase modulation and (anti)-stokes Raman shift amplification occur and broaden the fundamental beam [75]. To avoid any damage on the  $\text{CaF}_2$  plate due to accumulated heat load,

the crystal was mounted on a motorized stage horizontally wobbling. Adjustment on the fundamental beam size and pulse energy to generate white light was fulfilled by a fine adjustable aperture and a variable neutral density filter, respectively. The white light was then collimated by a UV-enhanced parabolic mirror ( $f = 100$  mm), and the fundamental beam was filtered out by a 2-mm-thick short-pass filter (BG40 from Schott). The polarization of the white light was vertical and parallel to the fundamental beam. Since  $\text{CaF}_2$  shows a nonlinear anisotropic birefringency, the crystal has been mounted on a rotational stage to optimize the mutual orientation of the crystal axis at the laser polarization by means of a polarizer. This optimal orientation corresponds to an optimal spectral bandwidth and stability. The polarization of the white light was double-checked at the sample position to ensure that other optical components or misalignments did not affect the polarization.

After the supercontinuum generation, the probe pulse was collimated by a  $f = 50$  mm parabolic mirror (PM-WL in Fig. 3.4), and then splitted into two by a 50%-50% UV beamsplitter. One of the two pulses was focused by PM3 to spatially overlap with the pump pulse at the sample position. The temporal overlap and time delay between the pump and probe pulses were controlled by a 30 cm motorized delay stage placed in the pump path. The delay stage can move down to  $\sim 0.15$   $\mu\text{m}$  ( $\sim 0.5$  fs) per step and span up to 2 ns. The other probe pulse passes through another sample region not overlapped with the pump pulse, and was exploited for the reference spectrum. The probe beam size at the sample position was  $\sim 30$   $\mu\text{m}$  in diameter ( $1/e^2$ ). Both the reference and probe beam after the interaction with the sample system were re-collimated by another  $f = 120$  mm parabolic mirror (PM4). Their polarization were rotated to be horizontal by a  $90^\circ$  periscope, and then both beam were dispersed by a prism on two Hamamatsu CMOS sensors (S11105 series) with two chips (Fig. 3.4). Each sensor consists of an array of 512 pixels with the pixel dimension of 12.5 by 250  $\mu\text{m}$ , and the achieved spectral resolution was  $\sim 1$  to 2 nm (FWHM). Two cylindrical lenses ( $f = 20$  mm) were placed in front of the sensors to focus the reference and probe beam vertically onto each pixel, to improve the photon collection and thus the SNR.

Using the frequency-doubled NOPA pump pulse centered at  $\sim 425$  nm ( $\Delta\lambda \sim 3$  nm; MLCT transition) and the supercontinuum probe pulse covering from  $\sim 320$  nm to  $\sim 720$  nm, the TOAS experiments were conducted on two bimetallic photocatalysts, namely Ir(III)-Co(III) triads and Ru(II)-Mo(VI) dyad, to figure out how the excited electron in the photoactive moiety contributes to the enhanced catalytic performance on the other moiety. The fitting analysis and interpretation of the reduced TOAS data will be further discussed in Chapter 4 and 5.

---

### 3.3 Synchrotron light source

The unoccupied valence electronic structure seen by the GS and ES in a femtosecond-resolved manner reveals plenty of information on the relevant ultrafast dynamics particularly dealing with the global electron density changes in the inorganic chelates (e.g. an electron, energy transfer process or a conformational relaxation upon optical photoabsorption; [7]). Nevertheless, the limited photon energy window between  $\sim 1.5$  eV and  $\sim 3.5$  eV cannot fully unravel the strongly coupled vibration, spin, and nuclear dynamics because there are numerous resonant states simultaneously detectable in such a complex system within the optical regime.

To further gain the selectivity and sensitivity to specific and localized dynamics in the inorganic chelates, the hard X-ray probe pulse suits our needs well (see also the Section 2.3). Therefore, the endstations at the two contemporary X-ray facilities, i.e. synchrotron light source and XFEL, have been employed for such scientific cases where the geometric structure changes with a picometer-scale spatial resolution and spin density changes to shed light on a complete relaxation scheme can be studied. In this and the next section, the instrumentations and corresponding hard X-ray methods exploited for this thesis will be introduced along with the X-ray light sources. Detailed data reduction and fitting analysis will be followed in Chapter 6, 7, and 8.

The whole history of Nobel Prizes in physics has started with the discovery of X-rays in November 1895 at the University of Würzburg by W. C. Röntgen, and until today  $\sim 40$  Nobel Prizes were awarded to the X-ray sciences. However, progress in both the theoretical understanding of the X-ray light-matter interaction and the experimental methodology was steady from the period covering their discovery through to the mid 1970s [3]. The central limitation in that period was the source, which had remained essentially unchanged from about 1912 [84].

In a conventional X-ray laboratory, the X-ray beam was generated in a so-called X-ray tube (or is still generated in airports and hospitals). The tube basically consists of two parts; the filament and the water-cooled target material. A large voltage difference (20 kV to 50 kV) is produced between the filament and target, while the filament is operated by a small voltage of approximately 6 to 20 V. This is sufficient to generate electrons from the filament by thermionic emission. The huge voltage difference between the filament and target material accelerates the generated electrons in the direction of the target material. When some of the accelerated electrons hit the target material, they are stopped abruptly and emit in turn an electromagnetic wave. The higher the voltage of the filament is, the more intense X-rays are generated.

The spectrum of the X-rays generated from the electrons impinging on a metal anode has two distinct components. There is a continuous part due to the electrons being decelerated, and eventually stopped in the metal (not all electrons are stopped at once but some have multiple collisions with the target, and this leads to a generation of further electromagnetic waves of increasing wavelengths). This is consequently known as bremsstrahlung, and has its maximum photon energy that corresponds to the high voltage applied to the tube regardless of the target material. Superimposed on this broad spectrum is a sharp and characteristic line spectrum from the target material (X-ray fluorescence; see also the Section 2.3.2).

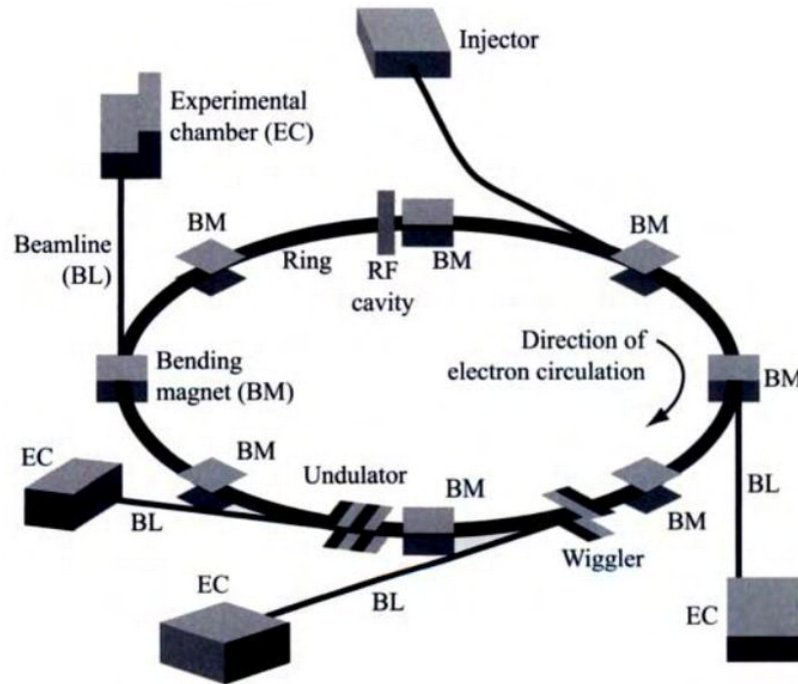


**Figure 3.5:** A generic scheme of the synchrotron facility (Figure from [136]). The electron bunches injected into a closed storage ring emit the X-rays while under the three light sources (Bending magnet (BM), Wiggler, and Undulator), that are delivered through the X-ray optics and diagnostics (BL) to the experimental chamber (EC). The partial electron energy lost during the X-ray emission (few keVs out of few GeVs) is compensated by the radiofrequency (RF) cavity, to keep the electrons in the orbit.

In the 1970s it was realized that the synchrotron radiation emitted from charged particles circulating in storage rings, that had been originally constructed for high-energy nuclear physics experiments, was potentially a much more intense and versatile source of X-rays [3]. Synchrotron radiation is hence named after a specific type of particle accelerator, but nowadays the synchrotron radiation has become a generic term to describe radiation from charged particles travelling at relativistic speeds in applied magnetic fields which force them to propagate in slalom paths. Besides synchrotrons themselves, the synchrotron radiation is produced in storage

rings where electrons or positrons are kept circulating at constant energy of few GeVs [3]. In a storage ring (Fig. 3.5), the synchrotron radiation is generated either in the bending magnets (BMs) needed to keep the electrons in a closed orbit, or in the insertion devices (IDs) such as wigglers or undulators situated in the straight sections of the storage ring.

The core of a synchrotron light source is an electron accelerator of the storage ring class [165]. This consists of an injector (Fig. 3.5), where electrons are generated and pre-accelerated to a high energy corresponding to a speed close to that of light,  $c$ . From the injector, the electrons are sent into a closed path inside an ultra-high-vacuum chamber. The electrons are then kept in the closed orbit by a sophisticated system of bending and focusing magnets. Fundamental electrodynamics however shows that a charge subjected to an acceleration must emit electromagnetic waves, and this is the origin of the synchrotron radiation in the storage ring. The electrons therefore partially lose their energy from the emission in the magnetic systems (few keVs out of few GeVs), and this gets compensated by one or more RF cavities applying an electric field to periodically accelerate the electrons in the longitudinal direction to keep them circulating around the ring [165].

Among the three magnetic systems in the storage ring, we will focus on the undulator light source that was employed for the experiments in Chapter 6, 7, and 8. The undulator is a periodic series of alternating magnets, usually 1 to 5 m long, inserted along an otherwise straight portion of the closed trajectory of the electrons (Fig. 3.6; [165]). The Lorentz force caused by the magnets makes the electrons slightly oscillate in the transverse direction, typically on the plane of the storage ring. Such oscillations (accelerations) thus lead to the emission of synchrotron light waves.

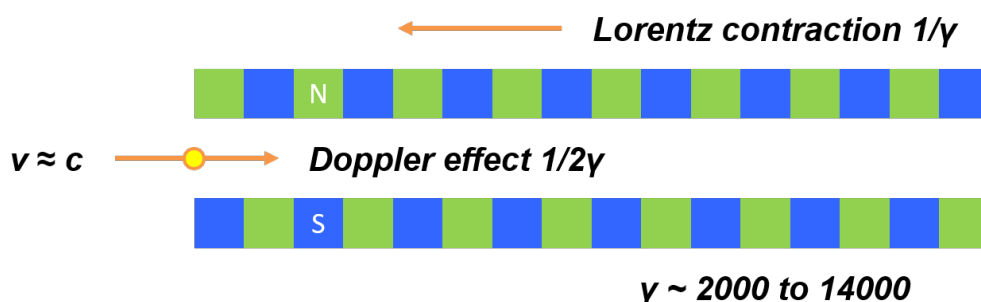


**Figure 3.6:** A representative illustration of the undulator light source with the electron bunch entering at a relativistic speed. The electron bunch accordingly experiences the undulator magnetic field corrected for the Lorentz contraction ( $1/\gamma$ ). The consequent dipole radiation from the oscillating and moving electrons gets further Doppler-shifted in the endstation frame ( $1/2\gamma$ ).

Since the electrons are approaching with the kinetic energy of few GeVs, i.e. the

Lorentz factor ( $\gamma$ ) of  $\sim 10^4$ , the dipole radiation from the oscillating and moving electrons must be considered in a proper reference frame. Under the two relativistic effects (Fig. 3.6), namely the Doppler effect and Lorentz contraction, the radiation wavelength observed in the endstation frame becomes  $\lambda \sim L/2\gamma^2$ , where  $L$  is the undulator period and  $\gamma$  is the electron energy in  $m_0c^2$  unit ( $\gamma = E_e/m_0c^2$ , where  $m_0$  is the electron rest mass and  $m_0c^2$  is hence  $\sim 0.5$  MeV; [135]). Furthermore, the angular distribution of the dipole radiation observed in the endstation frame becomes smaller than  $1/\gamma\sqrt{N_u}$  (angular collimation), where  $N_u$  is the number of undulator periods. That means, with the  $\gamma$ -factor of  $\sim 10^4$ , the emitted X-rays propagate within an angular spread of few tens of microradians.

In addition to this relativistic collimation effect, the total emitted power also becomes proportional to  $\sim \gamma^4$  in the endstation frame, therefore the peak brilliance (brightness; [photons/s/mm<sup>2</sup>/mrad<sup>2</sup>/0.1% bandwidth]) of the undulator light source gets extremely high compared to that of the X-ray tubes (Fig. 3.7; [165]). The magnetic field of the undulator  $B_L$  also affects the electron oscillations and thereby the radiation wavelength as well, and this is commonly reflected in the  $K$  parameter of the undulator ( $K = eB_L L/2\pi m_0 c$ ), which represents the deviation angle of the electron beam with respect to the propagation axis [135]. As noted earlier, in the course of dipole radiation the electrons partially lose their energy but only infinitesimally. Accordingly, the  $\gamma$ -factor does not really change during the undulations.

The undulator emits not only the first-harmonic, fundamental photon energy described above, but also higher-order harmonics with a certain spectral bandwidth ( $\Delta\lambda/\lambda \sim 1/N_u$ ) that can be filtered out by the following X-ray optics. This originates primarily from the stochastic nature of the synchrotron radiation, namely the electrons are not an ideal point source but repelling each other (the electron "bunch") and have individual energies from slightly different trajectories in the storage ring and thus different interaction with the magnetic systems (electron beam cross section; [165]).

When it comes to the time-resolved experiments however, the emitted X-rays in a pulsed structure or a certain timing mode are crucial. The pulsed structure in fact comes from that of the bunched electrons, which are generated from the injector and compressed into an ultrashort duration. Such a bunched structure is necessary to periodically restore the electron energy lost from the synchrotron radiation by RF cavities, and the collective radiation of one electron bunch in the undulator hence results in an ultrashort hard X-ray pulse [165]. With this, we will now move on to the actual parameters in the endstation at the synchrotron light source that are designed for the time-resolved XAS and XSS experiments, e.g. 11-ID-D endstation at the Advanced Photon Source (APS) storage ring facility.

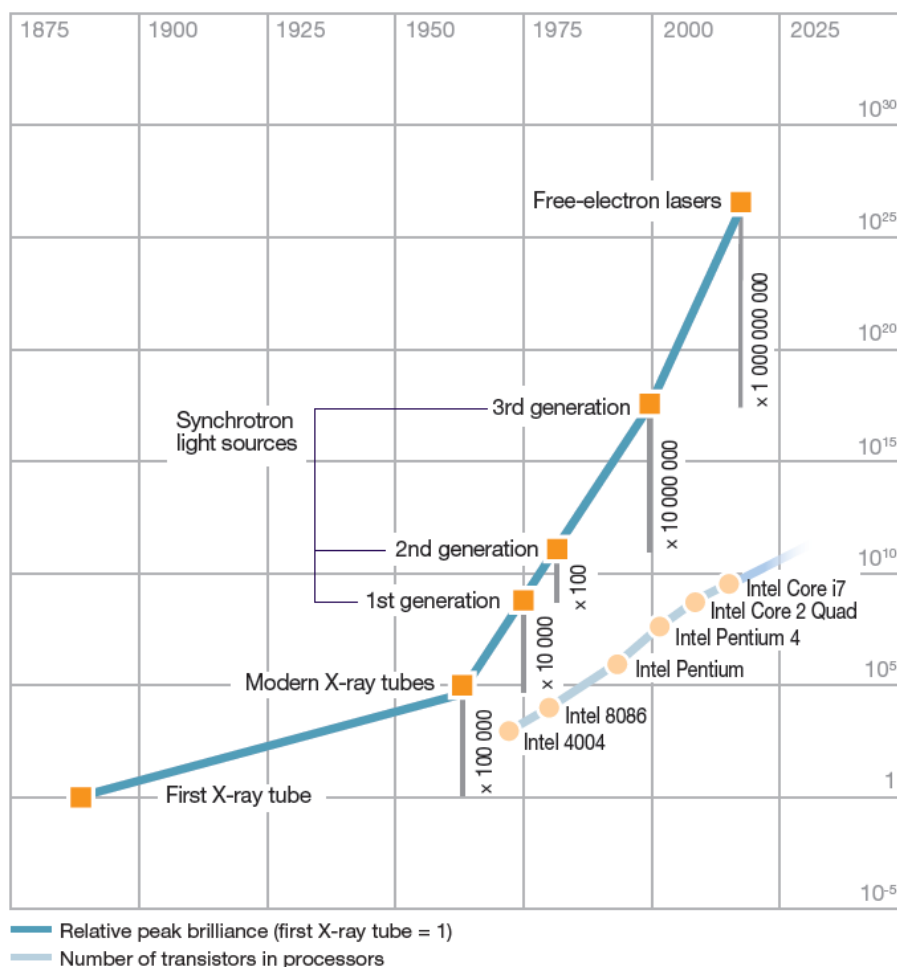


**Figure 3.7:** The evolution of the relative peak brilliance of the X-ray light sources over the last 14 decades, and the comparison with the increase in the number of transistors on a silicon processor chip (Moore’s law; Figure from European XFEL).

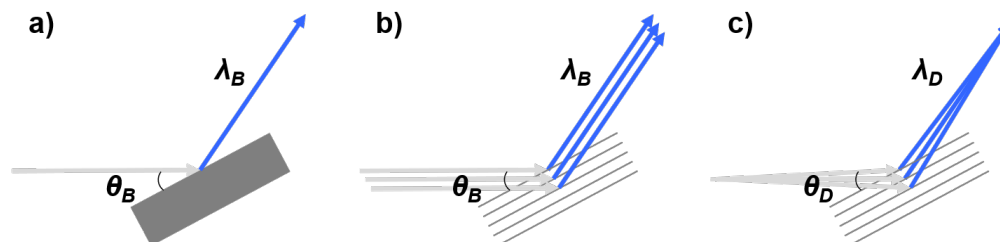
### 3.3.1 11-ID-D Endstation at APS

The 11-ID-D endstation is a beamline dedicated to optical pump hard X-ray probe XAS and XSS experiments, receiving the hard X-ray probe pulses from the APS storage ring through two in-line undulator sources (U2.3, U3.3). Specifically for our time-resolved EXAFS experiments in 2018 (Chapter 6), the hard X-ray pulses were generated from the electron bunches delivered at 6.52 MHz under the 24-bunch timing mode (i.e. 153 ns equal bunch spacing; the "distance" between the bunches to be re-accelerated depends on the length of the ring and the number of bunches circulating around it), and had a pulse duration of ~78.8 ps in FWHM [35; 128; 91].

The undulator radiation at ~22 keV (Ru K-edge) was monochromatized by a Si(111) double crystal monochromator (DCM;  $\Delta E/E \sim 10^{-4}$ ) to achieve an energy resolution

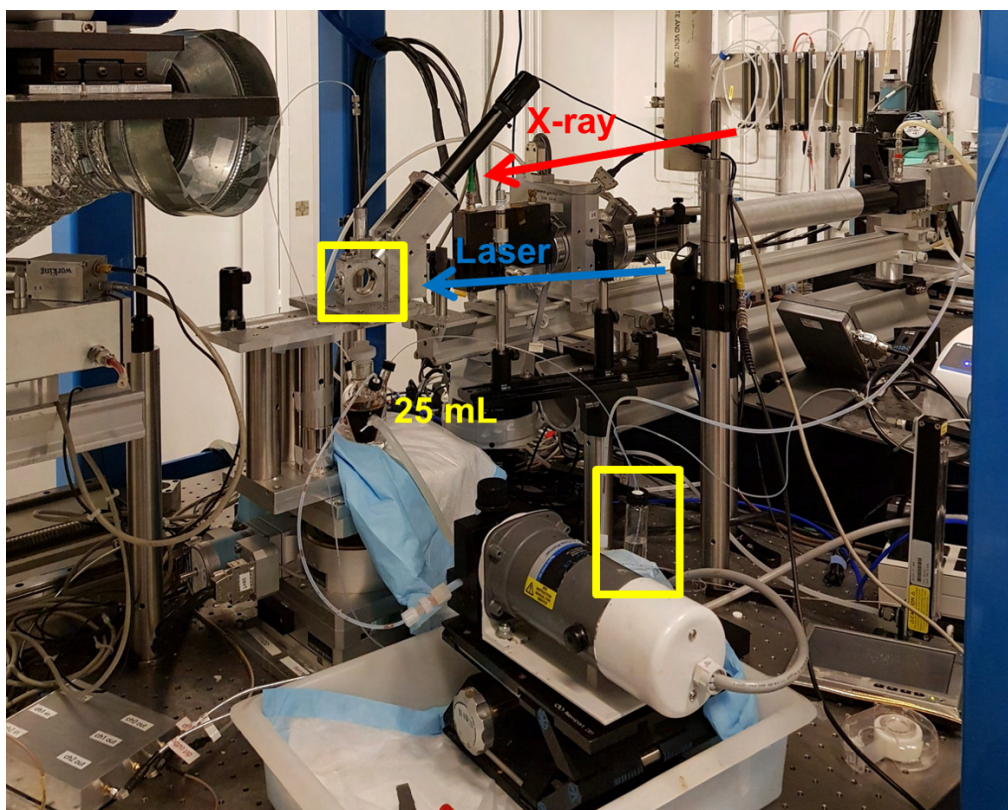
better than the Ru 1s core-hole lifetime-broadening [116; 74]. The afterwards focused monochromatic X-rays consisted of  $\sim 4 \cdot 10^{12}$  photons per second, and had a beam size of  $\sim 500 \mu\text{m}$  (horizontal) by  $\sim 70 \mu\text{m}$  (vertical) at the interaction point (FWHM). During the experiments the DCM was being scanned from the Bragg angle corresponding to  $\sim 22 \text{ keV}$  to that for  $\sim 22.47 \text{ keV}$  (Fig. 2.15), and the difference in propagated distance between the Bragg's conditions was automatically compensated to keep the probe pulse delay to the optical pump be constant.

Figure 3.8 illustrates the working principle of a single crystal monochromator in reflection geometry (Bragg's law; the Laue equations in transmission geometry will not be discussed in this thesis). In ideal case, the diffracted plane waves satisfying the Bragg's condition (Fig. 3.8 a), b)) will interfere constructively, leading to the monochromatic ( $\lambda_B$ ) plane wave. In practical cases however, the undulator radiation transported through the X-ray optics and diagnostics is divergent and sometimes induces a thermal deformation (heat load) on the crystal (Fig. 3.8 c); [165]). Therefore, the reflectivity curve of the single crystal monochromator with respect to the incidence angle is not a delta function but has at least an inherent bandwidth (Darwin width; [41; 140]) that is shifted due to the refraction. In other words, the interaction of the diffracted beam ( $\lambda_D$ ) with the crystal (multiple reflection) as well as the interference between the diffracted and incident beam should be taken into account (the dynamical diffraction theory; [11]).



**Figure 3.8:** Schematic illustration of the working principle of a single crystal monochromator in ideal a), b) and practical c) cases.

Figure 3.9 shows the standard experimental setup at the 11-ID-D beamline for the time-resolved EXAFS measurements. In a liquid sample environment the 25 mL sample solution in the reservoir (kept at 5 °C and bubbled with N<sub>2</sub>) was flowed by the liquid jet system (yellow) through an injector with its inner diameter of 600 μm, to prevent compound precipitation and multiple photoexcitation during the measurement. An additional dose of fresh acetonitrile was regularly refilled into the reservoir such that the sample concentration was kept stable (this was however not that critical for water solvent). The optical pump pulse (blue) and the monochromatic X-ray probe pulse (red) were then synchronized and intersected on the free-flowing sample jet spatially and temporally.



**Figure 3.9:** Standard experimental setup at the 11-ID-D beamline for the time-resolved EXAFS measurements in 2018. The sample reservoir was cooled down to  $\sim 5$  °C and refluxed under nitrogen, and an additional dose of fresh acetonitrile was regularly refilled to keep the sample concentration stable (yellow). The 400 nm pump pulse (blue) and the monochromatic X-ray pulse (red) were spatially and temporally overlapped on the 600- $\mu\text{m}$ -thick liquid jet.

The 400 nm pump pulse was the second-harmonic output from a 10 kHz Coherent Legend Elite Ti:sapphire ultrafast amplifier laser system. The pump pulses were then further stretched to  $\sim 1.6$  ps (FWHM) by a pair of prisms. The optical laser spot size was  $\sim 800$   $\mu\text{m}$  (horizontal) by  $\sim 130$   $\mu\text{m}$  (vertical) at the interaction point (FWHM), yielding a fluence of  $\sim 75$   $\text{mJ cm}^{-2}$ .

The emitted X-ray photons from the sample compound were then recorded at  $90^\circ$  with respect to the incident X-ray beam on both sides by two avalanche photodiodes (APDs; TFY mode). A combination of soller slits and a Mo filter, custom-designed for this sample environment and the distance between the sample and detectors, was inserted between the liquid jet system and the APDs. The first 12 X-ray pulses before the optical photoexcitation were accumulated for the GS XAFS spectrum, whereas the later X-ray pulses were used for the ES XAFS spectrum at 150 ps probe delay after the 400 nm photoexcitation. Each energy point was integrated for 4 s.

---

## 3.4 X-ray free-electron laser (XFEL)

The modern accelerator science and thus the synchrotron light sources are so sophisticated that the electron bunches are well under control in terms of the electron energy, source size, and angular deflection, with a very high accuracy [165]. Yet, the electron bunches circulating around the ring do experience many different perturbations in their journey to the light source (undulator in our case), such that the consequent X-ray parameters cannot exceed the state-of-the-art values, e.g. the pulse duration, spectral bandwidth, coherence, and brilliance.

This confined destiny of the electrons has been liberated by the successful realization of the XFELs [53; 168; 137; 92; 188; 146; 63; 109], whose unique characteristics are represented by the electron bunch compressed into a few femtoseconds and its self-amplified spontaneous emission (SASE) in a much longer undulator system. In fact, now the well-defined femtosecond electron bunch without any previous usage can be further optimized for the specific undulator parameters, and the linear accelerator (Linac) can be stretched for the electron energy above 10 GeV.

These extraordinary electron bunches will however undergo the Lorentz interaction maximum two or three times until they are dumped. In contrast to the electron bunches in a storage ring delivering X-rays to more than 40 beamlines for days, such an ultrashort lifetime of the electron bunches in XFEL for max. 2 or 3 beamlines accordingly increases the price per pulse that can be only justified by its exceptional beam quality.

First of all, the final electron energy at XFEL usually reaches a higher value than that at the storage ring, corresponding to the higher  $\gamma$ -factor and hence much more angular collimation and higher brilliance. Furthermore, the fine electron bunches propagating through a long undulator will generate quasi-monochromatic, femtosecond, and almost spatially coherent X-rays [165; 137].

The coherence predominantly originates from the correlation between the electron bunch and its synchrotron radiation waves in the advanced undulator system (Fig. 3.10). Here, both the electric and magnetic field of the initial X-rays work negatively (i.e. the electrons transfer energy to the X-rays) and force the "heavy" electrons towards the nodes of the waves respectively. Such a microbunching process aligning the relativistic electrons into a periodic structure equal to the emitted wavelength and continuous radiation in a correlated way therefore exponentially amplify the total wave intensity and let the X-rays become more coherent (SASE; [53]).

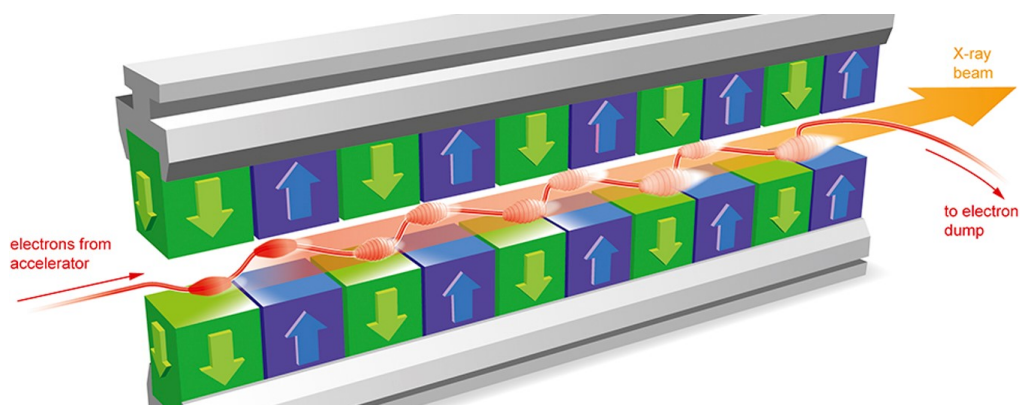


**Figure 3.10:** A simplified illustration of the SASE process by the femtosecond electron bunch at XFEL, undergoing the microbunching in a much longer undulator system (Figure from European XFEL).

The microbunching requires not only the well-defined electron beam but also enough "time" to happen, so that the storage ring with its 5 to 10-m-long undulator cannot result in the SASE [137]. As the negative work proceeds in an undulator longer than 100 m, a continuous energy loss of the electrons causes an increasing phase mismatch between the electric field of the X-rays and electron oscillations, thus at some point the work becomes positive. This in turn slightly accelerates the electrons, and the energy in fact starts oscillating between the X-rays and electrons (saturation).

The advanced Linac system at XFEL supplies unprecedentedly robust electron bunches for the SASE process, from which the femtosecond X-ray pulses with  $\sim 10^{10}$  times higher peak brilliance than that at a storage ring are transported to the beamline. Still, the stochastic nature of the SASE process involves the electron energy spread, angular divergence, and diffraction of the waves, that affect both the intensity amplification and saturation mechanism [165; 137]. Consequently, the so-called spatial and temporal jitter are inevitable, although the lateral coherence of the X-rays is very high.

In this Section, the BL3EH2 endstation at SPring-8 Angstrom Compact free-electron LAser (SACLA) and the femtosecond X-ray experiments (FXE) endstation at European XFEL, both dedicated to the optical pump hard X-ray probe experiments, will be introduced. The femtosecond-resolved XES and XSS experiments for Chapter 7 and 8 were conducted with von Hamos dispersive spectrometers in Bragg reflection geometry and in the forward wide-angle X-ray scattering geometry respectively. The characteristic repetition rates at each XFEL facility and their consequences will be remarked as well.

### 3.4.1 BL3EH2 Endstation at SACLA

SACLA, the world's second hard X-ray free-electron laser in Japan (2011), consists of a compact-scaled Linac system (8 GeV) and a short-period undulator (18 mm). A high-density electron beam with a low transverse emittance is generated by a pulsed thermionic electron gun with a single-crystal CeB<sub>6</sub> cathode and accelerated by a high-gradient, C-band Linac system [92]. The electron beam with a high peak current of >3 kA then propagates through the in-vacuum undulator system with the total number of ~5000 periods (max.  $K \sim 2.2$ ), resulting in the SASE X-ray pulses.

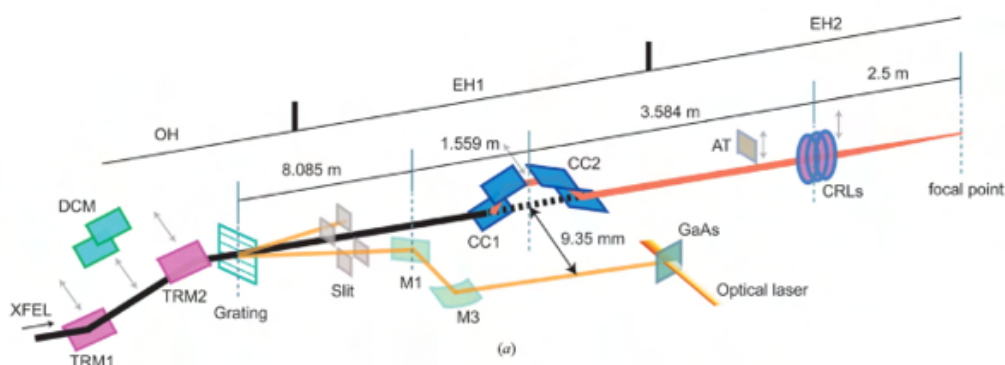


**Figure 3.11:** An overview of the X-ray optics and diagnostics for the pump-probe experiments at BL3 of SACLA (Figure from [101]). TRM stands for a total reflection mirror, CC for a channel-cut crystal, AT for a silicon attenuator, and CRL for a compound refractive lens. The focal point of the CRLs at the BL3EH2 endstation is the interaction point of the optical pump, hard X-ray probe pulses with the target sample.

Figure 3.11 shows how the X-ray pulses are transported to the interaction point at the BL3EH2 beamline [188; 104; 101]. The higher-order harmonics from the undulator are first filtered out by a certain configuration of so-called cutoff mirrors (TRM; the critical angle for the total reflection in the X-ray regime depends on the photon energy and the coating material), and the fundamental SASE spectrum can be checked by inserting and scanning the DCM (rocking curve). The diffraction grating then splits the incident beam into multiple branches, one of which (through M1 and M3) is exploited for the arrival-timing diagnostics between the X-ray and optical laser pulses (timing tool; [104]). For our femtosecond-resolved XES and XSS experiments we used the SASE X-ray pulses without monochromatization (pink beam; without CC1 and CC2), and the pink beam was focused down to ~5  $\mu\text{m}$  by beryllium CRLs [101].

The focused pink beam enters the He-filled chamber specialized for the pump-probe experiments (Fig. 3.12 left; [103]), whose scattering signal is recorded by two silicon photodiodes (Hamamatsu, S3590-09) as its  $I_0$  transmissive intensity. At the interaction point, both optical laser and hard X-ray pulses are overlapped spatially and temporally,

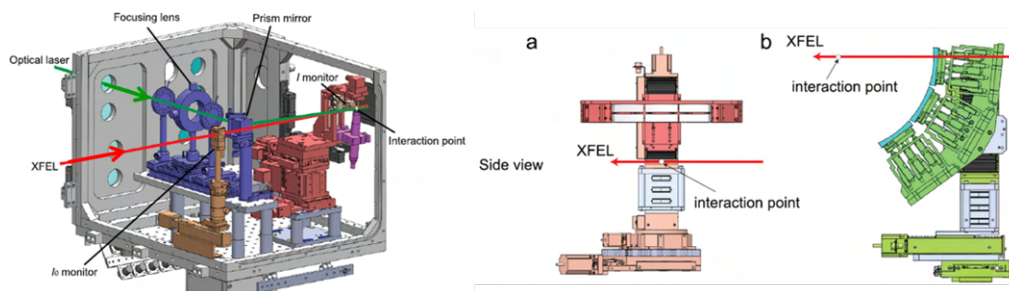


**Figure 3.12:** (left) The He-filled chamber customized for the pump-probe experiments at BL3EH2 endstation, and (right) two von Hamos dispersive spectrometers next to the chamber in vertical (a) and backscattering horizontal (b) geometry (Figures from [103]).

and the corresponding X-ray fluorescence as well as the forward scattering signals are measured on a per-shot basis.

Considering the stochastic X-ray intensities at XFELs, the point-to-line dispersive spectrometer in Bragg reflection geometry (von Hamos spectrometer; Fig. 3.12 right) with cylindrically bent crystals is optimal for the XES [178]. The von Hamos dispersive geometry to diffract the X-ray fluorescence signals from the sample onto a 2D position-sensitive detector is illustrated in Fig. 3.13 [85; 184].

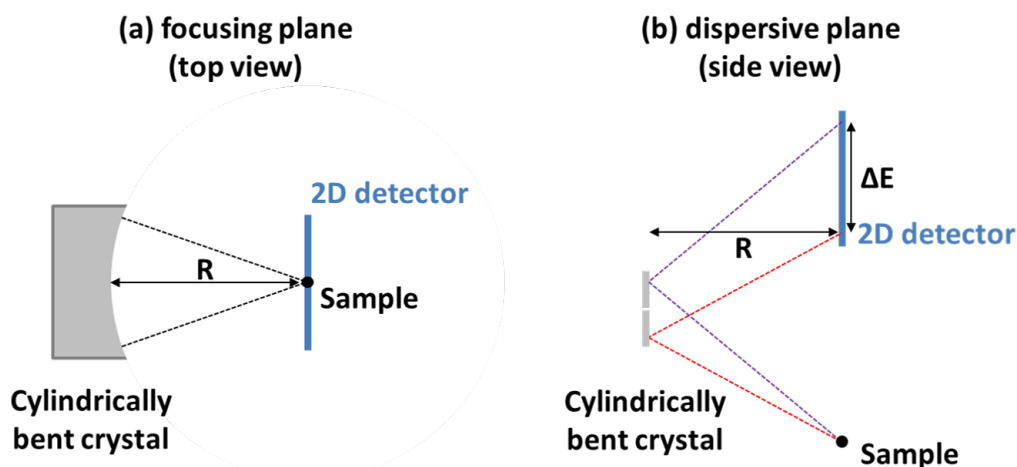


**Figure 3.13:** Schematic illustration of the von Hamos dispersive geometry with a cylindrically bent crystal and 2D detector. Here,  $R$  stands for the radius of crystal curvature and  $\Delta E$  for the X-ray fluorescence energy range that can be covered by the crystal and 2D detector according to the Bragg's law (red = lower fluorescence energy, purple = higher fluorescence energy).

Basically, the geometry corresponds to the Bragg diffraction in a nearly perfect crystal with a certain solid angle coverage, hence the Darwin width should be considered (Section 3.3.1). The Miller index and material of the cylindrically bent crystal and the feasible Bragg angles onto the position-sensitive detector then determine the

X-ray fluorescence energy range that can be covered ( $\Delta E$ ). Another variable in this geometry is the radius of crystal curvature  $R$ , typically either 500 mm or 250 mm, that changes the Bragg angle coverage and the energy resolution of the spectrometer [80; 2]. The energy resolution  $\Delta E_G$  (energy broadening due to geometrical contributions) means how wide range of the X-ray fluorescence energy is read as an energy point per detector pixel in the dispersive plane (Fig. 3.13 (b)). A derivative of the Bragg's law describes this as,

$$\frac{\Delta E_G}{E_i} \cong \frac{s+d}{f} * \cot\theta_B \quad (3.1)$$

where  $E_i$  is the incident photon energy,  $s$  is the X-ray beam size,  $d$  is the detector pixel size in the dispersive plane, and  $f$  is the diffraction path length from the sample to the detector [80; 2].

The von Hamos geometry at SACLA for example has  $s \sim 5 \mu\text{m}$ ,  $d = 50 \mu\text{m}$  (multiport charge-coupled device (MPCCD) detector), and  $f \sim 500 \text{ mm}$ . Thus, the  $\theta_B \sim 62.66^\circ$  and  $E_i \sim 10 \text{ keV}$  result in the  $\Delta E_G$  of  $\sim 0.57 \text{ eV}$ . There are still other energy broadening factors in addition to the Darwin width, that are associated with any angular deviation from the exact Bragg condition, e.g. the lattice plane stress in the bent crystal and slightly tilted alignment of the crystal [80; 2]. However, the  $\Delta E_G$  is usually dominant over all other possible energy broadening.

Currently 6 cylindrically bent crystals of Si(111) and Si(531) are available at SACLA (25 mm  $\times$  100 mm  $\times$  150  $\mu\text{m}$  (dispersive  $\times$  focusing  $\times$  thickness); 2020). Two identical MPCCD detectors with an active area of 25.6 mm  $\times$  51.2 mm are located according to the two von Hamos spectrometers in vertical and backscattering horizontal geometry respectively. During the femtosecond-resolved XES experiments, one in the vertical geometry (Fig. 3.12 a) records certain emission lines at  $90^\circ$  with respect to the incident X-ray beam, while the other (Fig. 3.12 b) can record different emission lines. On the other side of the interaction point, another silicon photodiode measures the per-shot TFY at  $90^\circ$  with respect to the incident X-ray beam, that can be employed to normalize the X-ray intensity fluctuations. For the XES measurements in general, it is extremely important to provide He or vacuum environment and reject any elastically scattered X-ray photons on the diffraction paths of the emission lines.

The femtosecond-resolved XSS measurements can be simultaneously performed with a MPCCD SWD (short working distance) detector in the forward wide-angle X-ray scattering geometry ( $2\theta$  up to  $45^\circ$ ; [103]). Further information on the experimental parameters as well as the data reduction and fitting analysis will be followed in Chapter 7, 8, and Appendix B.

### 3.4.2 FXE Endstation at European XFEL

The first designs of the XFEL generate the respective electron bunch at a repetition rate lower than 1 kHz [53; 92]. Accordingly, the XFELs with an unprecedented peak brilliance cannot provide much higher SNRs than the contemporary storage rings that can deliver its synchrotron radiation at over 1 MHz. Intuitively, one can imagine that the free-electrons being accelerated at RF can be also operated at the same RF. A difficulty here comes however from the fact that the free-electrons are only for a single use, i.e. the electron bunches must be generated at the same RF by the electron gun. Such a photocathode ( $\text{Cs}_2\text{Te}$ ) RF-gun was successfully implemented at European XFEL [18], reliably yielding the electron bunches up to 4.5 MHz.

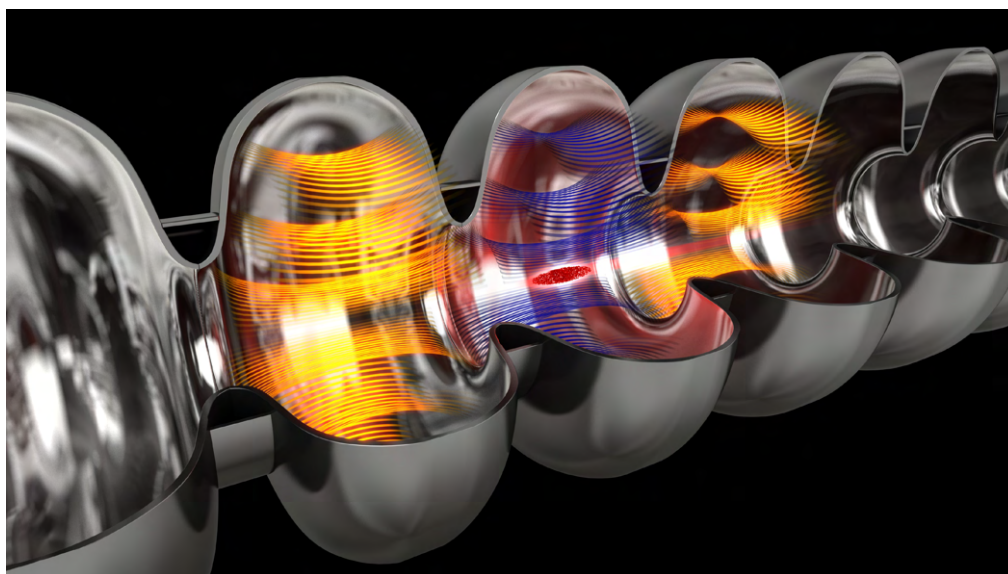


**Figure 3.14:** Simulated image of the acceleration of the free-electrons in the superconducting Linac system at European XFEL capable of the high-repetition rate operation up to 4.5 MHz (Figure from European XFEL).

The electron bunches are subsequently fed into a Linac system (Fig. 3.14), and the 2-km-long superconducting cavities (resonators) made of niobium at European XFEL can accelerate them up to  $\sim 17.5$  GeV [189]. This in turn enables a record-breaking angular collimation and emitted power of the SASE X-rays radiated in the following 175-m-long advanced undulator system. Moreover, the photon energy up to  $\sim 30$  keV is theoretically feasible, although the X-ray optics do not allow reaching that high photon energy yet. The total 3.4-km-long European XFEL is therefore a research facility of superlatives, namely all its components are state-of-the-art.

The world's most powerful SASE X-rays are then transported to the FXE endstation dedicated to the optical pump hard X-ray probe experiments, *via* the specialized

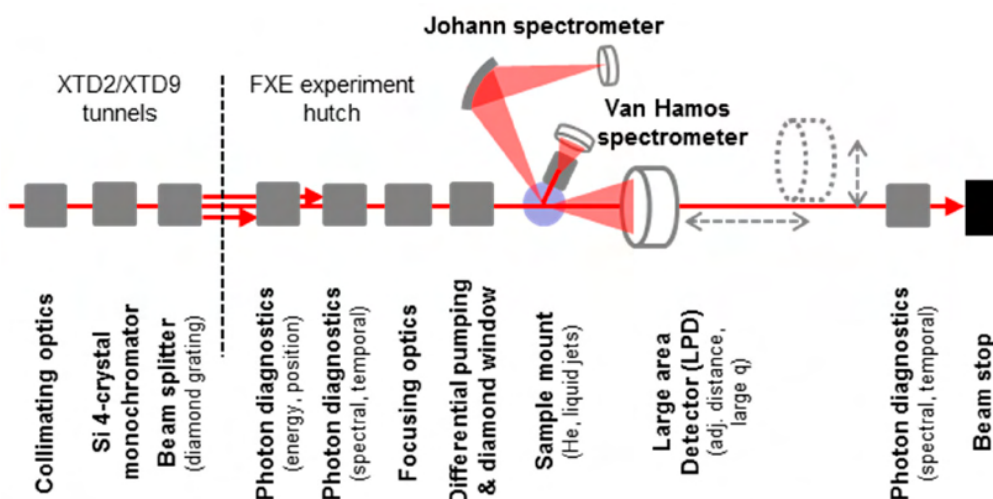


**Figure 3.15:** An overview schematic of the FXE endstation. The sketch includes major instrumentation components installed in the photon beam transport tunnel and experimental hutch (Figure from [189]).

X-ray optics and diagnostics (Fig. 3.15; [63]). The FXE beamline is equipped with a standard 4-crystal Si(111) monochromator and the subsequent photon diagnostics. At the interaction point, a sample solution is flowed by a high-performance liquid chromatography (HPLC) high-pressure-gradient pump system at a rather high speed, to avoid multiple photoexcitation by the high-repetition rate optical and X-ray pulses.

Two X-ray emission spectrometers in von Hamos geometry and Johann geometry are located at  $90^\circ$  with respect to the incident X-ray beam on each side of the interaction point respectively. The von Hamos dispersive spectrometer can accommodate up to 16 cylindrically bent crystals with its focal length of 500 mm. The Bragg angles between  $67^\circ$  and  $83^\circ$  are feasible, and the diffracted fluorescence signals are then acquired at 10 Hz by 2D JUNGFRAU 1M and 500k detectors. The Johann focusing spectrometer can accommodate up to 5 spherically bent crystals with its focal length of 1000 mm. Such a hybrid geometry will be especially efficient when it comes to the so-called photon-hungry experiments like RIXS or HERFD-XAS.

The femtosecond-resolved XSS experiments can be simultaneously performed in the forward wide-angle X-ray scattering geometry with a large pixel detector (LPD;  $2\theta$  up to  $65^\circ$ ), and the LPD is capable of recording the scattering signals on a per-shot basis (up to 4.5 MHz). After the interaction with the sample, the primary beam can further proceed through the LPD central hole to the post-sample diagnostics. Figure 3.16 shows the 3D illustration of the sample interaction area at the FXE beamline.

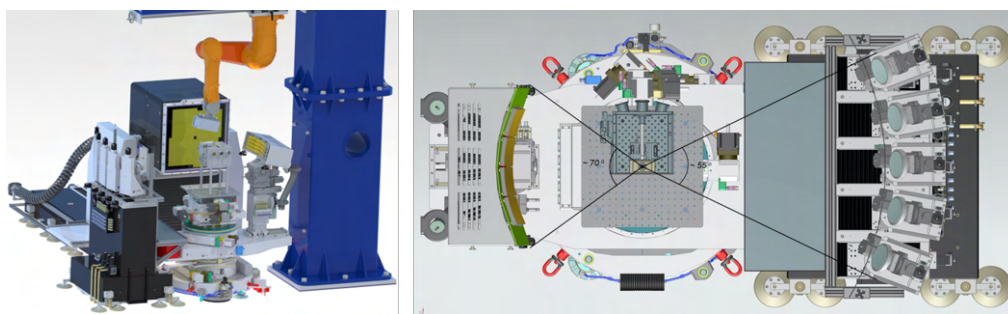


**Figure 3.16:** 3D illustration of the sample interaction area at the FXE beamline. The von Hamos and Johann spectrometers are located at  $90^\circ$  with respect to the incident X-ray beam, whereas the LPD is in the forward wide-angle X-ray scattering geometry (Figure from [63]).

Even though the reduced data obtained from the FXE beamline are not shown in this thesis, it is noteworthy to briefly mention some discrepancies in the time-resolved XES and XSS measurements at between SACLA and European XFEL. First of all, the front-end pulse energy at  $\sim 9$  keV is  $\sim 0.6$  mJ at SACLA, while is  $\sim 3$  mJ at European XFEL. This makes a big difference in deploying the X-ray optics and diagnostics, particularly in terms of the thermal deformation (heat load) on each component. Such an extraordinary X-ray pulse is even delivered at around 1 MHz to the FXE beamline, whereas only at 60 Hz to the BL3EH2 beamline. Hence, some of the components inevitably either accumulate continuous fatigue or can break down at some point.

The high-repetition rate also directly affects the liquid jet flow-speed. The X-ray vertical beam size of  $\sim 10$   $\mu\text{m}$  for instance must be renewed within  $\sim 1$   $\mu\text{s}$  (1 MHz), corresponding to the flow-speed of  $\sim 10$  m/s at slowest. This accompanies significant amount of solvent vapor near the interaction point, especially if the solvent is volatile, that attenuates the X-ray signals and changes the sample concentration. On the other hand, the SNR of the data can be prominently improved within the limited time of the experiment.

## 4 5d<sup>6</sup> Ir(III)-Co(III) photocatalyst

[A] being consumed does not mean [B] being produced.

4.1 Introduction .....	70
4.2 Experimental details .....	74
4.3 TOAS on Ir(III) photosensitizers.....	75
4.4 TOAS on Ir(III)-Co(III) triads.....	77
4.5 Conclusion and outlook .....	79

The first chelates we will visit are 5d<sup>6</sup> Ir(III) photosensitizers and their derivatives with the cyclometalating ligands. The 5d<sup>6</sup> Ir(III) photosensitizers are well-known for their superior functionalities under the optical photoabsorption, acting as an excellent reservoir of the incident photon energy to be converted into a chemical energy or a variable luminescence [191; 190; 132; 48; 111; 86; 15; 60; 119]. The very advantage of the bis-cyclometalated [Ir(C $\wedge$ N)<sub>2</sub>(N $\wedge$ N)]<sup>+</sup> complexes is the tunability of its photophysical properties by substituting either the monoanionic cyclometalating ligand (C $\wedge$ N), or the ancillary diimine ligand (N $\wedge$ N). As noted in Section 2.1.1, the cyclometalating ligand (C $\wedge$ N) as well as the d<sub>x<sup>2</sup>-y<sup>2</sup></sub> orbital always correspond to the HOMO orbitals, whereas the diimine ligand (N $\wedge$ N) always corresponds to the LUMO orbital ( $\pi^*$  orbital) [132; 15].

With this, our working group has designed a new series of phen-ligands fused with thiophenes to improve the reactivity of the photocatalytic proton reduction in the MLCT excited states [191; 192]. Furthermore, the [Ir(ppy)<sub>2</sub>(5,7-disubstituted thieno[3,4-*f*]phen)]<sup>+</sup> (ppy = monodeprotonated 2-phenylpyridine) was covalently linked to two chloro(pyridine)cobaloxime(III) catalysts, to fully take advantage of the MLCT states on the newly synthesized ligand after the directional charge separation. The photocatalytic proton reduction showed higher performance with the triadic system, and accordingly we conducted the TOAS experiments on both the Ir(III) photosensitizers and Ir(III)-Co(III) photocatalysts to visualize the ultrafast global interaction in the molecular system. Upon 425 nm photoexcitation, a great portion of the electron density in the <sup>3</sup>MLCT state on the diimine ligand got transferred to the cobaloxime(III) catalyst with a ~100 ps time constant. Further investigation with the local hard X-ray probe will clearly show the formal oxidation state and spin density changes in the Co(III) moiety as well as its nuclear dynamics.

## 4.1 Introduction

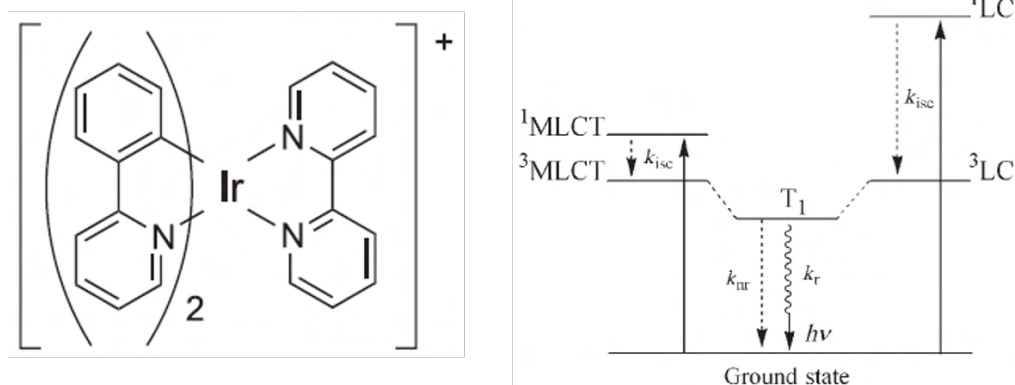


**Figure 4.1:** (left) A structural formula of  $[\text{Ir}(\text{ppy})_2(\text{bpy})]^+$  and (right) a simplified dipole transition scheme in the  $[\text{Ir}(\text{C}^{\wedge}\text{N})_2(\text{N}^{\wedge}\text{N})]^+$  complexes upon optical photoabsorption (Figures from [14; 132]). Both  $^1\text{MLCT}$  and  $^1\text{LC}$  states can be initially populated, followed by ISC and a mixture of the  $^3\text{MLCT}$  and  $^3\text{LC}$  states, which will decay back to the GS either non-radiatively or radiatively.

$[\text{Ir}(\text{ppy})_2(\text{bpy})]^+$ , one of the simplest  $[\text{Ir}(\text{C}^{\wedge}\text{N})_2(\text{N}^{\wedge}\text{N})]^+$  complexes, and its photophysics have been researched over the last 4 decades to understand and hence to control the nature of its excited states [110; 90; 199; 14; 190; 15]. Due primarily to its  $C_2$  point group symmetry, no symmetry-based selection rules can be applied, and the optical dipole transitions mostly concern MLCT and LC excited states (Fig. 4.1). The  $^3\text{MC}$  state is hardly accessible because of a sufficiently large ligand field splitting ( $\Delta$ ) in 5d-orbitals, but in few cases the thermal accessibility to the  $^3\text{MC}$  state becomes critical especially when it comes to the deactivation of the luminescence from the  $^3\text{MLCT}/^3\text{LC}$  states or the photodegradation [60].

Optical photoabsorption in the  $[\text{Ir}(\text{C}^{\wedge}\text{N})_2(\text{N}^{\wedge}\text{N})]^+$  complexes therefore often leads to either the MLCT ( $d_{x^2-y^2} \rightarrow \pi^*(\text{N}^{\wedge}\text{N})$ ) or LC ( $\pi(\text{C}^{\wedge}\text{N}) \rightarrow \pi^*(\text{N}^{\wedge}\text{N})$ ) transition [132; 14; 15], and the high spin-orbit coupling constant of the iridium ( $\zeta = 431, 1042, 3909 \text{ cm}^{-1}$  for Fe, Ru, and Ir respectively) facilitates ISC to energetically similar triplet states within the first 100 fs [60; 132; 190]. Since the relative energy between the  $^3\text{MLCT}$  and  $^3\text{LC}$  states can vary depending on nearby circumstances such as solvent or temperature, a mixing between them can occur accordingly with sufficient overlap. Thus, it is possible to control the relaxation dynamics by deliberately adjusting the valence electronic structure, which can be achieved through substituent effects or by changing the ligand parent structure entirely [132].

In addition to the so far thorough experimental and computational studies, Tschierlei *et al.* carried out the TOAS experiments on  $[\text{Ir}(\text{ppy})_2(\text{bpy})]^+$  to further specify the

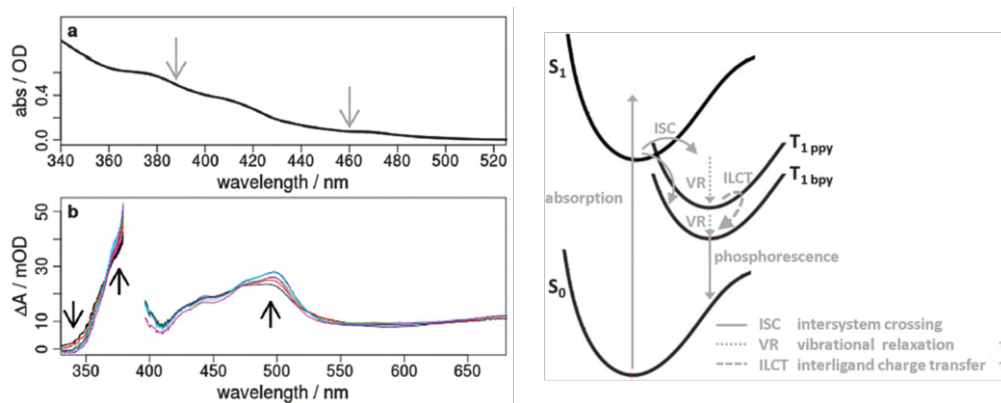


**Figure 4.2:** (left) Optical photoabsorption spectrum (above) of [Ir(ppy)<sub>2</sub>(bpy)]<sup>+</sup> in acetonitrile and (below) its TA spectra at probe delays of 0.5, 0.8, 1.25, 2, 5, and 50 ps after the 388 nm photoexcitation perpendicularly polarized to the probe pulse. (right) Schematic representation of the relaxation processes in [Ir(ppy)<sub>2</sub>(bpy)]<sup>+</sup> (Figures from [190]).

relevant relaxation cascade leading to the luminescence [190]. Together with parallel and perpendicular polarization of the optical pump pulse relative to the probe pulse, they reported that both 388 nm and 460 nm photoexcitation resulted in the <sup>3</sup>MLCT state on the bpy-ligand, and the interligand charge transfer (ILCT) from π\*(ppy) to π\*(bpy) on the picosecond timescale followed the femtosecond vibrational cooling (Fig. 4.2). That means, the charge transfer nature involving a change of the transient dipole moment in the system can be disclosed with the polarization anisotropy TOAS measurements.

The same working group has recently introduced a phen-5,6-dithiolate ligand instead of the bpy-ligand that can be readily linked to the second transition metal ion (Fig. 4.3), to achieve either a stable charge separation towards the second metal ion with significant thermodynamic driving force, or an energy transfer by electronic coupling between two active sites [55; 170]. Such dyadic systems are useful models in understanding the extent of intermetallic cooperativity which results in an effective luminescence quenching [58; 124; 96]. To trace back the excited electron dynamics in the dyadic system, the TOAS experiments were performed on both the Ir(III) photosensitizer (IrS<sub>2</sub>) and [Ir(ppy)<sub>2</sub>(phen-5,6-dithiolate)Co(C<sub>5</sub>H<sub>5</sub>)]<sup>+</sup>. The TA spectra of IrS<sub>2</sub> upon 388 nm photoexcitation showed pretty much similar features bathochromically shifted compared to those of [Ir(ppy)<sub>2</sub>(bpy)]<sup>+</sup>, and this indicates that the lowest <sup>3</sup>MLCT state lies on the phen-5,6-dithiolate ligand.

In contrast, the TA spectra of [Ir(ppy)<sub>2</sub>(phen-5,6-dithiolate)Co(C<sub>5</sub>H<sub>5</sub>)]<sup>+</sup> revealed completely different behaviours. Based on the fact that the quenching of the luminescent ES in this molecular system is exergonic towards the cobalt moiety, the

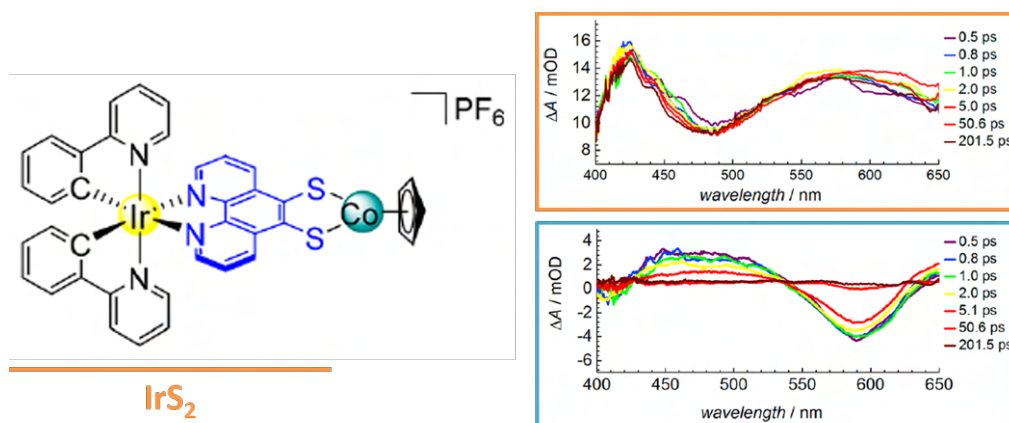


**Figure 4.3:** (left) A structural formula of  $[\text{Ir}(\text{ppy})_2(\text{phen-5,6-dithiolate})\text{Co}(\text{C}_5\text{H}_5)]^+$  and (right) its TA spectra (below) in comparison with those of  $\text{IrS}_2$  (above) at certain probe delays after the 388 nm photoexcitation (Figures from [55]).

absence of the  $^3\text{MLCT}$  state features can be explained by either an excited electron transfer or an energy transfer shortly after the photoabsorption. However, the TA signatures were equally present upon 590 nm photoexcitation as well as from the sole cobalt moiety complex, disproving a reasonable long-living charge separation in the dyadic system. In the end, the Franck-Condon state branched out into two relaxation pathways, one to the luminescent  $^3\text{MLCT}$  state on the phen-5,6-dithiolate ligand, and another to the singlet ES on the cobalt moiety *via* the singlet-singlet Dexter energy transfer [7; 55]. This experiment nevertheless verified that the bridging ligand (BL) can provide a highly effective coupling of linked metal centers.

A new series of phen-ligands fused with thiophenes by our working group were also introduced to the Ir(III) photosensitizer as an alternative planar and rigid diimine ligand ( $\text{N}^{\wedge}\text{N}$ ) that is suitable for the electron or energy transfer facilitating the photocatalytic proton reduction [191; 192]. Figure 4.4 shows two Ir(III) photosensitizers with the 5,7-disubstituted thieno[3,4-*f*]phen ligands, namely **Ir-O** and **Ir-th**, together with their optical photoabsorption spectra. The new ligands were then covalently linked to two chloro(pyridine)cobaloxime(III) catalysts (**Ir-O-Co** and **Ir-th-Co**), to again fully take advantage of the significant thermodynamic driving force towards the cobaloxime(III) (see also Appendix D.1). The reactivity of the photocatalytic proton reduction, i.e. turnover number (TON), became higher with the presence of an effective luminescence quenching, hence we carried out the TOAS experiments on these 4 molecular systems to visualize the ultrafast electronic coupling between two active sites.

Cobaloxime(III) originally refers to the cobalt(III)-dimethylglyoximato unit with two bidentate anions of dimethylglyoxime occupying the axial positions in coordination

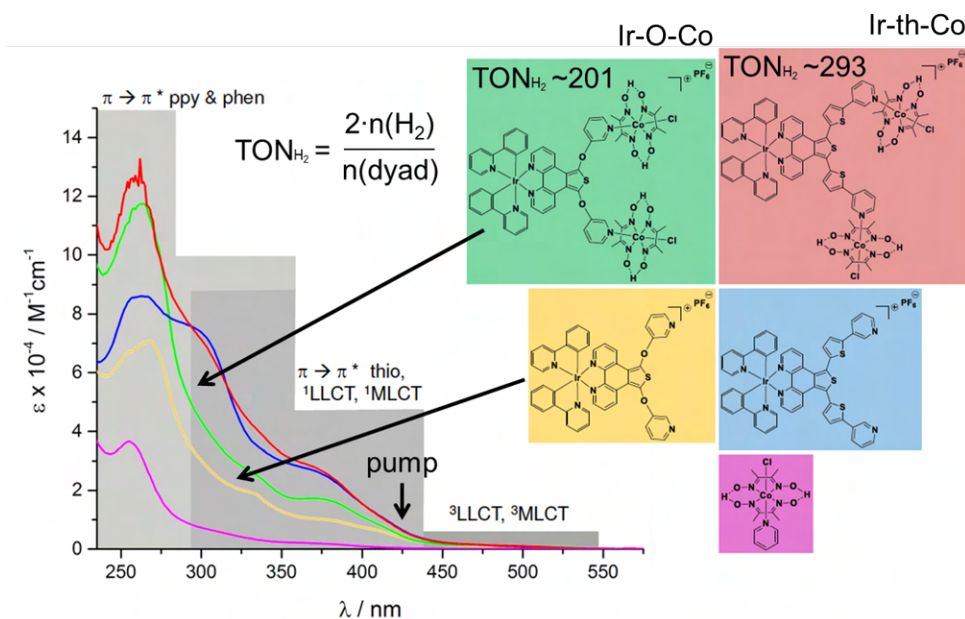


**Figure 4.4:** Optical photoabsorption spectra of **Ir-O** (yellow), **Ir-O-Co** (green), **Ir-th** (blue), **Ir-th-Co** (red), and chloro(pyridine)cobaloxime(III) (purple). The corresponding dipole transitions to the absorption bands are denoted (LLCT = Ligand-to-Ligand Charge Transfer). The TON of the photocatalytic proton reduction was higher with the triadic system (**Ir-O-Co** and **Ir-th-Co**) than with the two-component system (**Ir-O** + cobaloxime(III) and **Ir-th** + cobaloxime(III)). The TOAS experiments were performed accordingly with the pump laser centered at 425 nm.

(Co(III)(dmgH)<sub>2</sub>), and was for the first time used as a water reduction catalyst in 1983 with [Ru(bpy)<sub>3</sub>]<sup>2+</sup> as a photosensitizer [172; 191; 79; 8; 131]. Among its derivatives, the chloro(pyridine)cobaloxime(III) (purple in Fig. 4.4) has been studied for over a century and widely applied as a proton reduction catalyst [87; 200; 99]. With its relatively simple synthesis and high efficiency, the cobaloxime(III) and Ir(III) photosensitizer with cyclometalating ligands have been covalently linked and showed in general enhanced hydrogen production compared to the separate entities [58; 96; 124]. In these Ir(III)-Co(III) photocatalysts, the coordination of cobaloxime(III) to the Ir(III) photosensitizer appeared to be a crucial factor for the efficiency and stability of the photocatalytic proton reduction. In other words, the spatial interaction of two active sites through a coordination bond enhanced an electron transfer and therefore stabilized the system.

In line with this, the **Ir-O-Co** and **Ir-th-Co** are two new photocatalysts also with enhanced hydrogen production compared to the two-component system [191], thus their ultrafast dynamics upon MLCT photoexcitation were investigated in comparison with those of the **Ir-O** and **Ir-th**.

---

## 4.2 Experimental details

The **Ir-O**, **Ir-th**, **Ir-O-Co**, and **Ir-th-Co** were synthesized [191], and dissolved in degassed acetonitrile at the concentration of 1.544 mM, 2.541 mM, 4.03 mM, and 4 mM respectively for the optical density (OD) between 0.1 and 0.3 at 425 nm photoabsorption and 200  $\mu\text{m}$  optical path length. The 425 nm pump pulse was chosen to selectively excite the Ir(III) moiety and populate its MLCT state accordingly (Fig. 4.4). To prevent compound precipitation and multiple photoexcitation during the TOAS measurements, each solution was flowed by a micro-gear pump (mzr-2505) through a microfluidic flat jet system.

Fundamental pulses at 850 nm were first generated by a commercial NOPA (Topas White by Light conversion) pumped with 800 nm pulses in  $0.5 \text{ mJ pulse}^{-1}$  and  $\sim 100 \text{ fs}$  (FWHM) from a 5 kHz Ti:sapphire chirped pulse amplifier (Legend Elite by Coherent). Afterwards the pump pulses at 425 nm ( $\Delta\lambda \sim 3 \text{ nm}$ ) were generated by focusing the collimated 850 nm pulses into a BBO crystal (250  $\mu\text{m}$  thickness) and by means of the second-harmonic generation (SHG) at the right phase matching angle. The residual 850 nm pulses were then filtered out by a BG38 filter, and the pump pulses were recollimated and focused at the interaction point ( $\sim 60 \mu\text{m}$  diameter in  $1/e^2$ ). The pump laser power was set to be less than  $6 \text{ mJ cm}^{-2}$ , and the power-dependence measurement was regularly carried out to ensure that the experiments are conducted in a linear absorption regime.

The probe pulse was a broadband supercontinuum covering from 320 nm to 720 nm, generated by focusing a fraction of the Ti:sapphire laser source into a 5-mm-thick  $\text{CaF}_2$  crystal. To avoid thermal damage, the crystal was mounted on a motorized stage horizontally wobbling. The residual 800 nm pulses after the supercontinuum generation were then filtered out by a BG40 filter, and the probe pulses were split by a 50/50 beam-splitter and focused at two spots ( $\sim 30 \mu\text{m}$  diameter in  $1/e^2$ ) on the sample. One of them was spatially overlapped with the pump pulses, and the other passed through an unexcited sample position to be used as a reference.

After the interaction with the sample, both supercontinuum pulses were collected and collimated by a parabolic mirror and then dispersed by a  $\text{CaF}_2$  prism onto two 512-pixel CMOS sensors (S11105 series by Hamamatsu). The overall time resolution of the measurements was  $\sim 30 \text{ fs}$  ( $\sigma$ ). More details on the experimental setup and calculation of the TA signal in a single-shot detection scheme can be found in the literature [150; 156].

## 4.3 TOAS on Ir(III) photosensitizers

The correction of the probe pulse GVD inside the sample solution as well as the singular value decomposition (SVD) and global fit (GF) analysis on the reduced TOAS data to further exclude any irrelevant noises are well-described elsewhere [23; 68; 150; 156]. For the following analysis only the first two singular values were taken into account, and the reconstructed data successfully resembled the original ones. The sequential first-order rate equation was then used to model the corresponding relaxation dynamics.

In this section, we will first start with interpreting the TA spectra from the **Ir-O** and **Ir-th** in comparison with those from the aforementioned Ir(III) photosensitizers. Basically all the Ir(III) photosensitizers introduced in this thesis contain two ppy-ligands as cyclometalating ligands (C^N), and a different diimine ligand (N^N) whose  $\pi^*$  orbital hence always corresponds to the LUMO orbital in the molecular system [15].

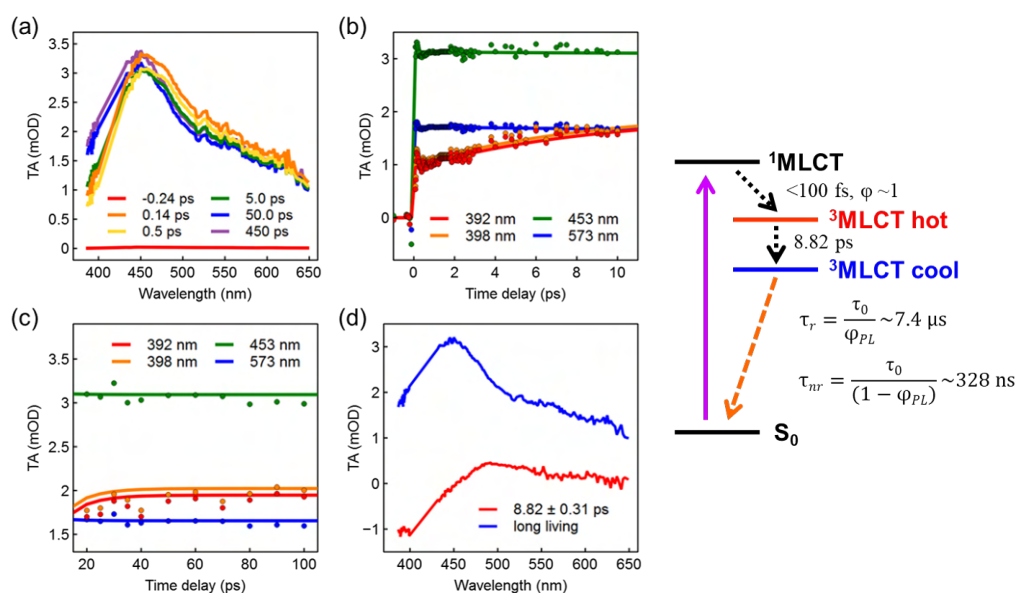


**Figure 4.5:** (a) TA spectra of **Ir-O** at certain probe delays after the 425 nm photoexcitation measured at magic angle of the probe pulse polarization with respect to the pump pulse, (b) transient signal kinetics at different probe wavelengths (dot) together with the SVD-GF results (solid line) up to 10 ps, (c) up to 100 ps, and (d) the corresponding decay-associated spectra (DAS) with two time constants considered. The  $\sim 9$  ps time constant represents the vibrational cooling in the  $^3MLCT$  state. The time constants of the radiative ( $\tau_r$ ) and non-radiative ( $\tau_{nr}$ ) GS recovery were calculated from the quantum yield and lifetime of the phosphorescence.

Figure 4.5 summarizes the results of the SVD-GF analysis on the reduced TOAS data from the **Ir-O**. The TA spectra up to 450 ps probe delay shows an ESA band centered

at ~450 nm with a weak but broad absorption tail at the longer wavelengths, and this ESA band looks quite similar to that from the  $^3\text{MLCT}$  state of the  $[\text{Ir}(\text{ppy})_2(\text{bpy})]^+$  and  $\text{IrS}_2$  (Fig. 4.2, 4.3). Therefore this ESA band is attributed to the  $^3\text{MLCT}$  state on the diimine ligand, which is initially in a higher vibronic state ( $^3\text{MLCT}$  hot) and while being cooled its absorption band becomes narrower and blue-shifted. Thus, the ~9 ps time constant corresponds to the vibrational cooling in the  $^3\text{MLCT}$  state, and neither GSB nor SE signals were identified.

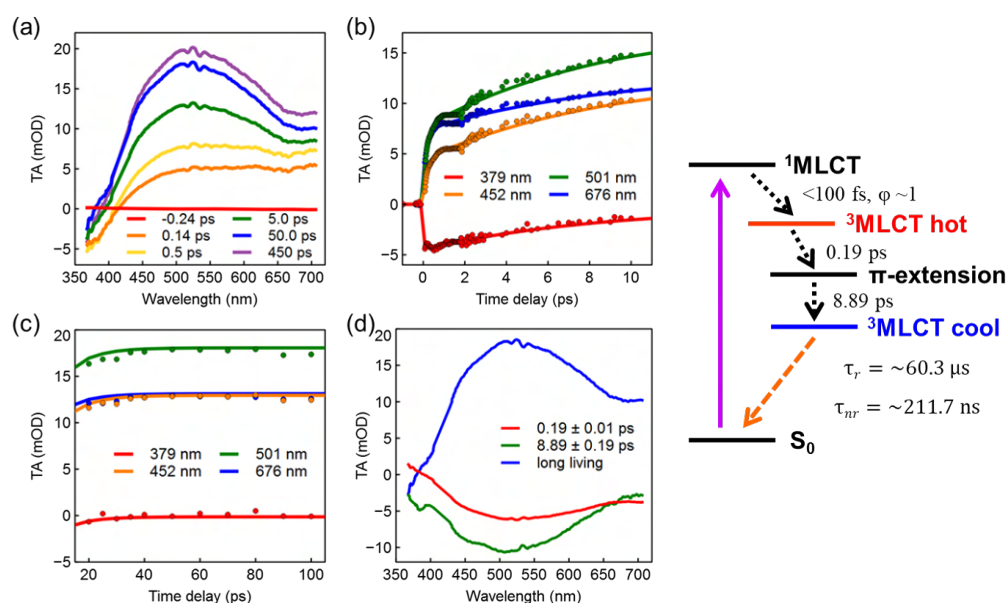


**Figure 4.6:** (a) TA spectra of **Ir-th** at certain probe delays after the 425 nm photoexcitation measured at magic angle of the probe pulse polarization with respect to the pump pulse, (b) transient signal kinetics at different probe wavelengths (dot) together with the SVD-GF results (solid line) up to 10 ps, (c) up to 100 ps, and (d) the corresponding DASs with three time constants considered. The ~0.2 ps and ~9 ps time constants represent the  $\pi$ -extension and vibrational cooling in the  $^3\text{MLCT}$  state respectively. The time constants of the radiative ( $\tau_r$ ) and non-radiative ( $\tau_{nr}$ ) GS recovery were calculated from the quantum yield and lifetime of the phosphorescence.

The TA spectra of **Ir-th** shows an ESA band centered at ~510 nm with again a broad absorption tail at the longer wavelengths (Fig. 4.6). The ESA band is however almost absent right after the photoexcitation, and evolves with two time constants that are well-separated (~0.2 ps and ~9 ps). The increasing cross section can be explained by the increasing electron density in the  $^3\text{MLCT}$  state on the diimine ligand. Compared to the **Ir-O**, the **Ir-th** has three thiophenes connected to each other *via*  $\sigma$ -bonds that can be rotated. In the GS, the angle between two neighboring thiophene planes is ~70° [191], and in the  $^3\text{MLCT}$  state the  $\pi^*$  orbital on the diimine ligand can be further delocalized to the neighboring thiophenes and eventually up to the pyridines, forming

a much larger  $\pi$ -conjugation on the diimine ligand. In other words, the 0.14 ps TA spectrum represents the  $^3\text{MLCT}$  state before the  $\pi$ -extension, and the ESA band centered at  $\sim 510$  nm originates from the larger  $\pi$ -conjugation which develops in two steps, finally reaching the vibrationally cooled state. Here again, neither GSB nor SE signals were identified from the TA spectra.

The polarization anisotropy TOAS measurements were also conducted with the parallel and perpendicular polarization of the pump pulse with respect to the probe pulse, to further investigate the charge transfer nature involving a change of the transient dipole moment in the system. The results are summarized in Appendix D.1.

## 4.4 TOAS on Ir(III)-Co(III) triads

The same TOAS experiments were carried out on the **Ir-O-Co** and **Ir-th-Co** to prove the electronic coupling between the Ir(III) and Co(III) moiety.

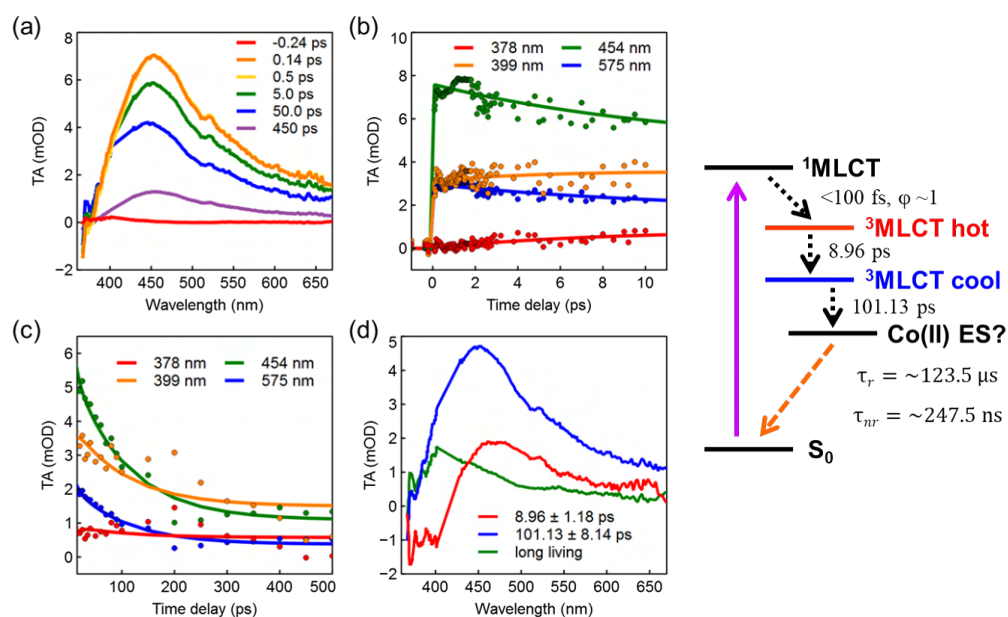


**Figure 4.7:** (a) TA spectra of **Ir-O-Co** at certain probe delays after the 425 nm photoexcitation measured at magic angle of the probe pulse polarization with respect to the pump pulse, (b) transient signal kinetics at different probe wavelengths (dot) together with the SVD-GF results (solid line) up to 10 ps, (c) up to 500 ps, and (d) the corresponding DASs with three time constants considered. The  $\sim 9$  ps time constant represents the vibrational cooling in the  $^3\text{MLCT}$  state, whereas the  $\sim 100$  ps decay time constant represents an electron transfer to the cobaloxime(III). The time constants of the radiative ( $\tau_r$ ) and non-radiative ( $\tau_{nr}$ ) GS recovery were calculated from the quantum yield and lifetime of the phosphorescence.

In contrast to the  $[\text{Ir}(\text{ppy})_2(\text{phen-5,6-dithiolate})\text{Co}(\text{C}_5\text{H}_5)]^+$  case (Fig. 4.3; [55]), the TA spectra of **Ir-O-Co** apparently resemble those of the **Ir-O** in line shape after the 425 nm photoexcitation, and the ESA band from the  $^3\text{MLCT}$  state on the diimine ligand decreases effectively but not completely with the time constant of  $\sim 100$  ps (Fig. 4.7). Since the DAS of the  $\sim 9$  ps time constant looks quite similar to that from the **Ir-O**, this dynamics is again attributed to the vibrational cooling process. The following  $\sim 100$  ps decay dynamics therefore proceeds in the  $^3\text{MLCT}$  state, leaving the 450 ps TA spectrum in almost identical line shape. This can be interpreted as a decrease of the excited electron density, namely a great portion of the excited electron gets transferred to the cobaloxime(III). This then results in two co-existing ESs, the  $^3\text{MLCT}$  state and a Co(II) ES [26], in accordance with the well-known catalytic mechanism of the cobaloxime(III) [200; 99; 8; 131]. Nevertheless, we cannot explicitly indicate the electron transfer nature on rather long timescale, because the cobaloxime(III) does not reveal any transient signals in the optical regime ([87]; see also Appendix D.1).

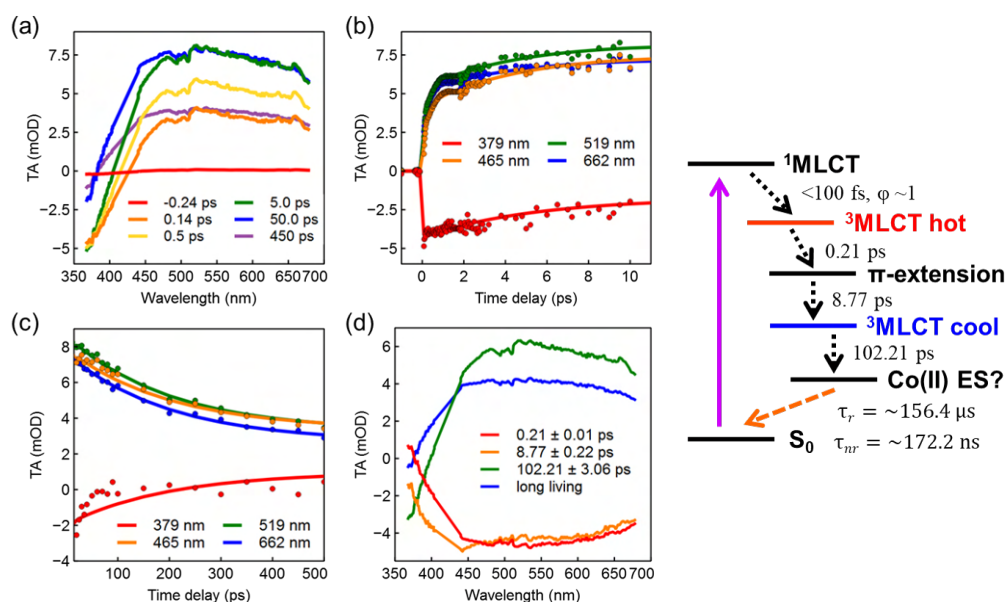


**Figure 4.8:** (a) TA spectra of **Ir-th-Co** at certain probe delays after the 425 nm photoexcitation measured at magic angle of the probe pulse polarization with respect to the pump pulse, (b) transient signal kinetics at different probe wavelengths (dot) together with the SVD-GF results (solid line) up to 10 ps, (c) up to 500 ps, and (d) the corresponding DASs with four time constants considered. The  $\sim 0.2$  ps and  $\sim 9$  ps time constants represent the  $\pi$ -extension and vibrational cooling in the  $^3\text{MLCT}$  state respectively, whereas the  $\sim 100$  ps decay time constant represents an electron transfer to the cobaloxime(III). The time constants of the radiative ( $\tau_r$ ) and non-radiative ( $\tau_{nr}$ ) GS recovery were calculated from the quantum yield and lifetime of the phosphorescence.

The same interpretation applies to the TA spectra of **Ir-th-Co** (Fig. 4.8). Both DASs of

the  $\sim 0.2$  ps and  $\sim 9$  ps time constants are very similar to those from the **Ir-th**, and the following  $\sim 100$  ps decay dynamics again leads to the 450 ps TA spectrum in almost identical line shape. Hence, regardless of the number of thiophenes in the diimine ligand, the electron transfer to the cobaloxime(III) occurs in the Ir(III)-Co(III) triadic system effectively but not completely after the 425 nm photoabsorption with a  $\sim 100$  ps time constant.

In addition to the Ir(III)-Co(III) photocatalysts with the 5,7-disubstituted thieno[3,4-*f*]phen ligands, our working group has synthesized another Ir(III)-Co(III) dyadic system with a bpy-derivative BL [143], and the TOAS experiments were performed on this dyad as well as its respective Ir(III) photosensitizer. The results are summarized in Appendix D.1.

## 4.5 Conclusion and outlook

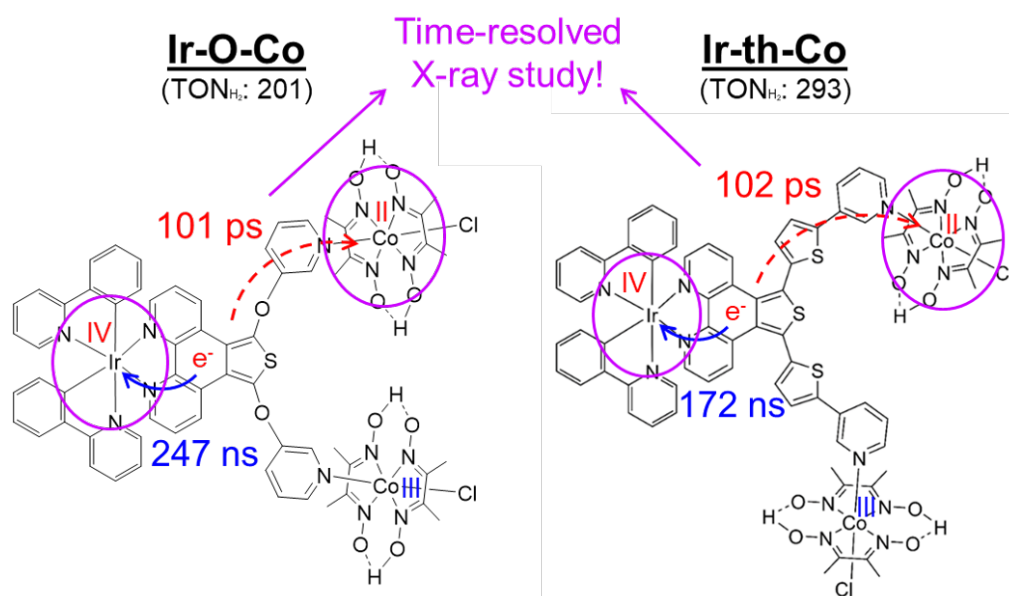


**Figure 4.9:** A summary of the TOAS experiments on **Ir-O-Co** and **Ir-th-Co** photocatalysts. Upon 425 nm photoabsorption, a great portion of the  $^3\text{MLCT}$  excited electron density gets transferred to the cobaloxime(III) with a  $\sim 100$  ps time constant (dashed red), and the rest decays back to the GS *via* phosphorescence (blue). A time-resolved X-ray study is foreseen to close-up the localized dynamics in both Ir(III) and Co(III) moieties (purple) as well as the BL.

Two Ir(III)-Co(III) photocatalysts, i.e. the **Ir-O-Co** and **Ir-th-Co** (Fig. 4.9), with the new 5,7-disubstituted thieno[3,4-*f*]phen BLs were synthesized in order to improve their photocatalytic proton reduction. The ultrafast dynamics in these triadic systems were investigated in the optical regime upon 425 nm photoexcitation, to visualize the corresponding global interaction *via* the electronic coupling between the Ir(III) and

Co(III) moiety. The TOAS experiments disclosed that a great portion of the electron density in the  $^3\text{MLCT}$  state on the diimine ligand gets transferred to the cobaloxime(III) catalyst with a  $\sim 100$  ps time constant, regardless of the number of thiophenes in the BL.

Such an intramolecular electron transfer in a covalently linked bimetallic system is known to be much faster than  $\sim 100$  ps [87; 26; 157], although its thermodynamic viability does not necessarily mean that its kinetics is favorable [7]. That means, a new charge distribution in the Ir(III)-Co(III) photocatalysts can trigger for instance a structural reorganization that takes time, which is in this experiment not clearly visible with the optical probe window. Besides, the decrease of the  $^3\text{MLCT}$  ESA band also doesn't necessarily mean that the electron density has moved to the cobaloxime(III). Since there was no transient signal appearing from the Co(III) moiety as a response, it is still not evident that the electron density has arrived in the Co(III) moiety.

As we noted in Chapter 3, the local hard X-ray probe pulse can be exploited to unravel the formal oxidation state and spin density changes in the Co(III) moiety upon the same 425 nm photoexcitation. In addition, the nuclear dynamics in the Co(III) moiety or the thiophenes as well as the GS recovery in the Ir(III) moiety can be monitored. Thereby the TOAS experiments and time-resolved X-ray studies can deliver complementary information on the ultrafast dynamics in inorganic chelates.

## 5 4d<sup>6</sup> Ru(II)-Mo(VI) photocatalyst

Picosecond "electron" transfer in a dyadic system.

5.1 Introduction .....	82
5.2 Experimental details .....	84
5.3 TOAS on Ru(II) photosensitizers.....	85
5.4 TOAS on Ru(II)-Mo(VI) dyad .....	87
5.5 Conclusion and outlook .....	89

Unlike 5d<sup>6</sup> Ir(III) photosensitizers, 4d<sup>6</sup> Ru(II) photosensitizers often show their GSB as well as ESA signals in the optical probe window upon MLCT photoexcitation [157; 180; 201; 185]. In other words, the GS recovery dynamics can be easily recognized from the 4d<sup>6</sup> Ru(II) photosensitizers, and therefore disentangled from the relaxation dynamics in the ES manifold.

In accordance with the previous chapter, herein the TOAS methodology with the 425 nm photoexcitation was again exploited to visualize the ultrafast global interaction in another dyadic system with the Ru(II) photosensitizer. A so-called photo-induced intramolecular electron transfer (PIET) in a bimetallic system can promote various catalytic reactions, such as oxygen atom transfer (OAT) by Ru(II)-Mo(VI) photocatalyst [50]. The picosecond PIET dynamics to activate the Mo(VI) moiety were then identified as the oxidation of a non-innocent phenol-thiosemicarbazone ligand, by comparing the difference absorption spectrum from the spectroelectrochemical oxidation of the catalytic Mo(VI) complex [MoO<sub>2</sub>(L<sup>Me</sup>)MeOH] with the results of the SVD-GF analysis. This let us to propose a revised mechanism of the PIET-enhanced OAT catalysis on our biomimetic Ru(II)-Mo(VI) dyad, [Ru(bpy)<sub>2</sub>(L<sup>2</sup>)MoO<sub>2</sub>(solvent)]<sup>2+</sup>, in which the <sup>3</sup>MLCT state of the Ru(II) moiety spontaneously perturbed the Mo(VI) moiety to be activated, resulting in two co-existing charge separations.

Since the ultrafast dynamics of the Ru(II)-Mo(VI) dyad within the probe delay window of 500 ps were dominated by the Ru(II) moiety, explicit designation of the oxidation of the chromophoric part and the concomitant reduction in the Mo(VI) moiety was not possible. This chapter was written primarily based on our peer-reviewed work [157].

---

## 5.1 Introduction

Metalloenzymes often regenerate their active sites *via* efficient electron transfer between spatially-separated electron transfer units [76]. Thus, the comprehension of electronic relays between these components in bio-inspired redox catalysts is attracting increasing interests [198; 44].

Electrochemical approaches to mimic such a process include for instance the attachment of reversible electron transfer components to metalloenzyme-mimics [71; 22; 187]. PIET processes have also been explored to harness solar energy and thereby to accelerate redox catalysis. For example, Ru(II) photosensitizers covalently linked to Mn-based photosystem II models were introduced to mimic the four-electron oxidation of two water molecules by light-induced electron transfer [82]. Similarly, hydrogenase-mimics with reversible photosensitizers attached have been investigated with the aim of catalysing the light-driven production of H<sub>2</sub> [155; 183].

Photo-redox processes have also been utilized to catalyse oxygenation reactions with environmentally-benign O-atom sources [120; 5; 162], in particular <sup>3</sup>O<sub>2</sub> or H<sub>2</sub>O [89]. Enemark and Kirk *et al.* for instance demonstrated that oxo-molybdenum(V) can be photo-activated *via* an antenna-mediated electron transfer process by covalently linking the oxo-molybdenum(V) to porphyrin-Fe(III) or Zn(II) complexes [197; 12].

Recently, Duhme-Klair *et al.* have developed biomimetic *cis*-dioxo Mo(VI) complexes with appended Ru(II) photosensitizers to facilitate the OAT catalysis *via* the PIET (Fig. 5.1; [51]). They reported that the attachment of a bis(bipyridyl)-phenanthroline Ru(II) complex to a *cis*-dioxo Mo(VI) thiosemicarbazone allows the OAT from dimethyl sulfoxide (DMSO) to triphenyl phosphine (PPh<sub>3</sub>) to be accelerated upon irradiation with visible light. It was therefore proposed that the oxidation of the bpy<sup>-</sup>-ligand upon MLCT photoexcitation by an oxidizing agent (Ox<sup>A</sup>) leads to a highly reactive, one-electron oxidized phenol-thiosemicarbazone ligand in the catalytic Mo(VI) moiety *via* the PIET ((3) in Fig. 5.1), being the key to accelerate the rate-determining step of the OAT catalysis [50].

Since the oxidative quenching process of the bpy<sup>-</sup>-ligand is diffusion-limited, the highly reactive one-electron oxidized Mo(VI) moiety is expected to be present on rather microsecond to millisecond timescale. It is worth noting that the formal oxidation state of the molybdenum is already 6+ and cannot increase further. Thus, the electron transfer following the oxidative quenching is most likely from the non-innocent phenol-thiosemicarbazone ligand in the catalytic Mo(VI) moiety, towards

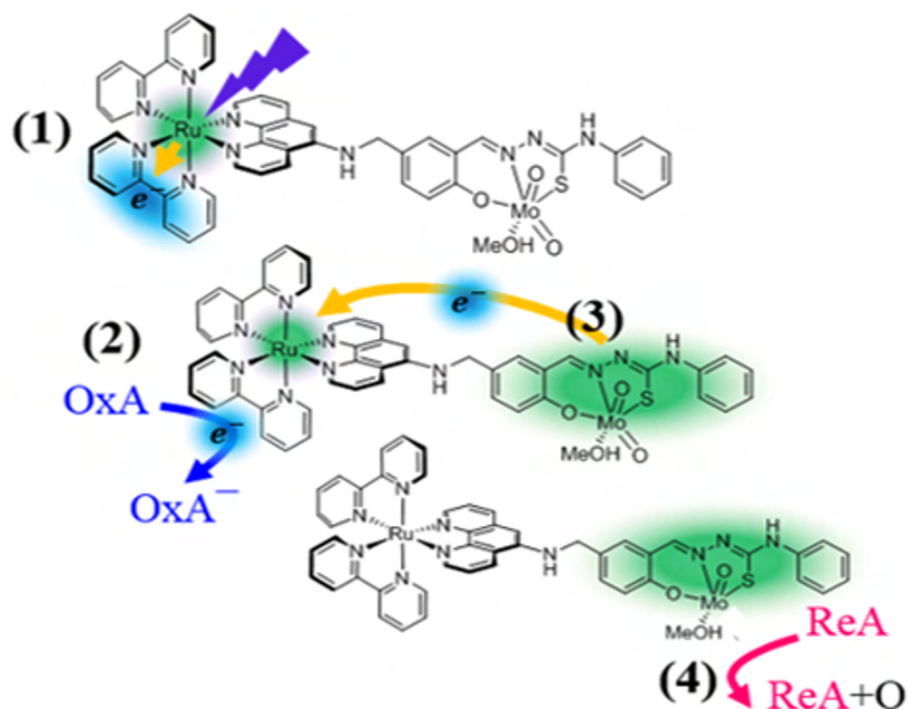


**Figure 5.1:** Light-induced activation of *cis*-dioxo Mo(VI) catalytic moiety in Ru(II)-Mo(VI) dyad  $[\text{Ru}(\text{bpy})_2(\text{L}^2)\text{MoO}_2(\text{MeOH})]^{2+}$ , as proposed in [50]: (1) The MLCT photoexcitation to one of the bpy-ligands, (2) the oxidative quenching of the bpy<sup>-</sup> ligand by a diffusion-limited reaction with an OxA, followed by (3) the activation of the Mo(VI) moiety by an electron transfer to the Ru(II) moiety. (4) An OAT catalysis taking place to a reducing agent (ReA) from the activated *cis*-dioxo Mo(VI) moiety.

the Ru(II) moiety. As this kinetic model was proposed based on catalytic studies and steady-state characterization methods, a further validation with the time-resolved techniques is highly desirable.

With this motivation we carried out the TOAS experiments on the Ru(II)-Mo(VI) photocatalyst upon 425 nm photoexcitation. Additionally, we performed control experiments on the Ru(II) photosensitizer  $[\text{Ru}(\text{bpy})_2(\text{phen-NH}_2)]^{2+}$  and  $[\text{Ru}(\text{bpy})_3]^{2+}$  to disentangle the ultrafast dynamics in the Ru(II) moiety from those in the Mo(VI) moiety, and ultimately to identify the initial steps of the PIET-enhanced OAT catalysis.

---

## 5.2 Experimental details

The  $[\text{Ru}(\text{bpy})_2(\text{phen-NH}_2)]^{2+}$ ,  $[\text{Ru}(\text{bpy})_3]^{2+}$ , and Ru(II)-Mo(VI) dyad were synthesized [50], and dissolved in degassed acetonitrile at the concentration of  $\sim 1.2$  mM,  $\sim 1.3$  mM, and  $\sim 0.5$  mM respectively for the OD between 0.1 and 0.3 at 425 nm photoabsorption and 200  $\mu\text{m}$  optical path length. The 425 nm pump pulse was chosen to selectively excite the Ru(II) moiety and populate its MLCT state accordingly. To prevent compound precipitation and multiple photoexcitation during the TOAS measurements, each solution was flowed by a micro-gear pump (mzr-2505) through a microfluidic flat jet system.

Fundamental pulses at 850 nm were first generated by a commercial NOPA (Topas White by Light conversion) pumped with 800 nm pulses in  $0.5 \text{ mJ pulse}^{-1}$  and  $\sim 100$  fs (FWHM) from a 5 kHz Ti:sapphire chirped pulse amplifier (Legend Elite by Coherent). Afterwards the pump pulses at 425 nm ( $\Delta\lambda \sim 3$  nm) were generated by focusing the collimated 850 nm pulses into a BBO crystal (250  $\mu\text{m}$  thickness) and by means of the second-harmonic generation (SHG) at the right phase matching angle. The residual 850 nm pulses were then filtered out by a BG38 filter, and the pump pulses were recollimated and focused at the interaction point ( $\sim 60 \mu\text{m}$  diameter in  $1/e^2$ ). The pump laser power was set to be less than  $6 \text{ mJ cm}^{-2}$ , and the power-dependence measurement was regularly carried out to ensure that the experiments are conducted in a linear absorption regime.

The probe pulse was a broadband supercontinuum covering from 320 nm to 720 nm, generated by focusing a fraction of the Ti:sapphire laser source into a 5-mm-thick  $\text{CaF}_2$  crystal. To avoid thermal damage, the crystal was mounted on a motorized stage horizontally wobbling. The residual 800 nm pulses after the supercontinuum generation were then filtered out by a BG40 filter, and the probe pulses were split by a 50/50 beam-splitter and focused at two spots ( $\sim 30 \mu\text{m}$  diameter in  $1/e^2$ ) on the sample. One of them was spatially overlapped with the pump pulses, and the other passed through an unexcited sample position to be used as a reference.

After the interaction with the sample, both supercontinuum pulses were collected and collimated by a parabolic mirror and then dispersed by a  $\text{CaF}_2$  prism onto two 512-pixel CMOS sensors (S11105 series by Hamamatsu). The overall time resolution of the measurements was  $\sim 30$  fs ( $\sigma$ ). More details on the experimental setup and calculation of the TA signal in a single-shot detection scheme can be found in the literature [150; 156].

## 5.3 TOAS on Ru(II) photosensitizers

The correction of the probe pulse GVD inside the sample solution as well as the SVD-GF analysis on the reduced TOAS data to further exclude any irrelevant noises are well-described elsewhere [23; 68; 150; 156]. For the following analysis the first five singular values were taken into account, and the reconstructed data successfully resembled the original ones. The sequential first-order rate equation was then used to model the corresponding relaxation dynamics [157].

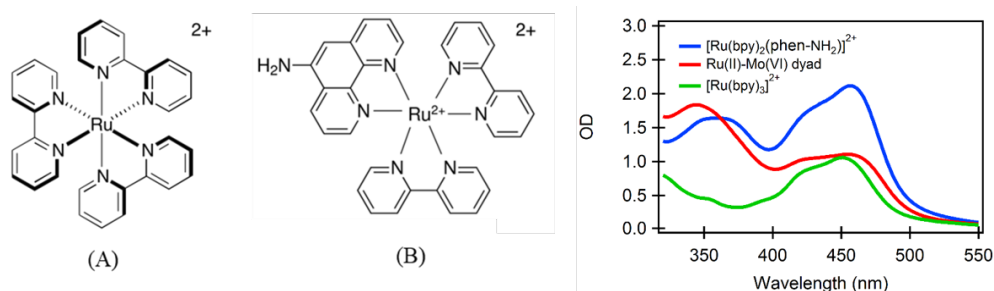


**Figure 5.2:** A structural formula of (A) [Ru(bpy)<sub>3</sub>]<sup>2+</sup> and (B) [Ru(bpy)<sub>2</sub>(phen-NH<sub>2</sub>)]<sup>2+</sup> together with their optical absorption spectra.

First of all, both [Ru(bpy)<sub>3</sub>]<sup>2+</sup> and [Ru(bpy)<sub>2</sub>(phen-NH<sub>2</sub>)]<sup>2+</sup> (Fig. 5.2) were subjected to the TOAS experiments to serve as a basis set for the Ru(II)-Mo(VI) dyad. The corresponding ultrafast dynamics have been extensively researched over the last few decades [201; 25; 68; 180; 47; 185], and will be revisited in this section with the 425 nm photoexcitation. The following comparison of the TA spectra and their kinetics will then allow us to distinguish the transient signal from the Mo(VI) moiety out of the others. Figure 5.3 summarizes the results of the SVD-GF analysis on the reduced TOAS data from the [Ru(bpy)<sub>3</sub>]<sup>2+</sup>, [Ru(bpy)<sub>2</sub>(phen-NH<sub>2</sub>)]<sup>2+</sup>, and Ru(II)-Mo(VI) dyad.

The TA spectra of the [Ru(bpy)<sub>3</sub>]<sup>2+</sup> (Fig. 5.3 A) shows its prominent ESA (~365 nm) and GSB (~450 nm) signals. This ESA occurs at the bpy<sup>-</sup>-ligand [185], and the GSB matches well with the inverted OA in line shape. The femtosecond DAS (Fig. 5.3 B) can be rationalized as the modulation of the electron density in the MLCT state due to the solvation [23], whereas the picosecond DAS is assigned to the vibrational cooling.

The TA spectra of the [Ru(bpy)<sub>2</sub>(phen-NH<sub>2</sub>)]<sup>2+</sup> (Fig. 5.3 C) show slightly different behaviours especially in the ESA band, due predominantly to the GS absorption band of the phen-NH<sub>2</sub>-ligand at the similar wavelength [202]. In other words, the suppressed ESA band on the femtosecond timescale that differs from the [Ru(bpy)<sub>3</sub>]<sup>2+</sup> corresponds to the ESA at the phen-NH<sub>2</sub><sup>-</sup>-ligand, and ILCT follows to the bpy-ligand, fully recovering its ESA band line shape on the picosecond timescale [180; 47].

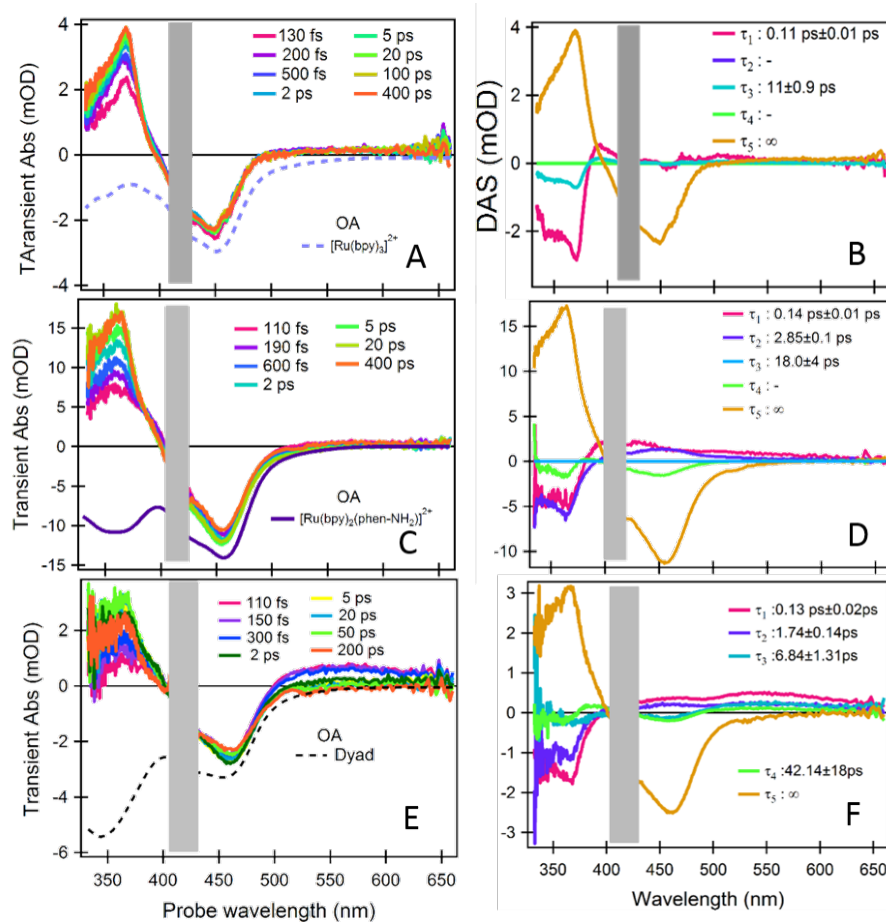


**Figure 5.3:** A representative selection of the TA spectra from the (A)  $[\text{Ru}(\text{bpy})_3]^{2+}$ , (C)  $[\text{Ru}(\text{bpy})_2(\text{phen-NH}_2)]^{2+}$ , and (E) Ru(II)-Mo(VI) dyad, together with their inverted optical absorption (OA) spectra and (B, D, F) DASs. For the comparison of the results, the number of spectral components was kept to 5 and the ones not used in the SVD-GF analysis are labelled with "-". The spectral range contaminated with pump scattering is masked with a grey box.

That means, the 425 nm photoexcitation resulted in the prompt population of the phen-NH<sub>2</sub><sup>-</sup>-ligand as well as the bpy<sup>-</sup>-ligand, and the <sup>3</sup>MLCT state became localized onto the latter. This is now reflected in the DAS of the ~3 ps time constant (Fig. 5.3 D), and the other DASs can be interpreted as before.

The same ILCT dynamics is also observed in the TA spectra of the Ru(II)-Mo(VI) dyad (Fig. 5.3 E), and detailed interpretation of the DASs (Fig. 5.3 F) as well as an additional signal appearing at  $\lambda_{\text{probe}} > 500$  nm will follow in the next section. During the TOAS experiments, no SE signal was observed in agreement with its non-allowed character [25].

Figure 5.4 again compares the TA spectra at representative probe delays of 110 fs, 2

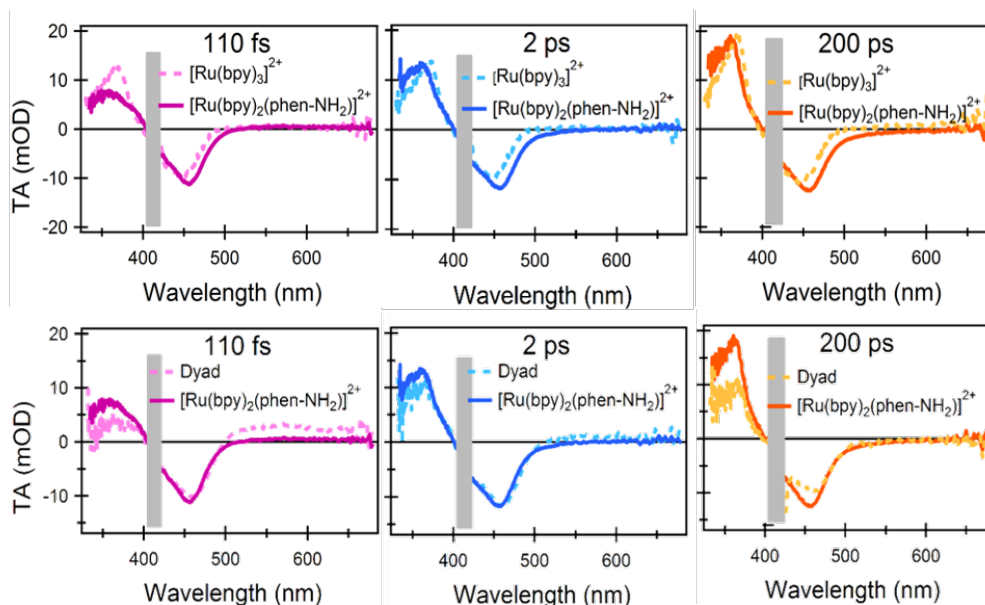


**Figure 5.4:** Comparison of the TA spectra at certain probe delays after the 425 nm photoexcitation between (above)  $[\text{Ru}(\text{bpy})_3]^{2+}$  and  $[\text{Ru}(\text{bpy})_2(\text{phen-NH}_2)]^{2+}$ , and between (below)  $[\text{Ru}(\text{bpy})_2(\text{phen-NH}_2)]^{2+}$  and Ru(II)-Mo(VI) dyad. The spectral range contaminated with pump scattering is masked with a grey box.

ps, and 200 ps between the  $[\text{Ru}(\text{bpy})_3]^{2+}$  and  $[\text{Ru}(\text{bpy})_2(\text{phen-NH}_2)]^{2+}$ , and between  $[\text{Ru}(\text{bpy})_2(\text{phen-NH}_2)]^{2+}$  and Ru(II)-Mo(VI) dyad. From the first comparison, we clearly notice a transition in the ESA band from 110 fs to 2 ps by the ILCT dynamics. This transition is also present in the Ru(II)-Mo(VI) dyad, although two additional dynamics at  $\lambda_{\text{probe}} > 500$  nm on the femtosecond timescale and at  $\lambda_{\text{probe}} < 500$  nm on the picosecond timescale will be further analysed in the next section.

## 5.4 TOAS on Ru(II)-Mo(VI) dyad

Figure 5.5 is a reprint of the Fig. 5.3 E and F as well as the difference TA (DTA) spectra of the Ru(II)-Mo(VI) dyad at certain probe delays after the 425 nm photoexcitation with respect to the 200 fs TA spectrum. Here we will further interpret two distinctive dynamics appearing at  $\lambda_{\text{probe}} > 500$  nm on the femtosecond timescale and at  $\lambda_{\text{probe}} < 500$  nm on the picosecond timescale.

Both dynamics are visible in presence of the catalytic Mo(VI) moiety, and by assuming that the dyadic system contains only the  $^3\text{MLCT}$  state at 200 fs probe delay, we can separate the contribution from the Mo(VI) moiety by subtracting the 200 fs TA spectrum. Among the obtained DTA spectra, it is undoubtful that the (200 ps-200 fs) DTA spectrum and the inverse sum of the  $\text{DAS}_{6.8\text{ps}}$  and  $\text{DAS}_{42\text{ps}}$

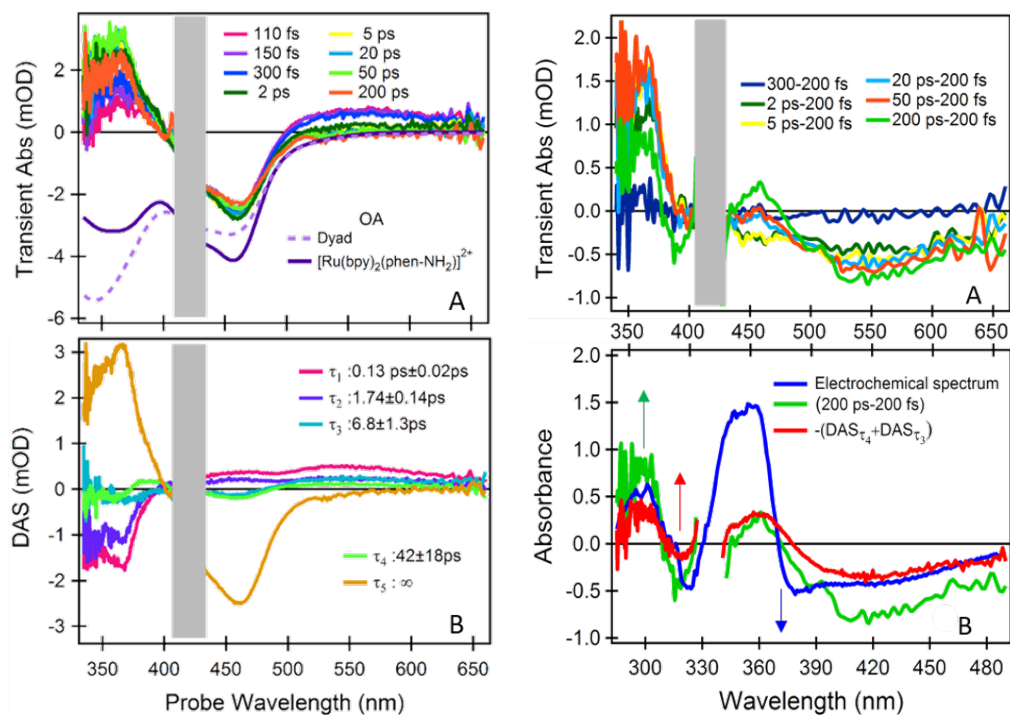


**Figure 5.5:** (left) A representative selection of the TA spectra from the Ru(II)-Mo(VI) dyad (A), together with its inverted OA spectrum and (B) DASs. (right) DTA spectra at certain probe delays after the 425 nm photoexcitation with respect to the 200 fs TA spectrum (A), and a comparison of the difference spectrum from the spectroelectrochemical oxidation of the catalytic Mo(VI) complex  $[\text{MoO}_2(\text{L}^{\text{Me}})\text{MeOH}]$  with the (200 ps-200 fs) DTA spectrum and the inverse sum of the DAS<sub>6.8ps</sub> and DAS<sub>42ps</sub> [50]. A relative shift of 0.65 eV was applied in the energy domain and the spectral range contaminated with pump scattering is masked with a grey box.

show strong similarities at any wavelength with the difference spectrum from the spectroelectrochemical oxidation of the catalytic Mo(VI) complex  $[\text{MoO}_2(\text{L}^{\text{Me}})\text{MeOH}]$  [50], after applying a relative shift of 0.65 eV (Fig. 5.5 right). This spectral shift is justified since the global charge of the electrochemically oxidized Mo(VI) catalyst  $[\text{MoO}_2(\text{L}^{\text{Me}})\text{MeOH}]$  and the photoexcited dyad are different. Hence, we can deduce that (1) the femtosecond signals at  $\lambda_{\text{probe}} > 500$  nm originate from the LC transitions in the neutral Mo(VI) moiety, which are just red-shifted by the strong electrostatic field from the transient dipole moment in the Ru(II) moiety [115; 144], and (2) the picosecond signals are an oxidative process of the chromophoric part in the Mo(VI) moiety, i.e. the conjugated phenolate-thiosemicarbazone ligand [179].

In other words, the GS absorption signal of the neutral Mo(VI) moiety at  $\lambda_{\text{probe}} > 500$  nm starts disappearing on the picosecond timescale, in accordance with a new charge distribution from the Mo(VI) coordination ligand sphere towards acceptor

orbitals on the non-innocent ligand close to the BL or on the BL itself. The dyadic system is also not as flat and stretched as in Fig. 5.1 since the linker is very flexible, thus a folded structure is possible. That means, we cannot exclude a (partial) charge localization on the *cis*-dioxo Mo(VI) or Ru(II) moiety, but this did not cause any detectable distortion in the associated TA spectra.

The inverse sum of the DAS<sub>6.8ps</sub> and DAS<sub>42ps</sub> from the SVD-GF analysis hence describes the oxidation dynamics of the Mo(VI)-coordinated chromophoric ligand spanning from 2 to 60 ps. Therefore, we can understand that upon the MLCT photoexcitation the oxidation of the non-innocent phenol-thiosemicarbazone ligand in the catalytic Mo(VI) moiety occurs on the picosecond timescale, while the <sup>3</sup>MLCT state in the Ru(II) moiety is still intact. The complete bleaching of the GS absorption signal of the neutral Mo(VI) moiety at  $\lambda_{probe} > 500$  nm can be then interpreted as the unitary quantum yield of the second ES in the dyadic system.

In addition to the 425 nm photoexcitation, we conducted the same TOAS experiments and SVD-GF analysis with 450 nm photoexcitation to rule out that the observed dynamics resulted from the direct photoabsorption by the Mo(VI) moiety. The results are consistent and can be found in Appendix D.2.

---

## 5.5 Conclusion and outlook

In conclusion, our study revealed that the enhanced OAT on a Mo(VI) oxotransferase model in the Ru(II)-Mo(VI) dyad stems from the picosecond PIET in the Mo(VI) moiety resulting in the second ES upon the MLCT photoexcitation. An oxidative process of the chromophoric part in the Mo(VI) moiety, namely the conjugated phenolate-thiosemicarbazone ligand, spans from 2 to 60 ps and leads to the catalytic activation of the Mo(VI) moiety. These dynamics do not accompany any GS recovery in the Ru(II) moiety, indicating that the dynamics in Ru(II) and Mo(VI) moieties are not coupled within our probe delay window.

Accordingly we propose a revised mechanism of the PIET-enhanced OAT catalysis as in Fig. 5.6. Without any diffusion-limited process considered, the simultaneous presence of both photo-activated states in the Ru(II) and Mo(VI) moieties unveiled an unexpected scenario, where the second excited electron from the non-innocent ligand is not transferred to the Ru(II) moiety but only to the acceptor orbitals close to the BL, or on the *cis*-dioxo Mo(VI) moiety.

This novel and ultrafast photocatalytic trigger in such a small supramolecular dyadic system has not been reported before, and therefore it will have an important impact

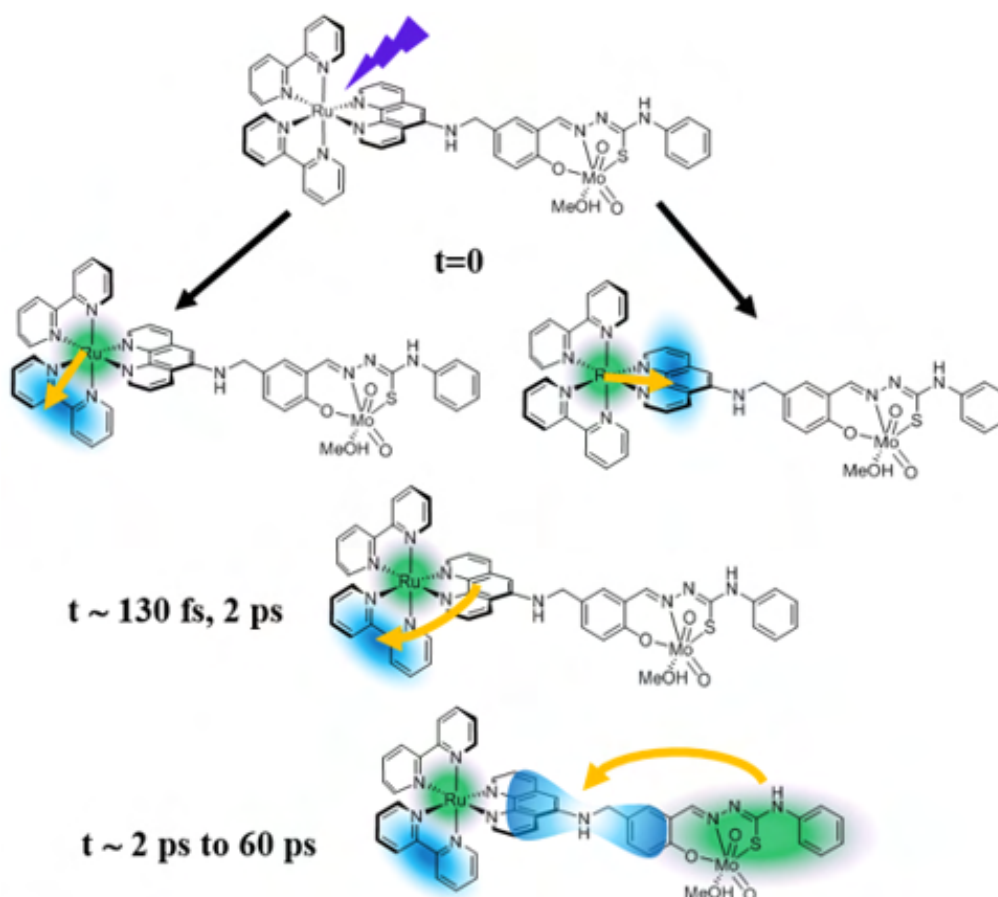


**Figure 5.6:** Proposed mechanism for the initial steps leading to the light-induced activation of the catalytic Mo(VI) moiety.

on modelling photocatalytic processes in bimetallic dyads, not only concerning the ultrafast timescale but also much longer timescales, such as  $\mu\text{s}$  or even to  $\text{ms}$  which is way slower than the expected lifetime of the bi-activated dyadic system. For instance, one of the first implications is that both the neutralization of the  $\text{bpy}^-$ -ligand by an OxA such as  $\text{MV}^{2+}$  and the reduction of the catalytic Mo(VI) moiety by a ReA such as  $\text{PPh}_3$  can potentially proceed in parallel. On the other hand, the OAT can be much slower (seconds to minutes; [83]) than the oxidative quenching process (typically  $\mu\text{s}$ ).

In fact the PIET-enhanced OAT was only feasible in the presence of  $\text{MV}^{2+}$  [50], and the OAT to the  $\text{PPh}_3$  was an extremely slow process (several minutes). This discloses that the oxidative quenching by the  $\text{MV}^{2+}$  prolongs the lifetime of the second ES in the Mo(VI) moiety beyond the microsecond timescale, letting the PIET-enhanced OAT process be feasible. Remarkably, despite the slow catalytic activity at the Mo(VI) moiety cannot be directly correlated to the ultrafast formation of the bi-activated state, the presence of this state is still crucial for the catalytic function.

While this study revealed the formation of two photo-activated states and their dynamics, it raises yet more questions relating to the role of the solvent or specific nuclear coordinates in modulating the sequence of the reactions, as well as the local electronic and structural changes involved in the process. In perspective it will be crucial to carry out the time-resolved XAS and XSS experiments with the hard X-ray probe pulse, together with the polarization anisotropy TOAS experiments.

## 6 4d<sup>6</sup> Ru(II) photosensitizer

We know, that we don't know.

6.1 Introduction .....	93
6.2 Experimental details .....	96
6.3 Time-resolved EXAFS on Ru(II) photosensitizers.....	97
6.4 Lifetime studies in acetonitrile and water .....	101
6.5 Conclusion and outlook .....	102

As noted in Chapter 4 and 5, a long-lived <sup>3</sup>MLCT state (>100 ps) of the inorganic chelates upon optical photoabsorption is crucial to the light-harvesting applications [141; 190; 191; 157]. Compared to the 5d<sup>6</sup> Ir(III) photosensitizers, the 4d<sup>6</sup> Ru(II) photosensitizers have weaker ligand field splitting, letting the <sup>3</sup>MC state be placed closer to the <sup>3</sup>MLCT state ( $\Delta E \sim 0.5$  eV; [60]). This opens up a thermal population of the <sup>3</sup>MC state in the second relaxation pathway, often lowering the phosphorescence quantum yield and causing the photodegradation [194].

The <sup>3</sup>MLCT state population and depopulation kinetics with respect to the solvent, temperature, and presence of oxygen have been therefore extensively studied starting with the [Ru(bpy)<sub>3</sub>]<sup>2+</sup> and [Ru(phen)<sub>3</sub>]<sup>2+</sup> [59; 194; 139; 193; 127; 68]. The localization of the excited electron and the following transient dipole moment within the first picosecond are also of great importance to direct the excited electron to a particular ligand [201; 180; 193; 127], especially in the heteroleptic complexes with a dipyrido[2,3-a:3',2'-c]phenazine (dppz) ligand known for its "light-switch" effect [171; 153]. With a highly  $\pi$ -deficient ligand such as 1,4,5,8-tetraazaphenanthrene (TAP) instead of bpy or phen however, the [Ru(TAP)<sub>2</sub>(dppz)]<sup>2+</sup> becomes again strongly luminescent in water by having the excited electron localized on the TAP-ligand [154].

Complementary to the thorough researches so far, herein we report the results of the time-resolved EXAFS experiments on the light-switching and photo-oxidizing Ru(II) complexes, i.e. [Ru(phen)<sub>3</sub>]<sup>2+</sup>, [Ru(phen)<sub>2</sub>(dppz)]<sup>2+</sup>, [Ru(TAP)<sub>2</sub>(dppz)]<sup>2+</sup>, and [Ru(TAP)<sub>3</sub>]<sup>2+</sup> in degassed acetonitrile upon 400 nm photoexcitation. In addition, their transient absorption signal kinetics measured in degassed water and acetonitrile further confirmed the non-radiative deactivation processes previously reported from the luminescence lifetime studies [127; 152; 139; 154].

## 6.1 Introduction

Based on the Fourier analysis of the EXAFS at its K- and L<sub>3</sub>-edge (Section 2.3.1), the coordination shell structures of the [Ru(bpy)<sub>3</sub>]<sup>2+</sup> and its derivatives have shown their changes with respect to the surrounding elements [88], different ligands [16; 72; 166; 167], and photoabsorption [70; 169]. In general the first and second coordination shell structure differ only on the picometer-scale regardless of the chemical environment, and this predominantly comes from a structural reorganization by different charge distribution in the system [182]. When it comes to the <sup>3</sup>MLCT state structure, a contraction of Ru-N bonds by ~0.03 Å on average is caused by the strong transient dipole moment with the localized excited electron.

The localized excited electron in the <sup>3</sup>MLCT state has its own lifetime and usually decays radiatively back to the GS. The oxidative quenching as well as the thermal population of the <sup>3</sup>MC state are however two representative non-radiative decay pathways present at the same time [194; 59; 139], and depending on its chemical environment the Ru(II) photosensitizer can be either "switched-on" or off [148]. Such a luminescent probe with its readily tunable photophysical and electrochemical properties has been accordingly introduced to some biological applications [147; 30].

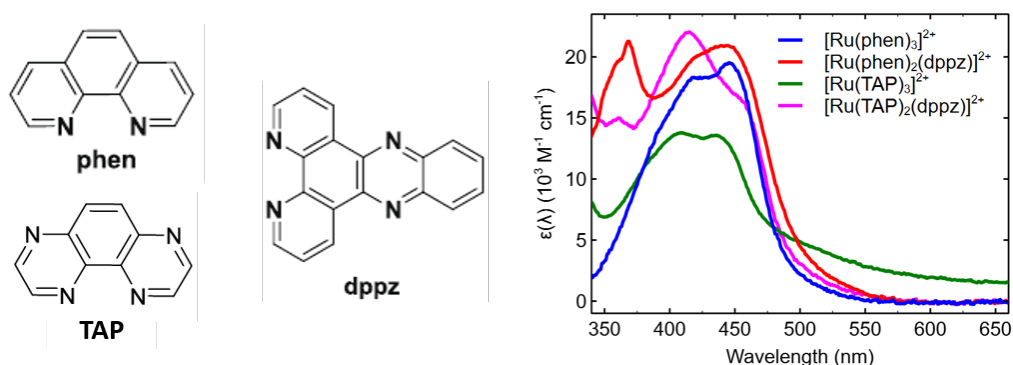


**Figure 6.1:** (left) A structural formula of phen-, TAP-, and dppz-ligand and (right) optical photoabsorption spectra of [Ru(phen)<sub>3</sub>]<sup>2+</sup>, [Ru(phen)<sub>2</sub>(dppz)]<sup>2+</sup>, [Ru(TAP)<sub>3</sub>]<sup>2+</sup>, and [Ru(TAP)<sub>2</sub>(dppz)]<sup>2+</sup> in acetonitrile.

The Ru(II) photosensitizers (Fig. 6.1) that recognize and react with nucleic acids have been reported since the 1980s [78; 30], affording a rich vein of insight into the relationship between biomolecular structure and photophysical dynamics. The early work on the interaction of the Δ and Λ enantiomers of [Ru(phen)<sub>3</sub>]<sup>2+</sup> with double-stranded DNA showed that the Δ enantiomer bound more strongly to B-DNA than the Λ one, by insertion of a phen-ligand between the base-pairs of the polynucleotide (intercalation; [30]). A clear way to increase the strength of

binding interactions through intercalation is thus to incorporate a more extended heteroaromatic ligand, such as a dppz-ligand (Fig. 6.2; [78; 152]).



**Figure 6.2:** Intercalated  $[\text{Ru}(\text{L})_2(\text{dppz})]^{2+}$  in double-stranded DNA fragment (CG-GC; Figure from [4]).

A striking property of  $[\text{Ru}(\text{phen})_2(\text{dppz})]^{2+}$  for example is that it is non-emissive in aqueous solution but luminesces strongly when it binds to DNA [30]. The first TOAS measurement on the  $[\text{Ru}(\text{phen})_2(\text{dppz})]^{2+}$  in aqueous media was made by the group of Barbara with the 400 nm photoexcitation [152]. The results unveiled two ultrafast dynamics, one with the lifetime of 3 ps and the other with 250 ps. In  $\text{D}_2\text{O}$  however, the lifetime was determined with a single time constant of 560 ps, indicating that the non-radiative deactivation process strongly depends on the -OH or -OD vibration. From a subsequent study, it was also concluded that in the ES both phenazine nitrogens (N9 and N14) of the dppz-ligand were coordinated to water [151].

It is well-known that the electrochemical properties of the Ru(II) photosensitizers can be modified by change of ligands. One system that has been largely investigated in this regard is TAP, where the electron-withdrawing nature of the ligand makes the complex a much stronger OxA. A consequence of this is, for instance, that  $[\text{Ru}(\text{TAP})_3]^{2+}$  causes significantly more photo-damage to DNA than does  $[\text{Ru}(\text{phen})_3]^{2+}$ , as was first demonstrated using plasmid DNA to monitor single strand breaks [108]. However, later work using  $^{32}\text{P}$ -labelled DNA showed that a more important reaction is the formation of photo-adducts [57]. Subsequently this adduct was isolated and characterized, and shown to involve covalent attachment of the TAP-ligand to the exocyclic 2-N of guanine [97].

It is clear from these early studies that TAP-complexes such as  $[\text{Ru}(\text{TAP})_3]^{2+}$  make an interesting system to study the photo-oxidation of DNA, but they suffer from the disadvantage that the binding to DNA is relatively weak and the mode of binding is uncertain. A much better option is to study complexes which can be expected to bind *via* intercalation. Such a complex is  $[\text{Ru}(\text{TAP})_2(\text{dppz})]^{2+}$ , which was found to

bind strongly to a wide range of DNAs [154]. However, unlike its phen-analogue,  $[\text{Ru}(\text{TAP})_2(\text{dppz})]^{2+}$  is luminescent in aqueous solution. This emission is quenched when the complex binds to guanine-containing DNA, presumed to be due to a photo-induced electron transfer (PET) from guanine to the ES, as is the case for other complexes having at least two TAP-ligands [121].

To further investigate the primary processes of these photo-oxidation reactions, TOAS experiments were carried out. Initial experiments were performed with nucleotides, and showed that the ES of  $[\text{Ru}(\text{TAP})_3]^{2+}$  was efficiently quenched by 5'-guanosine-monophosphate (GMP) at rates close to diffusion-controlled but much less efficiently by 5'-adenosine-monophosphate (AMP), and not measurably by the pyrimidine nucleotides [122]. In the case of GMP, quenching caused the production of the reduced species  $[\text{Ru}(\text{TAP})_2(\text{TAP}^{\cdot-})]^+$  or  $[\text{Ru}(\text{TAP})_2(\text{TAPH}^{\cdot})]^{2+}$  ( $\text{p}K_a = 7.6$ ) and the guanine radical (which is formed by deprotonation of the guanine radical cation at neutral pH as it has a  $\text{p}K_a$  of 3.9). The back reaction of the reduced species and the guanine radical proceeds with a rate constant close to that of diffusion control. Below we summarize the results of TOAS and luminescence lifetime studies on both the light-switching and photo-oxidizing complexes (Table 6.1).

Lifetimes	MeCN	H <sub>2</sub> O
$\text{Ru}(\text{phen})_3$ [127]	320 ns	920 ns
$\text{Ru}(\text{phen})_2(\text{dppz})$	180 ns [147; 148]	3 ps, 250 ps [152]
$\text{Ru}(\text{TAP})_2(\text{dppz})$	N/A [161]	820 ns [154]
$\text{Ru}(\text{TAP})_3$ [139]	68 ns	223 ns

**Table 6.1:** The <sup>3</sup>MLCT state lifetimes of the Ru(II) light-switching and photo-oxidizing complexes in acetonitrile and water.

The homoleptic  $[\text{Ru}(\text{TAP})_3]^{2+}$ , famous for its photo-oxidation on the  $\pi$ -deficient ligand *via* the PET, is also famous for its peculiar photophysics in the <sup>3</sup>MLCT state [139; 100]. From the temperature dependence studies [194], the lower energy barrier to the thermal population of the <sup>3</sup>MC state makes the non-radiative deactivation roughly twice faster than the  $[\text{Ru}(\text{bpy})_3]^{2+}$ , responsible for the photolability of the  $[\text{Ru}(\text{TAP})_3]^{2+}$ . This is now reflected in its relatively short phosphorescence lifetimes (Table 6.1), arising a question on its ES geometric structure.

Even shorter lifetime has been reported from the heteroleptic  $[\text{Ru}(\text{phen})_2(\text{dppz})]^{2+}$  in water [152; 153; 39], and this extraordinary dynamics was then understood as the lowest <sup>3</sup>MLCT state on the phenazine is induced by an exergonic ILCT (Fig. 6.3), where its two nitrogens (N9 and N14) can be coordinated to water molecules and

efficiently quenched by the partial proton donation [151]. On the other hand, the  $[\text{Ru}(\text{TAP})_2(\text{dppz})]^{2+}$  with its prominently enhanced photo-oxidizing ability showed that its lowest  $^3\text{MLCT}$  state is on one of the TAP-ligands acting as the electronic "sink" electrochemically and photophysically [147; 38; 52; 173]. Their geometric structure changes in both  $^3\text{MLCT}$  states on different ligands have been yet visited so far.

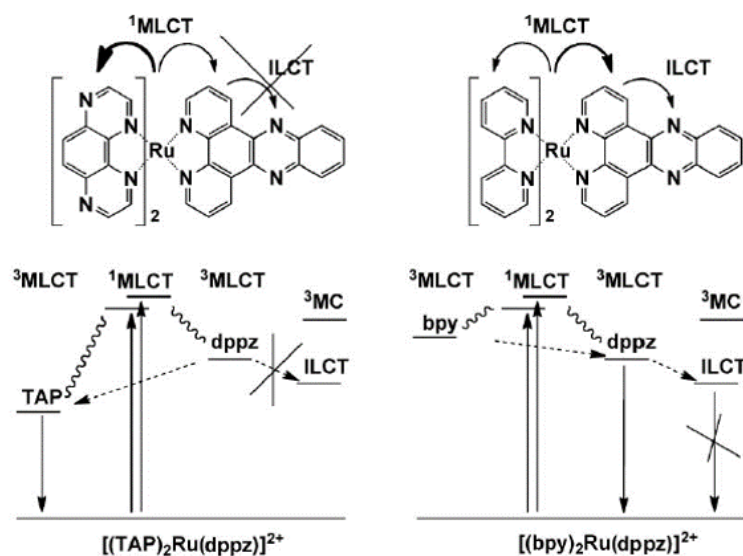


**Figure 6.3:** Simplified Jablonski diagrams of  $[\text{Ru}(\text{TAP})_2(\text{dppz})]^{2+}$  (left) and  $[\text{Ru}(\text{bpy})_2(\text{dppz})]^{2+}$  (right) with their dipole transitions upon MLCT photoexcitation denoted (Figure from [173]).

In this Chapter, the results of the time-resolved EXAFS experiments on  $[\text{Ru}(\text{phen})_3]^{2+}$ ,  $[\text{Ru}(\text{phen})_2(\text{dppz})]^{2+}$ ,  $[\text{Ru}(\text{TAP})_2(\text{dppz})]^{2+}$ , and  $[\text{Ru}(\text{TAP})_3]^{2+}$  dissolved in acetonitrile will be discussed. The experiments were carried out at the 11-ID-D beamline of the APS upon 400 nm photoexcitation, and the sample solution at 278 K was always bubbled with nitrogen gas during the measurements.

## 6.2 Experimental details

The time-resolved EXAFS experiments on the  $[\text{Ru}(\text{phen})_3]^{2+}$ ,  $[\text{Ru}(\text{phen})_2(\text{dppz})]^{2+}$ ,  $[\text{Ru}(\text{TAP})_2(\text{dppz})]^{2+}$ , and  $[\text{Ru}(\text{TAP})_3]^{2+}$  dissolved in degassed acetonitrile were performed at the 11-ID-D beamline of the APS upon 400 nm photoexcitation. The sample concentration was set to 4 mM except  $[\text{Ru}(\text{phen})_3]^{2+}$  (2.5 mM), and flowed in the liquid jet system through an injector with its inner diameter of 600  $\mu\text{m}$ , to prevent compound precipitation and multiple photoexcitation during the measurement.

The 400 nm pump pulse was the second-harmonic output from a 10 kHz Coherent Legend Elite Ti:sapphire ultrafast amplifier laser system. The pump pulses were then further stretched to  $\sim 1.6$  ps (FWHM) by a pair of prisms. The monochromatized X-ray

probe pulses ( $\Delta E/E \sim 10^{-4}$ ) were delivered at 6.5 MHz with  $\sim 78.8$  ps (FWHM) from the APS storage ring under the 24-bunch operation mode with  $\sim 4 \times 10^{12}$  photons  $\text{sec}^{-1}$ . The optical laser spot size (FWHM) was  $\sim 800$   $\mu\text{m}$  (horizontal) by  $\sim 130$   $\mu\text{m}$  (vertical) at the interaction point, yielding a fluence of  $\sim 75$   $\text{mJ cm}^{-2}$ . The X-ray beam size (FWHM) was  $\sim 500$   $\mu\text{m}$  (horizontal) by  $\sim 70$   $\mu\text{m}$  (vertical) at the interaction point, hence completely covered by the optical laser.

The emitted X-ray photons from the Ru(II) photosensitizer were recorded at  $90^\circ$  with respect to the incident X-ray beam on both sides by two APDs (TFY mode). A combination of soller slits and Mo filter, custom-designed for the sample chamber configuration and the distance between the sample and detectors, was inserted between the liquid jet system and the APDs. The first 12 X-ray pulses before the optical photoexcitation were collected for the GS XAFS spectrum, whereas the later X-ray pulses for the ES XAFS spectrum at 150 ps probe delay after the 400 nm photoexcitation. Each energy point was integrated for 4 s.

---

### 6.3 Time-resolved EXAFS on Ru(II) photosensitizers

First of all, detailed EXAFS data reduction and fitting procedures are well-described elsewhere [163; 195; 19]. The molecular structures of each complex in its GS and  $^3\text{MLCT}$  state were obtained by applying the density functional theory (DFT; PBE0/def2-svp), and these structural models were then imported as an initial guess to simulate and fit the corresponding EXAFS spectra using FEFF8 and IFEFFIT codes respectively (Fig. 2.16; [6]).

Upon optical laser irradiation, the molecules that absorb optical photons as well as those not will be both exposed to the X-ray probe pulse. That means, what X-ray photons see is a mixture of the GS and ES molecules. The resulting transient signal  $T(E, t)$  can be therefore described as follows [17];

$$T(E, t) = f(t) * (ES(E, t) - GS(E)) = LaserOn(E, t) - GS(E) \quad (6.1)$$

where  $f(t)$  is the ES fraction that is presumed to be constant during each EXAFS measurement at probe delay of  $t$ , but can differ for each complex. So once we measure  $T(E, t)$  and know  $f(t)$  value for it, we can extract the "pure" ES EXAFS spectrum  $ES(E, t)$ . Since it is well-known that a charge redistribution in the  $^3\text{MLCT}$  state of Ru(II) photosensitizer will cause  $\sim 2$  eV shift of its XAFS spectrum [88; 16; 72; 166; 167; 169], by ranging the  $f(t)$  value from 0 % to 80 % we found the energy shift at three different features; the K-edge, white line, and peak position of the first derivative (Fig. 6.4).

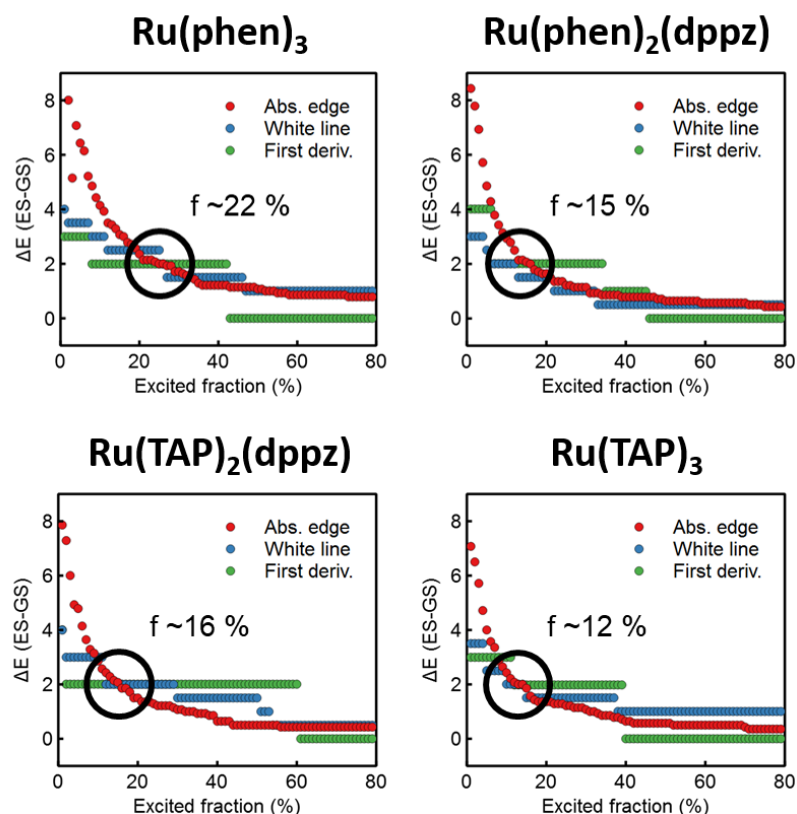


**Figure 6.4:** The energy shift at the K-edge, white line, and peak position of the first derivative of each Ru(II) XAFS spectrum with respect to the presumed  $f(t)$  value ranging from 0 % to 80 %. The  $f(t)$  value for each complex was then determined at  $\Delta E \sim 2$  eV.

Hereby we determined the  $f(t)$  value of each Ru(II) photosensitizer at probe delay of 150 ps and thus their pure ES EXAFS spectra. The  $\chi(k)$  spectra of  $[\text{Ru(phen)}_3]^{2+}$ ,  $[\text{Ru(phen)}_2(\text{dppz})]^{2+}$ ,  $[\text{Ru(TAP)}_2(\text{dppz})]^{2+}$ , and  $[\text{Ru(TAP)}_3]^{2+}$  in their GS and  $^3\text{MLCT}$  state weighted by  $k^2$  are shown in Fig. 6.5. In their comparison, there seems no difference in coordination shell structure between the GS and  $^3\text{MLCT}$  state at 150 ps probe delay, nor in scattering pathways between the Ru(II) photosensitizers. In other words, the localized excited electron on the dppz-ligand, TAP-ligand, or even in the  $^3\text{MC}$  state did not trigger any significant changes in their geometric structures.

This is also confirmed from a sanity checking the transient oscillatory structure by just comparing with the subtraction of the GS EXAFS spectrum from the 2-eV-shifted one (Fig. 6.6). Such a sanity check easily proves that the oscillations in the transient signal  $T(E, t)$  predominantly originated from the energy shift of the spectrum by the charge redistribution in the system, not from the geometric structure change.

Now to verify the first and second coordination shell structure changes in the ES,

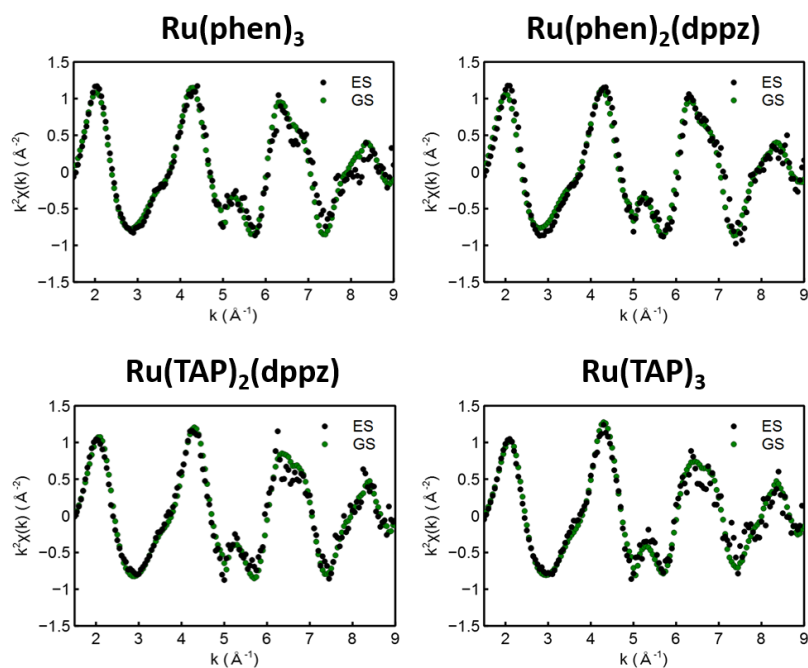


**Figure 6.5:** The  $\chi(k)$  spectra of the Ru(II) photosensitizers in their GS and  $^3\text{MLCT}$  state at the probe delay of 150 ps weighted by  $k^2$ .

the EXAFS equation (2.4) was fitted to each EXAFS spectrum. Based on the DFT-optimized molecular structures of the Ru(II) photosensitizers in their GS and  $^3\text{MLCT}$  state, the calculations of scattering amplitudes and phases for the simulated EXAFS spectra were carried out using the FEFF8 code. The simulated spectra were then fitted to the  $k^2$ -weighted  $\chi(k)$  spectra in  $R$ -space ( $|\chi(R)|$ ; see also the Section 2.3.1) with Artemis software (part of the IFEFFIT). The fitting results are summarized in Table 6.2 and Appendix D.3.

As expected, the coordination shell structure of the Ru(II) complexes did not change that much in their  $^3\text{MLCT}$  states. By setting two independent fitting parameters for the  $R(\text{Ru-N}_{\text{MLCT}})$  and  $R(\text{Ru-N})$ , we were however able to increase the spatial resolution of the experiment down to the picometer-scale. In general the bond lengths between the photo-oxidized metal ion and photo-reduced ligand became shorter than those in the GS, and others in return longer. The changes were most pronounced in the  $[\text{Ru}(\text{phen})_3]^{2+}$  and least in the  $[\text{Ru}(\text{TAP})_2(\text{dppz})]^{2+}$ , although their Debye-Waller factors are too large to confirm these changes. If the only one fitting parameter is set for the ES  $R(\text{Ru-N}_{\text{AVR}})$ , the bond lengths do not change in the  $^3\text{MLCT}$  state.

As noted in Section 6.1, at 150 ps probe delay after the 400 nm photoexcitation, the localized excited electron in the  $[\text{Ru}(\text{phen})_2(\text{dppz})]^{2+}$  should be on the phenazine and the  $[\text{Ru}(\text{TAP})_3]^{2+}$  may start populating its  $^3\text{MC}$  state on the way back to the GS.

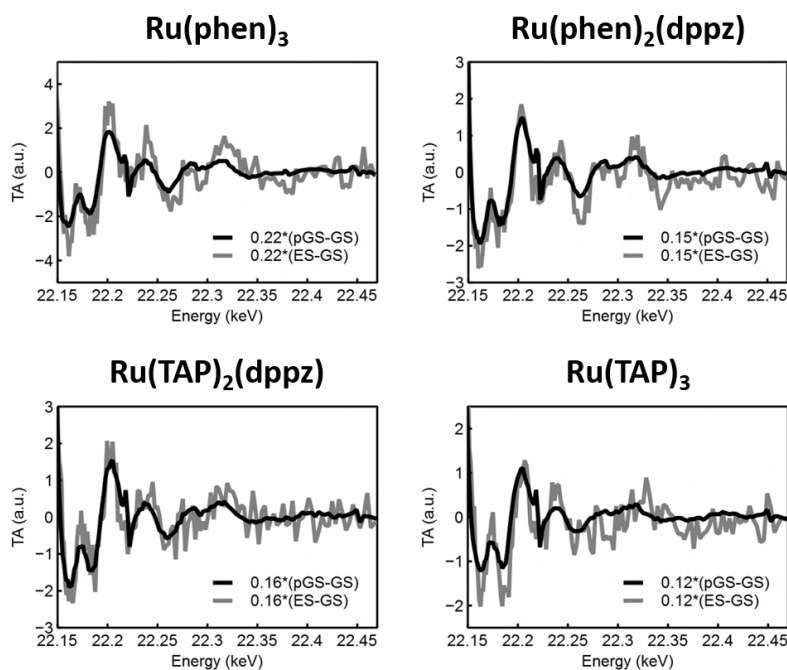


**Figure 6.6:** A sanity checking the transient oscillatory structures by comparing with the subtraction of the GS EXAFS spectrum from the 2-eV-shifted one (pGS). The close resemblance proves that the transient signal  $T(E, t)$  primarily originates from the energy shift of the spectrum by the charge redistribution in the system.

400 nm, 150 ps	GS $R(\text{Ru-N})$	ES $R(\text{Ru-N}_{\text{MLCT}})$	ES $R(\text{Ru-N})$	ES $R(\text{Ru-N}_{\text{AVR}})$	GS $\sigma^2(\text{N})$	ES $\sigma^2(\text{N})$
Ru(phen) <sub>3</sub>	2.06 Å	2.03 Å	2.11 Å	2.06 Å	0.0021	0.0028
Ru(phen) <sub>2</sub> (dppz)	2.06 Å	2.045 Å	2.096 Å	2.06 Å	0.0019	0.0019
Ru(TAP) <sub>2</sub> (dppz)	2.06 Å	2.06 Å	2.06 Å	2.06 Å	0.0026	0.0026
Ru(TAP) <sub>3</sub>	2.06 Å	2.037 Å	2.08 Å	2.06 Å	0.0031	0.0056

**Table 6.2:** Fitting results of the EXAFS equation (2.4) to the  $k^2$ -weighted  $\chi(k)$  spectra of the Ru(II) photosensitizers in their GS and <sup>3</sup>MLCT state at the probe delay of 150 ps after the 400 nm photoexcitation (Fig. 6.5).

Apparently from our EXAFS fitting analysis with the picometer-scale spatial resolution, both ultrafast dynamics were not able to be distinguished at the probe delay of 150 ps. Hence, we additionally measured the transient absorption signal kinetics of each Ru(II) photosensitizer in degassed acetonitrile and water, to monitor how the energy shift of the XAFS spectrum decays back to 0 depending on the solvents.

## 6.4 Lifetime studies in acetonitrile and water

The transient absorption signal kinetics were measured with the monochromatized X-ray pulse ( $\Delta E/E \sim 10^{-4}$ ) at the peak position of each transient XAFS spectrum, and fitted with the exponential function convoluted with the Heaviside step-function and instrumental response function (IRF; Gaussian profile). The fitting results as well as the model equation  $T(E_{peak}, t)$  are shown in Fig. 6.7 and (6.2) respectively,

$$T(E_{peak}, t) = \frac{T_0(E_{peak})}{2} * \exp\left(\frac{\sigma^2}{2\tau^2} - \frac{t-t_0}{\tau}\right) * \left[1 + \operatorname{erf}\left(\frac{\sigma}{\sqrt{2}\tau} - \frac{t-t_0}{\sqrt{2}\sigma}\right)\right] \quad (6.2)$$

where  $T_0(E_{peak})$  is an amplitude factor,  $\sigma$  is the standard deviation of the IRF,  $\tau$  is the decay time constant, and  $t_0$  is the instrumental time-zero.

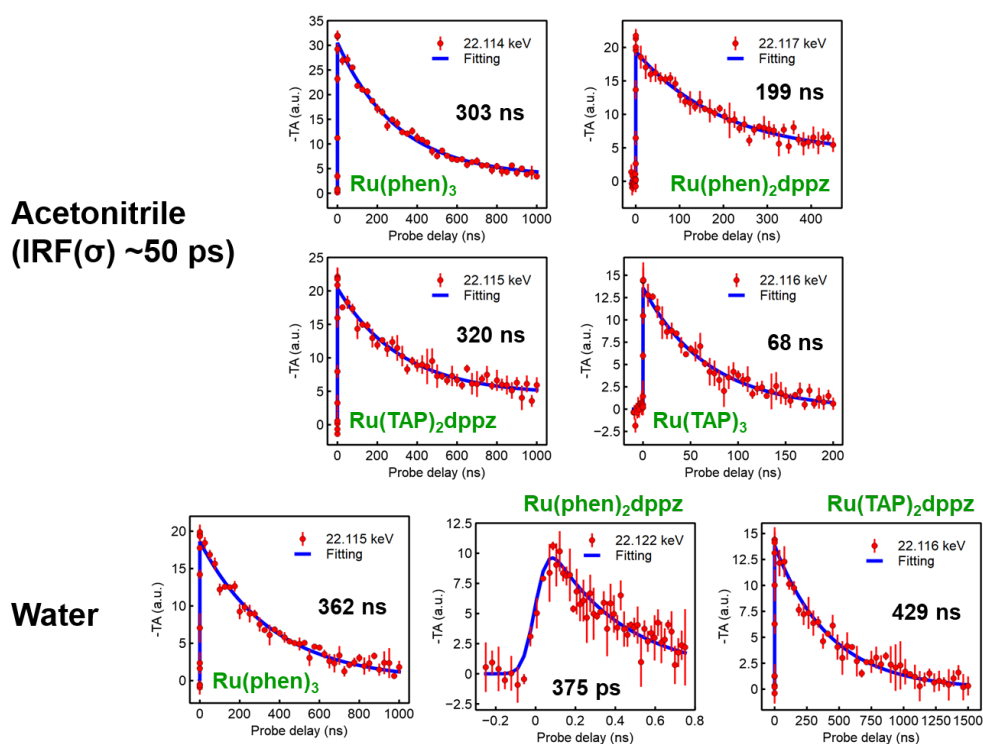


**Figure 6.7:** Fitting analysis of the transient absorption signal kinetics with the first-order rate equation (6.2). The Ru(II) complexes were dissolved in either degassed acetonitrile or water. The kinetics were measured with the monochromatized X-ray pulse ( $\Delta E/E \sim 10^{-4}$ ) at the peak position of each transient XAFS spectrum, and the IRF( $\sigma$ ) was evaluated to be ~50 ps. The error bars were calculated in propagated standard error.

All the kinetics were successfully fitted with one decay time constant each, and the results are consistent with the previous luminescence lifetime studies (Table 6.1). Small deviations predominantly originate from different molar concentrations (e.g. 10

$\mu\text{M}$  and 4 mM) and the fact that the transient signals in both studies involve different dipole transitions (e.g. phosphorescence (PL) and TFY), and thus probe the same ultrafast dynamics from different point of view. The comparison of the lifetime studies are summarized in Table 6.3.

Lifetimes (TFY)	MeCN (PL)	H <sub>2</sub> O (PL)
Ru(phen) <sub>3</sub>	303 ns (320 ns)	362 ns (920 ns)
Ru(phen) <sub>2</sub> (dppz)	199 ns (180 ns)	375 ps (250 ps)
Ru(TAP) <sub>2</sub> (dppz)	320 ns (N/A)	429 ns (820 ns)
Ru(TAP) <sub>3</sub>	68 ns (68 ns)	N/A (223 ns)

**Table 6.3:** Comparison of the <sup>3</sup>MLCT state lifetimes of the Ru(II) light-switching and photo-oxidizing complexes in acetonitrile and water, seen by TFY and phosphorescence.

The transient absorption signal kinetics of the Ru(II) photosensitizers upon 400 nm photoexcitation therefore further confirmed that the <sup>3</sup>MLCT state of the [Ru(phen)<sub>2</sub>(dppz)]<sup>2+</sup> in water gets efficiently quenched by the coordination of the water molecule to the phenazine nitrogens (N9 and N14; [152; 151]), and the thermal population of the <sup>3</sup>MC state in the [Ru(TAP)<sub>3</sub>]<sup>2+</sup> is in fact dominant in its second relaxation pathway [139; 100].

Moreover, the time-resolved EXAFS experiments on the Ru(II) complexes in degassed acetonitrile at the probe delay of 150 ps revealed that there is a minimal change in their geometric structures due primarily to the charge redistribution in the system.

## 6.5 Conclusion and outlook

The Ru(II) light-switching and photo-oxidizing complexes, namely the [Ru(phen)<sub>3</sub>]<sup>2+</sup>, [Ru(phen)<sub>2</sub>(dppz)]<sup>2+</sup>, [Ru(TAP)<sub>2</sub>(dppz)]<sup>2+</sup>, and [Ru(TAP)<sub>3</sub>]<sup>2+</sup> were subjected to the time-resolved EXAFS measurements in degassed acetonitrile at the probe delay of 150 ps after the 400 nm photoexcitation. With the picometer-scale spatial resolution achieved, the localized excited electron on a different ligand disclosed a minimal change in the first coordination shell structure mainly from the charge redistribution in the molecular system.

Additional measurements of the transient absorption signal kinetics at the peak position of each transient XAFS spectrum showed consistent results with the previous luminescence lifetime studies, further confirming the non-radiative deactivation

pathways in  $[\text{Ru}(\text{phen})_2(\text{dppz})]^{2+}$  and  $[\text{Ru}(\text{TAP})_3]^{2+}$  as well as the  $^3\text{MLCT}$  state in  $[\text{Ru}(\text{TAP})_2(\text{dppz})]^{2+}$  localized on one of the TAP-ligands.

A following EXAFS experiment on the  $[\text{Ru}(\text{TAP})_3]^{2+}$  at rather long probe delay of ~50 ns could show a more pronounced change in the geometric structure owing to the populated  $^3\text{MC}$  state. Furthermore, the time-resolved EXAFS experiments on the intercalated complexes between the base-pairs of the polynucleotide can reveal how the coordination shell structure accommodates itself in the light-switching or photo-oxidizing mechanism, as the extensive number of structure determinations has been carried out on the DNA-intercalated species.

# 7 3d<sup>10</sup> Cu(I) photosensitizer

Strongly coupled dynamics for the first picosecond.

7.1 Introduction .....	105
7.2 Experimental details .....	108
7.3 Femtosecond-resolved K $\alpha$ and K $\beta_{1,3}$ XES .....	109
7.4 Femtosecond-resolved K $\beta_{2,5}$ XES and XSS.....	114
7.5 Conclusion and outlook .....	116

The 3d-chelates such as [Fe(bpy)<sub>3</sub>]<sup>2+</sup> or [Co(terpy)<sub>2</sub>]<sup>2+</sup> exhibit fairly different ultrafast electronic and nuclear dynamics with those of the 4d- and 5d-chelates upon optical photoexcitation [204; 123; 13]. As noted earlier, due primarily to the typically weak ligand field ( $\Delta$ ) in the 3d-chelates (Fig. 2.3; see also the Tanabe-Sugano diagram) the HS state lies energetically lower than the <sup>3</sup>MLCT state (Fig. 2.8, [123; 9]). Thus, the SCO becomes favorable in the second relaxation pathway (Section 2.2.2) and accordingly the molecular symmetry gets significantly distorted [125; 113; 13], which is not really desirable for the light-harvesting application.

The 3d<sup>10</sup> [Cu(dmp)<sub>2</sub>]<sup>+</sup> photosensitizer however shows a comparable lifetime of the <sup>3</sup>MLCT state (>40 ns) thanks to its fully occupied 3d-orbitals in the GS (Fig. 2.12) [94]. Therefore, the ultrafast dynamics in the [Cu(dmp)<sub>2</sub>]<sup>+</sup> has been intensively studied with the time-resolved optical and X-ray absorption spectroscopies as well as theoretical calculations [176; 34; 175; 93; 95; 65; 66; 49; 158; 29; 27; 28; 107; 102; 126]. Nevertheless, the strongly coupled electronic and nuclear dynamics in the photoexcited [Cu(dmp)<sub>2</sub>]<sup>+</sup> within the first picosecond were not clearly unraveled.

In this chapter, we will discuss the femtosecond-resolved XES and XSS data from the [Cu(dmp)<sub>2</sub>]<sup>+</sup> simultaneously measured at SACLA upon 550 nm photoexcitation [37]. Particularly for the first picosecond, one time constant of 400-700 fs was found consistently from the Cu K $\alpha$ , K $\beta_{1,3}$ , and XSS transient signal kinetics, which is hence attributed to the pseudo Jahn-Teller (PJT) distortion [94]. The fingerprint of the ISC from <sup>1</sup>MLCT to <sup>3</sup>MLCT state was not able to be identified from the Cu K $\beta_{2,5}$  fluorescence signals with respect to the probe delay, due predominantly to the relatively low SNR [37].

## 7.1 Introduction

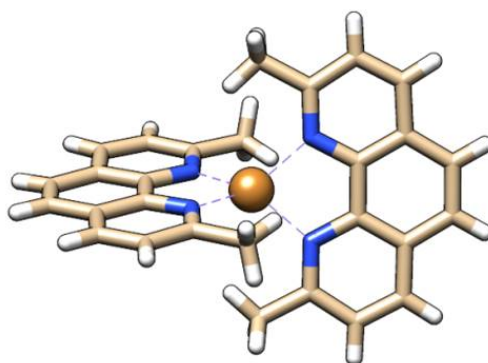


**Figure 7.1:** A geometric structure of the  $[\text{Cu}(\text{dmp})_2]^+$  illustrated by Chimera (center brown:  $\text{Cu}^+$ , blue: Nitrogen, beige: Carbon, white: Hydrogen).

$[\text{Cu}(\text{dmp})_2]^+$  (Fig. 7.1) is one of the most promising candidates for the future light-harvesting agents with its long-lived  $^3\text{MLCT}$  charge-separated state ( $>40$  ns) upon visible light absorption and excellent chemical tunability [94]. Thus, the photophysics of the  $[\text{Cu}(\text{dmp})_2]^+$  has been studied a lot over the last two decades in both empirical and quantum chemical manners [175; 27; 28; 95; 102; 126; 37].

In its GS, the Cu(I) metal ion with its electronic configuration of  $[\text{Ar}]3\text{d}^{10}$ , is coordinated with two dmp ligands *via* the  $\sigma$ -character overlaps between the vacant  $sp^3$ -hybrid orbitals and the nonbonding  $sp^2$ -hybrid orbitals, as well as the corresponding  $\pi$ -character overlaps (Fig. 2.12). The molecule therefore forms a tetrahedral symmetry ( $D_{2d}$ ) with the dihedral angle (dha; the angle between the two dmp ligands) of  $90^\circ$  [93].

In its  $^1,^3\text{MLCT}$  state however, the molecular symmetry becomes weaker due to now the formal electronic configuration of  $3\text{d}^9$  in the metal ion, and hence reduced to  $D_2$  with the dha of  $\sim 70^\circ$  [126]. Such a structural change to lower the molecular symmetry and thus the overall potential energy of the system is understood as the PJT distortion (the second-order Jahn-Teller effect, [93]), and has been characterized by many different methodologies [34; 175; 94; 107; 126]. For example, Iwamura *et al.* reported the ultrafast photoemission dynamics of the  $[\text{Cu}(\text{dmp})_2]^+$  after the photoexcitation at 420 nm, which partially visualized its PESs [93].

Figure 7.2 summarizes the results and interpretation reported by Iwamura *et al.* The photoexcitation to the  $^1,^3\text{MLCT}$  state manifold was immediately followed by a very intense fluorescence signal centered at  $\sim 500$  nm with its time constant of  $\sim 45$  fs, which originates from the Franck-Condon state, i.e. the  $S_2$  state, by directly

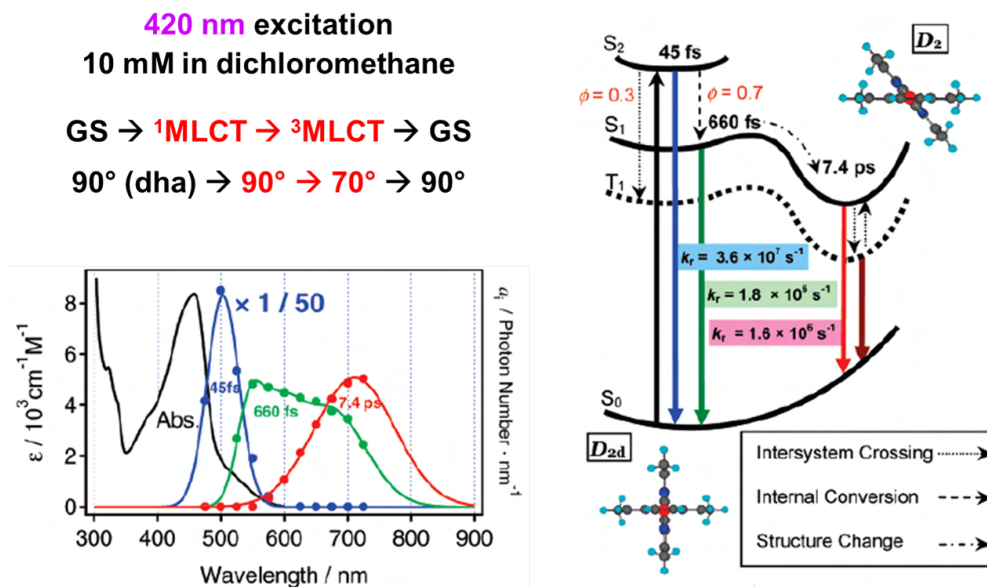


**Figure 7.2:** (left) The ultrafast photoemission dynamics of the  $[\text{Cu}(\text{dmp})_2]^+$  upon photoexcitation at 420 nm and (right) its corresponding PESs (Figures from [93]). Two relevant parameters of the system, namely the dha and molecular spin multiplicity, are also properly indicated in the PESs.

decaying back to the GS. Here the dipole transition to the lowest singlet MLCT state ( $S_1$ ) is formally symmetry-forbidden, whereas that to the higher singlet MLCT state is formally symmetry-allowed, as reflected in their molar attenuation coefficients (Fig. 7.2, [175]). The resulting  $S_2$  state can afterwards undergo the first relaxation dynamics either to the  $S_1$  state (internal conversion; IC) or to the  $T_1$  state (ISC). The relative quantum yields of these two competing pathways were then evaluated from the fluorescence intensity comparison between upon the 420 nm excitation ( $S_2$ ) and the 550 nm excitation ( $S_1$ ) (Fig. 7.2, [93]).

After the  $S_2$  state had disappeared with its decay time constant of  $\sim 45$  fs, the second emission dynamics showed up as an intermediate transition from a higher emission energy to a lower one, with its decay time constant of  $\sim 660$  fs (Fig. 7.2, [93]). This relaxation is attributed to the so-called flattening motion (PJT distortion) of the  $[\text{Cu}(\text{dmp})_2]^+$  where the dha changes from  $90^\circ$  ( $D_{2d}$ ) to  $\sim 70^\circ$  ( $D_2$ ). The assignment is not only based on the lower potential energy in the flattened state compared to the Franck-Condon geometry (Fig. 7.2), but also on the fact that this time constant is in fact dependent on the solvent viscosity and the substituents at 2,9-positions of the ligands [93; 94]. In other words, the flattening motion proceeds either on the  $S_1$  state manifold or on the  $T_1$  state manifold.

The last emission dynamics appearing at  $\sim 700$  nm with its decay time constant of  $\sim 7.4$

ps is then assigned to the "delayed" ISC from the  $S_1$  state to the  $T_1$  state, primarily owing to the weakened spin-orbit coupling by the flattening motion [93; 175]. In the end, the lowest long-lived  $^3\text{MLCT}$  state decays back to the GS *via* phosphorescence after few tens of nanoseconds.

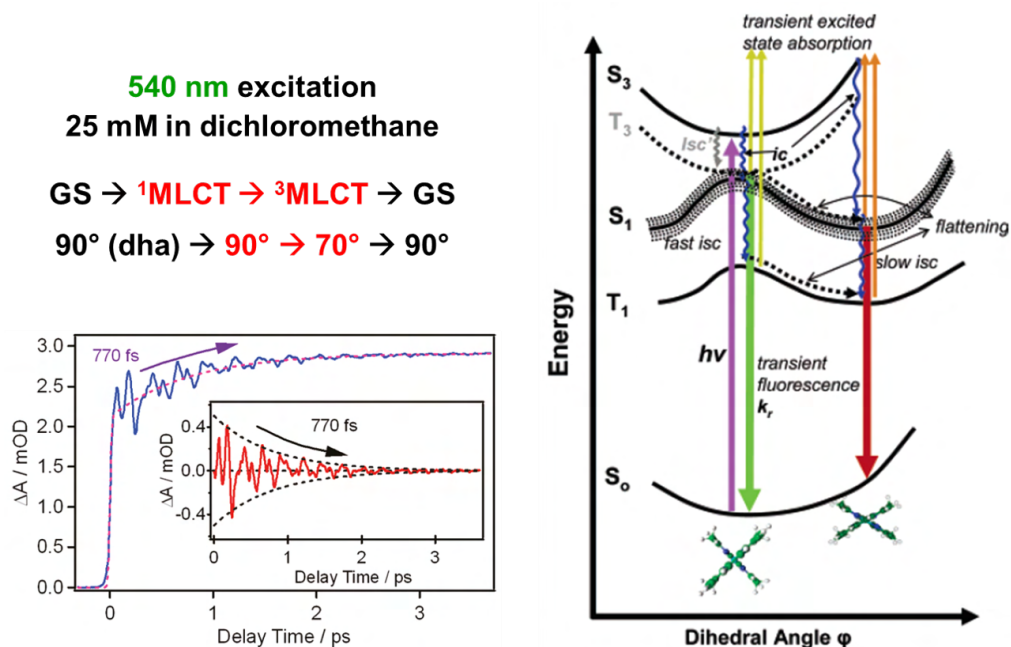


**Figure 7.3:** (left) The coherent nuclear wavepacket motion in the  $[\text{Cu}(\text{dmp})_2]^+$  appearing on the transient optical absorption signal kinetics upon photoexcitation at 540 nm, and (right) a relevant PES diagram (Figures from [95; 175]). The vibrational coherence is coupled with the PJT distortion, revealing the same damping time constant of 770 fs.

The understanding didn't change much from the TOAS experiments. Shaw *et al.* reported a very similar PES diagram to the previous one (Fig. 7.3), describing that the optical methods are probing the structural changes indirectly, and the optical signals originating from different transient species often overlap with one another [175]. That means, it is still complicated to identify the ultrafast electronic and nuclear dynamics even from the thorough examinations in the optical regime, especially when the degrees of freedom in the system are strongly coupled to each other.

Iwamura *et al.* however found an additional oscillatory component appearing on the transient optical absorption signal kinetics at the probe wavelength of 650 nm, upon the photoexcitation at 540 nm directly to the  $S_1$  state (Fig. 7.3, [95]). Right after the time-zero, the instantaneous transient absorption intensity keeps increasing with its time constant of 770 fs, which corresponds to the PJT distortion. The oscillation of the transient absorbance was then extracted by fitting the exponential function to the data, and the damping time constant of the oscillation was found to be same with the

time constant of the structural change. This implies that the oscillation arises from the coherent nuclear motion in the  $S_1$  Franck-Condon state, and the vibrational coherence gets damped as the flattening motion proceeds [95]. In other words, the excessive vibrational energy in the  $S_1$  Franck-Condon state dissipates effectively into other degrees of freedom through the anharmonic coupling between the ligand twisting motion ( $\nu_{25}$ ) and the flattening distortion.

The coherent nuclear wavepacket was also observed by our working group from the femtosecond-resolved XAS experiment at SACLA [102]. The time-dependent Fourier transform analysis on the wavepacket unveiled the central component of Cu-N breathing mode ( $\nu_8$ ) together with the ligand twisting mode ( $\nu_{25}$ ), consistent with the previous results from Iwamura *et al.* [95]

Despite the rigorous empirical studies so far, the ultrafast dynamics in  $[\text{Cu}(\text{dmp})_2]^+$  photosensitizer is still under active debate in the literature [175; 94; 107; 27; 28; 102; 126]. To further get insights into its electronic and nuclear dynamics, specifically the ISC from  $^1\text{MLCT}$  to  $^3\text{MLCT}$  state and the PJT distortion, our working group has conducted the femtosecond-resolved XES and XSS experiments simultaneously at SACLA, upon photoexcitation at 550 nm [37]. By employing these complementary hard X-ray techniques the structural changes can be disentangled from the spin state changes [109; 113; 117], especially also by covering the Cu  $K\beta_{2,5}$  emission lines [27].

---

## 7.2 Experimental details

The femtosecond-resolved XES and XSS experiments were simultaneously carried out at BL3EH2 of SACLA [188; 92; 101; 103]. The SASE X-ray pulse centered at  $\sim 10$  keV was focused down to  $\sim 5$   $\mu\text{m}$  by beryllium CRLs [101].  $[\text{Cu}(\text{dmp})_2](\text{PF}_6)$  salt (molar mass 625  $\text{g mol}^{-1}$ ) was dissolved in acetonitrile at the concentration of 100 mM (OD  $\sim 0.5$  with 50  $\mu\text{m}$  optical path length at 550 nm). During the whole measurement the sample solution was under magnetic stirring and purged with Ar gas. The solution was circulating in the liquid jet system inside the He-filled chamber [103], through an injector with its inner diameter of 50  $\mu\text{m}$ .

At the interaction point,  $[\text{Cu}(\text{dmp})_2]^+$  was excited directly to the  $S_1$  state by the 550 nm pump pulse ( $\sim 45$  fs FWHM) from a Ti:sapphire laser system and OPA (HE-TOPAS, Coherent). The optical laser fluence was set to  $\sim 209$   $\text{mJ cm}^{-2}$  that was slightly lower than the onset of the two-photon absorption process. The arrival-timing between X-ray and optical laser pulses was recorded by the timing diagnostics based on the X-ray beam splitting scheme [104]. For the temporal jitter correction, the interval bin width of 50 fs was used. The overall time resolution of the experiment was evaluated to be  $\sim 80$

fs (FWHM) by fitting a Gaussian profile to the first derivative of both Cu  $K\alpha$  and  $K\beta_{1,3}$  transient emission signal kinetics [102].

The XSS data at each probe delay point were measured in the forward wide-angle X-ray scattering geometry, and the XES data at each probe delay point were measured with two von Hamos dispersive spectrometers in Bragg reflection geometry. 6 Si(111) analyzer crystals were aligned for the Cu  $K\beta_{1,3}$  and  $K\beta_{2,5}$  emission lines in vertical direction, and 6 Si(531) analyzer crystals for the Cu  $K\alpha$  emission lines in horizontal direction [103].

### 7.3 Femtosecond-resolved $K\alpha$ and $K\beta_{1,3}$ XES

In this section, we will now focus on interpreting the reduced data (see also Appendix B and C) of the Cu  $K\alpha$  and  $K\beta_{1,3}$  fluorescence signal with respect to the probe delay. The Voigt profile fits to the GS emission lines were already discussed in the Section 2.3.2 [45; 134; 1; 37; 106], to grasp the origin of the line shapes. The changes in spectral features along the probe delay will be then understood by fitting the sequential first-order rate equation to the transient emission signal kinetics [102]. The kinetics were extracted by integrating the positive parts of the transient signals. We found however no difference in between integrating the negative transient signals and positive transient signals for the kinetics, as depicted in Fig. 7.4.

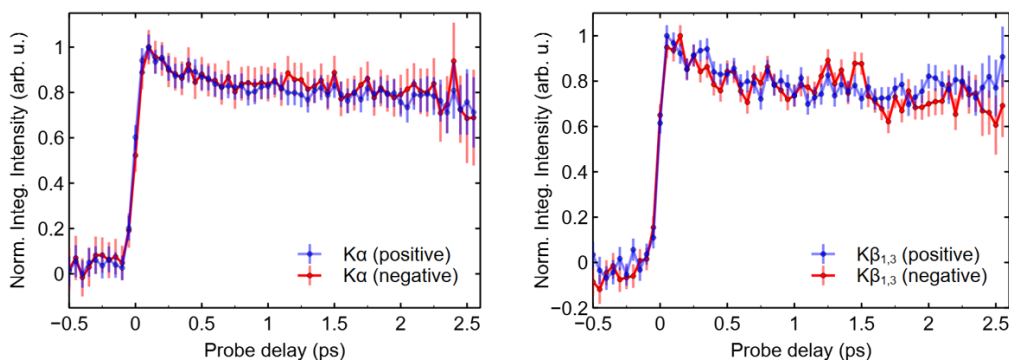


**Figure 7.4:** Comparison of the kinetics extracted by integrating the positive transient signals (blue) and negative transient signals (red) of the Cu  $K\alpha$  (left) and  $K\beta_{1,3}$  (right) fluorescence from  $[\text{Cu}(\text{dmp})_2]^+$  upon 550 nm photoexcitation. The error bars were calculated in propagated standard error.

Before we start analysing the kinetics, we need to first identify the instrumental time-zero and its response function (IRF) defining the overall time resolution of the experiment, by fitting a Gaussian profile to the first derivative of both the  $K\alpha$  and  $K\beta_{1,3}$  transient signal kinetics [102]. Figure 7.5 summarizes the results.

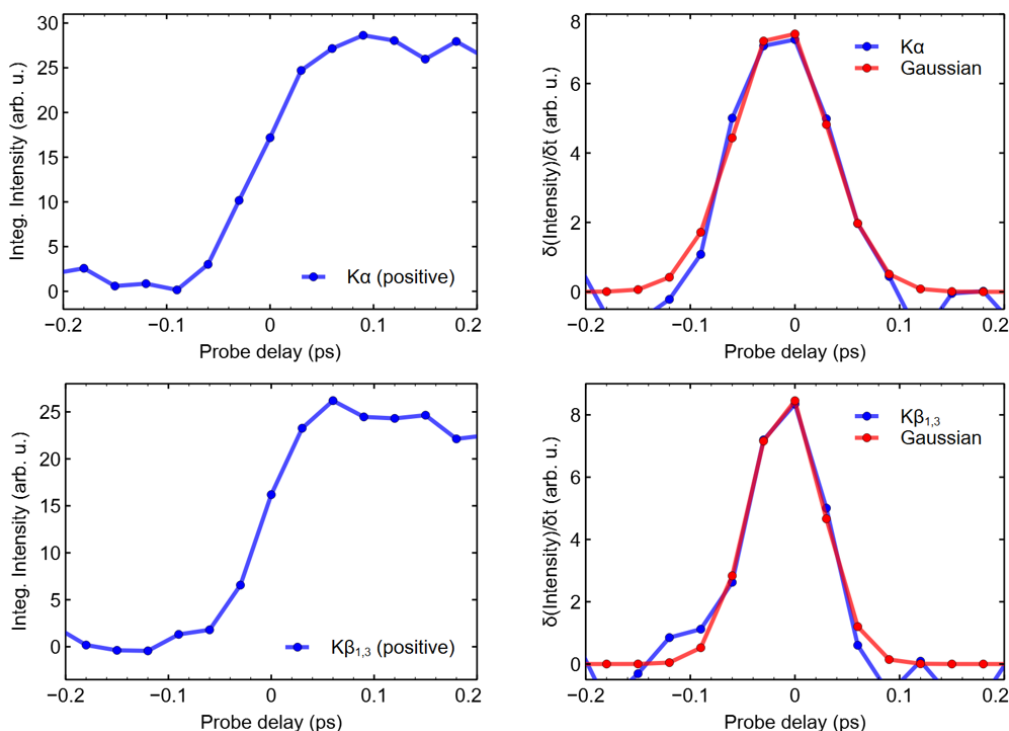


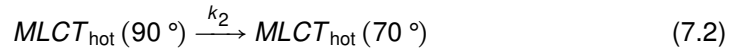
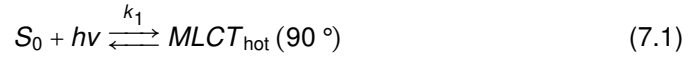
**Figure 7.5:** Instrumental time-zero and its response function (IRF) of this experiment found by the Gaussian fits to the first derivative of both Cu  $K\alpha$  (above) and  $K\beta_{1,3}$  (below) transient signal kinetics from  $[\text{Cu}(\text{dmp})_2]^+$  upon 550 nm photoexcitation [102]. The time-zero and IRF were evaluated to be  $t_0 = -13 \text{ fs} \pm 2.6 \text{ fs}$  and  $\text{IRF}(\sigma) = 44 \text{ fs} \pm 2.8 \text{ fs}$  for  $K\alpha$ , and  $t_0 = -8 \text{ fs} \pm 2.4 \text{ fs}$  and  $\text{IRF}(\sigma) = 34 \text{ fs} \pm 2.4 \text{ fs}$  for  $K\beta_{1,3}$ . Hereafter we will use these values to convolute the  $\text{IRF}(\sigma, t) = A_0 \cdot \exp[-(t - t_0)^2 / 2\sigma^2]$  and the rate equation. The interval bin width of 30 fs was used for the temporal jitter correction.

The origin of such a Gaussian broadening at time-zero, namely the convolution of a Gaussian profile and Heaviside step-function, is that in time domain both optical and X-ray pulses in Gaussian line shape convolute inside the cylindrical liquid jet stream, where the refractive index changes to  $\sim 1.3$  at 550 nm (acetonitrile), so that the GVD of 550 nm pulse also contributes to the Gaussian broadening [102]. In addition the jitter correction precision of the timing tool affects the actual time resolution as well [104], so the final  $\text{IRF}(\text{FWHM})$  can be estimated as  $\sqrt{45^2 + 6^2 + 50^2 + 16^2} \sim 69 \text{ fs}$ . Here the pulse duration of the pump laser ( $\sim 45 \text{ fs}$ ) was measured with an autocorrelator before the experiment, and that of the X-ray pulse ( $\sim 6 \text{ fs}$ ) was estimated by an autocorrelation measurement.

Both IRF values from the Gaussian fit ( $\sim 80 \text{ fs}$  FWHM) and instrumental estimation ( $\sim 69 \text{ fs}$  FWHM) are in good agreement, even though the Gaussian fit may turn out to be incorrect if the initial population would take much longer than the calculated IRF. The corresponding population in the Franck-Condon state occurs however faster

than ~100 fs as we noted earlier from the ultrafast dynamics of  $[\text{Cu}(\text{dmp})_2]^+$  reported by Iwamura *et al* [95]. Therefore, the instrumental time-zero and response function determined by the Gaussian fits will be applied to the following analysis.

The sequential first-order rate equation for the fitting analysis was built based on the proposed photophysical mechanism so far in the  $[\text{Cu}(\text{dmp})_2]^+$  after 550 nm photoexcitation [94; 102; 37].



Since all reactions throughout the photocycle are unimolecular, each reaction rate is proportional to the time-dependent quantum yield of the reactant (first-order reaction). Only the (7.1) is a reversible reaction, but the reaction (7.2) and (7.3) also have another competing radiative decay back to the GS ( $S_0$ ) as reported by Iwamura *et al* [93]. The rate constants of non-radiative decay pathways ( $k_2, k_3$ ) are however much larger than those of radiative ones [25; 69; 24; 94; 102], hence we don't take account of the radiative decay pathways into our model equation for the picosecond time window. The Heaviside step-function convoluted with the IRF( $\sigma, t$ ) can therefore describe the forward reaction of (7.1), whose rate constant ( $k_1$ ) must be  $>10^{13} \text{ s}^{-1}$  upon the 550 nm photoexcitation, as remarked earlier [102; 94].

From (7.2) onward we should be careful, because some relaxation pathways do not appear in the kinetics depending on the ultrafast methodologies [94; 102; 26] (see also the Section 3.3). The X-ray emission lines are obviously sensitive to the effective charge density change in the system, i.e.  $\text{Cu}(\text{I}) 3d^{10} \rightarrow \text{Cu}(\text{II}) 3d^9$  (7.1), and thus are also sensitive to the structural rearrangement such as the flattening motion (7.2, [117]). The vibrational cooling process however (7.3, [102]) does not affect the X-ray fluorescence as the process occurs in one electronic state.

Accordingly the sequential first-order rate equation for the transient emission signal kinetics was formulated to reflect the corresponding photophysical mechanism (7.1, 7.2, and 7.4). The ISC from  $^1\text{MLCT}$  to  $^3\text{MLCT}$  state was also excluded from the model equation, since both the Cu  $K\alpha$  and  $K\beta_{1,3}$  emission lines were not sensitive to the process, as we will see soon from the data.

$$[MLCT_{hot,90^\circ}](t) = [MLCT_{hot,90^\circ}]_0 * \exp(-k_2 * t) \quad (7.5)$$

$$[MLCT_{hot,70^\circ}](t) = B_0 * [MLCT_{hot,90^\circ}]_0 * \{1 - \exp(-k_2 * t)\} * \exp(-k_4 * t) \quad (7.6)$$

$$= B_0 * [MLCT_{hot,90^\circ}]_0 * \exp(-k_4 * t) - B_0 * [MLCT_{hot,90^\circ}]_0 * \exp\{-(k_2 + k_4) * t\} \quad (7.7)$$

The first-order rate equation (7.5) is the non-radiative decay of the quantum yield of  $MLCT_{hot, 90^\circ}$  state, where  $[MLCT_{hot, 90^\circ}]_0$  appears with the  $k_1 > 10^{13} \text{ s}^{-1}$  in the forward reaction of (7.1). As the  $[MLCT_{hot, 90^\circ}](t)$  decays (7.2), the  $[MLCT_{hot, 70^\circ}](t)$  arises accordingly with  $[MLCT_{hot, 70^\circ}]_0(t) = [MLCT_{hot, 90^\circ}]_0 * \{1 - \exp(-k_2 * t)\}$ , which at the same time starts decaying in the first-order with the rate constant of  $k_4$  (7.4). In (7.6) a constant value of  $B_0$  is multiplied to consider the different X-ray fluorescence yields from different excited states. The value for the rate constant  $k_4$ , which corresponds to the GS recovery from the lowest long-lived  $^3MLCT$  state, was adopted from the literature [94; 102]. Hence, in (7.7) we have three unknowns ( $B_0$ ,  $[MLCT_{hot, 90^\circ}]_0$ ,  $k_2$ ) to be fitted to the kinetics. The sequential first-order rate equation was then convoluted with the  $IRF(\sigma, t)$ , and the following equation (7.8) was used to analyse the transient emission signal kinetics from  $[Cu(dmp)_2]^+$  upon 550 nm photoexcitation.

$$\Delta I_{XES}(t) = [MLCT_{hot,90^\circ}](t) * H(t) \otimes IRF(\sigma, t) + [MLCT_{hot,70^\circ}](t) * H(t) \otimes IRF(\sigma, t) \quad (7.8)$$

where  $H(t)$  is the Heaviside step-function and  $\otimes$  is the convolution operator.

Figure 7.6 shows the results from the Cu  $K\alpha$  fluorescence signals with respect to the probe delay. First of all, we compared the emission spectra with and without the optical photoexcitation at the probe delay of 19 ps (Fig. 7.6 (a), (b)), where we know that the system is in the lowest long-lived  $^3MLCT$  ( $T_1$ ) state [94; 107]. The difference is quite small ( $\sim 1\%$ ), and looks dominated by the effective charge density change in the system ( $Cu(I) 3d^{10} \rightarrow Cu(II) 3d^9$ ), which made the spectrum be red-shifted [27]. In addition to this, the discrepancy between the positive and negative transient line shape of  $K\alpha_1$  originates from the slightly more broadened emission spectrum in the ES due to the spin density change [74].

Both kinetics with the time window of  $\sim 3$  ps (Fig. 7.6 (c)) and  $\sim 20$  ps (Fig. 7.6 (d)) were obtained by integrating the blue-shaded areas of the transient emission signals. The fitting analysis with the sequential first-order rate equation (7.8) disclosed a decay time constant of  $\sim 410$  fs ( $1/k_2$ ), and no additional dynamics was noticed within the time window of  $\sim 20$  ps. This femtosecond dynamics was then tentatively attributed to the flattening motion, because the so-called core-to-core transitions from 2p to 1s ( $K\alpha$  fluorescence; Fig. 2.12) cannot detect a spin-flip on the ligand, but rather can probe the structural rearrangement as discussed before [117].

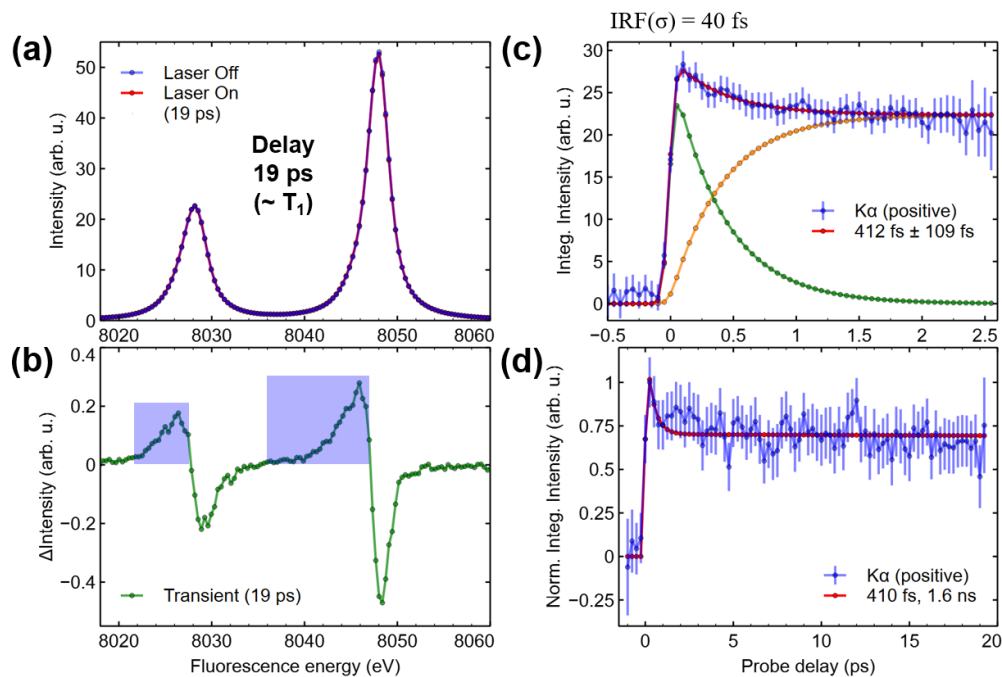


**Figure 7.6:** (a) Cu K $\alpha$  emission spectra of [Cu(dmp) $_2$ ] $^+$  in its GS (blue) and T $_1$  state (red) at the probe delay of 19 ps as well as (b) their difference. The blue shaded areas were integrated to extract the kinetics (c) up to 2.5 ps and (d) 20 ps. The sequential first-order rate equation (7.8) consisting of the [MLCT $_{\text{hot}, 90^\circ}$ ]( $t$ ) (green) and [MLCT $_{\text{hot}, 70^\circ}$ ]( $t$ ) (orange) was fitted to the kinetics (fitting range up to 2.2 ps), revealing a decay time constant of  $\sim$ 410 fs ( $1/k_2$ ). The error bars were calculated in propagated standard error.

From the Cu K $\beta_{1,3}$  fluorescence signals we obtained the very similar results as shown in Fig. 7.7. Again, we first compared the emission spectra with and without the optical photoexcitation at the probe delay of 19 ps (Fig. 7.7 (a), (b)), where we know that the system is in the lowest long-lived  $^3$ MLCT (T $_1$ ) state [94; 107]. The difference is quite small ( $\sim$ 1 %), and both the spectator-hole satellite lines gained higher transition rates in the ES, while the diagram transitions lost theirs (Section 2.3.2).

The kinetics with the time window of  $\sim$ 3 ps (Fig. 7.7 (c)) and  $\sim$ 20 ps (Fig. 7.7 (d)) were extracted by integrating the blue-shaded areas of the transient emission signals. The fitting analysis with the sequential first-order rate equation (7.8) again disclosed the same decay time constant of  $\sim$ 410 fs ( $1/k_2$ ), and no additional dynamics was noticed within the time window of  $\sim$ 20 ps. Here we confirmed that the femtosecond dynamics in fact corresponds to the flattening motion, which affects both the Cu K $\alpha$  and K $\beta_{1,3}$  fluorescence signals consistently [117].

The core-to-core emission lines, namely the Cu K $\alpha$  (2p to 1s) and K $\beta_{1,3}$  (3p to 1s), could not capture the molecular spin multiplicity nor the coherent molecular

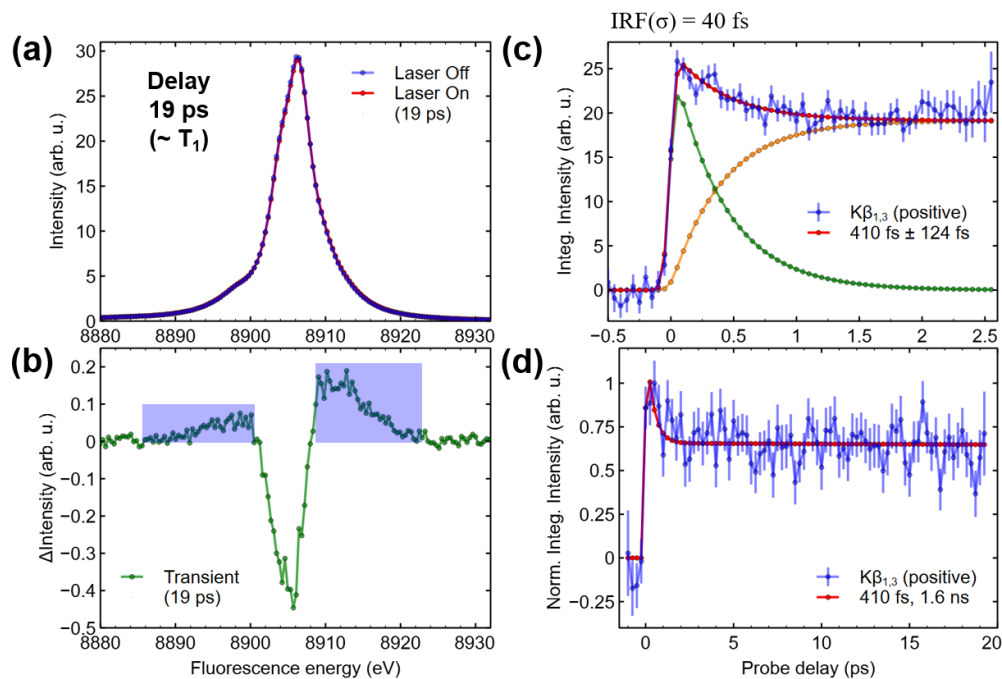


**Figure 7.7:** (a) Cu  $K\beta_{1,3}$  emission spectra of  $[\text{Cu}(\text{dmp})_2]^+$  in its GS (blue) and  $T_1$  state (red) at the probe delay of 19 ps as well as (b) their difference. The blue shaded areas were integrated to extract the kinetics (c) up to 2.5 ps and (d) 20 ps. The sequential first-order rate equation (7.8) consisting of the  $[\text{MLCT}_{\text{hot}, 90^\circ}](t)$  (green) and  $[\text{MLCT}_{\text{hot}, 70^\circ}](t)$  (orange) was fitted to the kinetics (fitting range up to 2.2 ps), revealing a decay time constant of  $\sim 410$  fs ( $1/k_2$ ). The error bars were calculated in propagated standard error.

vibrations. To further facilitate disentangling the strongly coupled electronic and nuclear dynamics in the photoexcited  $[\text{Cu}(\text{dmp})_2]^+$  within the first picosecond, we will now analyse the simultaneously-collected XSS data as well as the reduced data of the Cu  $K\beta_{2,5}$  fluorescence signal with respect to the probe delay. Additional analysis on the Cu  $K\alpha$  and  $K\beta_{1,3}$  data can be found in Appendix D.4.

## 7.4 Femtosecond-resolved $K\beta_{2,5}$ XES and XSS

Figure 7.8 shows the results from the Cu  $K\beta_{2,5}$  fluorescence signals with respect to the probe delay. The Voigt profile fits to the GS emission lines were already discussed in the Section 2.3.2 [54], to grasp the origin of the line shapes [138; 134; 159; 43; 196]. The emission spectra with and without the optical photoexcitation at the probe delay of 19 ps (Fig. 7.8 (a), (b)) were compared, where we know that the system is in the lowest long-lived  $^3\text{MLCT}$  ( $T_1$ ) state [94; 107]. The difference is there, but the SNR is less than 1 even though  $\sim 1129422$  SASE X-ray pulses were invested in the Laser Off and On emission spectra respectively. Nevertheless we gave a try on extracting

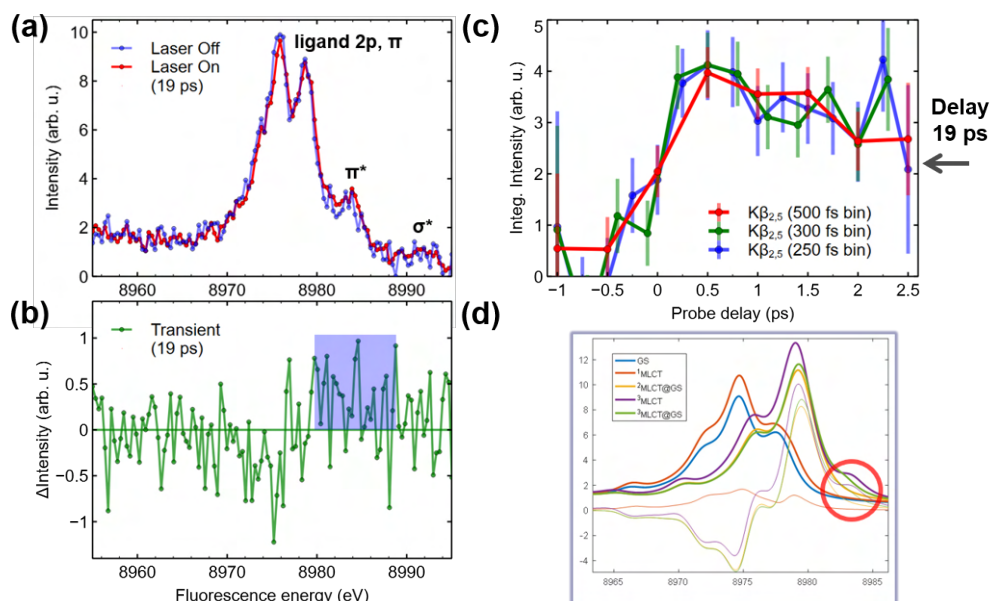


**Figure 7.8:** (a) Cu  $K\beta_{2.5}$  emission spectra of  $[\text{Cu}(\text{dmp})_2]^+$  in its GS (blue) and  $T_1$  state (red) at the probe delay of 19 ps as well as (b) their difference. The blue shaded areas were integrated to extract the kinetics (c) up to 2.5 ps. The DFT calculations (d) suggested that the shoulder peak from the occupied  $\pi^*$  molecular orbital could be sensitive to the ISC. The error bars were calculated in propagated standard error.

the kinetics by integrating the blue-shaded area, which corresponds to the transient emission signal from the occupied  $\pi^*$  molecular orbital (Section 2.3.2).

As shown in Fig. 7.8 (c), the kinetics up to  $\sim 2.5$  ps clearly unveiled the femtosecond dynamics in three different interval bin widths, surviving for longer than 19 ps. The kinetics were however not able to be fitted with the sequential first-order rate equation (7.8) due predominantly to the limited number of data points, therefore the quantitative fitting analysis as well as our interpretation was also restricted. In other words, there are still uncertainties in identifying this femtosecond dynamics, although the DFT calculations suggested that the shoulder peak from the occupied  $\pi^*$  molecular orbital could be sensitive to the ISC (Fig. 7.8 (d)).

Another factor to be considered is the flattening motion which can also cause the transient signals of the Cu  $K\beta_{2.5}$  fluorescence [27; 42; 138]. To unravel this complexity in the femtosecond dynamics, the transient XSS signals with respect to the probe delay were simultaneously recorded in the forward wide-angle X-ray scattering geometry during the experiment (Fig. 7.9).

The preliminary analysis on the XSS data by just integrating the low- $q$  signals (0.3 ~

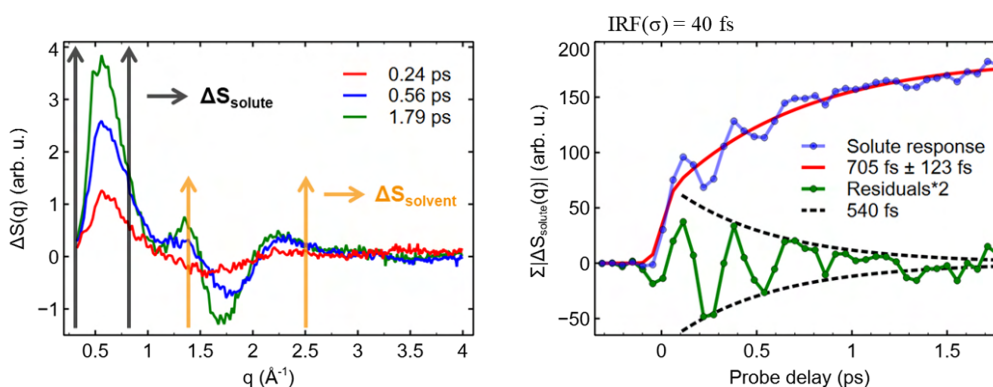


**Figure 7.9:** (left) Transient XSS signals at selected probe delays and (right) the transient signal kinetics obtained by integrating the  $\Delta S_{\text{solute}}$  response ( $0.3 \sim 0.8 \text{ \AA}^{-1}$ ) from the  $[\text{Cu}(\text{dmp})_2]^+$  upon 550 nm photoexcitation. The sequential first-order rate equation (7.8) was fitted to the kinetics, returning a time constant of  $\sim 705 \text{ fs}$  ( $1/k_2$ ). The residual signals ( $\Sigma|\Delta S_{\text{solute}}| - \text{fit}$ ) showed the coherent vibrational motion with a period of  $\sim 330 \text{ fs}$  (Cu-N breathing mode,  $\nu_8$ ), which has its damping time constant of  $\sim 540 \text{ fs}$  [102].

$0.8 \text{ \AA}^{-1}$ ;  $\Delta S_{\text{solute}}$  response) revealed the consistent femtosecond dynamics originating from the PJT distortion (400-700 fs). Without yet sophisticated data processes, the residual signals ( $\Sigma|\Delta S_{\text{solute}}| - \text{fit}$ ) clearly retained the coherent vibrational motion with a period of  $\sim 330 \text{ fs}$  (Cu-N breathing mode,  $\nu_8$ ), which has its damping time constant of  $\sim 540 \text{ fs}$  [102]. As noted earlier, this wavepacket motion is believed to be coupled to the flattening distortion, i.e. the symmetry breaking in photoexcited  $[\text{Cu}(\text{dmp})_2]^+$  [95].

Comprehensively speaking, within the first picosecond after the 550 nm photoexcitation, the nuclear dynamics with the time constant of 400-700 fs seem dominant in all XES and XSS transient signal kinetics. That means, what we noticed from the Cu  $K\beta_{2,5}$  transient emission signal kinetics probably also corresponds to the PJT distortion. Much higher SNR is thus required to explicitly identify the femtosecond dynamics from the Cu  $K\beta_{2,5}$  fluorescence signals, which can only be accomplished at the high-repetition rate XFEL facilities such as European XFEL and LCLS-II [63; 109].

## 7.5 Conclusion and outlook

Complementary to the previous studies, herein we reported the femtosecond nuclear dynamics in photoexcited  $[\text{Cu}(\text{dmp})_2]^+$  investigated with the femtosecond-resolved XES and XSS methodologies available at SACLA. With the overall time resolution of  $\sim 94 \text{ fs}$  (FWHM) achieved, we observed that the molecular structure flattening (PJT distortion) proceeds with the time constant of 400-700 fs after 550 nm photoexcitation, affecting both the  $K\alpha$  and  $K\beta_{1,3}$  core-to-core fluorescence. The XSS data further

confirmed this dynamics, and were additionally sensitive to the coherent vibrational motion of  $[\text{Cu}(\text{dmp})_2]^+$  primarily from the Cu-N breathing mode ( $\nu_8$ ). The ISC from  $^1\text{MLCT}$  ( $S_1$ ) to  $^3\text{MLCT}$  ( $T_1$ ) state was not identified from the femtosecond-resolved  $K\beta_{2,5}$  XES, however we expect much better resolution on the line shapes of the valence-to-core fluorescence as well as the pre-edge absorption structure at the high-repetition rate XFEL facilities such as European XFEL and LCLS-II.

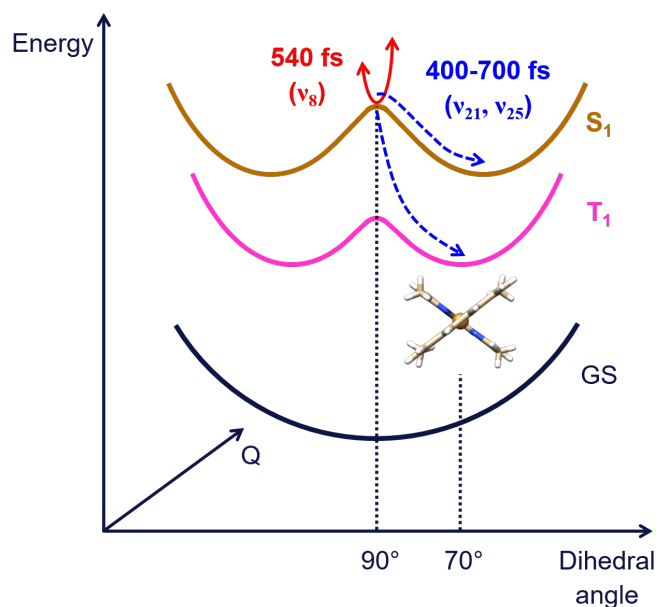


**Figure 7.10:** The summarized PESs of the  $[\text{Cu}(\text{dmp})_2]^+$  with its representative femtosecond relaxation dynamics upon 550 nm photoexcitation. Following the two branching PJT distortions (blue), the coherent nuclear wavepacket decays with 540 fs time constant (red).

Figure 7.10 shows the summarized PESs of the  $[\text{Cu}(\text{dmp})_2]^+$  along the dha coordinate and the Cu-N bond length coordinate. The photoabsorption at 550 nm promotes the system to the  $S_1$  Franck-Condon state where the coherent molecular vibrations start dissipating their energy into different nuclear and electronic degrees of freedom (540 fs,  $\nu_8$ ), as the PJT distortion proceeds (400-700 fs,  $\nu_{21}$ ,  $\nu_{25}$ ). Whether the PJT distortion occurs on the  $^1\text{MLCT}$  state manifold or the  $^3\text{MLCT}$  state manifold is still an open question.

## 8 $3d^6$ Fe(II)-Co(III) photocatalyst

Femtosecond "energy" transfer in a dyadic system.

8.1 Introduction .....	119
8.2 Experimental details .....	122
8.3 Femtosecond-resolved XES on Fe(II)-Co(III) dyad.....	123
8.4 Femtosecond-resolved XES on Fe(II) photosensitizer .....	128
8.5 Conclusion and outlook .....	131

The  $3d^6$  chelates have exhibited their rich dynamics on the ultrafast timescale as well as their intriguing spectral features in the hard X-ray domain [84; 74; 24; 123; 177; 160; 113; 61; 13; 174; 204]. Many of them however have been only spotted over the last two decades, in accordance with the emergence of femtosecond light sources that allow us to clock the very initial step of the light-harvesting mechanism. The typically weak ligand fields in the  $3d^6$  chelates let their electronic structures undergo the SCO within the first picosecond after the MLCT photoexcitation, leading to their own interesting photophysical properties.

These unique characteristics are unfortunately not favorable to the light-harvesting, as the electronic and geometric structure in the MC excited state cannot possess the desired transient dipole moment nor the long enough lifetime. Hence, there have been enormous chemical efforts to destabilize the MC states or alternatively much more stabilize the MLCT states [114; 77; 33; 56; 207; 32; 205; 186; 117; 87; 206; 105; 208; 129; 130; 62]. One of the most effective modifications is to replace the nearest atoms which directly form valence orbital overlaps with the metal ion (Fig. 2.9, Section 2.1.1).

Herein, one of the newly synthesized Fe(II) NHC chelates by our working group and its ultrafast dynamics will be introduced and discussed [205; 206; 87]. The prototype Fe(II) photosensitizer and its derivative with a cobaloxime(III) attached showed their activity in the photocatalytic proton reduction, and the performance was roughly twice higher in case of the dyadic system [87]. The femtosecond-resolved XES measurements were conducted at SACLA upon 515 nm photoexcitation to explore their ultrafast dynamics, and disclosed the femtosecond energy transfer occurring from Fe(II) to Co(III) moiety that was not unveiled from the TOAS measurements.

## 8.1 Introduction

Iron, the element right above Ruthenium, is the fourth most abundant element on Earth, and therefore is very tempting to be introduced to the light-harvesting applications.  $[\text{Fe}(\text{bpy})_3]^{2+}$  for example (Fig. 2.8, 8.1), has been extensively studied over the last few decades as an analogy to the  $[\text{Ru}(\text{bpy})_3]^{2+}$  [204; 24; 69; 67; 68; 113; 123]. Even though the complex has similar structural parameters in the GS and high photostability, its relaxation dynamics is quite different with the Ru(II) analogy upon the MLCT photoexcitation. Due primarily to the weak ligand field (small  $\Delta$ ; Fig. 2.3) the electronic configuration of the  $^3\text{MC}$  or  $^5\text{MC}$  state becomes energetically more stable than that of the  $^3\text{MLCT}$  state, letting the SCO in the second relaxation pathway be dominant (Section 2.2.2), and accordingly the molecular symmetry get significantly distorted (Fig. 8.1; [204; 123; 113]).

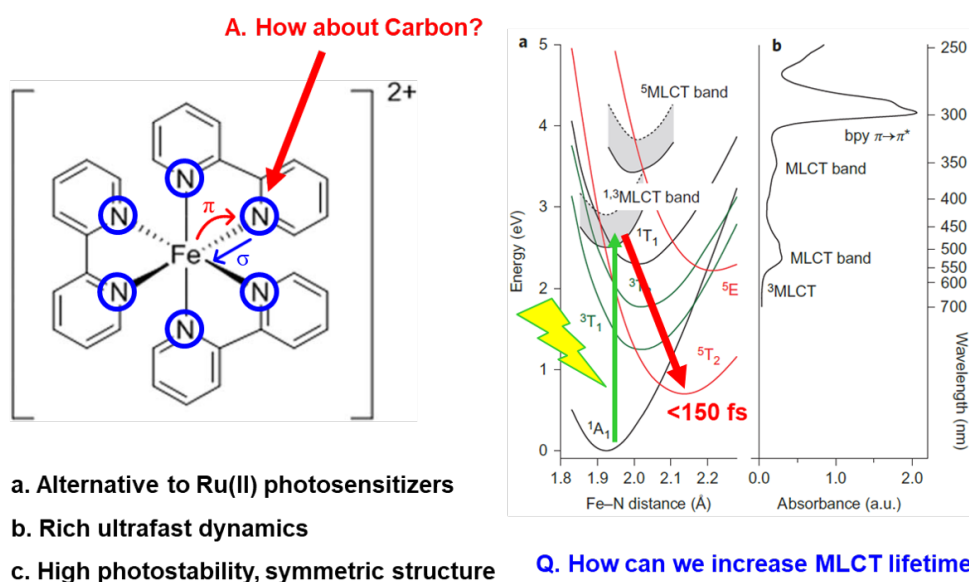


**Figure 8.1:** (left) A structural formula of  $[\text{Fe}(\text{bpy})_3]^{2+}$  and (right) its projected PESs together with absorption bands (Figures from [9]). The complex has been introduced as an alternative to the Ru(II) photosensitizers with its high photostability and symmetric structure. Its rich dynamics on the femtosecond timescale however lead to an instantaneous extinction of the MLCT state, whose lifetime can be prolonged by altering the nitrogen coordinations to the carbon ones.

To detour the femtosecond SCO, there have been many different approaches such as extending the  $\pi$ -conjugation or adding some electron-withdrawing groups and so on [129; 130; 77; 56], but our working group has decided to introduce the NHC ligand to the complex [207; 205; 206; 208; 87]. As discussed in Section 2.1.1, the stabilized carbon atom *via* the  $\sigma$ -coordination bond from the NHC ligand cannot form any  $\pi$ -character bond, i.e. any  $\pi$ -donation backbond with the metal ion (Fig. 8.2).

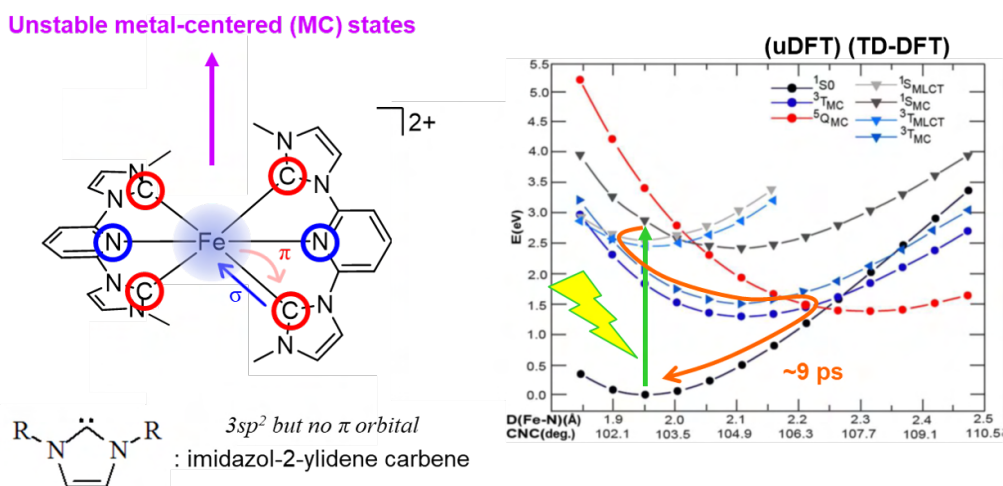


**Figure 8.2:** (left) A model complex with the NHC ligands and (right) its projected PESs (Figure from [62]). The carbene forms three  $sp^2$ -hybrid orbitals but no  $\pi$  orbital, thus the  $\pi$ -donation backbond to compensate the  $\sigma$ -coordination bond cannot be properly followed. This results in a prolonged lifetime of the MLCT state [129; 77; 205; 206; 117; 87].

Figure 8.2 shows a model complex with the NHC ligands and its projected PESs as an example [129; 62; 77; 125; 117]. Although the coordinated carbon may have the  $\pi$ -character bond shared from the nonbonding electrons of the nearest nitrogens, still the excessive electron density on the metal ion cannot be balanced out, such that the MC states become energetically higher and less probable to be populated, whereas the MLCT state on the NHC ligand ( $\pi^*$  orbital) becomes relatively lower and more probable to be populated. Hence, it has been reported experimentally and computationally that the model complex in the MLCT state decays to the GS with a time constant of  $\sim 9$  ps *via* the  $^3MC$  state upon 400 nm photoabsorption.

In line with the previous achievements our working group has designed another model complex with the extended  $\pi$ -conjugation and thus the enhanced steric hindrance (Fig. 8.3; [207; 205; 206; 87]), which is readily attached to the cobaloxime(III) thanks to the heteroleptic NHC ligands. Our hypothesis here is that after the charge separation upon the MLCT photoexcitation, the excited electron has now sufficient time to proceed further to the cobaloxime(III), where the chloride ion departs away from the photocatalyst and two protons get reduced to a hydrogen molecule on the same site. In this way the Fe(II)-Co(III) dyadic system ([Fe-BL-Co]) would show higher performance in the photocatalytic proton reduction compared to the two-component system ([Fe-BL]+[Co]). To examine this intramolecular electron transfer process we performed the TOAS measurements on both [Fe-BL] and [Fe-BL-Co] with the pump laser centered at 515 nm, where the Fe(II) moiety will be selectively excited and its MLCT state will be populated [87].

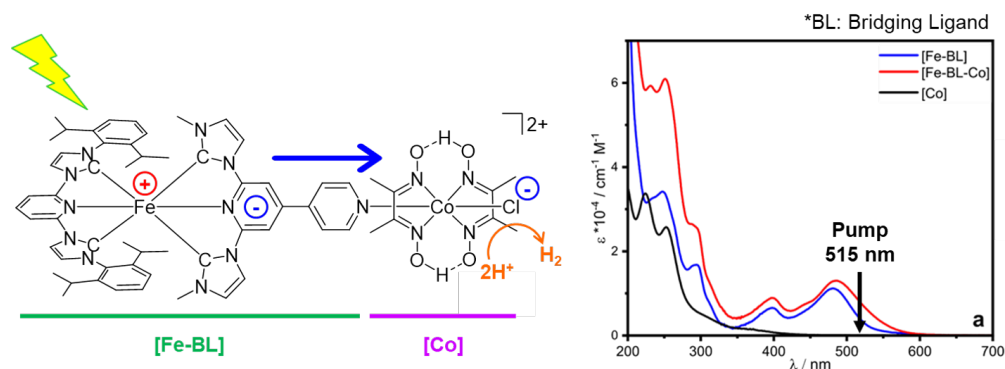


**Figure 8.3:** (left) The Fe(II)-Co(III) photocatalyst synthesized by our working group and (right) its optical absorption bands together with those of the two separate components [87]. The close absorption bands of [Fe-BL] and [Fe-BL-Co] indicate that the attenuation cross sections are predominantly from the Fe(II) moiety. The pump laser was therefore centered at 515 nm to exclusively excite the Fe(II) moiety and populate its MLCT state.

Figure 8.4 summarizes the results of the TOAS measurements, and both TA signals resemble each other a lot because their GS absorption spectra also look very similar to each other within our probe wavelength window. What we clearly see first from the reference system (a) and our dyadic system (b) is a  $\sim 10$  ps decay time constant (blue arrow) that corresponds to the GS recovery. There seems otherwise no additional dynamics appearing in the reference system, whereas another dynamics with a  $\sim 2$  ps time constant is clearly noticed in the dyadic system at the probe wavelength longer than  $\sim 600$  nm (red arrow). According to our assumption this dynamics should correspond to the excited electron transfer from the Fe(II) to Co(III) moiety, before the system returns back to the GS.

The optical probe window was however not enough to convince the electron transfer process, as the signal at the probe wavelength longer than  $\sim 600$  nm can be anything (see also the Section 2.2.1). Hence we decided to employ another probe pulse that is locally sensitive to the electronic and geometric structure change in both the [Fe-BL] and [Fe-BL-Co]. With the SASE X-ray pulse centered at  $\sim 9$  keV, we successfully obtained both Fe  $K\alpha$  and Co  $K\alpha_1$  emission spectra simultaneously from the [Fe-BL-Co], in addition to the XSS data at SACLA. Besides, we measured Fe  $K\beta_{1,3}$  emission spectra from the [Fe-BL] and Co  $K\beta_{1,3}$  emission spectra to get further selectivity and sensitivity to the local electronic structure. In the following sections, the reduced data (see also Appendix B and C) with respect to the probe delay will be interpreted step-by-step, and thereby show the resolving power of the X-ray probe pulse in this research field.

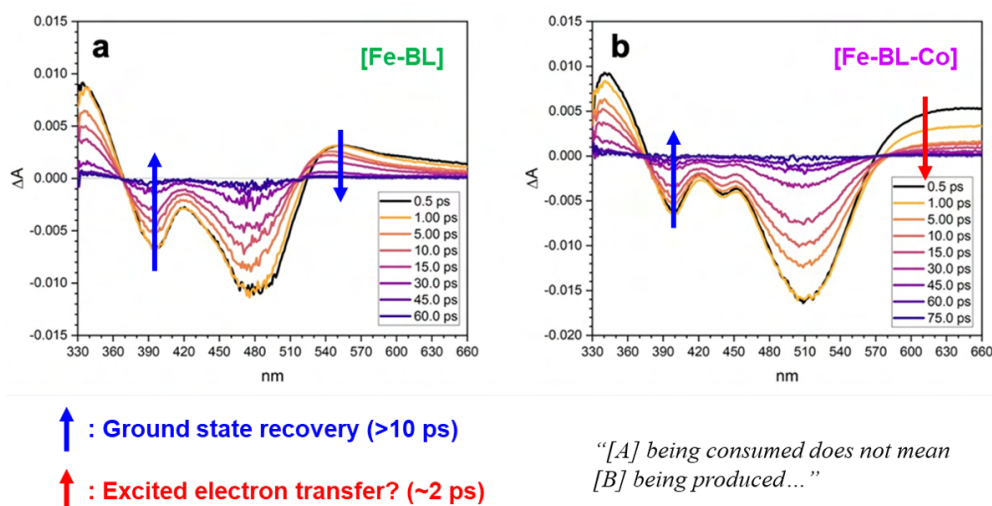


**Figure 8.4:** TA spectra of the [Fe-BL] (a) and [Fe-BL-Co] (b) at certain probe delays upon 515 nm photoexcitation. Only one dynamics of the GS recovery is present in the [Fe-BL], whereas an additional dynamics with a shorter time constant has appeared in the [Fe-BL-Co]. The TOAS experiments were however not conclusive.

## 8.2 Experimental details

The femtosecond-resolved XES and XSS experiments were simultaneously carried out at BL3EH2 of SACLA [188; 92; 101; 103]. The SASE X-ray pulse centered at  $\sim 9$  keV was focused down to  $\sim 10$   $\mu\text{m}$  by beryllium CRLs [101]. The [Fe-BL] and [Fe-BL-Co] were dissolved in acetonitrile at the concentration of 9.4 mM and 11.3 mM respectively (OD < 1 with 100  $\mu\text{m}$  optical path length at 515 nm). During the whole measurement the sample solution was refilled with acetonitrile and purged with Ar gas. The solution was circulating in the liquid jet system inside the He-filled chamber [103], through an injector with its inner diameter of 100  $\mu\text{m}$ .

At the interaction point, the sample molecule was excited to the MLCT state by the 515 nm pump pulse ( $\sim 45$  fs FWHM) from a Ti:sapphire laser system and OPA (HE-TOPAS, Coherent). The optical laser fluence was set to  $\sim 80$   $\text{mJ cm}^{-2}$  that was slightly lower than the onset of the two-photon absorption process. The arrival-timing between X-ray and optical laser pulses was recorded by the timing diagnostics based on the X-ray beam splitting scheme [104]. For the temporal jitter correction, the interval bin width of 50 fs was used. The overall time resolution of the experiment was evaluated to be  $\sim 113$  fs (FWHM) by fitting a Gaussian profile to the first derivative of both Fe  $K\alpha_1$  and Co  $K\alpha_1$  transient emission signal kinetics [102].

The XSS data at each probe delay point were measured in the forward wide-angle X-ray scattering geometry, and the XES data at each probe delay point were measured with two von Hamos dispersive spectrometers in Bragg reflection geometry. 6 Si(531) analyzer crystals were aligned for the Co  $K\alpha_1$ , Fe  $K\beta_{1,3}$ , and Co  $K\beta_{1,3}$  emission lines in vertical direction, and 6 Si(111) analyzer crystals for the Fe  $K\alpha$  emission lines in horizontal direction [103].

### 8.3 Femtosecond-resolved XES on Fe(II)-Co(III) dyad

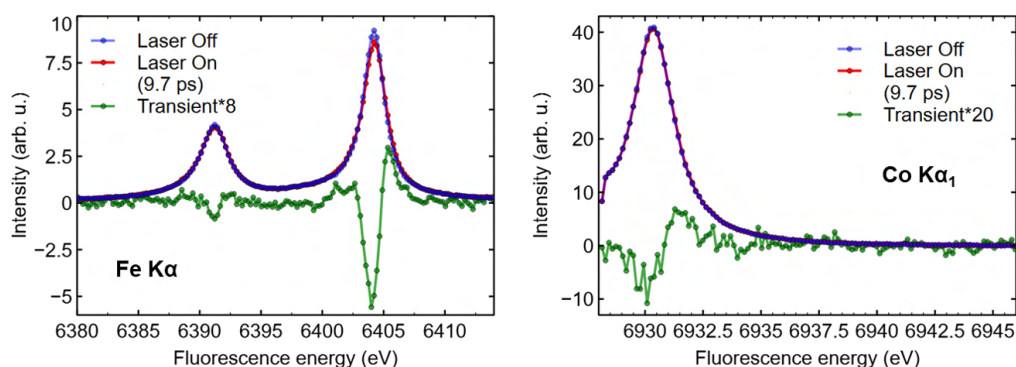


**Figure 8.5:** Fe  $K\alpha$  (left) and Co  $K\alpha_1$  (right) emission spectra of the [Fe-BL-Co] in its GS (blue) and the lowest ES (red) at the probe delay of 10 ps after the 515 nm photoabsorption, and their difference (green).

Now we know from the TOAS results that the GS will be recovered with the time constant of  $\sim 10$  ps after the 515 nm photoexcitation [87]. That means, the transient emission signals at 10 ps probe delay should come from the lowest ES of the system. Figure 8.5 shows the Fe  $K\alpha$  and Co  $K\alpha_1$  emission spectra and their transients from the Fe(II)-Co(III) photocatalyst. It is already quite impressive that the Co  $K\alpha_1$  fluorescence signals disclosed any difference, since it indicates that in fact something had happened between the Fe(II) and Co(III) moiety and was still present at 10 ps probe delay.

By first looking at the line shapes of the transients we can deduce the change in the local electronic structure [117], for instance the Fe  $K\alpha_1$  emission lines were not only blue-shifted in the ES owing to the formal oxidation state change, but also broadened due to the spin density change. On the other hand, the Co  $K\alpha_1$  emission lines were primarily blue-shifted because of the formal oxidation state change. During the measurements the Co  $K\alpha_2$  emission lines were not able to be recorded due predominantly to the limited Bragg angle (up to  $\sim 77^\circ$ ) for the von Hamos dispersive geometry at SACLA.

To figure out the interaction between the Fe(II) and Co(III) moiety, we obtained the transient signal kinetics by integrating the positive parts of the Fe  $K\alpha_1$  and Co  $K\alpha_1$  transients. As compared in Fig. 8.6, there was however no critical difference in between integrating the negative transient signals and positive transient signals.

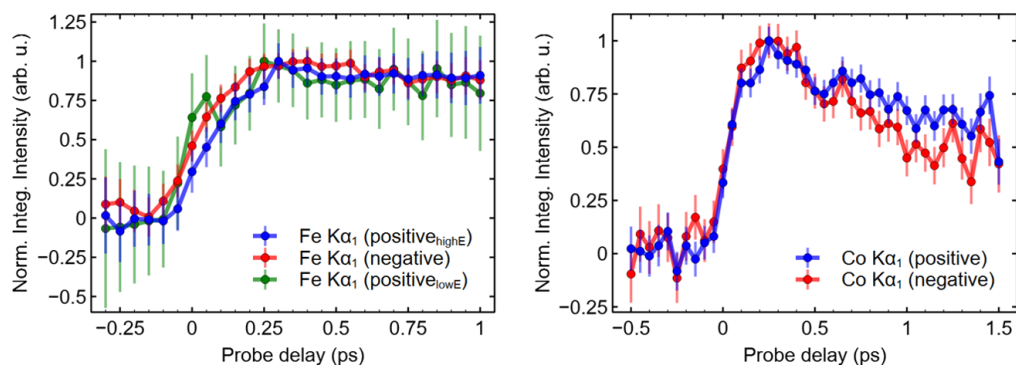


**Figure 8.6:** Comparison of the kinetics extracted by integrating the positive transient signals (blue, green) and negative transient signals (red) of the Fe  $K\alpha_1$  (left) and Co  $K\alpha_1$  (right) fluorescence from the [Fe-BL-Co] upon 515 nm photoexcitation. The error bars were calculated in propagated standard error.

Before we start analysing the kinetics, we need to again specify the instrumental time-zero and its response function (IRF) determining the overall time resolution of the experiment, by fitting a Gaussian profile to the first derivative of both the Fe  $K\alpha_1$  and Co  $K\alpha_1$  transient signal kinetics [102]. Figure 8.7 summarizes the results.

The origin of such a Gaussian broadening at time-zero, namely the convolution of a Gaussian profile and Heaviside step-function, is that in time domain both optical and X-ray pulses in Gaussian line shape convolute inside the cylindrical liquid jet stream, where the refractive index changes to  $\sim 1.3$  at 515 nm (acetonitrile), so that the GVD of 515 nm pulse also contributes to the Gaussian broadening [102]. In addition the jitter correction precision of the timing tool affects the actual time resolution as well [104], so the final IRF(FWHM) can be estimated as  $\sqrt{45^2 + 6^2 + 99^2 + 16^2} \sim 110$  fs. Here the pulse duration of the pump laser ( $\sim 45$  fs) was measured with an autocorrelator before the experiment, and that of the X-ray pulse ( $\sim 6$  fs) was estimated by an autocorrelation measurement.

Both IRF values from the Gaussian fit ( $\sim 113$  fs FWHM) and instrumental estimation ( $\sim 110$  fs FWHM) are in good agreement, even though the Gaussian fit may turn out to be incorrect if the initial population would take much longer than the calculated IRF. The corresponding population in the Franck-Condon state occurs however faster than  $\sim 100$  fs as we noted earlier from the ultrafast dynamics of Fe(II) NHC complexes [77; 205; 117]. Therefore, the instrumental time-zero and response function determined by

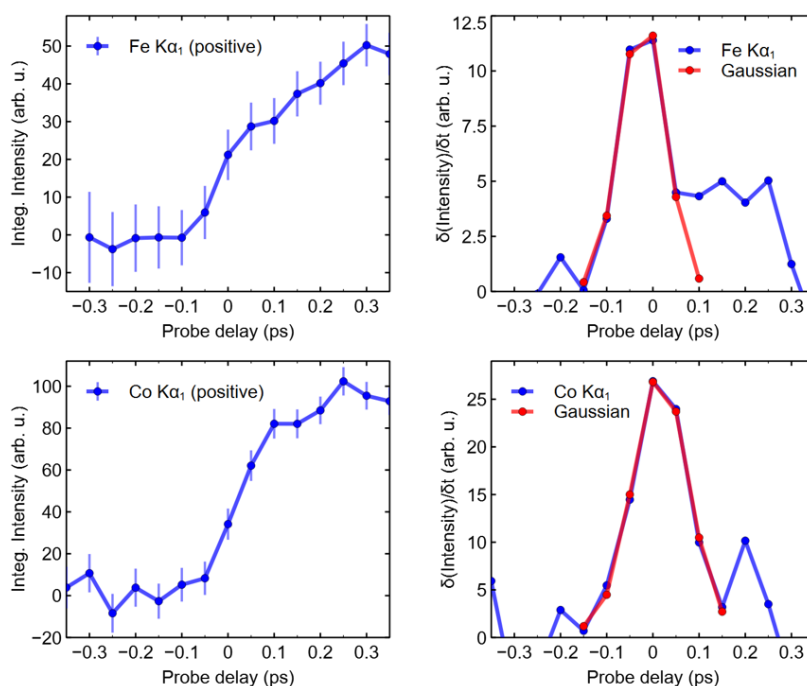


**Figure 8.7:** Instrumental time-zero and its response function (IRF) of this experiment defined by the Gaussian fits to the first derivative of both Fe  $K\alpha_1$  (above) and Co  $K\alpha_1$  (below) transient signal kinetics from the [Fe-BL-Co] upon 515 nm photoexcitation [102]. The time-zero and IRF were evaluated to be  $t_0 = -21.5$  fs and  $\text{IRF}(\sigma) = 48$  fs for Fe  $K\alpha_1$ , and  $t_0 = 16.3$  fs and  $\text{IRF}(\sigma) = 58$  fs for Co  $K\alpha_1$ . Hereafter we will use  $t_0 = -2.6$  fs and  $\text{IRF}(\sigma) = 48$  fs to convolute the  $\text{IRF}(\sigma, t) = A_0 \cdot \exp[-(t - t_0)^2 / 2\sigma^2]$  and the rate equation. The interval bin width of 50 fs was used for the temporal jitter correction. The error bars were calculated in propagated standard error.

the Gaussian fits will be applied to the following analysis.

At the moment we don't know yet how many excited states are involved in the kinetics nor whether in parallel or sequence, we will thus first assume that only one ES shows up, i.e. only the first term of the first-order rate equation (7.8) will be used to analyse the transient emission signal kinetics.

Figure 8.8 shows the fitting results of the Fe  $K\alpha_1$  transient signal kinetics with the first-order rate equation, and this revealed a decay time constant of 8.4 ps which corresponds to the GS recovery [87]. The time constant alone was however not sufficient to also cover the femtosecond dynamics, so we need another term for the sequential first-order rate equation like (7.8).

With two excited states in sequence considered, now the fitting analysis shows much better results (Fig. 8.9), and the femtosecond time constant was attributed to the transition from the  $^3\text{MLCT}$  state to the  $^3\text{MC}$  state [205; 206; 186; 117; 87].

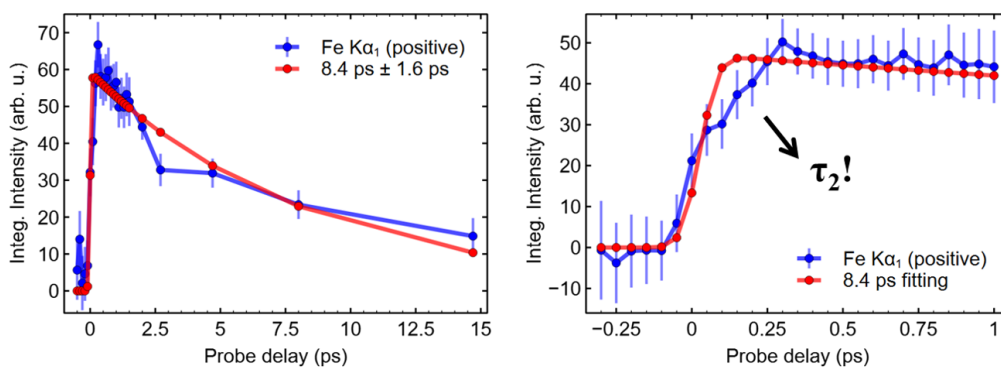


**Figure 8.8:** Fitting analysis of the Fe  $K\alpha_1$  transient signal kinetics with the first-order rate equation. One decay time constant of 8.4 ps (GS recovery) was not enough to cover the femtosecond dynamics ( $\tau_2$ ). The error bars were calculated in propagated standard error.

This assignment was based on another fitting analysis as well, namely the FWHM of the Voigt profile fits to the Fe  $K\alpha_1$  Laser On emission spectra was fitted with the sequential first-order rate equation (7.8) and revealed the same  $\sim 110$  fs time constant. Since the FWHM of the Fe  $K\alpha_1$  emission line is dependent on the spin density of the metal ion [74], hereby we confirmed that the  $^3MC$  state (spin multiplicity = 3) follows the  $^3MLCT$  state (spin multiplicity = 2) after the 515 nm photoabsorption and recovers back to the GS.

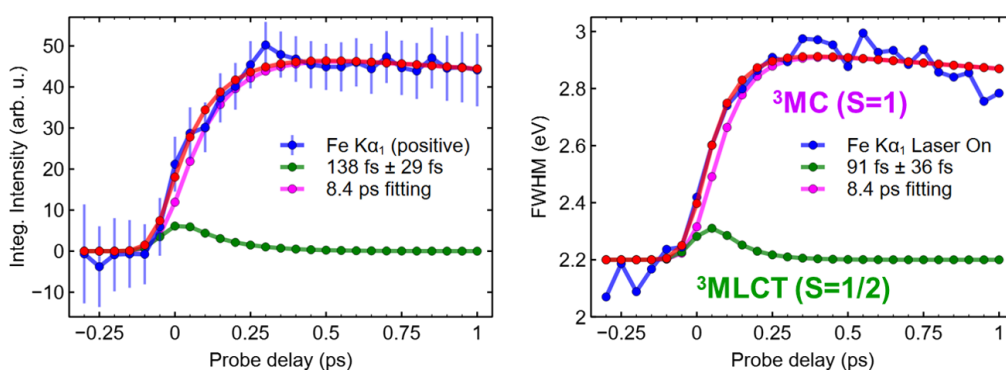


**Figure 8.9:** Fitting analysis of the Fe  $K\alpha_1$  transient signal kinetics (left) and the FWHM of the Voigt profile fits to the Fe  $K\alpha_1$  Laser On emission spectra (right) with the sequential first-order rate equation (7.8). The  $\sim 110$  fs time constant ( $\tau_2$ ) was hence assigned to the transition from the  $^3MLCT$  state to the  $^3MC$  state. The error bars were calculated in propagated standard error.

For the Co  $K\alpha_1$  transient signal kinetics we start again back from the simplest rate equation, and the fitting results unveiled a decay time constant of  $\sim 2.5$  ps for the GS recovery, which was also able to explain the dynamics on the femtosecond timescale (Fig. 8.10). This indicates that in fact only one ES is involved in the kinetics, and because the GS of the cobaloxime(III) is in LS (see also Appendix D.5), the ES could be either Co(II) LS state or Co(III) HS state.

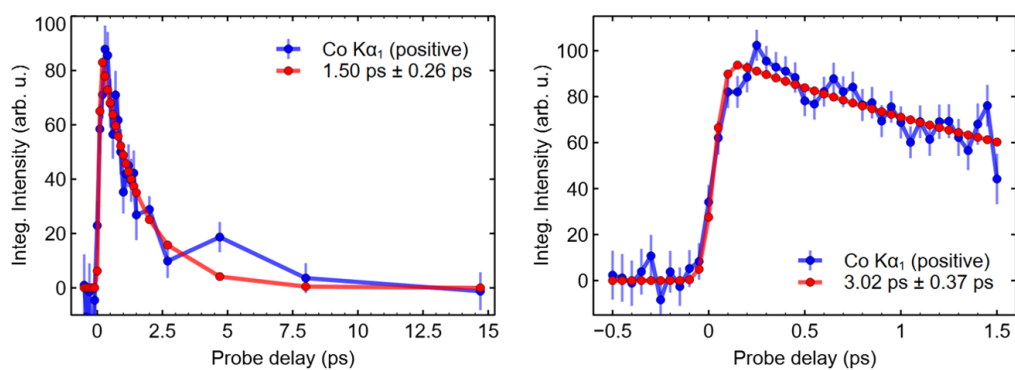


**Figure 8.10:** Fitting analysis of the Co  $K\alpha_1$  transient signal kinetics with the first-order rate equation. One decay time constant of  $\sim 2.5$  ps (GS recovery) was already sufficient to explain the femtosecond dynamics. The error bars were calculated in propagated standard error.

To clarify the spin density of the metal ion, we further measured the Co  $K\beta_{1,3}$  emission spectra and their transients from the [Fe-BL-Co] at certain probe delays (Fig. 8.11). Although the Co  $K\beta_{1,3}$  fluorescence was quite effectively absorbed by the Fe(II) moiety, we were still able to see that at least for the first picosecond the Co(III) moiety was not in HS. In comparison with the reference spectra from the Co(II) HS and Co(III) HS states, the fingerprint of the HS state which is the shoulder peak of  $K\beta'$  is now missing in our case [74]. Therefore we confirmed that the Co(II) LS state appears in the [Fe-BL-Co] upon 515 nm photoexcitation, and decays to the Co(III) LS state with the time constant of  $\sim 2.5$  ps. But how can the Co(II) LS state be induced?

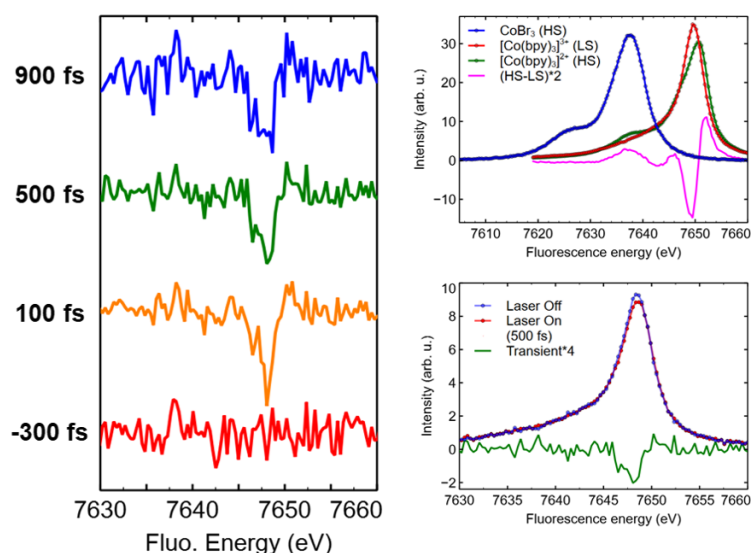


**Figure 8.11:** (left) The Co  $K\beta_{1,3}$  transient emission signals at certain time delays and (right) the Co  $K\beta_{1,3}$  emission spectra of the [Fe-BL-Co] in its GS and ES at the probe delay of 0.5 ps after the 515 nm photoabsorption, together with the reference spectra from the Co(II) HS, Co(III) HS, and Co(III) LS states (courtesy of Florian Otte).

In the end, the fitting analysis of the Co  $K\alpha_1$  transient signal kinetics as well as the FWHM of the Voigt profile fits to the Co  $K\alpha_1$  Laser On emission spectra with the sequential first-order rate equation (7.8) unveiled the second time constant of  $\sim 110$  fs (Fig. 8.12). Thus, the Fe(II) and Co(III) moieties were coupled for the first picosecond after the 515 nm photoabsorption, and the  $^3\text{MLCT}$  state of the Fe(II) moiety promptly perturbed the Co(III) moiety such that the second excited electron from one of the dmgH ligands was transferred onto the Co(III) metal ion (pseudo-Förster energy transfer; [7]). Afterwards, both the  $^3\text{MC}$  state of the Fe(II) moiety and the Co(II) LS state of the Co(III) moiety decayed back to the GS with their own time constant of  $\sim 8$  ps and  $\sim 2.5$  ps respectively. That means, not the excited electron but the energy was transferred from the Fe(II) to Co(III) moiety on the femtosecond timescale.

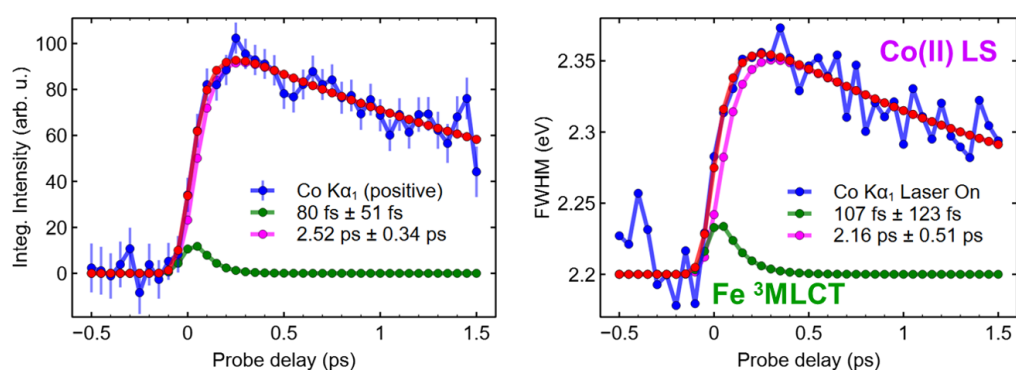


**Figure 8.12:** Fitting analysis of the Co  $K\alpha_1$  transient signal kinetics (left) and the FWHM of the Voigt profile fits to the Co  $K\alpha_1$  Laser On emission spectra (right) with the sequential first-order rate equation (7.8). The  $\sim 110$  fs time constant was hence attributed to the perturbation from the  $^3\text{MLCT}$  state of the Fe(II) moiety to the Co(III) moiety, which induced the Co(II) LS state. The error bars were calculated in propagated standard error.

## 8.4 Femtosecond-resolved XES on Fe(II) photosensitizer

From the previous section now we understand the  $\sim 2$  ps time constant appearing at the probe wavelength longer than  $\sim 600$  nm in TA spectra of the [Fe-BL-Co]. Moreover we understand the electronic structure change in both the Fe(II) and Co(III) moieties primarily based on the fitting analysis of the FWHM changes in the  $K\alpha_1$  emission line [74]. We can therefore already guess the ultrafast dynamics of the [Fe-BL] upon 515 nm photoexcitation.

Figure 8.13 shows the Fe  $K\alpha$  and  $K\beta_{1,3}$  emission spectra and their transients from the Fe(II) photosensitizer at 10 ps probe delay after the 515 nm photoabsorption. The transients are again from the lowest ES of the system, and the line shape of the Fe  $K\alpha_1$  transient looks very similar with that from the [Fe-BL-Co] (Fig. 8.5). The line

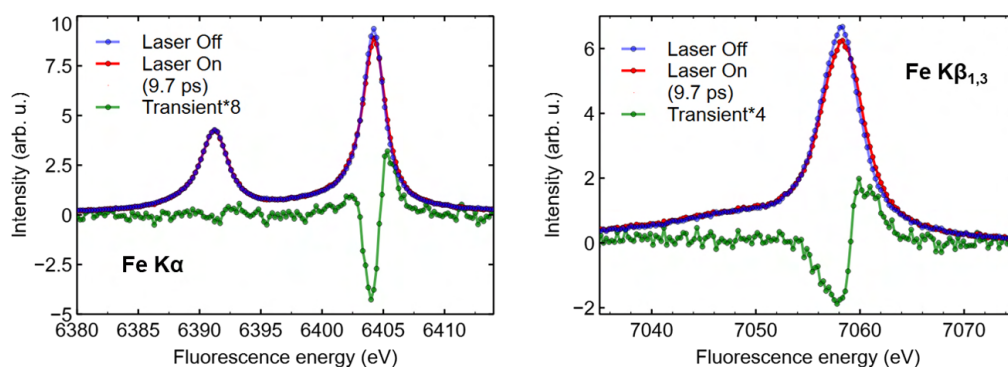


**Figure 8.13:** Fe K $\alpha$  (left) and K $\beta_{1,3}$  (right) emission spectra of the [Fe-BL] in its GS (blue) and the lowest ES (red) at the probe delay of 10 ps after the 515 nm photoabsorption, and their difference (green).

shape of the Fe K $\beta_{1,3}$  transient is quite distinct, and proves that the lowest ES of the system is not the  $^5\text{MC}$  state because of the missing shoulder peak of K $\beta'$  [74; 204; 113; 117]. Thus we can deduce that the ultrafast dynamics of the [Fe-BL] will be same with that of the Fe(II) moiety in [Fe-BL-Co].

The transient signal kinetics were obtained by integrating the positive parts of the Fe K $\alpha_1$  and K $\beta_{1,3}$  transients, and there was again no critical difference in between integrating the negative transient signals and positive transient signals (Fig. 8.14, see also Appendix D.5). As we expected, a decay time constant of  $\sim 7$  ps for the GS recovery was not sufficient to also cover the femtosecond dynamics, so we needed another term for the sequential first-order rate equation like (7.8).

With two excited states in sequence considered, now the fitting analysis shows much better results (Fig. 8.15), and the femtosecond time constant was attributed to the transition from the  $^3\text{MLCT}$  state to the  $^3\text{MC}$  state [205; 206; 186; 117; 87], in accordance with the FWHM changes of the Fe K $\alpha_1$  emission line [74]. The femtosecond dynamics is however less pronounced than that in the Fe(II) moiety of the [Fe-BL-Co], i.e. the fitting errors are much larger than the previous case. This was understood as the dynamics becomes less prominent without the coupling with the cobaloxime(III). Nevertheless it is certain that the  $^3\text{MC}$  state (spin multiplicity = 3) follows the  $^3\text{MLCT}$  state (spin multiplicity = 2) after the 515 nm photoexcitation, and the cobaloxime(III) does not much influence the ultrafast dynamics in the [Fe-BL].

The same interpretation applies to the fitting results of the Fe K $\beta_{1,3}$  transient signal kinetics, and an additional kinetics extracted by integrating the transient signals at  $7054 \pm 1$  eV of the fluorescence energy can be another evidence of the  $^3\text{MC}$  state appearing right after the 515 nm photoexcitation [204; 113; 117] (see also Appendix

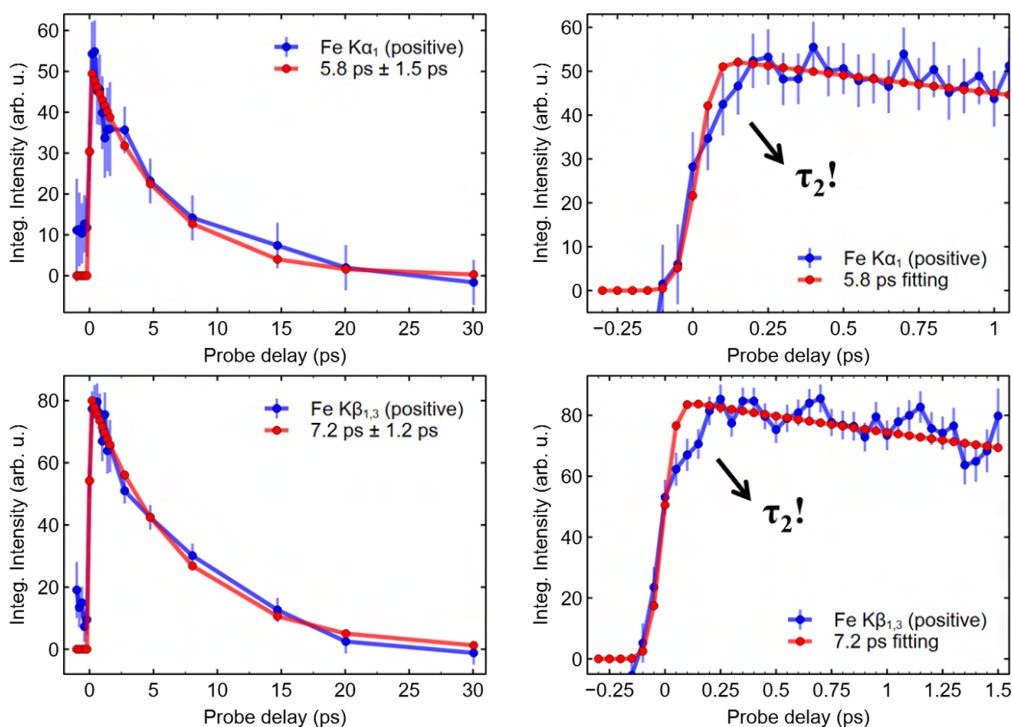


**Figure 8.14:** Fitting analysis of the Fe  $K\alpha_1$  (above) and  $K\beta_{1,3}$  (below) transient signal kinetics with the first-order rate equation. One decay time constant of  $\sim 7$  ps (GS recovery) was not enough to cover the femtosecond dynamics ( $\tau_2$ ). The error bars were calculated in propagated standard error.

D.5).

The Fe(II) NHC complex studied here is a close derivative of the model complex introduced in Fig. 8.2 [129; 62; 77; 125; 117]. Due predominantly to their similar chemical structure and optical absorption bands (Fig. 8.3 and [117]), we expect that our [Fe-BL] would have analogous PESs to those described in Fig. 8.2, and therefore follow the analogous relaxation pathways. Even though we successfully interpreted the Fe  $K\alpha_1$  and  $K\beta_{1,3}$  transient signal kinetics with the simplest model including the  $^3\text{MLCT}$  and  $^3\text{MC}$  states in sequence, the model complex shown in Fig. 8.2 decays along slightly different pathways upon the MLCT photoexcitation [117].

The most critical difference between two experiments and interpretation originates from the discrepancy in the optical pump wavelength, namely a bit higher photon energy can open up other relaxation pathways that are otherwise not accessible [94; 102; 129; 117]. The heteroleptic NHC ligands with two additional ring substituents on one side and a pyridine pendant on the other side in [Fe-BL] can be also critical [87], but in general both systems decay back to the GS within  $\sim 10$  ps after the MLCT photoexcitation *via* the  $^3\text{MC}$  state (see also Appendix D.5).

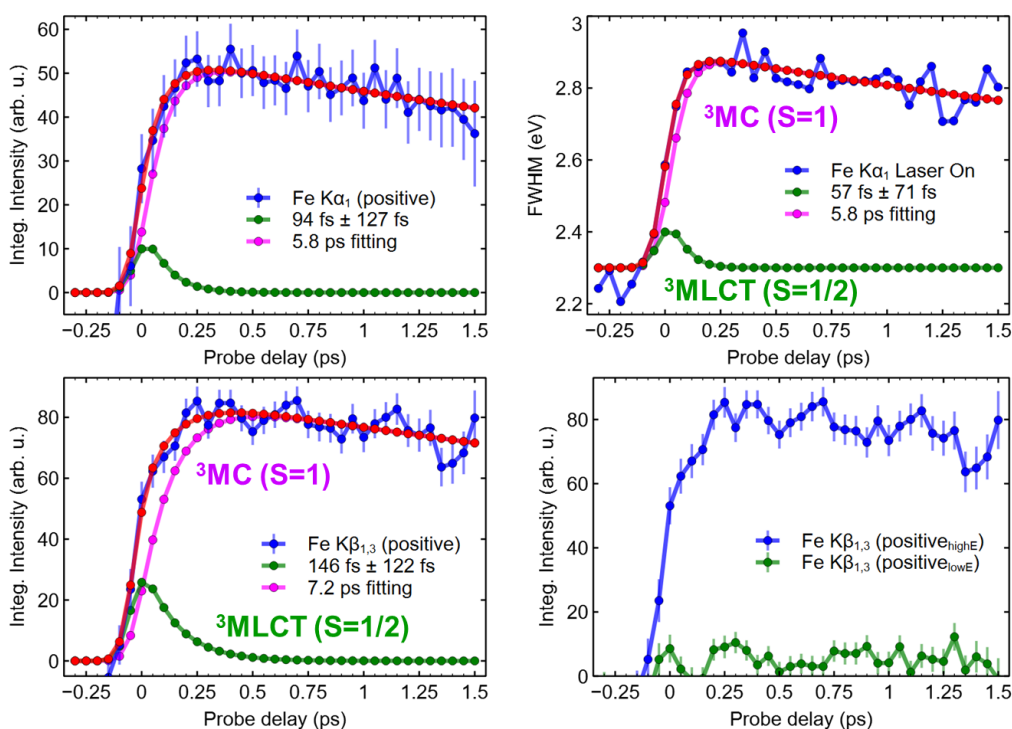


**Figure 8.15:** (above) Fitting analysis of the Fe  $K\alpha_1$  transient signal kinetics (left) and the FWHM of the Voigt profile fits to the Fe  $K\alpha_1$  Laser On emission spectra (right) with the sequential first-order rate equation (7.8). The  $\sim 110$  fs time constant ( $\tau_2$ ) was hence assigned to the transition from the  $^3\text{MLCT}$  state to the  $^3\text{MC}$  state. (below) Fitting analysis of the Fe  $K\beta_{1,3}$  transient signal kinetics (left) with the sequential first-order rate equation (7.8), and a comparison with the kinetics obtained by integrating the transient signal at  $7054 \pm 1$  eV of the fluorescence energy (right). The error bars were calculated in propagated standard error.

## 8.5 Conclusion and outlook

Complementary to the previous studies, in this chapter we report the femtosecond intramolecular energy transfer in a new Fe(II)-Co(III) photocatalyst observed with the femtosecond-resolved XES methodologies available at SACLA. With the overall time resolution of  $\sim 113$  fs (FWHM) achieved, we found the same arising time constant of  $\sim 110$  fs present in both Fe  $K\alpha_1$  and Co  $K\alpha_1$  transient signal kinetics upon 515 nm photoexcitation. This early coupling between Fe(II) and Co(III) moiety is understood as a pseudo-Förster energy transfer from the Fe(II) to Co(II) moiety [7], causing the second ES of Co(II) LS state as well as the  $^3\text{MC}$  state in the Fe(II) moiety. Eventually two ESs in our dyadic system recover back to the GS independently.

The Fe(II) photosensitizer without the cobaloxime(III) disclosed almost identical relaxation dynamics, and the line shapes of the Fe  $K\beta_{1,3}$  fluorescence with respect to

the probe delay further proved the absence of the  $^5\text{MC}$  state. The conclusion of this chapter is now summarized in Fig. 8.16.

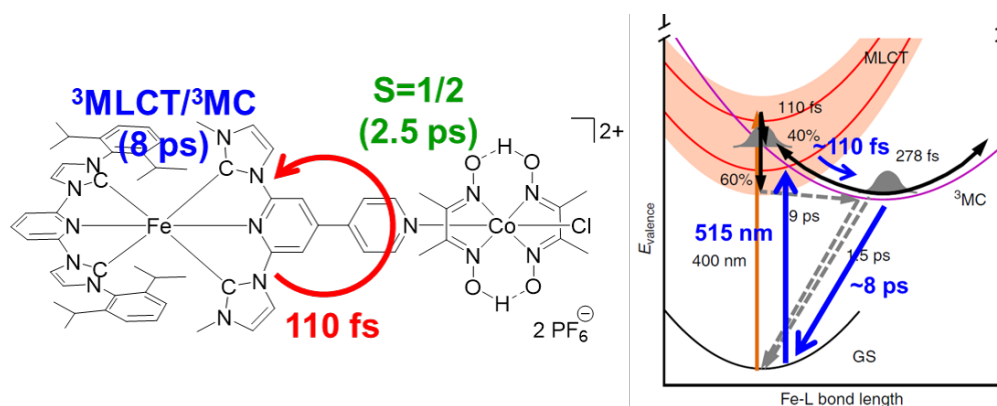


**Figure 8.16:** (left) The ultrafast dynamics in the Fe(II)-Co(III) dyadic system and (right) the relaxation pathways depicted in the projected PESs of the Fe(II) moiety upon 515 nm photoabsorption (Figures from [87; 117]). After the perturbation of the  $^3\text{MLCT}$  state, the following  $^3\text{MC}$  state and Co(II) LS state *via* an energy transfer return to the GS independently.

The Fe(II) NHC chelates have exhibited unprecedented tunability of their ligands fields and thus the extended lifetime of the MLCT state, primarily depending on the number of carbene coordinations [129; 62; 56; 130; 205; 206; 117; 87]. Our working group has linked the Fe(II) NHC complex directly to the cobaloxime(III) and shown that the catalytic activity became higher than that of the two-component system. Although the femtosecond "crosstalk" between the Fe(II) and Co(III) moiety seems not relevant to the prolonged lifetime, to the best of our knowledge this is the first-observed intramolecular energy transfer by exploiting the femtosecond X-ray pulses.

---

## 9 Outlook and perspective

It is all about electrons.

Chemical reactions are driven by the statistical thermodynamic factors, in most of the cases without any single photon involved. Still, many of the non-light-driven ultrafast dynamics in chemistry can be in fact mimicked by triggering them with optical photons [36]. Therefore, a broad range of the photo-induced "reactions" dealt with in this thesis can be generally applicable to the relevant dark chemistry.

The femto-chemistry and femto-biology for example determine the material properties on our daily timescale, thus their importance are particularly significant in the 21st century since A. H. Zewail was awarded the 1999 Nobel Prize in Chemistry for his studies of the transition states of chemical reactions using femtosecond spectroscopy [203]. A remarkable fact here is that the ratio of few hundreds of femtoseconds to a second is quite similar to that of a year to the age of the universe. In other words, every single femtosecond dynamics in a molecular system can be seen as a cycle of one universe!

Infinite number of microscopic dynamics are still appearing and disappearing, and the main character in this femtosecond world is of course an electron. Since we have successfully described a bound electron in various states, we may now notice that it resembles ourselves quite closely. After being promoted a new state distorts the system and perturbs another system in distance, eventually exchanging either an energy or itself. Sometimes the system forces it rather to come back to the original state, but it is noteworthy that a single electron's excitation and relaxation pathways, to some extent, determine the universe's identity (the butterfly effect).

Electron's wavelike nature and its interaction with the electromagnetic field force carrier (photon) literally govern the whole universe. Although the studies in this thesis are restricted to the transition metal complexes under the optical or hard X-ray irradiation, how the photon energy absorption transforms on the ultrafast timescale gives us valuable insights into the light-harvesting applications. The fitting analysis with the sequential first-order rate equation was especially impressive, because the chemical kinetics for molecular systems can in fact be also applied to the ultrafast

kinetics of the excited electron.

The shortest time resolution achieved with the light sources employed for the thesis was  $\sim 30$  fs ( $\sigma$ ) that is enough to resolve the coherent nuclear wavepacket in a molecular system. Even shorter light pulses with only few periods are in principle also available [40; 64; 21], and the so-called attosecond science intrinsically covers the most fundamental processes in nature. The orbital period of an electron in the GS hydrogen in Bohr's model for instance amounts to 150 as, hence the attosecond timescale mostly concerns the electronic motion on an atomic scale. In a molecular system however, an electron is moving in the combined potential of the nuclei and all other electrons, and undergoes a dipole transition in a strongly entangled way. Thus, the attosecond-resolved studies involve correlated multi-electron dynamics and higher frequency vibrations as well as what we have assumed to happen "instantaneously" (e.g. Franck-Condon principle).

Besides the attosecond-resolved experiments, the optical pump tender X-ray probe spectroscopies at between 2 and 5 keV are another milestone for the future research on the ultrafast dynamics in light-harvesting molecules. From instrumental point of view, the tender X-rays are transported in a similar way as for the hard X-rays, and still the fluorescence yield is dominant over the Auger electron yield [145]. Even though the attenuation cross section in light-element-environment becomes larger, at the same time the scattering cross section of the tender X-rays becomes also larger so that the so-called single-particle diffractive imaging benefits for example.

From spectroscopic point of view, the K-edges (e.g. phosphorus or sulfur) and L-edges (e.g. Mo or Ru) concern dipole-allowed X-ray absorptions and fluorescences that accordingly reveal their fine features and changes with high SNRs [178]. The same geometries as for the hard X-ray absorption and emission spectroscopies can be exploited (Fig. 3.1), namely that the von Hamos spectrometer with different analyzer crystals can be set for the fluorescence energies between 2 and 5 keV.

# A PETRA III P01 data reduction

This chapter describes how to reduce the raw data obtained at P01 beamline in PETRA III storage ring with a Pilatus 100k detector from the XES measurements in vertical von Hamos dispersive geometry. The corresponding python code is shared in Appendix C.

After each run, a .fio file is created and contains all relevant information of the run. From this .fio file the values of the monochromator energy and all PIN diodes will be imported.

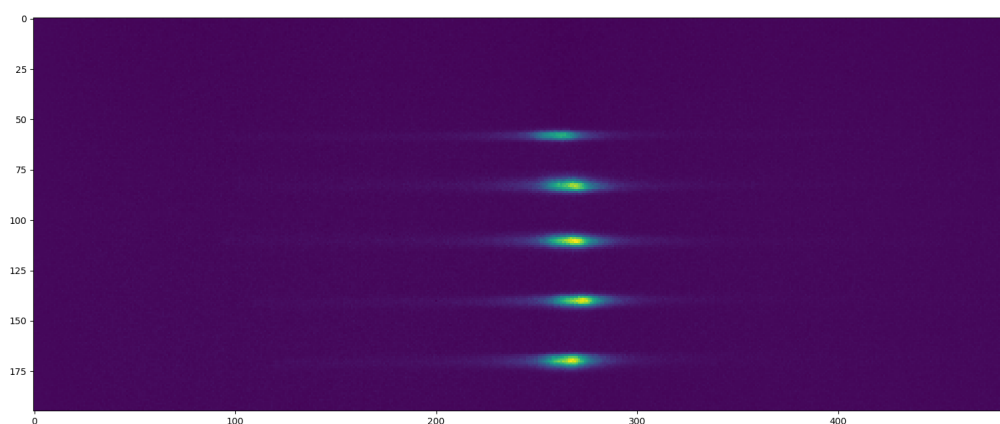


**Figure A.1:** An image from the Pilatus 100k detector in vertical von Hamos dispersive geometry exposed to the emitted and scattered X-ray photons. The Cu  $K\beta_{1,3}$  fluorescence signals diffracted by the Ge(400) crystals were recorded. The x-axis corresponds to the dispersive plane (lower value = lower Bragg energy) and the y-axis to the focusing plane (Darwin width).

Figure A.1 shows an image of the Cu  $K\beta_{1,3}$  fluorescence signals recorded on the Pilatus 100k detector as an example. This image consists of 5 signals from 5 analyzer crystals, and background noises from electronics and scattered photons. Here we assume that the experimental setup was well-aligned that on the Pilatus 100k detector mostly the emitted X-ray photons were recorded.

Several region-of-interests (ROIs) are first defined as the background noises and averaged along the y-axis, and subtracted from other 5 ROIs containing the emission signals. Each of the 5 ROIs is then also averaged along the y-axis, and aligned to each other e.g. by matching the max. intensity x-values, to be averaged into a 1-D array. If available the obtained spectrum can be normalized by the corresponding incident photon flux  $I_0$  or TFY, otherwise the spectrum is normalized by its area.

For the x-axis calibration (fluorescence energy), a so-called elastic scan is performed by recording the scattered X-ray photons from the analyzer crystals while scanning the monochromator energy across the expected fluorescence energy range. Once the monochromatized X-rays are scattered at the interaction point, those satisfying the Bragg's condition will be reflected by the analyzer crystals and therefore appear on the detector as a peak (Fig. A.2). By scanning the monochromator energy in the expected fluorescence energy range, we can obtain the linear relationship between the monochromator energy and the x-value on the detector.

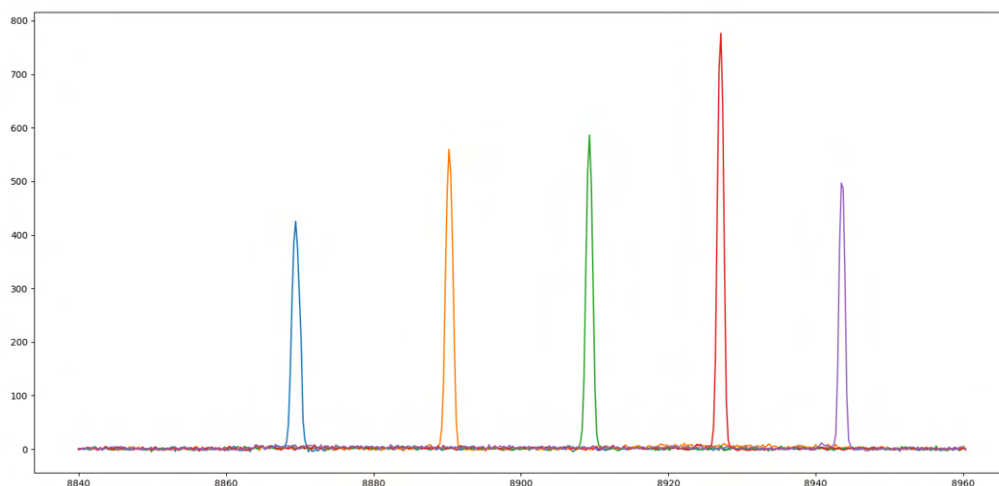


**Figure A.2:** 5 monochromatized X-ray photons scattered at the interaction point and reflected by the analyzer crystals. The x-axis is thereby calibrated from the x-values to the monochromator energies. The FWHM of each peak (Gaussian profile) is dominated by the energy resolution of the Si(111) monochromator ( $\Delta E/E \sim 10^{-4}$ ).

Figure A.3 shows some of the reference Cu  $K\beta_{1,3}$  and Co  $K\alpha$  emission spectra measured at P01 beamline. Apart from the difference in their covalency, there is no significant change in the line shapes between the Cu(I) and Cu(II) compounds, whereas a remarkable shift of the emission lines is noticed between the Co(II) and Co(III) compounds. This result already reveals a very difference between the copper and cobalt chelates, namely the SCO in the Co(II) chelates dramatically affects the core-to-core fluorescence.

With the same experimental setup, the RIXS spectroscopy can be carried out by scanning the monochromator energy in the vicinity of the K-edge of target element. As discussed in section 2.3.3, a 1s2p RIXS plane like in Fig. 2.23 can be plotted and interpreted. Besides, a XANES spectrum like in Fig. 2.13 can be simultaneously obtained by following a specific transition channel, in addition to that measured by PIN diodes either in transmission mode or TFY mode.

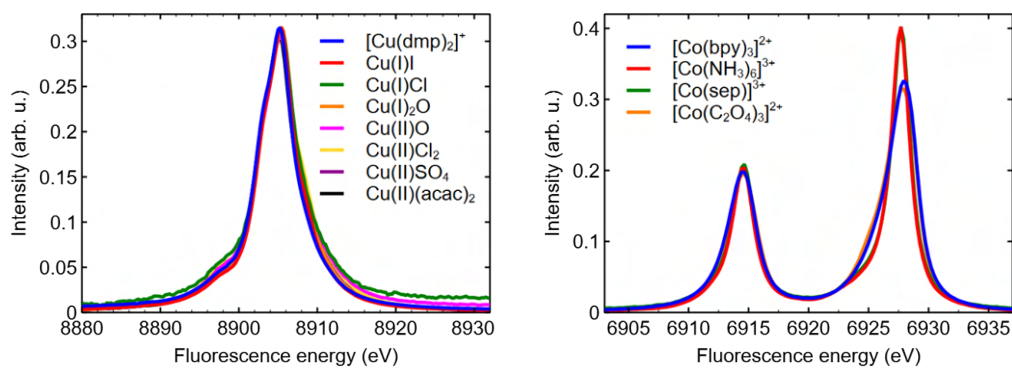


**Figure A.3:** Cu  $K\beta_{1,3}$  (left) and Co  $K\alpha$  (right) emission spectra from several reference samples measured at P01 beamline in vertical von Hamos dispersive geometry. The SCO in the Co(II) chelates dramatically changes the line shapes.

The data reduction for the RIXS plane follows the same procedure for the XES except the spectrum area normalization, but when it comes to the XAFS measurement in transmission mode or TFY mode a different process is applied.

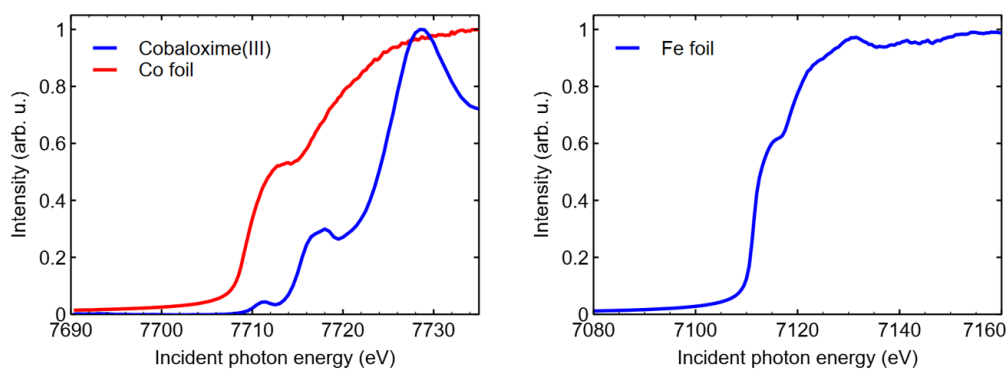


**Figure A.4:** XANES spectra of cobaloxime(III) in solution phase, cobalt foil (left), and iron foil (right) measured at P01 beamline in TFY mode.

## B SACLA XES data reduction

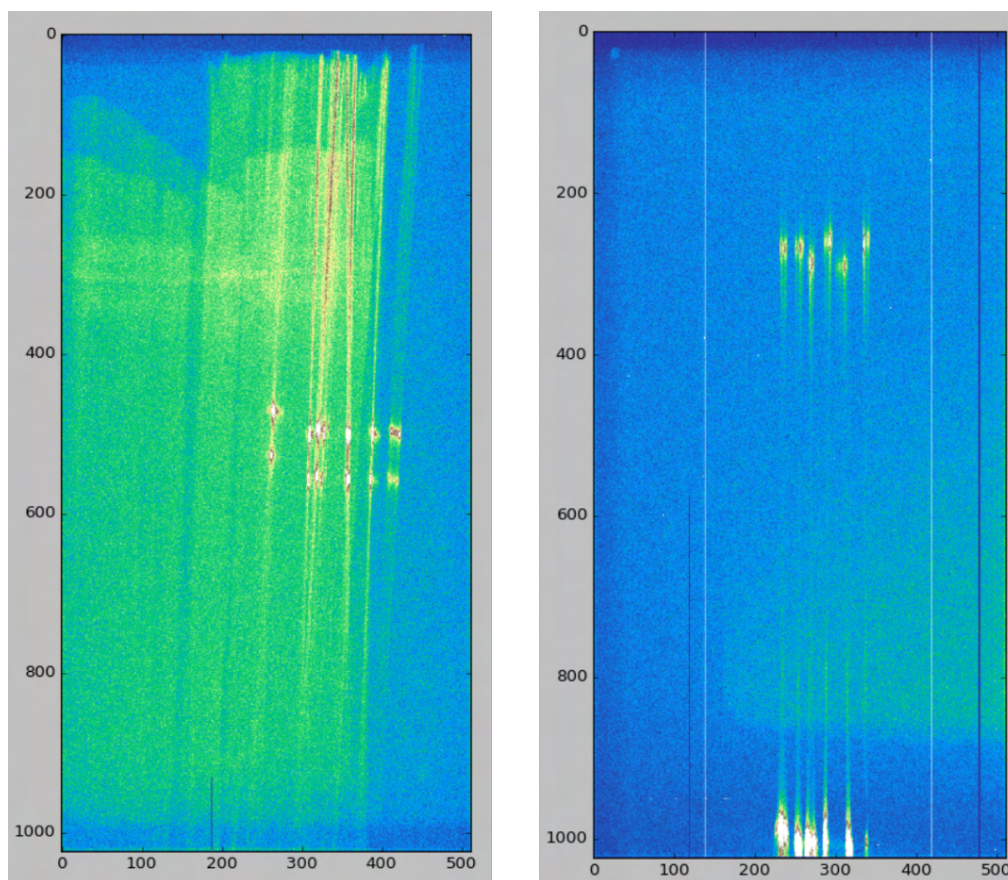


**Figure B.1:** Raw images from the MPCCD detectors in horizontal (left) and vertical (right) von Hamos dispersive geometries exposed to the emitted and scattered X-ray photons. The left image contains the Fe  $K\alpha$  emission lines diffracted by the Si(111) crystals, whereas the right image contains the Co  $K\alpha$  and Fe  $K\beta_{1,3}$  emission lines diffracted by the Si(531) crystals. The y-axis corresponds to the dispersive plane (lower value = higher Bragg energy) and the x-axis to the focusing plane (Darwin width).

Basically the same logic as in Appendix A applies to the SACLA XES data reduction. Each MPCCD detector image recorded at 30 Hz is first reduced into a 1-D array by integrating 6 ROIs along the x-axis with proper background noise subtraction (Fig. B.1). If available the obtained spectrum can be normalized by the corresponding incident photon flux  $I_0$  or TFY, otherwise the spectrum is normalized by its area.

The emission spectra without optical photoexcitation are then all summed up and averaged after filtering out some outliers (Laser Off). The emission spectra with optical photoexcitation are first sorted out into the 50 fs interval bins after the temporal

jitter correction [149; 104], and then the emission spectra in each interval bin are summed up and averaged after filtering out some outliers (Laser On).

X-ray fluorescence energy axis (the y-axis) can be calibrated in comparison with the previous measurements at the storage ring. Transient signals, i.e. Laser On – Laser Off = (excited fraction  $f$ )\*(ES spectrum – GS spectrum), can be further normalized by their corresponding averaged optical pump laser power.

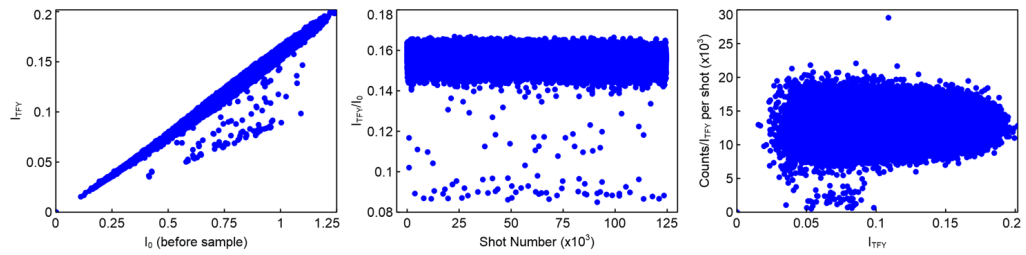


**Figure B.2:** Per-shot diagnostics of the raw data to filter out bad signals. Certain criteria (details can be referred to Appendix C) are set to exclude the outliers, e.g. from the liquid jet fluctuation. Counts on the right distribution stand for the integrated values over a fixed range of y-axis on the MPCCD detectors.

Figure B.2 shows the per-shot diagnostics to filter out bad signals. The outliers are primarily from the liquid jet fluctuation, and the same plot was used during the experiments to check the jet stability.

---

## C Python data analysis codes

The python data reduction and analysis codes written by Tae-Kyu Choi and used for this thesis can be found in the following links.

- **TOAS experiments at University of Bern**  
<https://github.com/choi-t/thesis/bern2.py>
- **XES and RIXS at PETRA III P01**  
<https://github.com/choi-t/thesis/petra.py>
- **Time-resolved EXAFS at APS 11-ID-D**  
<https://github.com/choi-t/thesis/aps.py>
- **Femtosecond-resolved XES at SACLA BL3EH2**  
<https://github.com/choi-t/thesis/1dsacla.py>

# D Supplementary information

## D.1 Chapter 4

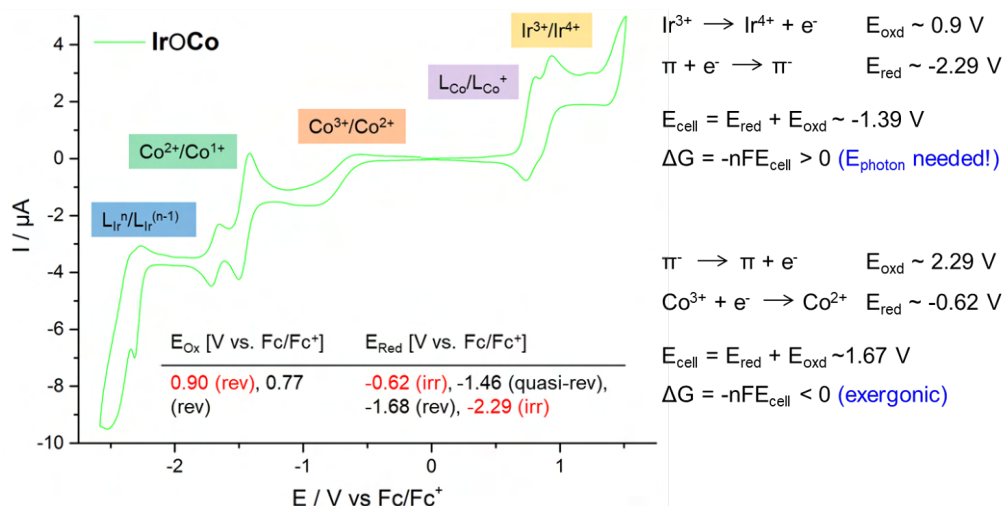


**Figure D.1:** Cyclic voltammogram of the **Ir-O-Co** measured in degassed acetonitrile at 1 mM [191]. A Pt working electrode, Ag/AgNO<sub>3</sub> reference electrode, and a Pt wire as a counter electrode were used ( $v_s = 0.1 \text{ V s}^{-1}$ ).

Cyclic voltammetry was performed on both the **Ir-O-Co** and **Ir-th-Co** in degassed acetonitrile to confirm that the excited electron transfer is exergonic towards the cobaloxime(III) catalyst (Fig. D.1; [191; 55]). The cyclic voltammogram of the **Ir-th-Co** showed similar redox potentials, but this thermodynamic driving force does not necessarily mean that its kinetics will be favorable [7].

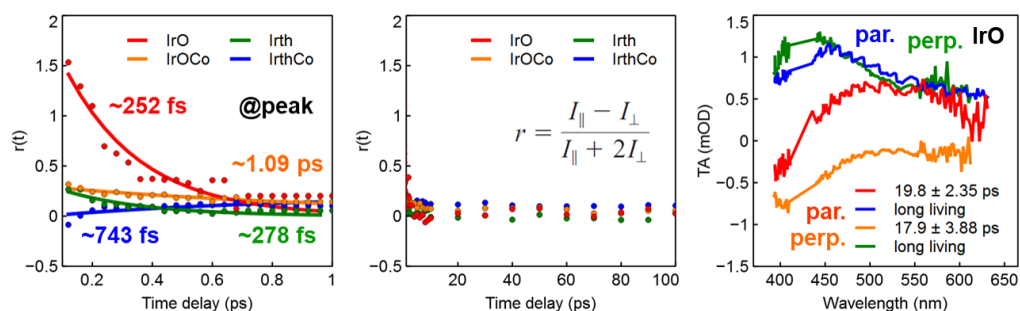


**Figure D.2:** (left) The anisotropic absorption  $r(t)$  of **Ir-O** (red), **Ir-th** (green), **Ir-O-Co** (orange), and **Ir-th-Co** (blue) up to 1 ps, (middle) up to 100 ps, and (right) DASs of the **Ir-O** with parallel and perpendicular polarization of the optical pump pulse relative to the probe pulse. The probe wavelength for the  $r(t)$  was chosen to be the peak of the corresponding ESA band [201; 47].

The polarization anisotropy TOAS measurements can distinguish not only the degeneracy of the transient dipole moment right after the MLCT photoexcitation [201; 47; 180], but also a change of the transient dipole moment in the system such as ILCT [190]. In accordance with their directional charge separation character, the four bis-cyclometalated Ir(III) complexes were subjected to the polarization anisotropy TOAS experiments (Fig. D.2).

The anisotropic absorption  $r(t)$  of all Ir(III) complexes were calculated based on [201] at the probe wavelength of the peak of each ESA band, and thus the major contribution to the anisotropy signal was ESA. There was no significant difference in between the measurements with parallel and perpendicular polarization except for the **Ir-O**, whose  $r(t)$  shows an exponential decay with the time constant of  $\sim 250$  fs. The DASs of the **Ir-O** revealed however quite similar line shapes and time constants ( $\sim 20$  ps), which is again assigned to the vibrational cooling in the  $^3\text{MLCT}$  state that causes its absorption band becoming narrower and blue-shifted.

The nevertheless pronounced  $r(t)$  of the **Ir-O** is understood as an ultrafast incoherent electron-hole hopping process (vibronic resonance) among the degenerate  $^3\text{MLCT}$  hot states within the first picosecond. Other three Ir(III) complexes have also shown a weak decay of their  $r(t)$ , and these are understood as a hole transfer in  $d\pi$  levels.

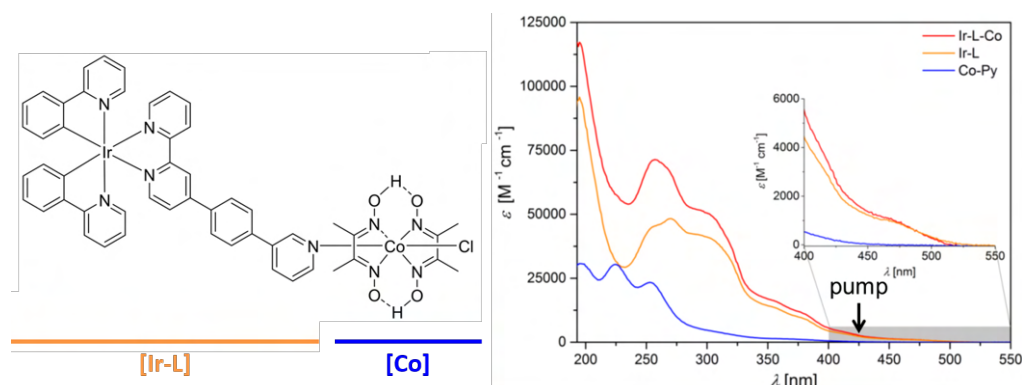


**Figure D.3:** (left) A new Ir(III)-Co(III) dyadic system with a bpy-derivative BL synthesized by our working group, and (right) its optical absorption bands together with those of the two separate components [143]. The close absorption bands of [Ir-L] and [Ir-L-Co] indicate that the attenuation cross sections are predominantly from the Ir(III) moiety. The pump laser was therefore centered at 425 nm to exclusively excite the Ir(III) moiety and populate its MLCT state.

In addition to the triadic systems introduced in Chapter 4, our working group has synthesized a new Ir(III)-Co(III) dyadic system (**Ir-L-Co**) with a bpy-derivative BL (Fig. D.3). In contrast with the triadic systems, the photocatalytic proton reduction was not improved compared to the two-component system (**Ir-L + Co**), hence the TOAS experiments were performed to investigate the corresponding ultrafast dynamics.

The **Ir-L** and **Ir-L-Co** were dissolved in degassed acetonitrile at the concentration of  $\sim 6.9$  mM and  $\sim 4.8$  mM respectively for the OD between 0.1 and 0.3 at 425 nm photoabsorption and 200  $\mu\text{m}$  optical path length.

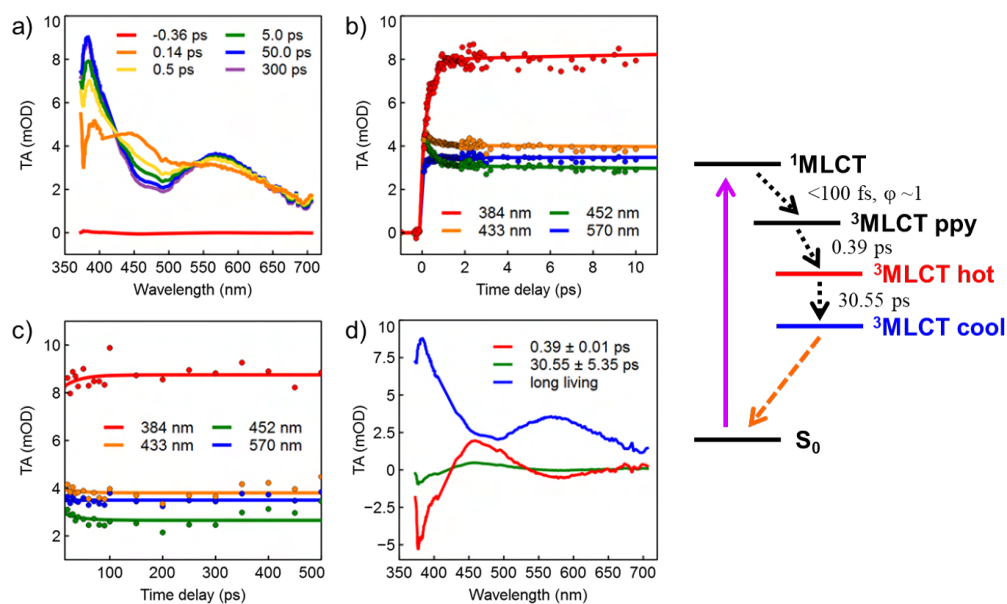


**Figure D.4:** a) TA spectra of **Ir-L** at certain probe delays after the 425 nm photoexcitation measured at magic angle of the probe pulse polarization with respect to the pump pulse, b) transient signal kinetics at different probe wavelengths (dot) together with the SVD-GF results (solid line) up to 10 ps, c) up to 500 ps, and d) the corresponding DASs with three time constants considered. The  $\sim 0.4$  ps time constant represents the ILCT from  $\pi^*(\text{ppy})$  to  $\pi^*(\text{bpy})$ , and the  $\sim 30$  ps time constant represents the vibrational cooling in the  $^3\text{MLCT}$  state.

Figure D.4 summarizes the results of the SVD-GF analysis on the reduced TOAS data from the **Ir-L**. Interestingly, the 0.14 ps TA spectrum shows three ESA bands centered at  $\sim 385$  nm,  $\sim 450$  nm, and  $\sim 570$  nm among which the  $\sim 450$  nm ESA band disappears afterwards while the others develop. The line shapes of the TA spectra up to 300 ps probe delay then resemble those from the  $[\text{Ir}(\text{ppy})_2(\text{bpy})]^+$  (Fig. 4.2), confirming that the lowest  $^3\text{MLCT}$  state lies on the diimine ligand. The  $\sim 450$  nm ESA band in the early stage is thus attributed to the ESA of the  $\pi^*(\text{ppy})$  orbital, and the corresponding  $\sim 0.4$  ps time constant is assigned to the ILCT process ( $\pi^*(\text{ppy}) \rightarrow \pi^*(\text{bpy})$ , [190]). The DAS of the  $\sim 30$  ps time constant has a quite similar line shape to that of the  $\sim 9$  ps time constant from the **Ir-O** (Fig. 4.5), so this dynamics corresponds to the vibrational cooling in the  $^3\text{MLCT}$  state on the diimine ligand. The  $\sim 385$  nm and  $\sim 570$  nm ESA bands are however also present in the 0.14 ps TA spectrum, unveiling the ultrafast incoherent electron hopping process among three ligands followed by the excited electron localization onto the diimine ligand within the first picosecond. Otherwise neither GSB nor SE signals were identified from the TA spectra.

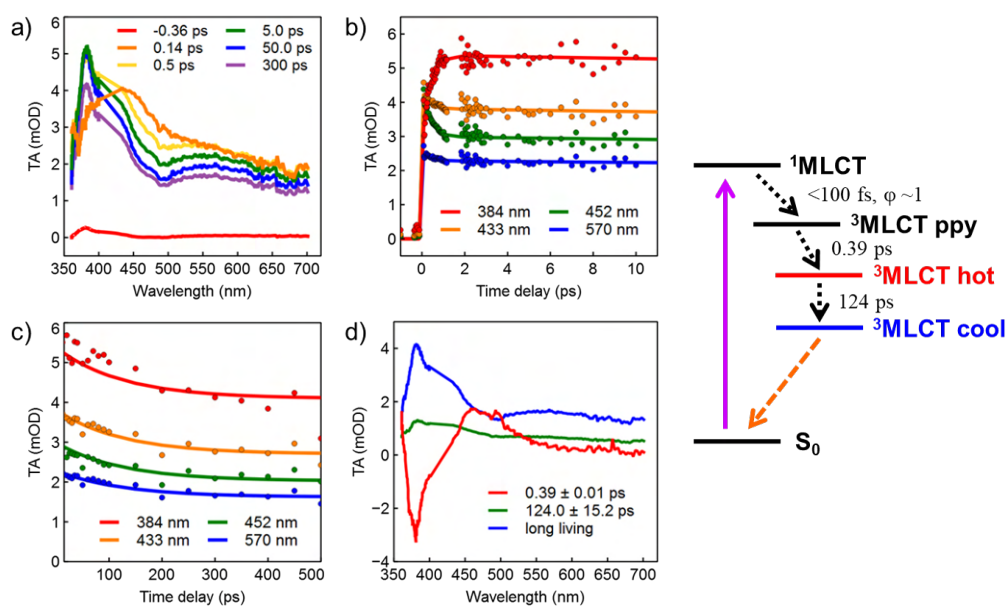


**Figure D.5:** a) TA spectra of **Ir-L-Co** at certain probe delays after the 425 nm photoexcitation measured at magic angle of the probe pulse polarization with respect to the pump pulse, b) transient signal kinetics at different probe wavelengths (dot) together with the SVD-GF results (solid line) up to 10 ps, c) up to 500 ps, and d) the corresponding DASs with three time constants considered. The  $\sim 0.4$  ps time constant represents the ILCT from  $\pi^*(ppy)$  to  $\pi^*(bpy)$ , and the  $\sim 124$  ps time constant represents the vibrational cooling in the  $^3MLCT$  state.

Figure D.5 summarizes the results of the SVD-GF analysis on the reduced TOAS data from the **Ir-L-Co**. Similar to the **Ir-L**, the  $\sim 450$  nm ESA band in the early stage corresponds to the ESA of the  $\pi^*(ppy)$  orbital and the  $\sim 0.4$  ps time constant is again assigned to the ILCT process ( $\pi^*(ppy) \rightarrow \pi^*(bpy)$ ). The following dynamics retains its TA spectrum from 0.5 ps to 300 ps with a slight decrease in intensity, hence this is attributed to the vibrational cooling in the  $^3MLCT$  state on the diimine ligand. In contrast to the **Ir-O-Co** and **Ir-th-Co**, there is no significant decrease of the excited electron density within the picosecond time window, namely there is no clue on the electron transfer to the cobaloxime(III) in **Ir-L-Co**. This is however in line with the same performance of both dyadic and two-component system in photocatalytic proton reduction [143].

The polarization anisotropy TOAS measurements were carried out on both **Ir-L** and **Ir-L-Co** to further study the charge transfer nature involving a change of the transient dipole moment in the system (Fig. D.6). The first DAS (red) in all configurations corresponds to the ultrafast incoherent electron hopping process among three ligands and therefore is less dependent on the relative polarization. The second DAS (green) however, that shows negative signals in parallel but positive signals in perpendicular

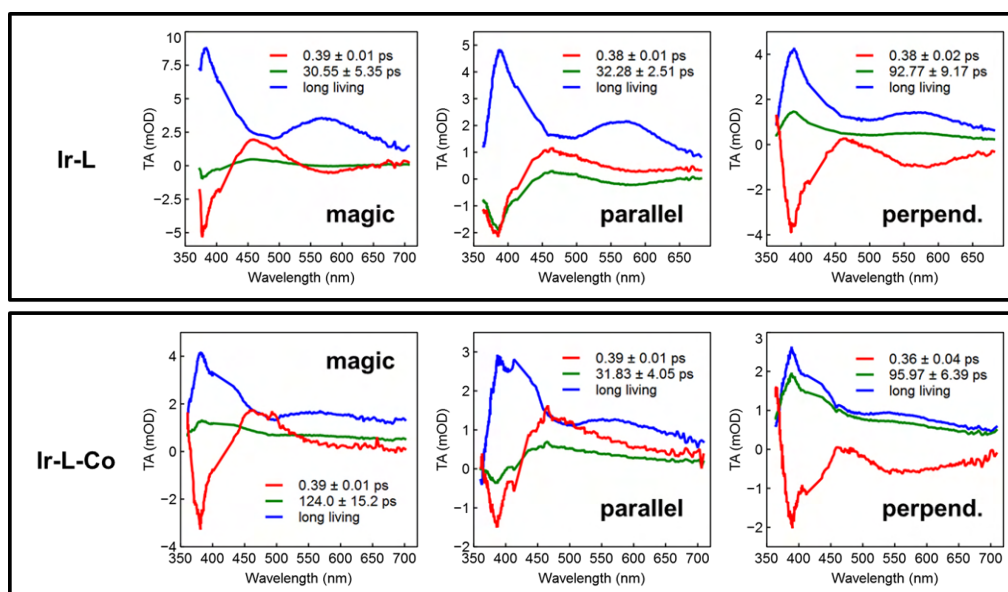


**Figure D.6:** The DASs of Ir-L (above) and Ir-L-Co (below) upon photoexcitation at 425 nm with magic angle, parallel, and perpendicular polarization of the probe pulse to the pump pulse.

polarization, corresponds to the vibrational cooling in the  $^3\text{MLCT}$  state on the diimine ligand. Since the transient dipole moment is now aligned to the diimine ligand, the parallel probe pulse can add more electron density into the  $\pi^*$  orbital while the perpendicular probe pulse can reduce the electron density by inducing an ILCT.

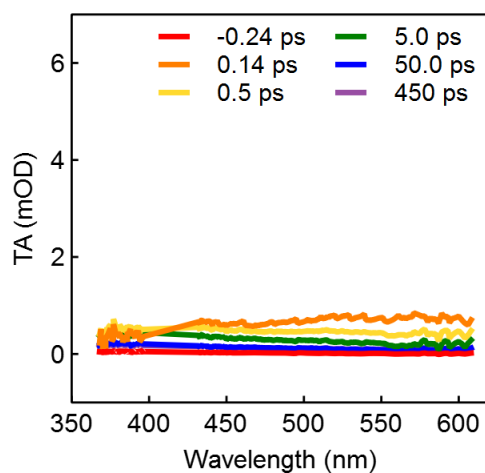


**Figure D.7:** TA spectra of the cobaloxime(III) at certain probe delays after the 425 nm photoexcitation measured at magic angle of the probe pulse polarization to the pump pulse.

The same TOAS experiment was also conducted on the cobaloxime(III) (Fig. D.7), and its TA spectra showed negligible signals in optical probe window [87], so that the ESA bands from the cobaloxime(III) are ignored in this thesis.

## D.2 Chapter 5

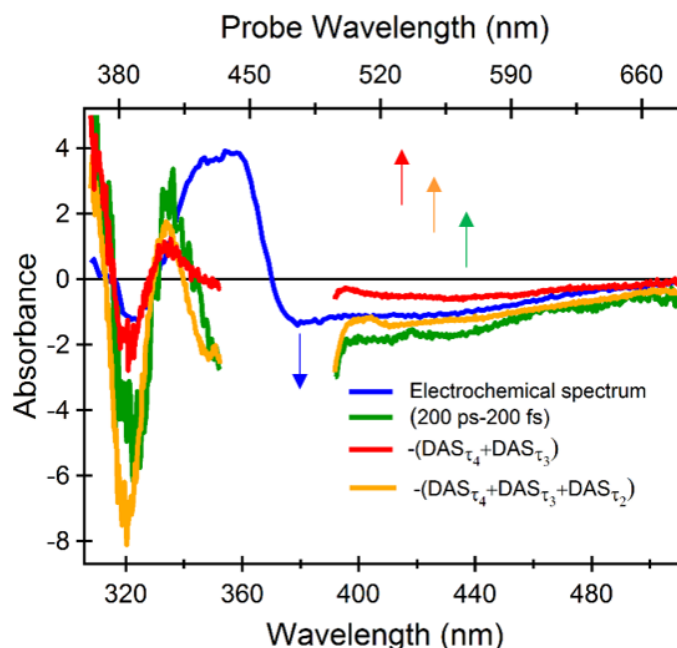


**Figure D.8:** Comparison of the difference spectrum from the spectroelectrochemical oxidation of the catalytic Mo(VI) complex  $[\text{MoO}_2(\text{L}^{\text{Me}})\text{MeOH}]$  (blue) with the (200 ps-200 fs) DTA spectrum (green) and the inverse sum of the  $\text{DAS}_{6.8\text{ps}}$  and  $\text{DAS}_{42\text{ps}}$  (red) as well as the inverse sum of the  $\text{DAS}_{2\text{ps}}$ ,  $\text{DAS}_{6.8\text{ps}}$ , and  $\text{DAS}_{42\text{ps}}$  (yellow) upon 450 nm photoexcitation [50]. A relative shift of 0.65 eV was applied in the energy domain.

To further prove that the spectral evolution on the picosecond timescale stems from the Mo(VI) moiety, we performed the same TOAS measurements and SVD-GF analysis with the 450 nm photoexcitation (Fig. D.8). The results consistently reproduced the spectral features from the oxidation dynamics of the Mo(VI)-coordinated chromophoric ligand spanning from 2 to 60 ps (Fig. 5.5). Thus, we confirmed that the catalytic Mo(VI) moiety was not directly photoexcited during the TOAS experiments but indirectly photo-activated due primarily to the spontaneous perturbation by the transient dipole moment in the Ru(II) moiety.

## D.3 Chapter 6

Figure D.9 shows the normalized XANES spectra of the Ru(II) photosensitizers in their GS and  $^3\text{MLCT}$  state at 150 ps probe delay. In general, the GS XANES features are simply shifted by  $\sim 2$  eV in the ES as also noticed in the EXAFS sanity check (Fig. 6.6), although a tiny pre-edge structure has appeared additionally.

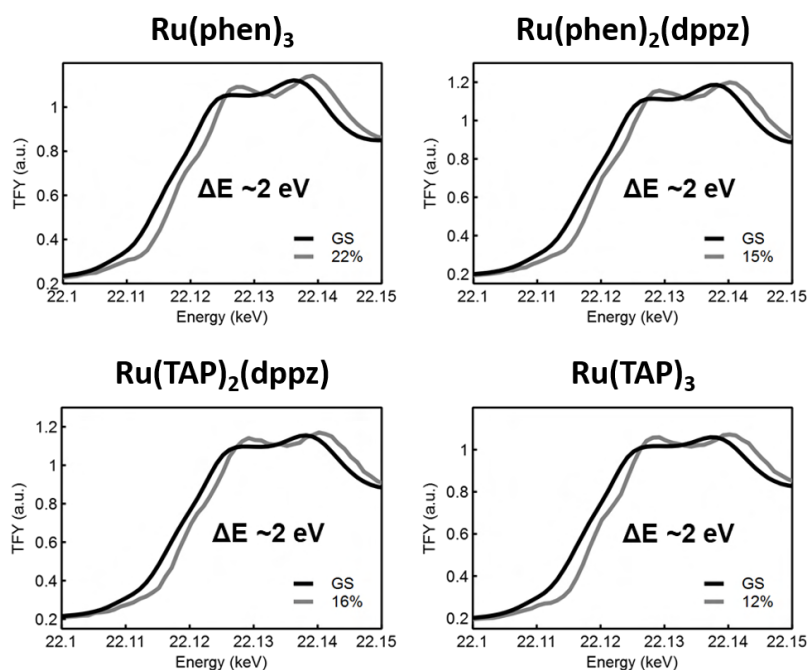


**Figure D.9:** XANES spectra of the Ru(II) photosensitizers in their GS and  $^3\text{MLCT}$  state at the probe delay of 150 ps.

Figure D.10 shows the fitting results of the ES  $\chi(k)$  spectra weighted by  $k^2$  with the EXAFS equation (2.4) using FEFF8 and IFEFFIT codes. The fitting was successfully performed in Fourier transform  $R$ -space  $|\chi(R)|$ , and the fitted parameters are summarized in Table 6.2.

By having two independent fitting parameters for the  $R(\text{Ru-N}_{\text{MLCT}})$  and  $R(\text{Ru-N})$ , we were able to visualize the picometer-scale changes in the first coordination shell structure, that were most pronounced in  $[\text{Ru}(\text{phen})_3]^{2+}$  and least in  $[\text{Ru}(\text{TAP})_2(\text{dppz})]^{2+}$ . However as we noticed from Fig. 6.5 and 6.6, there is hardly a difference in the geometric structure between the Ru(II) photosensitizers nor between the GS and  $^3\text{MLCT}$  state at 150 ps probe delay. In other words, with the degassed acetonitrile as solvent the localized excited electron on the dppz-ligand, TAP-ligand, or even in the  $^3\text{MC}$  state did not result in any distinct signals.

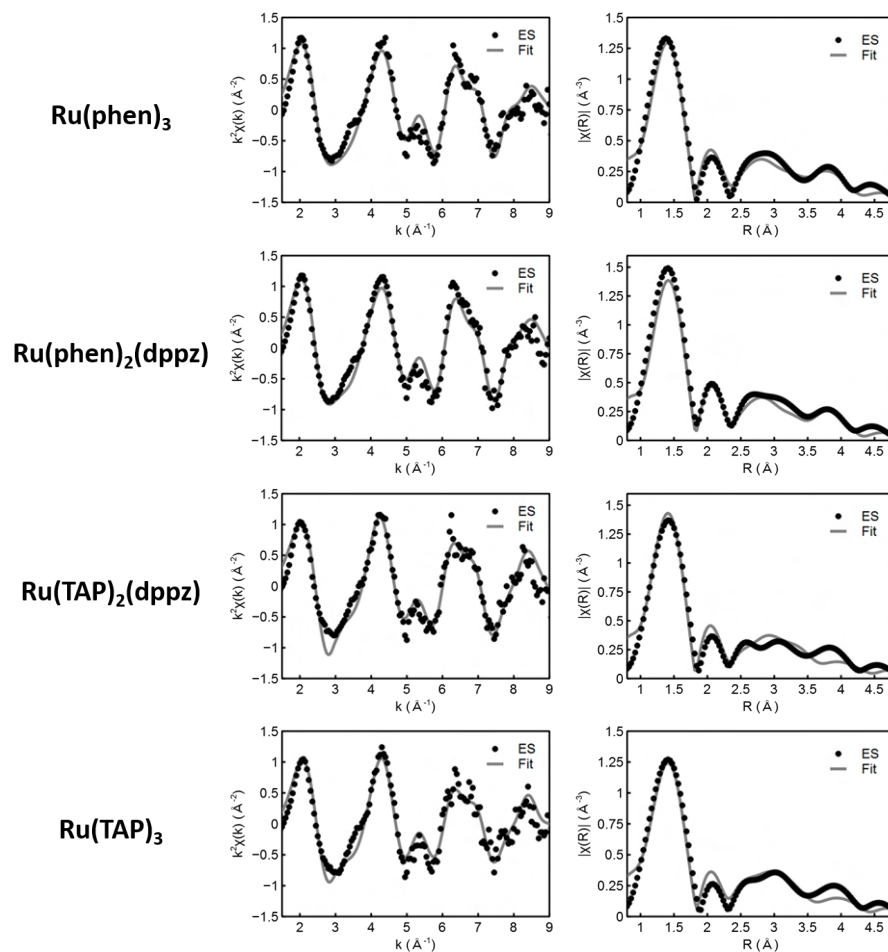


**Figure D.10:** Fitting analysis of the ES  $\chi(k)$  spectra of the Ru(II) photosensitizers weighted by  $k^2$  with the EXAFS equation (2.4). The fitting was performed in Fourier transform  $R$ -space  $|\chi(R)|$ .

The  $|\chi(R)|$  spectra in Fourier transform  $R$ -space show the first peak of the corresponding pseudo-radial distribution function (PDF) at around 1.5 Å that is shorter than the actual value of 2.06 Å. According to [181], such a shift ( $\sim 0.3$  to  $\sim 0.5$  Å) to a shorter value can be due to the core-hole lifetime-broadening which attenuates the amplitude of high- $R$  side peaks more than the low- $R$  side ones.

## D.4 Chapter 7

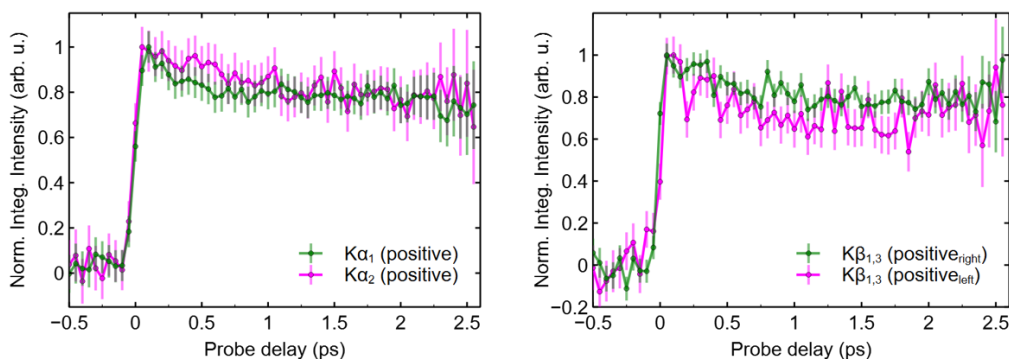


**Figure D.11:** (left) Comparison of the kinetics extracted from the positive transient signals of  $K\alpha_1$  (green) and  $K\alpha_2$  (pink). (right) Comparison of the kinetics extracted from the positive transient signals of  $K\beta_{1,3}$  at higher fluorescence energy (green) and at lower fluorescence energy (pink). The error bars were calculated in propagated standard error.

To further verify that there was no difference between the kinetics obtained from the positive transient signals of  $K\alpha_1$  and  $K\alpha_2$  as well as the left and right positive parts of the  $K\beta_{1,3}$  transient signals, we compared them together in Fig. D.11. Within the error range there was no significant difference, thus we integrated all the positive transient signals, to increase the SNR for the fitting analysis in the main text.

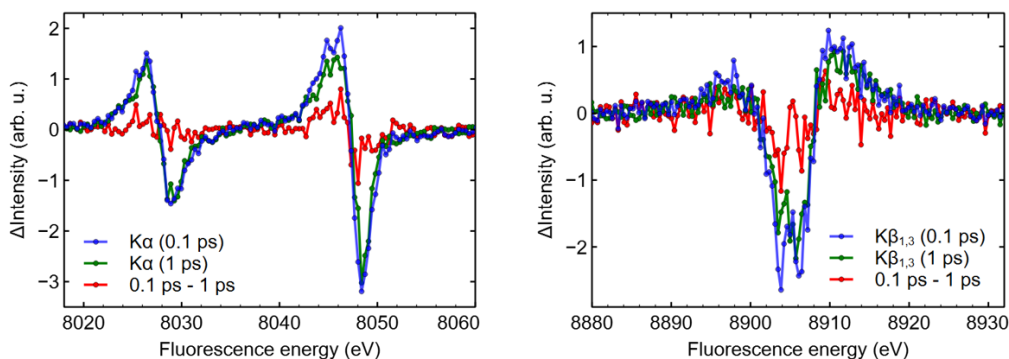


**Figure D.12:** Comparison of the transient signals of the Cu  $K\alpha$  (left) and  $K\beta_{1,3}$  (right) fluorescence at the probe delay of 0.1 ps and 1 ps.

The reduced data of the Cu  $K\alpha$  and  $K\beta_{1,3}$  fluorescence signals consistently revealed the femtosecond nuclear dynamics with a decay time constant of  $\sim 410$  fs. This very clear change in the kinetics originates from the overall intensity decrease of the transient signals (Fig. D.12). In other words, there is no significant change in the line shapes of the transient signals during the PJT distortion.

In addition to the main analysis, we also performed the SVD-GF analysis on the

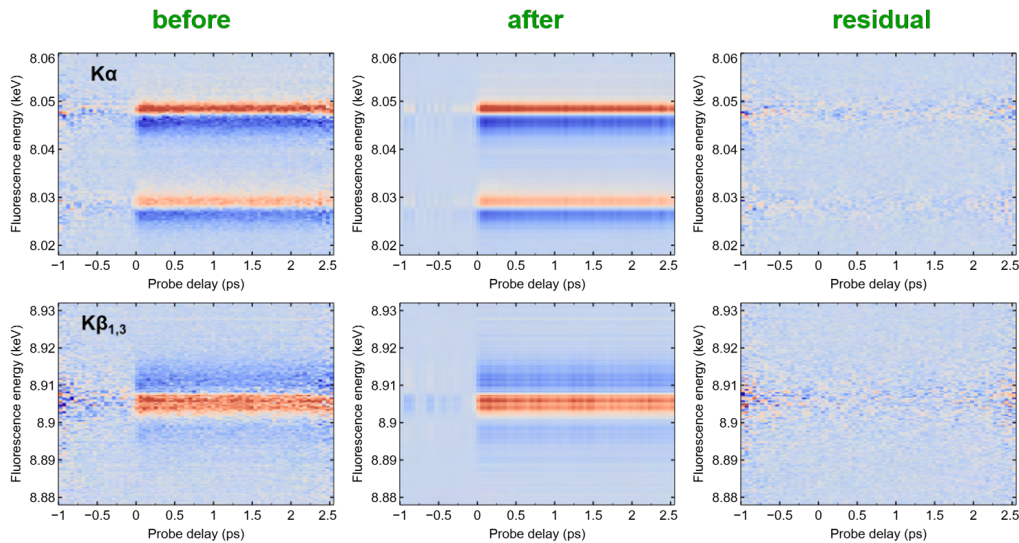


**Figure D.13:** 2-D plots of the Cu  $K\alpha$  and  $K\beta_{1,3}$  fluorescence signals with respect to the probe delay before (left) and after (middle) the SVD analysis and their difference (right). Only the first singular value was taken into account to exclude any other background noises, and the reconstructed data successfully resembled the original one.

reduced data of the Cu  $K\alpha$  and  $K\beta_{1,3}$  fluorescence signals to further exclude any irrelevant noises (Fig. D.13). The first singular value and the corresponding DAS as well as the singular vector of kinetics were already enough to reconstruct the data without missing any important signal. The first singular vectors of kinetics from the  $K\alpha$  and  $K\beta_{1,3}$  data were then fitted with the sequential first-order rate equation (7.8), and the fitting analysis returned a decay time constant of  $\sim 400$  fs consistently (Fig. D.14).

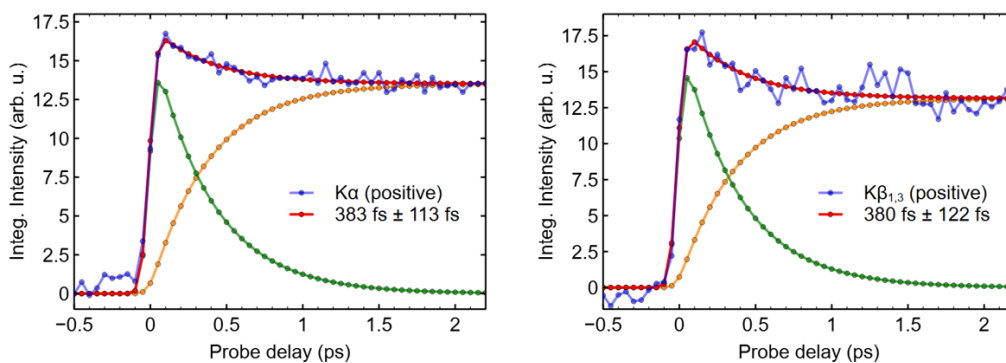


**Figure D.14:** The first singular vectors of kinetics from the SVD analysis on the  $K\alpha$  (left) and  $K\beta_{1,3}$  (right) data as well as the fitting results with the sequential first-order rate equation (7.8) consisting of the  $[\text{MLCT}_{\text{hot}, 90^\circ}](t)$  (green) and  $[\text{MLCT}_{\text{hot}, 70^\circ}](t)$  (orange), revealing a decay time constant of  $\sim 400$  fs ( $1/k_2$ ) consistently.

## D.5 Chapter 8

Prior to the femtosecond-resolved XES experiments at SACLA, the Co  $K\beta_{1,3}$  emission spectrum of the cobaloxime(III) in solution phase was measured at the P01 beamline in the PETRA III storage ring (Fig. D.15) and disclosed that the spin density is in LS.

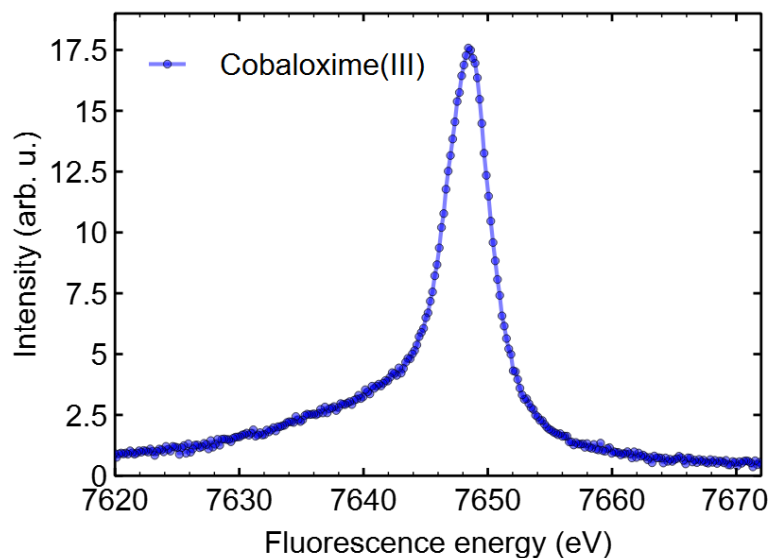


**Figure D.15:** Co  $K\beta_{1,3}$  emission spectrum of the cobaloxime(III) in solution phase measured at the P01 beamline. The spin density in the GS is LS.

To further verify that there was no difference between the kinetics obtained from the different parts of the Fe  $K\alpha_1$  and  $K\beta_{1,3}$  transient signals from the [Fe-BL] upon 515 nm photoexcitation, we compared them together in Fig. D.16. Within the error range there was no critical difference in between integrating the negative transient signals and positive transient signals. The kinetics below the time-zero show abnormal behaviours compared to Fig. 8.6, and this comes from the lack of shot numbers, i.e. the low SNR. The kinetics obtained by integrating the transient signals at  $7054 \pm 1$  eV of the fluorescence energy can be an evidence of the  $^3MC$  state appearing right after the 515 nm photoexcitation.

As noted in the main text, a comparison of the Fe  $K\beta_{1,3}$  transient line shapes from the [Fe-BL] and the model complex in [117] upon the MLCT photoexcitation is essential to understand the slightly different interpretation between them. Figure D.17 shows the Fe  $K\beta_{1,3}$  transient line shapes from the [Fe-BL], [117], and [204] at the probe delay of 0.1 ps and 10 ps. Both line shapes from the [Fe-BL] and [117] at 0.1 ps probe delay and 10 ps probe delay do not show any difference, and from the reference line shapes it is not clear in which state the complex resides. Nevertheless, it is certain that both

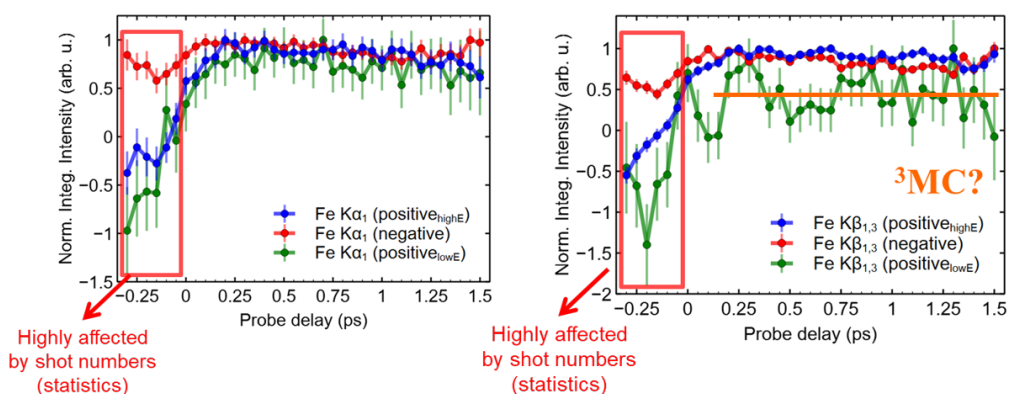


**Figure D.16:** Comparison of the kinetics extracted from the positive transient signals (blue, green) and negative transient signals (red) of the Fe  $K\alpha_1$  (left) and  $K\beta_{1,3}$  (right) fluorescence from the [Fe-BL] upon 515 nm photoexcitation. Owing to the lack of shot numbers, the kinetics below the time-zero behave abnormally. The error bars were calculated in propagated standard error.

the [Fe-BL] and the model complex in [117] disclosed the same transient line shapes at 0.1 ps and 10 ps probe delay, i.e. the same ESs populated and hence the same relaxation dynamics.

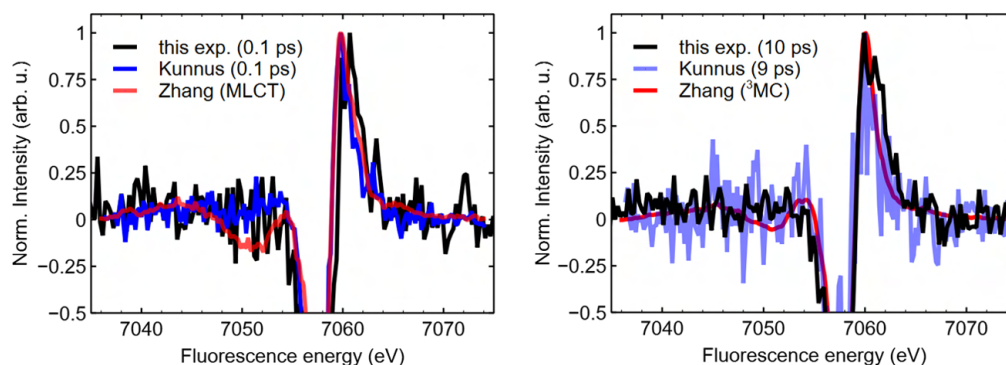


**Figure D.17:** Comparison of the Fe  $K\beta_{1,3}$  transient line shapes from the [Fe-BL], [117], and [204] at the probe delay of 0.1 ps and 10 ps.

Figure D.18 shows the preliminary analysis of the XSS data from the [Fe-BL-Co] measured at certain probe delays simultaneously with the XES, and the high-frequency component for the first picosecond indicates relatively long-distance nuclear dynamics, which is in line with the femtosecond coupling between the Fe(II) and Co(III) moiety.

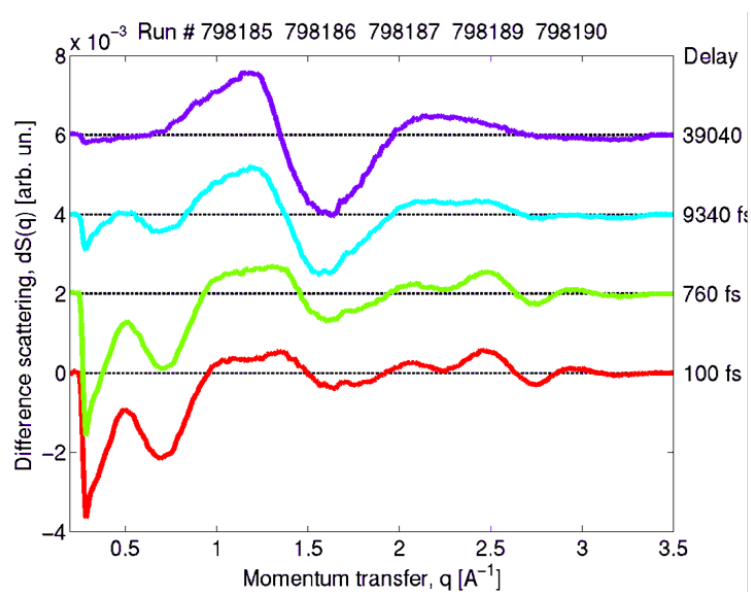


**Figure D.18:** Transient XSS signals from the [Fe-BL-Co] at selected probe delays after the 515 nm photoexcitation. The high-frequency component for the first picosecond indicates relatively long-distance nuclear dynamics, which is in line with the femtosecond coupling between the Fe(II) and Co(III) moiety.

## E List of hazardous substances

This chapter lists the hazardous substances that were handled in the experiments for this thesis. Their precautionary (P) and hazard (H) statements are listed together with the corresponding globally harmonized system of classification and labelling of chemicals (GHS) pictograms.

Substance	CAS Nr.	H-statement(s)	P-statement(s)	Pictogram(s)
Acetonitrile	75-05-8	225, 302, 312, 332, 319	210, 280, 301, 312, 303, 361, 353, 304, 340, 312, 305, 351, 338	
Bis(2-phenylpyridine) (dtbbpy) iridium(III) hexafluorophosphate*	676525-77-2	N/A	N/A	N/A
Chloro(pyridine) cobaloxime(III)	23295-32-1	315, 319, 335	261, 305, 351, 338	
Tris(2,2-bipyridine) ruthenium(II) hexafluorophosphate	60804-74-2	N/A	N/A	N/A
Bis(2,2-bipyridine) (5-aminophenanthroline) ruthenium(II) hexafluorophosphate	84537-86-0	N/A	N/A	N/A
Tris(1,10-phenanthroline) ruthenium(II) chloride*	23570-43-6	N/A	N/A	N/A
(1,10-phenanthroline) copper(II) chloride*	14783-09-6	315, 319	302, 352, 305, 351, 338	

**Table E.1:** List of the hazardous substances used in the experiments for this thesis. \* denotes the closest compound to those newly synthesized and consumed. All the statements refer to the respective safety data sheets from Sigma-Aldrich.

## F Bibliography

- [1] B. Abraham et al.: “A high-throughput energy-dispersive tender X-ray spectrometer for shot-to-shot sulfur measurements”, *Journal of synchrotron radiation* **26**, 629–634 (2019)
- [2] R. Alonso-Mori et al.: “A multi-crystal wavelength dispersive x-ray spectrometer”, *Review of Scientific Instruments* **83**, 073114 (2012)
- [3] J. Als-Nielsen, D. McMorrow: *Elements of modern X-ray physics* (John Wiley & Sons 2011)
- [4] D. Ambrosek et al.: “A theoretical study of Ru (II) polypyridyl DNA intercalators: structure and electronic absorption spectroscopy of [Ru (phen) 2 (dppz)] 2+ and [Ru (tap) 2 (dppz)] 2+ complexes intercalated in guanine–cytosine base pairs”, *Journal of inorganic biochemistry* **104**, 893–901 (2010)
- [5] R. A. Angnes et al.: “Recent synthetic additions to the visible light photoredox catalysis toolbox”, *Organic & biomolecular chemistry* **13**, 9152–9167 (2015)
- [6] A. L. Ankudinov, B. Ravel, J. Rehr, et al.: “Real-space multiple-scattering calculation and interpretation of x-ray-absorption near-edge structure”, *Physical Review B* **58**, 7565 (1998)
- [7] D. M. Arias-Rotondo, J. K. McCusker: “The photophysics of photoredox catalysis: a roadmap for catalyst design”, *Chemical Society Reviews* **45**, 5803–5820 (2016)
- [8] V. Artero, M. Chavarot-Kerlidou, M. Fontecave: “Splitting water with cobalt”, *Angewandte Chemie International Edition* **50**, 7238–7266 (2011)
- [9] G. Auböck, M. Chergui: “Sub-50-fs photoinduced spin crossover in [Fe (bpy) 3] 2+”, *Nature chemistry* **7**, 629–633 (2015)
- [10] G. Auböck, C. Consani, R. Monni, et al.: “Femtosecond pump/supercontinuum-probe setup with 20 kHz repetition rate”, *Review of Scientific Instruments* **83**, 093105 (2012)
- [11] A. Authier: “Dynamical theory of X-ray diffraction”, *International Tables for Crystallography*, 626–646 (2006)
- [12] P. Basu, A. M. Raitsimring, M. J. LaBarre, et al.: “Covalently linked oxomolybdenum (V) and iron (III) porphyrin centers: Synthetic models for the molybdenum-iron interaction in sulfite oxidase”, *Journal of the American Chemical Society* **116**, 7166–7176 (1994)
- [13] E. Biasin, T. B. van Driel, K. S. Kjær, et al.: “Femtosecond x-ray scattering study of ultrafast photoinduced structural dynamics in solvated [Co (terpy) 2] 2+”, *Physical review letters* **117**, 013002 (2016)

- [14] S. I. Bokarev, O. S. Bokareva, O. Kühn: “Electronic excitation spectrum of the photosensitizer [Ir (ppy) 2 (bpy)]<sup>+</sup>”, *The Journal of chemical physics* **136**, 214305 (2012)
- [15] O. S. Bokareva, T. Möhle, A. Neubauer, et al.: “Chemical tuning and absorption properties of iridium photosensitizers for photocatalytic applications”, *Inorganics* **5**, 23 (2017)
- [16] E. Borfecchia, C. Garino, L. Salassa, et al.: “X-ray transient absorption structural characterization of the 3 MLCT triplet excited state of cis-[Ru (bpy) 2 (py) 2] 2<sup>+</sup>”, *Dalton transactions* **42**, 6564–6571 (2013)
- [17] C. Bressler, M. Chergui: “Ultrafast X-ray absorption spectroscopy”, *Chemical reviews* **104**, 1781–1812 (2004)
- [18] F. Brinker et al.: “Commissioning of the European XFEL injector”, *proceedings of IPAC* (2016)
- [19] A. Britz: “Ultrafast X-ray Spectroscopies of Transition Metal Complexes Relevant for Catalysis”, PhD thesis (Universität Hamburg 2017)
- [20] M. I. Bruce: “Cyclometalation reactions”, *Angewandte Chemie International Edition in English* **16**, 73–86 (1977)
- [21] F. Calegari, G. Sansone, S. Stagira, et al.: “Advances in attosecond science”, *Journal of Physics B: Atomic, Molecular and Optical Physics* **49**, 062001 (2016)
- [22] J. M. Camara, T. B. Rauchfuss: “Combining acid–base, redox and substrate binding functionalities to give a complete model for the [FeFe]-hydrogenase”, *Nature chemistry* **4**, 26–30 (2012)
- [23] A. Cannizzo, A. M. Blanco-Rodríguez, A. El Nahhas, et al.: “Femtosecond fluorescence and intersystem crossing in rhenium (I) carbonyl- bipyridine complexes”, *Journal of the American Chemical Society* **130**, 8967–8974 (2008)
- [24] A. Cannizzo, C. Milne, C. Consani, et al.: “Light-induced spin crossover in Fe (II)-based complexes: The full photocycle unraveled by ultrafast optical and X-ray spectroscopies”, *Coordination Chemistry Reviews* **254**, 2677–2686 (2010)
- [25] A. Cannizzo, F. van Mourik, W. Gawelda, et al.: “Broadband femtosecond fluorescence spectroscopy of [Ru (bpy) 3] 2<sup>+</sup>”, *Angewandte Chemie* **118**, 3246–3248 (2006)
- [26] S. E. Canton, K. S. Kjær, G. Vankó, et al.: “Visualizing the non-equilibrium dynamics of photoinduced intramolecular electron transfer with femtosecond X-ray pulses”, *Nature communications* **6**, 1–10 (2015)
- [27] G. Capano, C. Milne, M. Chergui, et al.: “Probing wavepacket dynamics using ultrafast x-ray spectroscopy”, *Journal of Physics B: Atomic, Molecular and Optical Physics* **48**, 214001 (2015)

- [28] G. Capano, T. Penfold, M. Chergui, et al.: “Photophysics of a copper phenanthroline elucidated by trajectory and wavepacket-based quantum dynamics: a synergetic approach”, *Physical Chemistry Chemical Physics* **19**, 19590–19600 (2017)
- [29] G. Capano, M. Chergui, U. Rothlisberger, et al.: “A quantum dynamics study of the ultrafast relaxation in a prototypical Cu (i)–phenanthroline”, *The Journal of Physical Chemistry A* **118**, 9861–9869 (2014)
- [30] C. J. Cardin, J. M. Kelly, S. J. Quinn: “Photochemically active DNA-intercalating ruthenium and related complexes—insights by combining crystallography and transient spectroscopy”, *Chemical science* **8**, 4705–4723 (2017)
- [31] G. Cerullo, S. De Silvestri: “Ultrafast optical parametric amplifiers”, *Review of scientific instruments* **74**, 1–18 (2003)
- [32] P. Chábera, K. S. Kjaer, O. Prakash, et al.: “Fell hexa N-heterocyclic carbene complex with a 528 ps metal-to-ligand charge-transfer excited-state lifetime”, *The journal of physical chemistry letters* **9**, 459–463 (2018)
- [33] P. Chábera, Y. Liu, O. Prakash, et al.: “A low-spin Fe (III) complex with 100-ps ligand-to-metal charge transfer photoluminescence”, *Nature* **543**, 695–699 (2017)
- [34] L. X. Chen, G. B. Shaw, I. Novozhilova, et al.: “MLCT state structure and dynamics of a copper (I) diimine complex characterized by pump-probe X-ray and laser spectroscopies and DFT calculations”, *Journal of the American Chemical Society* **125**, 7022–7034 (2003)
- [35] L. X. Chen, X. Zhang: “Photochemical processes revealed by X-ray transient absorption spectroscopy”, *The Journal of Physical Chemistry Letters* **4**, 4000–4013 (2013)
- [36] M. Chergui: “1.19 Ultrafast Structural Dynamics of Biological Systems” (2012)
- [37] T.-K. Choi, D. Khakhulin, G. Vankó, et al.: “Femtosecond Molecular Flattening in [Cu (dmp) 2]+ Probed by X-ray Emission Spectroscopy and Solution Scattering”, *International Conference on Ultrafast Phenomena, Optical Society of America*, Th1A–5 (2020)
- [38] C. G. Coates, P. Callaghan, J. J. McGarvey, et al.: “Spectroscopic studies of structurally similar DNA-binding ruthenium (II) complexes containing the dipyrrophenazine ligand”, *Journal of Molecular Structure* **598**, 15–25 (2001)
- [39] C. G. Coates, J. Olofsson, M. Coletti, et al.: “Picosecond time-resolved resonance Raman probing of the light-switch states of [Ru (Phen) 2dppz] 2+”, *The Journal of Physical Chemistry B* **105**, 12653–12664 (2001)
- [40] P. B. Corkum, F. Krausz: “Attosecond science”, *Nature physics* **3**, 381–387 (2007)
- [41] C. G. Darwin: “XXXIV. The theory of X-ray reflexion”, *The London, Edinburgh, and Dublin Philosophical Magazine and Journal of Science* **27**, 315–333 (1914)

- [42] S. DeBeer, U. Bergmann: "X-Ray Emission Spectroscopic Techniques in Bioinorganic Applications", *Encyclopedia of Inorganic and Bioinorganic Chemistry*, 1–14 (2011)
- [43] M. U. Delgado-Jaime, B. R. Dible, K. P. Chiang, et al.: "Identification of a single light atom within a multinuclear metal cluster using valence-to-core X-ray emission spectroscopy", *Inorganic chemistry* **50**, 10709–10717 (2011)
- [44] J. L. Dempsey, J. R. Winkler, H. B. Gray: "Proton-coupled electron flow in protein redox machines", *Chemical reviews* **110**, 7024–7039 (2010)
- [45] M. Deutsch, G. Hölzer, J. Härtwig, et al.: " $K\alpha$  and  $K\beta$  x-ray emission spectra of copper", *Physical Review A* **51**, 283 (1995)
- [46] M. Diez, A. Galler, S. Schulz, et al.: "A self-referenced in-situ arrival time monitor for X-ray free-electron lasers", *Scientific reports* **11**, 1–11 (2021)
- [47] P. Dongare, B. D. Myron, L. Wang, et al.: "[Ru (bpy)  $3$ ]  $2+$  revisited. Is it localized or delocalized? How does it decay?", *Coordination Chemistry Reviews* **345**, 86–107 (2017)
- [48] C. Dragonetti, S. Righetto, D. Roberto, et al.: "Cyclometallated iridium (III) complexes with substituted 1, 10-phenanthrolines: a new class of highly active organometallic second order NLO-phores with excellent transparency with respect to second harmonic emission", *Chemical communications*, 4116–4118 (2007)
- [49] L. Du, Z. Lan: "Ultrafast structural flattening motion in photoinduced excited state dynamics of a bis (diimine) copper (I) complex", *Physical Chemistry Chemical Physics* **18**, 7641–7650 (2016)
- [50] A. B. Ducrot, B. A. Coulson, R. N. Perutz, et al.: "Light-Induced Activation of a Molybdenum Oxotransferase Model within a Ru (II)–Mo (VI) Dyad", *Inorganic chemistry* **55**, 12583–12594 (2016)
- [51] A. Ducrot, B. Scattergood, B. Coulson, et al.: "Electronic Fine-Tuning of Oxygen Atom Transfer Reactivity of cis-Dioxomolybdenum (VI) Complexes with Thiosemicarbazone Ligands", *European Journal of Inorganic Chemistry* **2015**, 3562–3571 (2015)
- [52] B. Elias, C. Creely, G. W. Doorley, et al.: "Photooxidation of guanine by a ruthenium dipyrrophenazine complex intercalated in a double-stranded polynucleotide monitored directly by picosecond visible and infrared transient absorption spectroscopy", *Chemistry—A European Journal* **14**, 369–375 (2008)
- [53] P. Emma, R. Akre, J. Arthur, et al.: "First lasing and operation of an ångstrom-wavelength free-electron laser", *nature photonics* **4**, 641–647 (2010)
- [54] H. Enkisch: "Bloch k-selective resonant inelastic scattering of hard X-rays from valence electrons of 3d-metals", PhD thesis (Universität Dortmund 2002)
- [55] E. Erdmann, M. Lütgens, S. Lochbrunner, et al.: "Ultrafast Energy Transfer in Dinuclear Complexes with Bridging 1, 10-Phenanthroline-5, 6-Dithiolate", *Inorganic chemistry* **57**, 4849–4863 (2018)

- [56] F. Ericson, A. Honarfar, O. Prakash, et al.: “Electronic structure and excited state properties of iron carbene photosensitizers—A combined X-ray absorption and quantum chemical investigation”, *Chemical Physics Letters* **683**, 559–566 (2017)
- [57] M. M. Feeney, J. M. Kelly, A. B. Tossi, et al.: “Photoaddition of ruthenium (II)-tris-1, 4, 5, 8-tetraazaphenanthrene to DNA and mononucleotides”, *Journal of Photochemistry and Photobiology B: Biology* **23**, 69–78 (1994)
- [58] A. Fihri, V. Artero, A. Pereira, et al.: “Efficient H<sub>2</sub>-producing photocatalytic systems based on cyclometalated iridium- and tricarbonylrhenium-diimine photosensitizers and cobaloxime catalysts”, *Dalton transactions*, 5567–5569 (2008)
- [59] D. W. Fink, W. E. Ohnesorge: “Temperature effects on charge-transfer luminescence intensity of some transition metal ion chelates”, *Journal of the American Chemical Society* **91**, 4995–4998 (1969)
- [60] L. Flamigni, A. Barbieri, C. Sabatini, et al.: “Photochemistry and photophysics of coordination compounds: iridium”, *Photochemistry and Photophysics of Coordination Compounds II*, 143–203 (2007)
- [61] S. Flesch, L. I. Domenianni, P. Vöhringer: “Probing the primary processes of a triazido–cobalt (III) complex with femtosecond vibrational and electronic spectroscopies. Photochemical selectivity and multi-state reactivity”, *Physical Chemistry Chemical Physics* **22**, 25618–25630 (2020)
- [62] L. A. Fredin, M. Pápai, E. Rozsályi, et al.: “Exceptional excited-state lifetime of an iron (II)–N-heterocyclic carbene complex explained”, *The journal of physical chemistry letters* **5**, 2066–2071 (2014)
- [63] A. Galler, W. Gawelda, M. Biednov, et al.: “Scientific instrument Femtosecond X-ray Experiments (FXE): instrumentation and baseline experimental capabilities”, *Journal of synchrotron radiation* **26**, 1432–1447 (2019)
- [64] L. Gallmann, C. Cirelli, U. Keller: “Attosecond science: recent highlights and future trends”, *Annual review of physical chemistry* **63**, 447–469 (2012)
- [65] S. Garakyaraghi, E. O. Danilov, C. E. McCusker, et al.: “Transient absorption dynamics of sterically congested Cu (I) MLCT excited states”, *The Journal of Physical Chemistry A* **119**, 3181–3193 (2015)
- [66] S. Garakyaraghi, P. Koutnik, F. N. Castellano: “Photoinduced structural distortions and singlet–triplet intersystem crossing in Cu (I) MLCT excited states monitored by optically gated fluorescence spectroscopy”, *Physical Chemistry Chemical Physics* **19**, 16662–16668 (2017)
- [67] W. Gawelda, V.-T. Pham, R. Van der Veen, et al.: “Structural analysis of ultrafast extended x-ray absorption fine structure with subpicometer spatial resolution: Application to spin crossover complexes”, *The Journal of chemical physics* **130**, 124520 (2009)

- [68] W. Gawelda: "Time-resolved x-ray absorption spectroscopy of transition metal complexes", PhD thesis (EPFL 2006)
- [69] W. Gawelda, A. Cannizzo, V.-T. Pham, et al.: "Ultrafast nonadiabatic dynamics of [FeII (bpy) 3] 2+ in solution", *Journal of the American Chemical Society* **129**, 8199–8206 (2007)
- [70] W. Gawelda, M. Johnson, F. M. de Groot, et al.: "Electronic and molecular structure of photoexcited [RuII (bpy) 3] 2+ probed by picosecond X-ray absorption spectroscopy", *Journal of the American Chemical Society* **128**, 5001–5009 (2006)
- [71] S. Ghosh, G. Hogarth, N. Hollingsworth, et al.: "Hydrogenase biomimetics: Fe 2 (CO) 4 ( $\mu$ -dppf)( $\mu$ -pdt)(dppf= 1, 1-bis (diphenylphosphino) ferrocene) both a proton-reduction and hydrogen oxidation catalyst", *Chemical Communications* **50**, 945–947 (2014)
- [72] D. Gianolio, E. Borfecchia, C. Garino, et al.: "The Use of Differential EXAFS Analysis for the determination of Small Structural Differences between two closely-related Ruthenium Complexes", *Journal of Physics: Conference Series*, vol. 430, 1, IOP Publishing, 012125 (2013)
- [73] P. Glatzel, U. Bergmann, F. De Groot, et al.: "Multiple excitations in the K fluorescence emission of Mn, Fe and Ni compounds", *AIP Conference Proceedings*, vol. 652, 1, American Institute of Physics, 250–255 (2003)
- [74] P. Glatzel, U. Bergmann: "High resolution 1s core hole X-ray spectroscopy in 3d transition metal complexes—electronic and structural information", *Coordination chemistry reviews* **249**, 65–95 (2005)
- [75] M. Gu, A. Satija, R. P. Lucht: "Effects of self-phase modulation (SPM) on femtosecond coherent anti-Stokes Raman scattering spectroscopy", *Optics express* **27**, 33954–33966 (2019)
- [76] A. Harel, Y. Bromberg, P. G. Falkowski, et al.: "Evolutionary history of redox metal-binding domains across the tree of life", *Proceedings of the National Academy of Sciences* **111**, 7042–7047 (2014)
- [77] T. C. Harlang, Y. Liu, O. Gordivska, et al.: "Iron sensitizer converts light to electrons with 92% yield", *Nature chemistry* **7**, 883–889 (2015)
- [78] R. M. Hartshorn, J. K. Barton: "Novel dipyrrophenazine complexes of ruthenium (II): exploring luminescent reporters of DNA", *Journal of the American Chemical Society* **114**, 5919–5925 (1992)
- [79] J. Hawecker, J. Lehn, R. Ziessel: "Efficient homogeneous photochemical hydrogen generation and water reduction mediated by cobaloxime or macrocyclic cobalt complexes", *Nouv. J. Chim.:(France)* **7**, 271–277 (1983)
- [80] S. Hayakawa, A. Yamaguchi, W. Hong, et al.: "A wavelength dispersive X-ray spectrometer for small area X-ray fluorescence spectroscopy at SPring-8 BL39XU", *Spectrochimica Acta Part B: Atomic Spectroscopy* **54**, 171–177 (1999)

- [81] D. Haynes, M. Wurzer, A. Schletter, et al.: “Clocking Auger electrons”, *Nature Physics*, 1–7 (2021)
- [82] C. Herrero, A. Quaranta, W. Leibl, et al.: “Artificial photosynthetic systems. Using light and water to provide electrons and protons for the synthesis of a fuel”, *Energy & Environmental Science* **4**, 2353–2365 (2011)
- [83] R. Holm: “Metal-centered oxygen atom transfer reactions”, *Chemical Reviews* **87**, 1401–1449 (1987)
- [84] G. Hölzer, M. Fritsch, M. Deutsch, et al.: “K  $\alpha$  1, 2 and K  $\beta$  1, 3 x-ray emission lines of the 3 d transition metals”, *Physical Review A* **56**, 4554 (1997)
- [85] J. Hozzowska, J.-C. Dousse, J. Kern, et al.: “High-resolution von Hamos crystal X-ray spectrometer”, *Nuclear Instruments and Methods in Physics Research Section A: Accelerators, Spectrometers, Detectors and Associated Equipment* **376**, 129–138 (1996)
- [86] H. Huang, S. Banerjee, P. J. Sadler: “Recent advances in the design of targeted iridium (III) photosensitizers for photodynamic therapy”, *ChemBioChem* **19**, 1574–1589 (2018)
- [87] M. Huber-Gedert et al.: “Fundamental Characterization, Photophysics and Photocatalysis of a Base Metal Iron (II)-Cobalt (III) Dyad”, *Chemistry—A European Journal* **27**, 9905–9918 (2021)
- [88] A. A. Hummer, P. Heffeter, W. Berger, et al.: “X-ray absorption near edge structure spectroscopy to resolve the in vivo chemistry of the redox-active indazolium trans-[tetrachlorobis (1 H-indazole) ruthenate (III)](KP1019)”, *Journal of medicinal chemistry* **56**, 1182–1196 (2013)
- [89] W. Iali, P.-H. Lanoe, S. Torelli, et al.: “A Ruthenium (II)–Copper (II) Dyad for the Photocatalytic Oxygenation of Organic Substrates Mediated by Dioxygen Activation”, *Angewandte Chemie* **127**, 8535–8539 (2015)
- [90] K. Ichimura, T. Kobayashi, K. King, et al.: “Excited-state absorption spectroscopy of ortho-metalated iridium (III) complexes”, *Journal of Physical Chemistry* **91**, 6104–6106 (1987)
- [91] S. Iglesias, A. Gamonal, A. Abudulimu, et al.: “Tracking the Light-Induced Excited-State Dynamics and Structural Configurations of an Extraordinarily Long-Lived Metastable State at Room Temperature”, *Chemistry-A European Journal* **26**, 10801–10810 (2020)
- [92] T. Ishikawa, H. Aoyagi, T. Asaka, et al.: “A compact X-ray free-electron laser emitting in the sub-ångström region”, *nature photonics* **6**, 540–544 (2012)
- [93] M. Iwamura, S. Takeuchi, T. Tahara: “Real-time observation of the photoinduced structural change of bis (2, 9-dimethyl-1, 10-phenanthroline) copper (I) by femtosecond fluorescence spectroscopy: a realistic potential curve of the Jahn- Teller distortion”, *Journal of the American Chemical Society* **129**, 5248–5256 (2007)

- [94] M. Iwamura, S. Takeuchi, T. Tahara: "Ultrafast excited-state dynamics of copper (I) complexes", *Accounts of chemical research* **48**, 782–791 (2015)
- [95] M. Iwamura, H. Watanabe, K. Ishii, et al.: "Coherent nuclear dynamics in ultrafast photoinduced structural change of bis (diimine) copper (I) complex", *Journal of the American Chemical Society* **133**, 7728–7736 (2011)
- [96] A. Jacques, O. Schott, K. Robeyns, et al.: "Hydrogen Photoevolution from a Green-Absorbing Iridium (III)–Cobalt (III) Dyad", *European Journal of Inorganic Chemistry* **2016**, 1779–1783 (2016)
- [97] L. Jacquet, R. J. H. Davies, A. Kirsch-De Mesmaeker, et al.: "Photoaddition of Ru (tap) 2 (bpy) 2+ to DNA: A new mode of covalent attachment of metal complexes to duplex DNA", *Journal of the American Chemical Society* **119**, 11763–11768 (1997)
- [98] R. M. Jay, S. Eckert, V. Vaz da Cruz, et al.: "Covalency-Driven Preservation of Local Charge Densities in a Metal-to-Ligand Charge-Transfer Excited Iron Photosensitizer", *Angewandte Chemie International Edition* **58**, 10742–10746 (2019)
- [99] Y.-K. Jiang, J.-H. Liu: "DFT studies of cobalt hydride intermediate on cobaloxime-catalyzed H<sub>2</sub> evolution pathways", *International Journal of Quantum Chemistry* **112**, 2541–2546 (2012)
- [100] S. Kajouj, L. Marcélis, V. Lemaury, et al.: "Photochemistry of ruthenium (ii) complexes based on 1, 4, 5, 8-tetraazaphenanthrene and 2, 2'-bipyridine: a comprehensive experimental and theoretical study", *Dalton Transactions* **46**, 6623–6633 (2017)
- [101] T. Katayama, T. Hirano, Y. Morioka, et al.: "X-ray optics for advanced ultrafast pump–probe X-ray experiments at SACLA", *Journal of synchrotron radiation* **26**, 333–338 (2019)
- [102] T. Katayama, T. Northey, W. Gawelda, et al.: "Tracking multiple components of a nuclear wavepacket in photoexcited Cu (I)-phenanthroline complex using ultrafast X-ray spectroscopy", *Nature communications* **10**, 1–8 (2019)
- [103] T. Katayama, S. Nozawa, Y. Umena, et al.: "A versatile experimental system for tracking ultrafast chemical reactions with X-ray free-electron lasers", *Structural Dynamics* **6**, 054302 (2019)
- [104] T. Katayama, S. Owada, T. Togashi, et al.: "A beam branching method for timing and spectral characterization of hard X-ray free-electron lasers", *Structural Dynamics* **3**, 034301 (2016)
- [105] S. Kaufhold, K. Wärnmark: "Design and synthesis of photoactive iron n-heterocyclic carbene complexes", *Catalysts* **10**, 132 (2020)
- [106] M. Kavčič, M. Petric, A. Rajh, et al.: "Characterization of Li–S Batteries Using Laboratory Sulfur X-ray Emission Spectroscopy", *ACS Applied Energy Materials* **4**, 2357–2364 (2021)

- [107] M. S. Kelley, M. L. Shelby, M. W. Mara, et al.: “Ultrafast dynamics of two copper bis-phenanthroline complexes measured by x-ray transient absorption spectroscopy”, *Journal of Physics B: Atomic, Molecular and Optical Physics* **50**, 154006 (2017)
- [108] J. M. Kelly, D. J. McConnell, C. OhUigin, et al.: “Ruthenium polypyridyl complexes; their interaction with DNA and their role as sensitizers for its photocleavage”, *Journal of the Chemical Society, Chemical Communications*, 1821–1823 (1987)
- [109] D. Khakhulin, F. Otte, M. Biednov, et al.: “Ultrafast x-ray photochemistry at European XFEL: Capabilities of the femtosecond x-ray experiments (FXE) instrument”, *Applied Sciences* **10**, 995 (2020)
- [110] K. King, R. Watts: “Dual emission from an ortho-metalated iridium (III) complex”, *Journal of the American Chemical Society* **109**, 1589–1590 (1987)
- [111] R. V. Kiran, C. F. Hogan, B. D. James, et al.: “Photophysical and Electrochemical Properties of Phenanthroline-Based Bis-cyclometallated Iridium Complexes in Aqueous and Organic Media”, *European Journal of Inorganic Chemistry* **2011**, 4816–4825 (2011)
- [112] K. S. Kjær, K. Kunnus, T. C. Harlang, et al.: “Solvent control of charge transfer excited state relaxation pathways in [Fe (2, 2-bipyridine)(CN) 4] 2-”, *Physical Chemistry Chemical Physics* **20**, 4238–4249 (2018)
- [113] K. S. Kjær, T. B. Van Driel, T. C. Harlang, et al.: “Finding intersections between electronic excited state potential energy surfaces with simultaneous ultrafast X-ray scattering and spectroscopy”, *Chemical science* **10**, 5749–5760 (2019)
- [114] K. S. Kjær, N. Kaul, O. Prakash, et al.: “Luminescence and reactivity of a charge-transfer excited iron complex with nanosecond lifetime”, *Science* **363**, 249–253 (2019)
- [115] M. Koch, M. Myahkostupov, D. G. Oblinsky, et al.: “Charge localization after ultrafast photoexcitation of a rigid perylene perylenediimide dyad visualized by transient stark effect”, *Journal of the American Chemical Society* **139**, 5530–5537 (2017)
- [116] M. O. Krause, J. Oliver: “Natural widths of atomic K and L levels, K  $\alpha$  X-ray lines and several KLL Auger lines”, *Journal of Physical and Chemical Reference Data* **8**, 329–338 (1979)
- [117] K. Kunnus, M. Vacher, T. C. Harlang, et al.: “Vibrational wavepacket dynamics in Fe carbene photosensitizer determined with femtosecond X-ray emission and scattering”, *Nature communications* **11**, 1–11 (2020)
- [118] S. Lafuerza, A. Carlantuono, M. Retegan, et al.: “Chemical Sensitivity of K $\beta$  and K $\alpha$  X-ray Emission from a Systematic Investigation of Iron Compounds”, *Inorganic Chemistry* **59**, 12518–12535 (2020)
- [119] S. Lamansky, P. Djurovich, D. Murphy, et al.: “Highly phosphorescent bis-cyclometalated iridium complexes: synthesis, photophysical

- characterization, and use in organic light emitting diodes”, *Journal of the American Chemical Society* **123**, 4304–4312 (2001)
- [120] X. Lang, J. Zhao, X. Chen: “Cooperative photoredox catalysis”, *Chemical Society Reviews* **45**, 3026–3038 (2016)
- [121] J.-P. Lecomte, A. Kirsch-De Mesmaeker, M. M. Feeney, et al.: “Ruthenium (II) complexes with 1, 4, 5, 8, 9, 12-hexaazatriphenylene and 1, 4, 5, 8-tetraazaphenanthrene ligands: key role played by the photoelectron transfer in DNA cleavage and adduct formation”, *Inorganic chemistry* **34**, 6481–6491 (1995)
- [122] J.-P. Lecomte, A. K.-D. Mesmaeker, J. M. Kelly, et al.: “PHOTO-INDUCED ELECTRON TRANSFER FROM NUCLEOTIDES TO RUTHENIUM-TRIS-1, 4, 5, 8TETRAAZAPHENANTHRENE: MODEL FOR PHOTOSENSITIZED DNA OXIDATION”, *Photochemistry and photobiology* **55**, 681–689 (1992)
- [123] H. T. Lemke, K. S. Kjær, R. Hartsock, et al.: “Coherent structural trapping through wave packet dispersion during photoinduced spin state switching”, *Nature communications* **8**, 1–8 (2017)
- [124] C. Lentz, O. Schott, T. Auvray, et al.: “Photocatalytic hydrogen production using a red-absorbing Ir (III)–Co (III) dyad”, *Inorganic chemistry* **56**, 10875–10881 (2017)
- [125] D. Leshchev, T. C. Harlang, L. A. Fredin, et al.: “Tracking the picosecond deactivation dynamics of a photoexcited iron carbene complex by time-resolved X-ray scattering”, *Chemical science* **9**, 405–414 (2018)
- [126] G. Levi, E. Biasin, A. O. Dohn, et al.: “On the interplay of solvent and conformational effects in simulated excited-state dynamics of a copper phenanthroline photosensitizer”, *Physical Chemistry Chemical Physics* **22**, 748–757 (2020)
- [127] C. Li, M. Z. Hoffman: “Electron Localization or Delocalization in the MLCT Excited States of Ru (bpy) 3<sup>2+</sup> and Ru (phen) 3<sup>2+</sup>. Consequences to Their Photochemistry and Photophysics in Fluid Solution”, *Inorganic Chemistry* **37**, 830–832 (1998)
- [128] C. Liu, J. Zhang, L. M. Lawson Daku, et al.: “Probing the impact of solvation on photoexcited spin crossover complexes with high-precision x-ray transient absorption spectroscopy”, *Journal of the American Chemical Society* **139**, 17518–17524 (2017)
- [129] Y. Liu, T. Harlang, S. E. Canton, et al.: “Towards longer-lived metal-to-ligand charge transfer states of iron (II) complexes: an N-heterocyclic carbene approach”, *Chemical communications* **49**, 6412–6414 (2013)
- [130] Y. Liu, P. Persson, V. Sundström, et al.: “Fe N-heterocyclic carbene complexes as promising photosensitizers”, *Accounts of chemical research* **49**, 1477–1485 (2016)

- [131] S. Losse, J. G. Vos, S. Rau: “Catalytic hydrogen production at cobalt centres”, *Coordination Chemistry Reviews* **254**, 2492–2504 (2010)
- [132] M. S. Lowry, S. Bernhard: “Synthetically tailored excited states: phosphorescent, cyclometalated iridium (III) complexes and their applications”, *Chemistry–A European Journal* **12**, 7970–7977 (2006)
- [133] T. H. Maiman: “Stimulated optical radiation in ruby”, *Nature* **187**, 493–494 (1960)
- [134] A. M. March, T. A. Assefa, C. Boemer, et al.: “Probing transient valence orbital changes with picosecond valence-to-core X-ray emission spectroscopy”, *The Journal of Physical Chemistry C* **121**, 2620–2626 (2017)
- [135] G. Margaritondo: “A primer in synchrotron radiation: everything you wanted to know about SEX (Synchrotron Emission of X-rays) but were afraid to ask”, *Journal of synchrotron radiation* **2**, 148–154 (1995)
- [136] G. Margaritondo: *Elements of synchrotron light: for biology, chemistry, and medical research* (Oxford University Press on Demand 2002)
- [137] G. Margaritondo, P. Rebernik Ribic: “A simplified description of X-ray free-electron lasers”, *Journal of synchrotron radiation* **18**, 101–108 (2011)
- [138] V. Martin-Diaconescu, K. N. Chacón, M. U. Delgado-Jaime, et al.: “K $\beta$  valence to core x-ray emission studies of Cu (I) binding proteins with mixed methionine–histidine coordination. Relevance to the reactivity of the M- and H-sites of peptidylglycine monooxygenase”, *Inorganic chemistry* **55**, 3431–3439 (2016)
- [139] A. Masschelein, L. Jacquet, A. Kirsch-De Mesmaeker, et al.: “Ruthenium complexes with 1, 4, 5, 8-tetraazaphenanthrene. Unusual photophysical behavior of the tris-homoleptic compound”, *Inorganic chemistry* **29**, 855–860 (1990)
- [140] T. Matsushita, H. Hashizume: “X-ray monochromators”, *Handbook on synchrotron radiation* **1**, 261–314 (1983)
- [141] J. K. McCusker: “Electronic structure in the transition metal block and its implications for light harvesting”, *Science* **363**, 484–488 (2019)
- [142] U. Megerle, I. Pugliesi, C. Schrieffer, et al.: “Sub-50 fs broadband absorption spectroscopy with tunable excitation: putting the analysis of ultrafast molecular dynamics on solid ground”, *Applied Physics B* **96**, 215–231 (2009)
- [143] R. Meinhardt: “Entwicklung und Synthese von Ein- und Mehrkomponentensystemen zur photokatalytischen Wasserreduktion”, PhD thesis (Universität Paderborn 2018)
- [144] M. Meister, B. Baumeier, N. Pschirer, et al.: “Observing charge dynamics in surface reactions by time-resolved stark effects”, *The Journal of Physical Chemistry C* **117**, 9171–9177 (2013)

- [145] C. J. Milne, P. Beaud, Y. Deng, et al.: “Opportunities for chemistry at the SwissFEL X-ray Free Electron Laser”, *CHIMIA International Journal for Chemistry* **71**, 299–307 (2017)
- [146] C. J. Milne, T. Schietinger, M. Aiba, et al.: “SwissFEL: the Swiss X-ray free electron laser”, *Applied Sciences* **7**, 720 (2017)
- [147] C. Moucheron, A. Kirsch-De Mesmaeker: “New DNA-binding ruthenium (II) complexes as photo-reagents for mononucleotides and DNA”, *Journal of physical organic chemistry* **11**, 577–583 (1998)
- [148] R. B. Nair, B. M. Cullum, C. J. Murphy: “Optical properties of [Ru (phen) 2dppz] 2+ as a function of nonaqueous environment”, *Inorganic chemistry* **36**, 962–965 (1997)
- [149] K. Nakajima, Y. Joti, T. Katayama, et al.: “Software for the data analysis of the arrival-timing monitor at SACLA”, *Journal of synchrotron radiation* **25**, 592–603 (2018)
- [150] M. Nazari, C. Bösch, A. Rondi, et al.: “Ultrafast dynamics in polycyclic aromatic hydrocarbons: the key case of conical intersections at higher excited states and their role in the photophysics of phenanthrene monomer”, *Physical Chemistry Chemical Physics* **21**, 16981–16988 (2019)
- [151] J. Olofsson, B. Önfelt, P. Lincoln: “Three-state light switch of [Ru (phen) 2dppz] 2+: Distinct excited-state species with two, one, or no hydrogen bonds from solvent”, *The Journal of Physical Chemistry A* **108**, 4391–4398 (2004)
- [152] E. Olson, D. Hu, A. Hörmann, et al.: “First observation of the key intermediate in the “light-switch” mechanism of [Ru (phen) 2dppz] 2+”, *Journal of the American Chemical Society* **119**, 11458–11467 (1997)
- [153] B. Önfelt, P. Lincoln, B. Nordén, et al.: “Femtosecond linear dichroism of DNA-intercalating chromophores: Solvation and charge separation dynamics of [Ru (phen) 2dppz] 2+ systems”, *Proceedings of the National Academy of Sciences* **97**, 5708–5713 (2000)
- [154] I. Ortman, B. Elias, J. M. Kelly, et al.: “[Ru (TAP) 2 (dppz)] 2+: a DNA intercalating complex, which luminesces strongly in water and undergoes photo-induced proton-coupled electron transfer with guanosine-5-monophosphate”, *Dalton transactions*, 668–676 (2004)
- [155] S. Ott, M. Borgström, M. Kritikos, et al.: “Model of the iron hydrogenase active site covalently linked to a ruthenium photosensitizer: synthesis and photophysical properties”, *Inorganic chemistry* **43**, 4683–4692 (2004)
- [156] M. N. H. Pashaki: “Long-range Energy Transfer in DNA-Hosted Multichromophoric Systems by Ultrafast 1D and 2D Fs UV-Vis Transient Absorption Spectroscopy: Inauguraldissertation Der Philosophisch-naturwissenschaftlichen Fakultät Der Universität Bern”, PhD thesis (Universität Bern 2018)

- [157] M. N. H. Pashaki, T.-K. Choi, E. J. Rohwer, et al.: “Unveiling the origin of photo-induced enhancement of oxidation catalysis at Mo (VI) centres of Ru (II)–Mo (VI) dyads”, *Chemical Communications* (2021)
- [158] T. J. Penfold, S. Karlsson, G. Capano, et al.: “Solvent-induced luminescence quenching: Static and time-resolved x-ray absorption spectroscopy of a copper (I) phenanthroline complex”, *The Journal of Physical Chemistry A* **117**, 4591–4601 (2013)
- [159] C. J. Pollock, S. DeBeer: “Insights into the geometric and electronic structure of transition metal centers from valence-to-core X-ray emission spectroscopy”, *Accounts of chemical research* **48**, 2967–2975 (2015)
- [160] C. J. Pollock, M. U. Delgado-Jaime, M. Atanasov, et al.: “ $K\beta$  mainline X-ray emission spectroscopy as an experimental probe of metal–ligand covalency”, *Journal of the American Chemical Society* **136**, 9453–9463 (2014)
- [161] B. C. Poulsen, S. Estalayo-Adrián, S. Blasco, et al.: “Luminescent ruthenium polypyridyl complexes with extended ‘dppz’-like ligands as DNA targeting binders and cellular agents”, *Dalton Transactions* **45**, 18208–18220 (2016)
- [162] C. K. Prier, D. A. Rankic, D. W. MacMillan: “Visible light photoredox catalysis with transition metal complexes: applications in organic synthesis”, *Chemical reviews* **113**, 5322–5363 (2013)
- [163] B. Ravel, M. Newville: “ATHENA, ARTEMIS, HEPHAESTUS: data analysis for X-ray absorption spectroscopy using IFEFFIT”, *Journal of synchrotron radiation* **12**, 537–541 (2005)
- [164] J. J. Rehr, R. C. Albers: “Theoretical approaches to x-ray absorption fine structure”, *Reviews of modern physics* **72**, 621 (2000)
- [165] P. Russo: *Handbook of X-ray imaging: physics and technology* (CRC press 2017)
- [166] L. Salassa, C. Garino, G. Salassa, et al.: “Ligand-selective photodissociation from [Ru (bpy)(4AP) 4] 2+: a spectroscopic and computational study”, *Inorganic chemistry* **48**, 1469–1481 (2009)
- [167] L. Salassa, D. Gianolio, C. Garino, et al.: “Structure of [Ru (bpy) n (AP)(6-2n)] 2+ homogeneous complexes: DFT calculation vs. EXAFS”, *Journal of Physics: Conference Series*, vol. 190, 1, IOP Publishing, 012141 (2009)
- [168] E. Saldin, E. Schneidmiller, M. V. Yurkov: *The physics of free electron lasers* (Springer Science & Business Media 1999)
- [169] T. Sato, S. Nozawa, A. Tomita, et al.: “Coordination and electronic structure of ruthenium (II)-tris-2, 2-bipyridine in the triplet metal-to-ligand charge-transfer excited state observed by picosecond time-resolved Ru K-edge XAFS”, *The Journal of Physical Chemistry C* **116**, 14232–14236 (2012)
- [170] D. Schallenberg, A. Neubauer, E. Erdmann, et al.: “Dinuclear Ru/Ni, Ir/Ni, and Ir/Pt Complexes with Bridging Phenanthroline-5, 6-Dithiolate: Synthesis,

- Structure, and Electrochemical and Photophysical Behavior”, *Inorganic chemistry* **53**, 8859–8873 (2014)
- [171] J. R. Schoonover, W. D. Bates, T. J. Meyer: “Application of resonance Raman spectroscopy to electronic structure in metal complex excited states. Excited-state ordering and electron delocalization in dipyrido [3, 2-a: 2', 3'-c] phenazine (dppz): Complexes of Re (I) and Ru (II)”, *Inorganic Chemistry* **34**, 6421–6422 (1995)
- [172] G. Schrauzer, G. Parshall, E. Wonchoba: “Bis (Dimethylglyoximato) Cobalt Complexes: (“Cobaloximes”)”, *Inorganic Syntheses* **11**, 61–70 (1968)
- [173] M. Schwalbe, M. Karnahl, S. Tschierlei, et al.: “The switch that wouldn't switch—unexpected luminescence from a ruthenium (ii)-dppz-complex in water”, *Dalton Transactions* **39**, 2768–2771 (2010)
- [174] K. Schwalenstocker, J. Paudel, A. W. Kohn, et al.: “Cobalt  $K\beta$  valence-to-core X-ray emission spectroscopy: a study of low-spin octahedral cobalt (III) complexes”, *Dalton Transactions* **45**, 14191–14202 (2016)
- [175] G. B. Shaw, C. D. Grant, H. Shirota, et al.: “Ultrafast structural rearrangements in the MLCT excited state for copper (I) bis-phenanthrolines in solution”, *Journal of the American Chemical Society* **129**, 2147–2160 (2007)
- [176] Z. A. Siddique, Y. Yamamoto, T. Ohno, et al.: “Structure-dependent photophysical properties of singlet and triplet metal-to-ligand charge transfer states in copper (I) bis (diimine) compounds”, *Inorganic chemistry* **42**, 6366–6378 (2003)
- [177] G. Smolentsev, B. Cecconi, A. Guda, et al.: “Microsecond X-ray absorption spectroscopy identification of Co (I) intermediates in cobaloxime-catalyzed hydrogen evolution”, *Chemistry (Weinheim an der Bergstrasse, Germany)* **21**, 15158 (2015)
- [178] G. Smolentsev, C. J. Milne, A. Guda, et al.: “Taking a snapshot of the triplet excited state of an OLED organometallic luminophore using X-rays”, *Nature communications* **11**, 1–9 (2020)
- [179] B. L. Souza, L. A. Faustino, F. S. Prado, et al.: “Spectroscopic characterization of a new Re (I) tricarbonyl complex with a thiosemicarbazone derivative: towards sensing and electrocatalytic applications”, *Dalton Transactions* **49**, 16368–16379 (2020)
- [180] C. W. Stark, W. J. Schreier, J. Lucon, et al.: “Interligand electron transfer in heteroleptic ruthenium (II) complexes occurs on multiple time scales”, *The Journal of Physical Chemistry A* **119**, 4813–4824 (2015)
- [181] D. Stearns: “Broadening of extended X-ray absorption fine structure arising from the finite lifetime of the K hole”, *Philosophical Magazine B* **49**, 541–558 (1984)
- [182] H. C. Stynes, J. A. Ibers: “Effect of metal-ligand bond distances on rates of electron-transfer reactions. Crystal structures of hexaammineruthenium (II)

- iodide, $[\text{Ru}(\text{NH}_3)_6] \text{I}_2$ , and hexaammineruthenium (III) tetrafluoroborate, $[\text{Ru}(\text{NH}_3)_6][\text{BF}_4]_3$ ”, *Inorganic Chemistry* **10**, 2304–2308 (1971)
- [183] P. A. Summers, J. A. Calladine, F. Ghiotto, et al.: “Synthesis and photophysical study of a [NiFe] hydrogenase biomimetic compound covalently linked to a Re-diimine photosensitizer”, *Inorganic chemistry* **55**, 527–536 (2016)
- [184] J. Szlachetko, M. Nachtegaal, E. De Boni, et al.: “A von Hamos x-ray spectrometer based on a segmented-type diffraction crystal for single-shot x-ray emission spectroscopy and time-resolved resonant inelastic x-ray scattering studies”, *Review of Scientific Instruments* **83**, 103105 (2012)
- [185] A. Tarnovsky, W. Gawelda, M. Johnson, et al.: “Photexcitation of aqueous ruthenium (ii)-tris-(2, 2'-bipyridine) with high-intensity femtosecond laser pulses”, *The Journal of Physical Chemistry B* **110**, 26497–26505 (2006)
- [186] H. Tatsuno, K. S. Kjær, K. Kunnus, et al.: “Hot Branching Dynamics in a Light-Harvesting Iron Carbene Complex Revealed by Ultrafast X-ray Emission Spectroscopy”, *Angewandte Chemie* **132**, 372–380 (2020)
- [187] A. Thapper, S. Styring, G. Saracco, et al.: “Artificial photosynthesis for solar fuels—an evolving research field within AMPEA, a joint programme of the European energy research alliance”, *Green* **3**, 43–57 (2013)
- [188] K. Tono, T. Togashi, Y. Inubushi, et al.: “Beamline, experimental stations and photon beam diagnostics for the hard x-ray free electron laser of SACLA”, *New Journal of Physics* **15**, 083035 (2013)
- [189] T. Tschentscher, C. Bressler, J. Grünert, et al.: “Photon beam transport and scientific instruments at the European XFEL”, *Applied Sciences* **7**, 592 (2017)
- [190] S. Tschierlei, A. Neubauer, N. Rockstroh, et al.: “Ultrafast excited state dynamics of iridium (III) complexes and their changes upon immobilisation onto titanium dioxide layers”, *Physical Chemistry Chemical Physics* **18**, 10682–10687 (2016)
- [191] M. Tünnermann: “Photocatalytic Water Reduction Systems Based on Iridium and Non-noble Metal Complexes”, PhD thesis (Universität Paderborn 2018)
- [192] M. Tünnermann, P. Rehsies, U. Flörke, et al.: “A Straightforward Synthesis to Novel 1, 10-Phenanthrolines with Fused Thiophene Structure”, *Synlett* **29**, 2638–2642 (2018)
- [193] C. Turro, Y. C. Chung, N. Leventis, et al.: “Resonance Raman Spectrum of the Phenanthroline Anion: Implications on Electron Delocalization in the MLCT Excited State of Ru (phen)  $32^+$ ”, *Inorganic chemistry* **35**, 5104–5106 (1996)
- [194] J. Van Houten, R. J. Watts: “Temperature dependence of the photophysical and photochemical properties of the tris (2, 2'-bipyridyl) ruthenium (II) ion in aqueous solution”, *Journal of the American Chemical Society* **98**, 4853–4858 (1976)
- [195] G. Vanko, A. Bordage, M. Pápai, et al.: “Detailed characterization of a nanosecond-lived excited state: X-ray and theoretical investigation of the

- quintet state in photoexcited [Fe (terpy) 2] 2+”, *The Journal of Physical Chemistry C* **119**, 5888–5902 (2015)
- [196] J. Vegelius, K. Kvashnina, M. Klintonberg, et al.: “Cu K $\beta$  2, 5 X-ray emission spectroscopy as a tool for characterization of monovalent copper compounds”, *Journal of Analytical Atomic Spectrometry* **27**, 1882–1888 (2012)
- [197] M. H. Wall, P. Basu, T. Buranda, et al.: “Photoinduced electron transfer in covalently linked oxomolybdenum (V) porphyrin systems”, *Inorganic chemistry* **36**, 5676–5677 (1997)
- [198] J. J. Warren, J. M. Mayer: “Moving protons and electrons in biomimetic systems”, *Biochemistry* **54**, 1863–1878 (2015)
- [199] A. P. Wilde, K. A. King, R. J. Watts: “Resolution and analysis of the components in dual emission of mixed-chelate/ortho-metalate complexes of iridium (III)”, *The Journal of Physical Chemistry* **95**, 629–634 (1991)
- [200] J. Willkomm, E. Reisner: “Photo- and electrocatalytic H<sub>2</sub> evolution with cobalt oxime complexes”, *Bulletin of Japan Society of Coordination Chemistry* **71**, 18–29 (2018)
- [201] A. T. Yeh, C. V. Shank, J. K. McCusker: “Ultrafast electron localization dynamics following photo-induced charge transfer”, *Science* **289**, 935–938 (2000)
- [202] S. Zális, C. Consani, A. El Nahhas, et al.: “Origin of electronic absorption spectra of MLCT-excited and one-electron reduced 2, 2'-bipyridine and 1, 10-phenanthroline complexes”, *Inorganica Chimica Acta* **374**, 578–585 (2011)
- [203] A. H. Zewail: “Femtochemistry: Atomic-scale dynamics of the chemical bond”, *The Journal of Physical Chemistry A* **104**, 5660–5694 (2000)
- [204] W. Zhang, R. Alonso-Mori, U. Bergmann, et al.: “Tracking excited-state charge and spin dynamics in iron coordination complexes”, *Nature* **509**, 345–348 (2014)
- [205] P. Zimmer, L. Burkhardt, A. Friedrich, et al.: “The connection between NHC ligand count and photophysical properties in Fe (II) photosensitizers: An experimental study”, *Inorganic chemistry* **57**, 360–373 (2018)
- [206] P. Zimmer, L. Burkhardt, R. Schepper, et al.: “Towards Noble-Metal-Free Dyads: Ground and Excited State Tuning by a Cobalt Dimethylglyoxime Motif Connected to an Iron N-Heterocyclic Carbene Photosensitizer”, *European Journal of Inorganic Chemistry* **2018** (2018)
- [207] P. Zimmer, P. Müller, L. Burkhardt, et al.: “N-Heterocyclic Carbene Complexes of Iron as Photosensitizers for Light-Induced Water Reduction”, *European Journal of Inorganic Chemistry* **2017**, 1504–1509 (2017)
- [208] J. P. Zobel, O. S. Bokareva, P. Zimmer, et al.: “Intersystem Crossing and Triplet Dynamics in an Iron (II) N-Heterocyclic Carbene Photosensitizer”, *Inorganic chemistry* **59**, 14666–14678 (2020)

---

# Eidesstattliche Versicherung

Hiermit versichere ich an Eides statt, die vorliegende Dissertation selbst verfasst und keine anderen als die angegebenen Hilfsmittel benutzt zu haben. Die eingereichte schriftliche Fassung entspricht der auf dem elektronischen Speichermedium. Ich versichere, dass diese Dissertation nicht in einem früheren Promotionsverfahren eingereicht wurde.

---

Tae Kyu Choi

Hamburg, den 23.07.2021